8-13-2020

Second Harmonic Generation Spectroscopy and Microscopy of Liposomes, Nanoparticles, and Cells

Prakash Hamal
Louisiana State University and Agricultural and Mechanical College

SECOND HARMONIC GENERATION SPECTROSCOPY AND MICROSCOPY OF LIPOSOMES, NANOPARTICLES, AND CELLS

A Dissertation

Submitted to the Graduate Faculty of the
Louisiana State University and
Agricultural Mechanical College
in partial fulfillment of the
requirements for the degree of
Doctor of Philosophy

in

The Department of Chemistry

by
Prakash Hamal
B.S. Southeastern Louisiana University, 2016
December 2020

This PhD Dissertation is
Dedicated to
My Father (Durga Bahadur Hamal),
My Mother (Gyanu Hamal),
My Brother (Pradip Hamal),
and My Wife (Amita Shrestha)

Acknowledgements

I express sincere gratitude to my advisor, Professor Louis Haber, for giving me this wonderful opportunity to join his group and for his immeasurable guidance during my time at Louisiana State University. I am very grateful for his support, advice, and having so much faith and patience with me. His immense vision to overcome the expected and unexpected obstacles we faced during different projects has been the strongest pillars of my graduate life. Lastly, I would like to mention that if I had to go over the Ph.D. journey again, I would definitely join Dr. Haber's group, as his tutelage in both science and life have been very inspiring for me.

I am thankful to Professor Robin McCarley for his thoughts and great suggestions in our collaborative projects. It has been a wonderful experience to work in close collaboration with Dr. McCarley's group as most of my projects were impossible to carry out without excellent samples from his group. Additionally, I am grateful to my committee members Dr. Robin McCarley, Dr. John Pojman, and Dr. J. Michael Mathis for their priceless time, encouragement, and on agreeing to serve as my committee members. Similarly, I would like to thank Dr. Daniel Hayes, Dr. Revati Kumar, and Dr. Manas Gartia for their support, ideas, suggestions, and valuable discussions in different collaborative projects. I am also thankful to Dr. Kresimir Rupnik for great suggestions and discussions. I must also thank the Dumas family and LSU Chemistry for selecting me as a recipient of the Jerry D. Dumas and Nancy L. Dumas Fellowship.

I have been very fortunate to have excellent collaborations with different research groups. I would like to thank Dr. Huy Nguyen and Visal Subasinghege Don for their

continuous participation in liposome projects. Similarly, I would like to thank Peter Piers, Dr. Sushant Sahu, and Dr. David Burk for their help in the SHG microscopy project. I am grateful to Dr. Mohammad Abu-Laban for collaborations in miRNA projects. I am also thankful to Ying Xiao for her help with electron microscopy and Dr. Rafael Cueto for help with dynamic light scattering measurements.

I must thank all the former and current members of the Haber group: Dr. Raju Kumal, Dr. Rami Khoury, Dr. Holden Smith, Dr. Jeewan Ranasinghe, Asela Sampath Dikkumbura, Min Chen, and Daniel Babayode. I have enjoyed your discussions, suggestions, and participations throughout my graduate journey. It has been my pleasure to know and work with each of you.

Friends and family are an integral part of my life. My father and mother have been instrumental in developing and nurturing me. My younger brother is a vital part of my life. I would like to thank Pratyush Charan Pradhanang and Apurba Adhikary for being exemplary friends. I am very grateful to have these wonderful people around me.

Finally, I would like to thank the most important person in my life; Amita Shrestha, my wife. I don’t think any words can describe your sacrifice, belief, and support towards me. Additionally, your optimism in every small thing has helped me to overcome many hurdles in our life. I am really excited and looking forward to our lifelong journey. I would just say this doctorate degree is equally yours.

Table of Contents

List of Figures

Abstract

Second harmonic generation (SHG) is used to investigate the factors that impact nanoparticle-based drug-delivery applications. In the first study, molecular adsorption and transport kinetics of a positively-charged dye, malachite green isothiocyanate (MGITC), is characterized at the surface of different colloidal liposomes in water using SHG spectroscopy. The molecular interactions of MGITC is compared to our previous investigations with malachite green (MG). In comparison to MG, MGITC demonstrates stronger adsorption and faster transport through lipid membranes. Correspondingly, the SHG experimental results are in excellent agreement with the molecular dynamics (MD) simulations results. A key finding illustrates the importance of functional groups, such as isothiocyanate, in controlling molecular translocation across the phospholipid-water interface. In a related study, temperature-dependent SHG measurements are performed to investigate the thermodynamics associated with the adsorption and transport kinetics of MG at the surface of 1,2-dioleoyl-sn-glycero-3phospho-(1'rac-glycerol) (DOPG) liposomes. The molecular transport is determined to be approximately 5 times faster at 40 ºC in comparison to the molecular transport at 25 ºC. Additionally, the changes in adsorption enthalpy and entropy are determined. The change in adsorption entropy is positive and the change in adsorption enthalpy is negative, indicating that the adsorption process is spontaneous at all aqueous temperatures. Similarly, SHG microscopy is used to probe the molecular interactions of MG and MGITC molecules at the surface of living human nonsmall adenosquamous lung cancer cells (H596 cells). The observed molecular translocation in living H596 cells is significantly faster for MGITC in comparison to MG. SHG microscopy is also used to probe fixed, dead H596 cells with MGITC dye molecules.

In comparison to fixed cells, living cells have pronounced fluctuations of SHG intensity which is attributed to more complicated interactions, including active transport and cell regulation. Finally, gold, silver, and gold-silver-gold core-shell-shell (CSS) plasmonic nanoparticles having size of 10-100 nm are synthesized and functionalized with miRNA molecules using Diels-Alder chemistry. The retro Diels-Alder thermal release of miRNA from the surface of novel plasmonic nanoparticles is investigated at their corresponding plasmon resonances using surface-specific SHG spectroscopy. In summary, these time-resolved studies highlight the importance of SHG as a sensitive, powerful, and versatile tool to monitor the real-time surface chemistry of colloidal nanoparticle-based drug-delivery systems.

Chapter 1. Introduction to Colloidal Nanoparticles and Second Harmonic Generation

1.1 Colloidal Nanoparticle Interfaces

Colloidal science has become an integral part of technological development as it encompasses a broad range of chemical and biological systems.[1-4] The structural modification of colloidal systems dates back to the earliest technological advances, such as pottery making or fabrication of soaps. A variety of colloidal systems are now used as advanced industrial products including papers, ceramics, and coatings in the chemical industry as well as aerosols, semiconductors, and solar cells in the materials industry.[4-13] The synthesis and characterization of nano- and micro-sized particles suspended in aqueous colloidal solutions are currently being investigated for potential applications in catalysis, sensing, photovoltaics, optoelectronics, solar cells, and drug delivery.[14-21] Figure 1.1 is the schematic representation of various colloidal-based nanoparticle and microparticle systems extensively investigated in the Haber lab. A typical colloidal system consists of two important phases; the colloidal particle and the solvent into which the particle is dispersed. These two phases are divided by an interface, where surface phenomena like adsorption, desorption, and formation of an electrical double layer take place.[2,3] Therefore, it is essential to characterize structural modifications and dynamic processes at colloidal interfaces to gain a critical and fundamental understanding of particle-solvent interactions. Additionally, the energetics, interactions, and associated kinetics are markedly different in the bulk and interface regions.

Various analytical tools have been developed to quantify the molecular and chemical interactions at the colloidal interfaces. One of the traditional techniques to study molecular adsorption is the centrifugation-separation method.[14] Additional techniques for investigating interfacial interactions include quartz-crystal microbalance (QCM),[22] fluorescence spectroscopy,[23] and surface plasmon resonance (SPR).[24] However, most of the developed techniques require additional labeling agents or larger molecular analytes (>10 kDa).[22-24] In order to study relevant interactions at colloidal interfaces, label-free techniques with high surface-sensitivity are highly advantageous for providing critical insights on interfacial properties of colloidal systems.

Nonlinear optical techniques like second harmonic generation (SHG) and sum frequency generation (SFG) provide high surface-sensitivity and selectivity to detect small molecules at colloidal interfaces of nano- and micro-sized particles.[14,25] In 1996, Eisenthal and coworkers first demonstrated that a strong SHG signal can be detected at the surface of a colloidal microparticle system.[26] This successful demonstration led to numerous studies on different colloidal interfaces using this technique. SHG has shown remarkable promise in the last 20 years as several groups have used SHG to study molecular orientations,[19] chemical reactions,[18,27] surface potentials of charged systems,[28-30] and the binding of molecules at a membrane.[25,31-35] A primary focus of this thesis is the use of the second harmonic generation technique to study equilibria and interfacial dynamics at biological membranes and plasmonic nanoparticles systems.

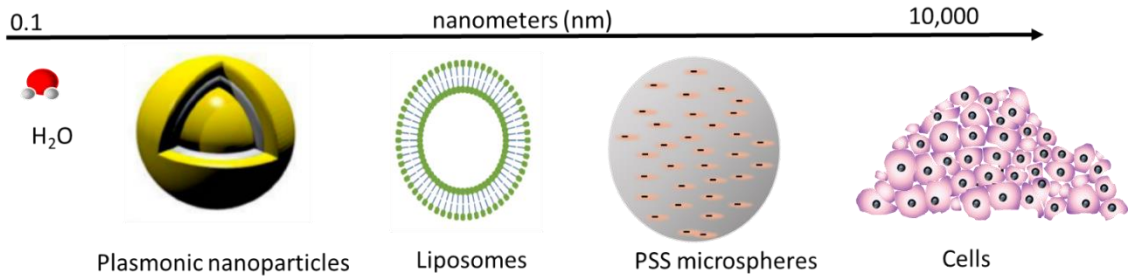

Figure 1.1. Schematic representation of colloidal systems studied in the Haber lab.

1.2 Biological Membranes

Living cells are the structural and functional unit of life.[36] A typical cell consists of several membrane-bound organelles such as the mitochondria and the cell nucleus, as well as internal vesicles for processes such as cellular digestion, secretion, and molecular transport.[37-39] Additionally, one of the integral components of a living cell is the cellular membrane, also known as a plasma membrane. The plasma membrane is a selectively permeable membrane that regulates the movement of molecules and ions between the cell and the surrounding environment.[36] Figure 1.2 depicts a generalized cell membrane morphology. The cell membrane is composed primarily of a phospholipid bilayer, where the outer layers on both sides are composed of hydrophilic phosphate groups that favor the aqueous environment while the inner portion of the bilayer is composed of hydrophobic groups that are mostly hydrocarbons, which are shielded by the outer hydrophilic groups.[25,36,40] Additionally, the cell membrane also has different types of membrane proteins. Integral membrane proteins are a major constituent in ion channels, which allows the ions to pass from one side of the membrane to the other.[41,42] Correspondingly, peripheral membrane proteins are involved in cell signaling and cell receptors.[41,42]

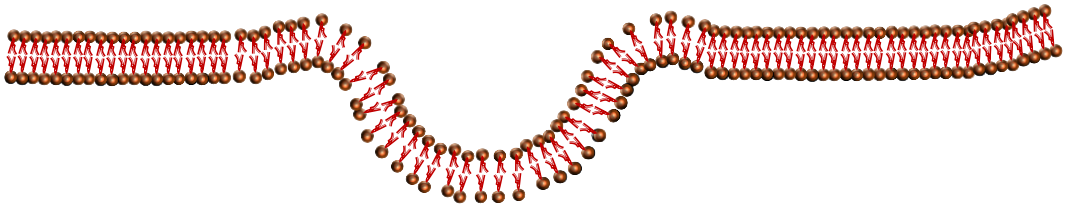

Figure 1.2. Illustration of a cell membrane composed of a lipid bilayer.

1.3 Colloidal Phospholipid Liposomes

Colloidal liposomes are small, spherical vesicles that are typically composed of phospholipids. Phospholipids are amphiphilic molecules, meaning they are composed of both hydrophobic and hydrophilic molecules, as shown in Figure 1.3. Cell membranes and liposomes have structural and chemical similarities so liposomes are considered to be models of cell membranes, especially when the liposomes are made of the same lipids found in cell membranes.[32,43,44] Additionally, liposomes are one of the very few nanoparticles that have been used in humans for drug-delivery purposes.[45-47] Drugs used for cancer treatments, like doxorubicin and paclitaxel, are embedded in liposome samples to increase the efficacy of these drugs. These salient features of liposomes make them excellent candidates for studying the relevant molecular and chemical interactions at lipid interfaces in water. Scheme 1.1 demonstrates a generalized principle where drug molecules with varying lipophilicities are encapsulated and introduced to diseased biological tissue for liposomes-based drug-delivery applications.[48-50]

In recent years, significant research has focused on gaining fundamental information regarding molecule-membrane interactions. Understanding the physiochemical interactions between small molecules and cell membranes can lead

to important progress in advancing pharmaceutical research and developing membrane-based drug-delivery applications. Methods such as electron spin resonance (ESR), the patch clamp technique, and fluorescence spectroscopy have all been used to investigate complicated aspects of molecule-membrane interactions.[23,51,52] In comparison to these techniques, SHG spectroscopy has shown incredible promise for providing enhanced surface sensitivity for studying biological membranes. This thesis describes the successful use of second harmonic generation to investigate interfacial interactions at biomolecular membranes.

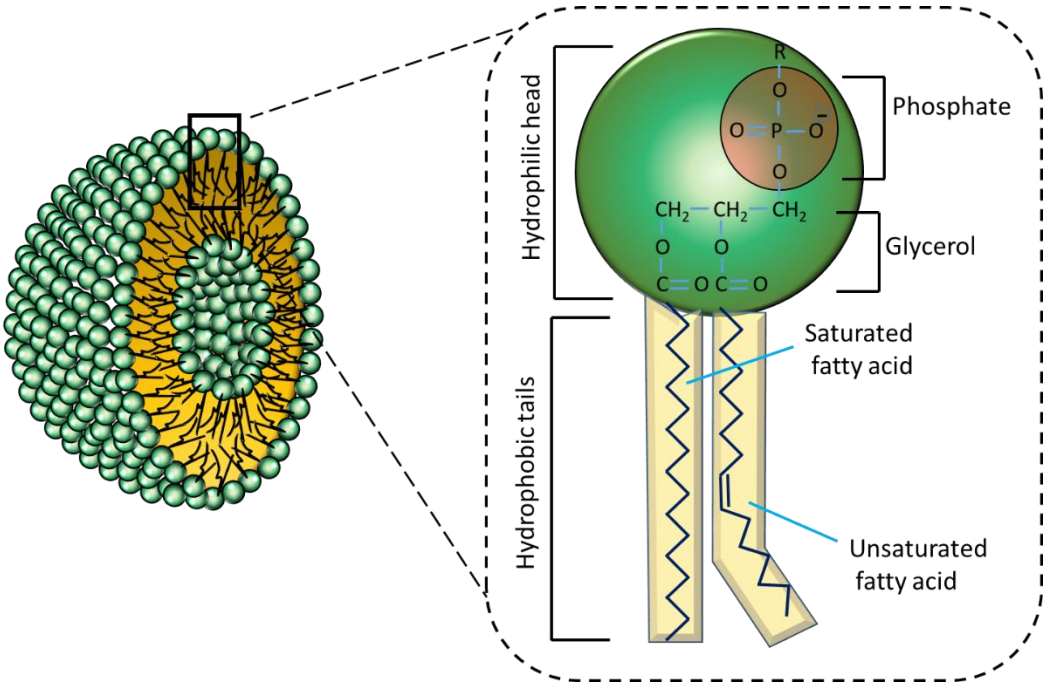

Figure 1.3. Chemical constituents of a colloidal phospholipid liposome.

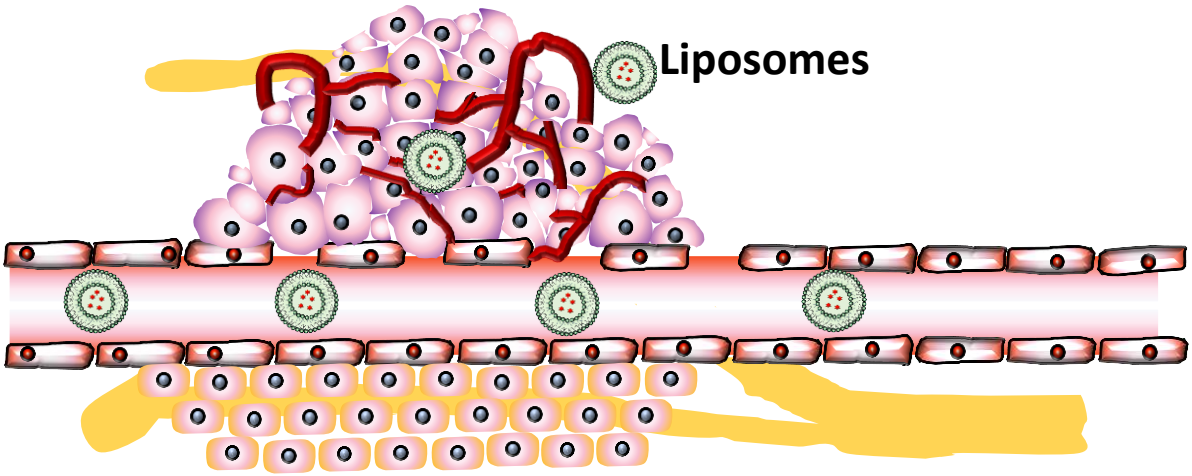

Scheme 1.1. General scheme for liposome samples used in membrane-based drug-delivery applications.

1.4 Colloidal Plasmonic Nanoparticles

Metallic nanoparticles possess unique optical, electric, and magnetic properties which make them potential candidates for applications in molecular sensing, catalysis, and nanomedicine.[18-20,27,53-57] Gold and silver nanoparticles are of especially significant interest due to their strong response in the visible and near-infrared optical wavelengths.[16,54-57] The development of these nanoparticles for biological applications is facilitated by several advantages including their large surface area to volume ratios, their low toxicities with excellent biocompatibilities, and the ease in modifying their chemical surface functionalities.[16,17,58-60] Additionally, the unique optical properties of these nanoparticles are derived from their localized surface plasmon resonances (LSPRs),[53,61] as shown in Figure 1.4, which is characterized by the coherent and collective oscillation of the free electrons under incident light. The LSPR depends on the shape, size, composition, and surrounding medium of the nanoparticle system.[18,27,57] LSPRs can also enhance the optical properties of these nanoparticles by several orders of magnitude,

making them ideal candidates for bio-imaging and bio-labeling.[56] In this thesis, the synthesis, characterization, and nonlinear spectroscopy of different monometallic and bimetallic plasmonic nanoparticles are described and studied in real-time for developing potential drug-delivery applications.

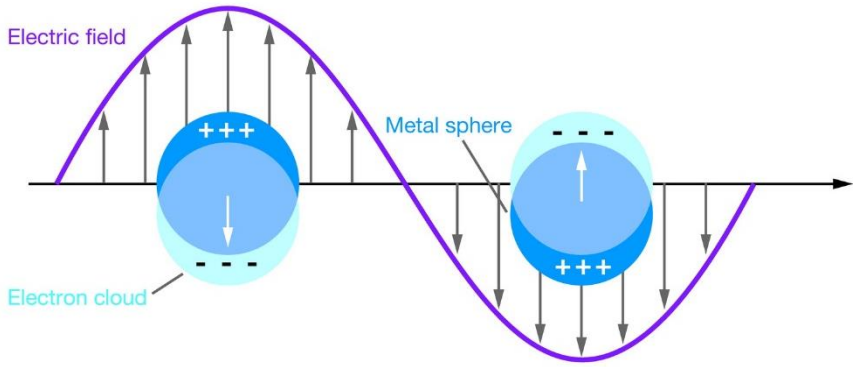

Figure 1.4. Schematic representation of the localized surface plasmon resonance of a spherical metallic nanoparticle under an incident optical electric field.

1.5 Second Harmonic Generation

Second harmonic generation spectroscopy provides detailed information to investigate chemical and physical processes in the colloidal-based systems.[14,19,62] Many spectroscopic techniques like absorption, fluorescence, light-scattering, and reflectometry[62] do not provide surface sensitivity and selectivity and are therefore dominated by bulk signals, making surface characterization problematic. However, nonlinear spectroscopic techniques like sum frequency generation and second harmonic generation overcome these difficulties by clearly distinguishing the signals generated from the interface.[14,26,61] For these second-order nonlinear spectroscopies, the frequency of the output signal lies in a different spectral region in comparison to the frequency of the incident light, enabling precise detection of the signal. These nonlinear optical techniques

typically require the use of ultrashort laser pulses, usually of femtosecond duration. The generated signal is quadratically dependent on the intensity of the incident light.[14,26] Additionally, several filters, a monochromator, and a high-sensitivity detector are required in the experimental setup to separate the signal from Rayleigh, fluorescence, or Raman scattering.

SFG is a second-order, nonlinear optical process where two incident photons with different frequencies ω_1 and ω_2 add to produce a third photon with a frequency of ω_3. SHG is a special case of SFG where two incident photons are of the same frequency, ω. The third photon produced in this case will be $\omega + \omega = 2\omega$, as demonstrated in Scheme 1.2. SHG is generally non-invasive, non-destructive, and highly surface specific. This thesis is focused primarily on SHG and its applications in studying nanoparticle-based systems.

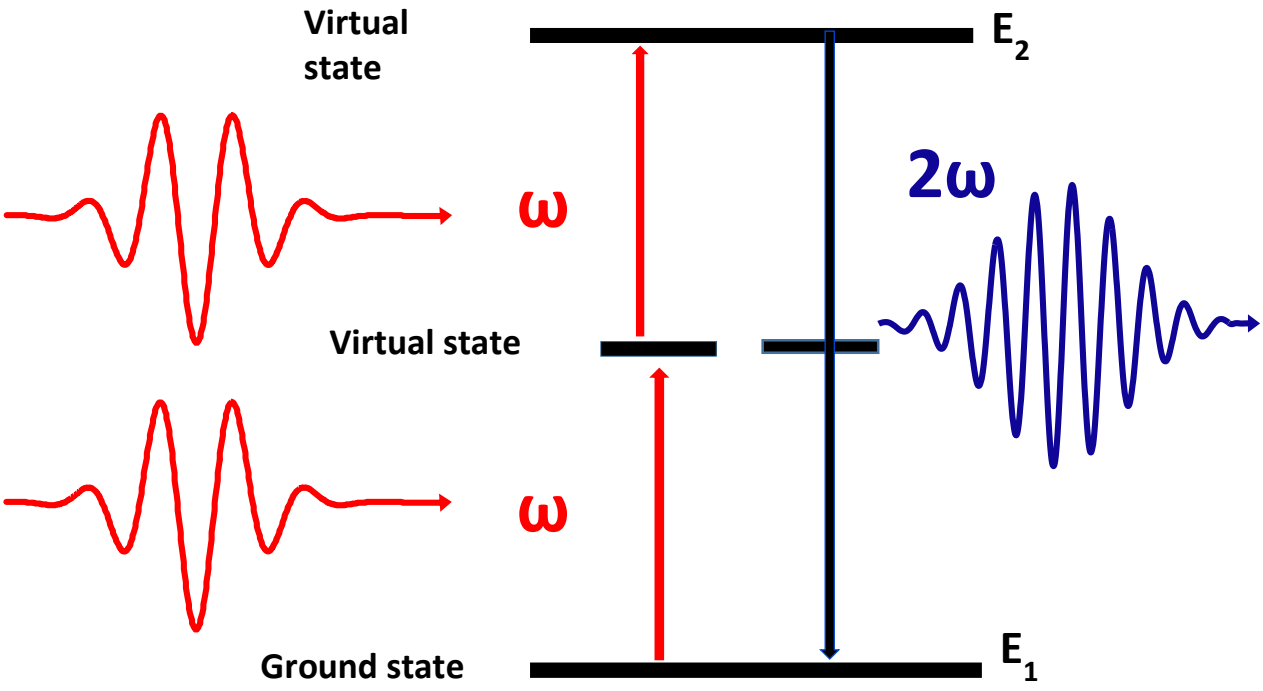

Scheme 1.2. Energy level diagram for an SHG process.

1.5.1 Theory of Second Harmonic Generation in Colloidal Nanoparticle Systems

Individual, isolated, non-centrosymmetric molecules can generate second harmonic signals. However, the net coherent signal produced from an ensemble of these molecules in bulk solution is zero for symmetry reasons. In a bulk phase, there is an isotropic distribution of molecules such that for every molecule oriented in one direction, there is another molecule oriented in the opposite direction, resulting in the condition where the net dipole moment and second-order polarizability are both zero.[14,26,61] However, at an interface such as the air-water interface or the interface of a colloidal nanoparticle in solution, the molecules are often specifically oriented because of asymmetric forces like hydrogen bonding or charge-charge interactions, as demonstrated in Scheme 1.3. These oriented molecules are the primary origin of the interface-specific SHG signal in colloidal-based systems.[14,26,30,63]

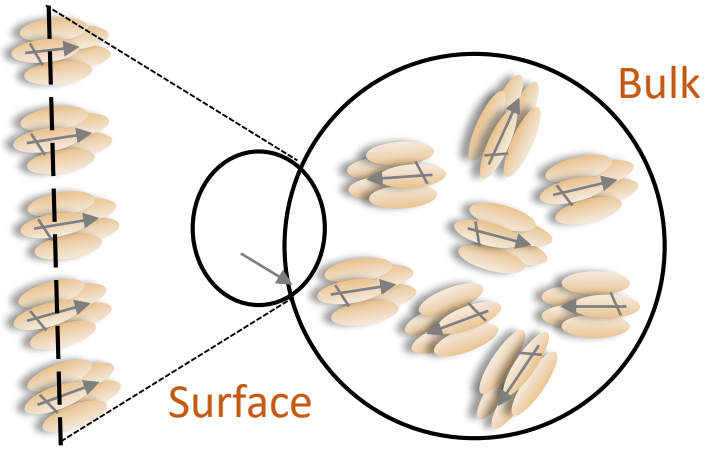

Scheme 1.3. Schematic of ordered molecules at the interface of a colloidal system.

SHG is an electric-dipole forbidden process in centrosymmetric systems, provided that the particle is centrosymmetric on length scales much less than the coherence length of the process.[14,26,64] The coherence length, L_c, of an SHG optical process is given by the relation $\overrightarrow{\Delta k} \times \overrightarrow{L_c} \sim \pi$, where $\Delta k \sim \frac{4\pi\,\Delta n}{\lambda_\omega}$, λ_ω is the fundamental frequency, and Δn is the change in the refractive index between light propagation vectors, $\overrightarrow{k_w}$ and $\overrightarrow{k_{2w}}$, respectively.[14,26,30,63] The total second harmonic signal radiated in the forward direction is given by[14,65,66]

$$E_{SHG} \propto \left|P^{(2)}\right| \sim \beta^2\, E_\omega\, E_\omega\, (1 - e^{-i\overrightarrow{\Delta k}\ \overrightarrow{L_c}})a^6 \qquad 1.1$$

where E_ω is the incident optical electric field at frequency ω, β^2 is the second-order polarizability, and a is the size of the nanoparticle. The SHG signal per nanoparticle is found to scale as a^6 so larger nanoparticles have higher SHG signal.

1.5.2 Macroscopic Origin of Second Order Non-Linear Susceptibility

In an ideal case, when electromagnetic fields interact with a medium, a polarization $\vec{P}$ is induced, which can be expressed as a power series expression, where

$$\vec{P} = \alpha\, E_\omega + \frac{1}{2}\beta^2 E_\omega E_\omega + \frac{1}{6}\beta^3 E_\omega E_\omega E_\omega + \ldots\ldots\ldots\ldots\ldots\ldots \qquad 1.2$$

Here, α is the linear polarizability, β^2 is the second-order polarizability (also called the first-order hyperpolarizability), and β^3 is the third-order polarizability. These polarizability terms describe the charge oscillation in molecules or materials which depends on the strengths of the interacting optical field E_ω. Higher terms of polarizability with increasing powers of E_ω are also present but are neglected in Equation 1.2. The second harmonic light originates from the second-order polarization that is proportional to the second-order

nonlinear susceptibility $\chi^{(2)}$ term such that $E_{SHG} \propto \left|P^{(2)}\right| = \chi^{(2)} E_{\omega} E_{\omega}$. The second-order nonlinear susceptibility term can be expressed as[14,67]

$$\chi^{(2)} \propto N_s \sum_j^k \frac{<i|\mu|j><j|\mu|k><k|\mu|i>}{\{(\omega_{ij}-\omega)-i\gamma_{ij})((\omega_{ki}-2\omega)-i\gamma_{ik})\}} \quad 1.3$$

where, N_s is the surface density of molecules, i, j, and k represent the initial, intermediate and final electronic states, $< i|\mu|j >$ represents the average transition dipole moment from the i to j state, μ is the dipole operator, ω_{ij} and ω_{ki} represents the corresponding optical frequency of transition, ω and 2ω are fundamental and second harmonic frequency respectively, and γ is the linewidth associated with the optical transition. The above equation demonstrates several important parameters affecting the second harmonic signal. First, $\chi^{(2)}$ is proportional to the number density of molecules at the surface. It should be noted that $E_{SHG} = \sqrt{I_{SHG}}$, where I_{SHG} is the measured SHG signal. Therefore, the second harmonic signal has a ${N^2}_s$ dependence. Secondly, the sensitivity of SHG is dictated by the orientational distribution of the molecules at the interface as indicated by the average overall dipole orientation of the surface molecules. When the net dipole orientation of the molecules is anisotropic or highly ordered, there is an overall increase in the associated $\chi^{(2)}$ term. Correspondingly, when the net dipole orientation of the molecules is highly isotropic, there is a reduced SHG response. Additionally, the SHG signal can be resonantly enhanced if the molecular species that are probed have a molecular absorption in resonance with the second harmonic frequency, where the reduced term in the denominator of Equation 1.3 leads to resonantly-enhanced second harmonic signals. Therefore, SHG-active molecules at a specific SHG frequency can be used to measure surface properties like adsorption, desorption, and molecular transport

as the cumulative SHG signal is proportional to the concentration and orientation of the molecules being interrogated.

1.5.3 Eisenthal $\chi^{(3)}$ Technique

A colloidal suspension of nano- or micro-sized particles typically contains charged particle-solvent interfaces, especially for polar solvents such as water. When we consider a charged surface in contact with water molecules, the static electric field generated by the surface charge can orient the water molecules at the interface, inducing a third-order polarization, as shown in Scheme 1.4.[14,28-30,68-72] Under incident light, the generated polarization can be expressed as $\left|P^{(3)}\right| = \chi^{(3)} E_\omega E_\omega \phi_0 cos\varphi e^{i\varphi}$, where ϕ_0 is the surface potential and φ is the phase angle. The phase angle is dependent on the wave vector mismatch and Debye screening length.[29,71,73] Additionally, for most colloidal nanoparticle samples, the inherent phase angle is expected to be either in phase ($\varphi = 0^o$) or out of phase ($\varphi = 180^o$).[29,69-71,73] This effectively leads to the simplified equation where $E_{SHG} \propto P^{(2)} + P^{(3)} = \chi^{(2)} E_\omega E_\omega + \chi^{(3)} E_\omega E_\omega \phi_0$.

The $\chi^{(3)}$ term contains important information about the population and structural arrangements of neutral and ionic species in the interfacial region. A fundamental understanding and determination of the surface potential, surface charge densities, and related electrochemistry parameters serve as an empirical quantity that is related with the local environment of the nanoparticles or microparticles in solution.

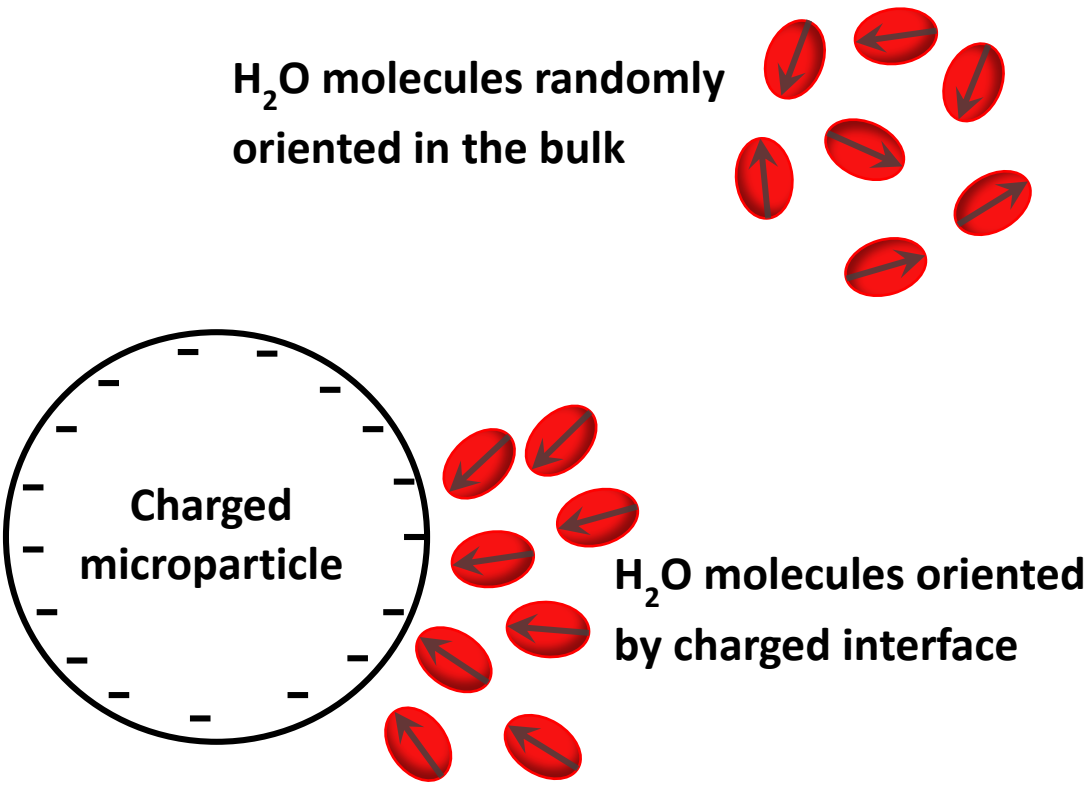

Scheme 1.4. Schematic of a charged microparticle inducing a static electric field by ordered water molecules at the interface.

The second harmonic contributions from the $\chi^{(3)}$ term is dictated by several parameters. One of the important parameters that has been found to affect the contribution from $\chi^{(3)}$ term is the role of electrolytes on the generated E_{SHG}. This effect was first observed at Prof. Eisenthal's Lab in 1998.[30] Since then, this SHG technique to determine the surface charge density or the electrostatic surface potential has often been called the Eisenthal $\chi^{(3)}$ technique. It was observed that the addition of an electrolye solution like potassium chloride or magnesium sulfate reduced the second harmonic signal from a sample of polystyrene sulfate (PSS) microspheres in water.[30] Additionally, the experimentally-obtained SHG data was fit with the Gouy-Chapman model to determine the surface-charge density and corresponding surface-potential. This

technique has been extended with different systems like liposomes[28,74] and drug-molecules.[68] The Haber lab has also successfully determined the surface charge density of colloidal gold nanospheres using SHG, as demonstrated in Figure 1.5.[59]

In summary, the overall SHG signal has significant contributions from both the $\chi^{(2)}$ and $\chi^{(3)}$ terms. The general principle described in this chapter allows for the investigation of surface properties of nano- and micro-sized colloidal particles.

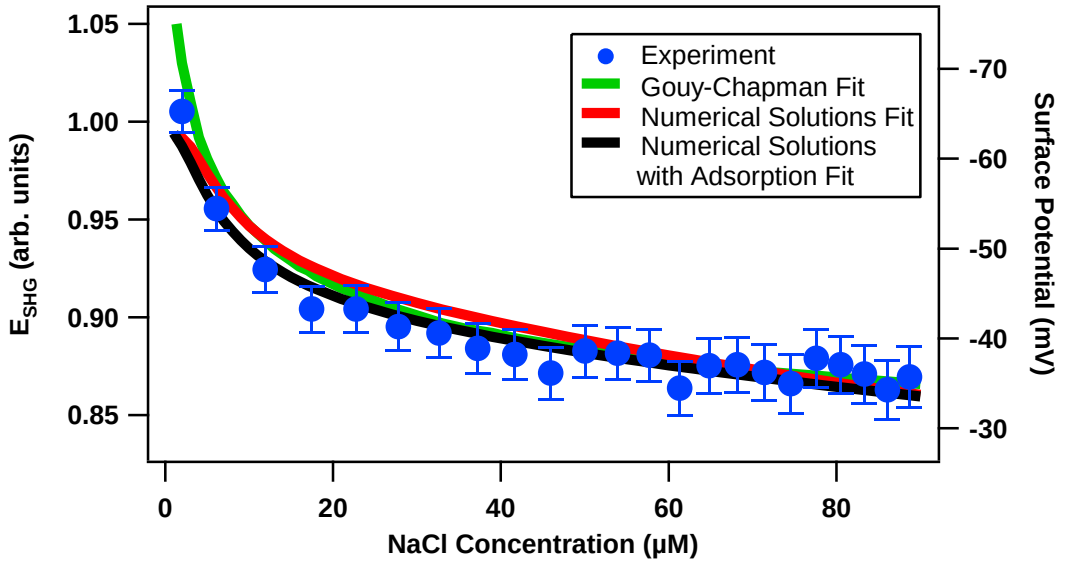

Figure 1.5. Second harmonic electric field as a function of electrolyte concentration. The blue circles are the experimental data. The green, red, and black solid curves are obtained by fitting the experimentally data with the Gouy-Chapman model, numerical-solutions to the Poisson-Boltzmann equation without adsorption, and numerical-solutions to the Poisson-Boltzmann equation with adsorption models, respectively.[59]

1.5.4 Experimental setup of SHG

The experimental setup for SHG in our lab consists of a titanium:sapphire oscillator laser as a source. The oscillator laser operates at a central wavelength of 800 nm with 75 fs pulses at a repetition rate of 80 Mhz. The output from the source passes through different optical elements and is focused to the colloidal sample, which is contained a 1

cm quartz cuvette. Optical filters are used to remove the residual SHG from the laser beam before hitting the sample and to remove the fundamental 800 nm of light after the sample. The SHG produced by the sample is detected in real time using a high- sensitivity charge-coupled device connected to a monochromator spectrograph.

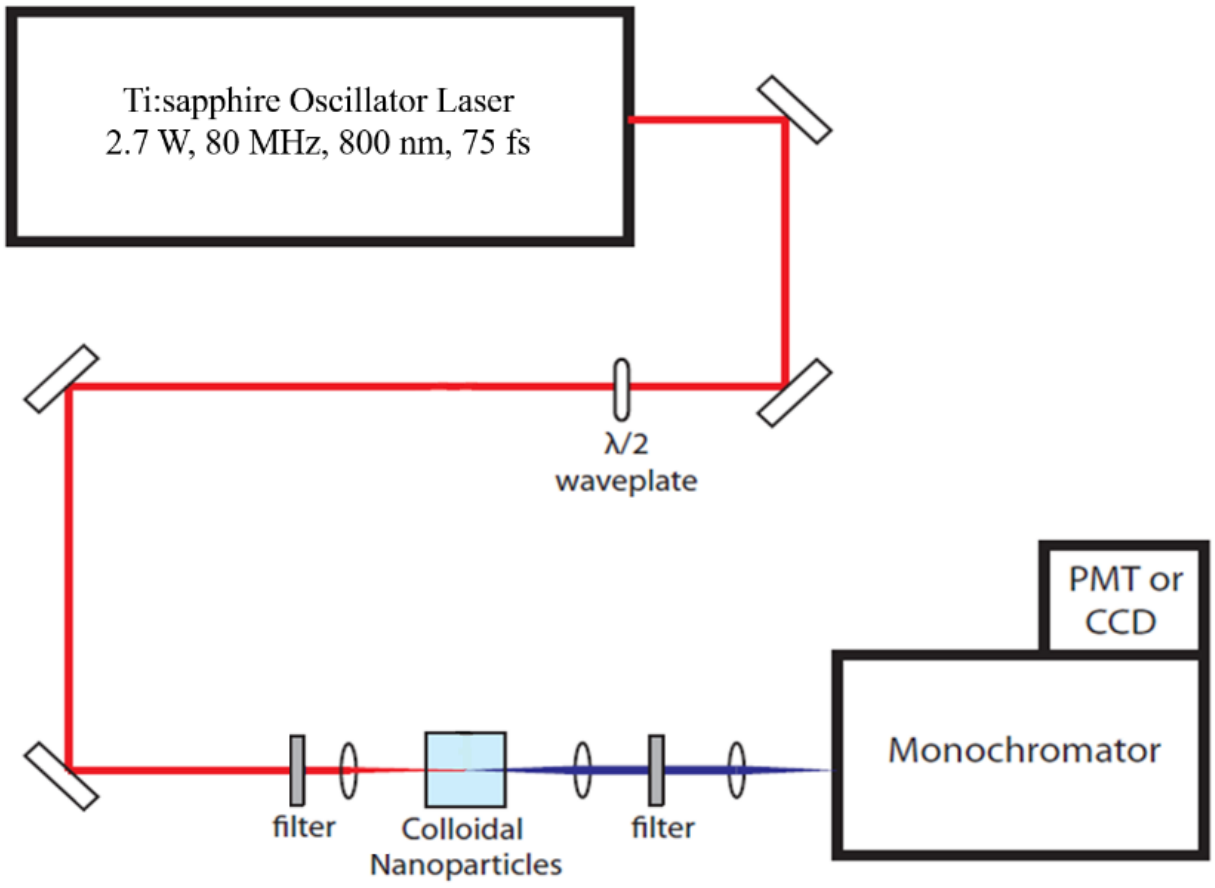

Figure 1.6 Home-built SHG setup showing the 800 nm (red beam) which is focused to the colloidal nanoparticle sample in a quartz cuvette, with the SHG signal detected using a CCD detector connected to a monochromator.

1.6 Scope of the Dissertation

This dissertation describes the use of the surface-sensitive second harmonic generation technique to interrogate molecular interactions at different colloidal nanoparticle systems. Chapter 2 describes real-time SHG studies to determine the effect of chemical functional groups on molecular adsorption and transport kinetics at the surface of phospholipid liposomes in water. Chapter 3 describes the role of temperature in molecular translocation of small molecules through a lipid bilayer. The temperature-dependent study also gives critical insights regarding thermodynamics associated with the molecule-lipid interactions. Chapter 4 describes the use of SHG microscopy to investigate molecular adsorption and transport of a cationic molecule in a living cell membrane. The SHG images of dye molecules added to cell samples are compared between living and fixed H596 cells using two similar triphenylmethane molecules. The results are in general agreement with the results from Chapter 2, as chemical functional groups are shown to affect the molecular interactions of adsorption and transport in a living cell membrane. Additionally, the retro Diel's-Alder thermal release of small miRNA mimics from the surface of novel plasmonic nanoparticles are studied in real-time using surface-sensitive SHG spectroscopy, as described in Chapter 5. This work showcases promising fundamental applications of plasmonic nanoparticles for nanomedicine, gene-silencing, and photothermal drug-delivery applications. Appendices A, B, C, and D provide additional information corresponding to the work presented in Chapters 2, 3, 4, and 5, respectively. Together, this dissertation describes a broad range of surface-specific measurements for investigating potential colloidal nanoparticle-based drug-delivery applications in aqueous solution.

1.7 Notes

(1) Evans, D. F.; Wennerström, H. The colloidal domain: where physics, chemistry, biology, and technology meet. **1999**.

(2) Antonietti, M.: *Colloid Chemistry II*; Springer, 2003; Vol. 227.

(3) Everett, D. H.: *Basic principles of colloid science*; Royal society of chemistry, 2007.

(4) Alivisatos, A. P. Semiconductor clusters, nanocrystals, and quantum dots. *science* **1996**, *271*, 933-937.

(5) Kolthoff, I.; Bovey, F.; Medalia, A.; Meehan, E. Emulsion Polymerization. *New York: Interscience* **1955**, 177.

(6) Henglein, A. Small-particle research: physicochemical properties of extremely small colloidal metal and semiconductor particles. *Chem. Rev.* **1989**, *89*, 1861-1873.

(7) Pieranski, P. Colloidal crystals. *Contemporary Physics* **1983**, *24*, 25-73.

(8) Pieranski, P.; Strzelecki, L.; Pansu, B. Thin colloidal crystals. *Phys. Rev. Lett.* **1983**, *50*, 900.

(9) Schmid, G. Large clusters and colloids. Metals in the embryonic state. *Chem. Rev.* **1992**, *92*, 1709-1727.

(10) Schmid, G.; Chi, L. F. Metal clusters and colloids. *Adv. Mater.* **1998**, *10*, 515-526.

(11) Schön, G.; Simon, U. A fascinating new field in colloid science: small ligand-stabilized metal clusters and possible application in microelectronics. *Colloid. Polym. Sci.* **1995**, *273*, 101-117.

(12) Weller, H. Colloidal semiconductor q-particles: chemistry in the transition region between solid state and molecules. *Angewandte Chemie International Edition in English* **1993**, *32*, 41-53.

(13) Steigerwald, M. L.; Brus, L. E. Semiconductor crystallites: a class of large molecules. *Acc. Chem. Res.* **1990**, *23*, 183-188.

(14) Eisenthal, K. B. Second harmonic spectroscopy of aqueous nano-and microparticle interfaces. *Chem. Rev.* **2006**, *106*, 1462-1477.

(15) Karam, T. E.; Siraj, N.; Zhang, Z.; Ezzir, A. F.; Warner, I. M.; Haber, L. H. Ultrafast and nonlinear spectroscopy of brilliant green-based nanoGUMBOS with enhanced near-infrared emission. *J. Chem. Phys.* **2017**, *147*, 144701.

(16) Kumal, R. R.; Abu-Laban, M.; Hamal, P.; Kruger, B.; Smith, H. T.; Hayes, D. J.; Haber, L. H. Near-Infrared Photothermal Release of siRNA from the Surface of Colloidal Gold–Silver–Gold Core–Shell–Shell Nanoparticles Studied with Second-Harmonic Generation. *J. Phys. Chem. C* **2018**, *122*, 19699-19704.

(17) Kumal, R. R.; Abu-Laban, M.; Landry, C. R.; Kruger, B.; Zhang, Z.; Hayes, D. J.; Haber, L. H. Plasmon-enhanced photocleaving dynamics in colloidal microRNA-functionalized silver nanoparticles monitored with second harmonic generation. *Langmuir* **2016**, *32*, 10394-10401.

(18) Ranasinghe, J. C.; Dikkumbura, A. S.; Hamal, P.; Chen, M.; Khoury, R. A.; Smith, H. T.; Lopata, K.; Haber, L. H. Monitoring the growth dynamics of colloidal gold-silver core-shell nanoparticles using in situ second harmonic generation and extinction spectroscopy. *J. Chem. Phys.* **2019**, *151*, 224701.

(19) Karam, T. E.; Haber, L. H. Molecular adsorption and resonance coupling at the colloidal gold nanoparticle interface. *J. Phys. Chem. C* **2014**, *118*, 642-649.

(20) Karam, T. E.; Khoury, R. A.; Haber, L. H. Excited-state dynamics of size-dependent colloidal TiO2-Au nanocomposites. *The Journal of chemical physics* **2016**, *144*, 124704.

(21) Li, Y.; Choudhry, U.; Ranasinghe, J.; Ackerman, A.; Liao, B. Probing Surface Photovoltage Effect Using Photo-Assisted Secondary Electron Emission. *The Journal of Physical Chemistry A* **2020**.

(22) Dixon, M. C. Quartz crystal microbalance with dissipation monitoring: enabling real-time characterization of biological materials and their interactions. *Journal of biomolecular techniques: JBT* **2008**, *19*, 151.

(23) Sezgin, E.; Schwille, P. Fluorescence techniques to study lipid dynamics. *Cold Spring Harbor perspectives in biology* **2011**, *3*, a009803.

(24) Patching, S. G. Surface plasmon resonance spectroscopy for characterisation of membrane protein–ligand interactions and its potential for drug discovery. *Biochimica et Biophysica Acta (BBA)-Biomembranes* **2014**, *1838*, 43-55.

(25) Wilhelm, M. J.; Dai, H. L. Molecule-Membrane Interactions in Biological Cells Studied with Second Harmonic Light Scattering. *Chemistry–An Asian Journal* **2019**.

(26) Wang, H.; Yan, E. C.; Borguet, E.; Eisenthal, K. B. Second harmonic generation from the surface of centrosymmetric particles in bulk solution. *Chem. Phys. Lett.* **1996**, *259*, 15-20.

(27) Khoury, R. A.; Ranasinghe, J. C.; Dikkumbura, A. S.; Hamal, P.; Kumal, R. R.; Karam, T. E.; Smith, H. T.; Haber, L. H. Monitoring the Seed-Mediated Growth of Gold

Nanoparticles using In-Situ Second Harmonic Generation and Extinction Spectroscopy. *J. Phys. Chem. C* **2018**, *122*, 244400-224406.

(28) Liu, Y.; Yan, E. C.; Zhao, X.; Eisenthal, K. B. Surface potential of charged liposomes determined by second harmonic generation. *Langmuir* **2001**, *17*, 2063-2066.

(29) Ohno, P. E.; Chang, H.; Spencer, A. P.; Liu, Y.; Boamah, M. D.; Wang, H.-f.; Geiger, F. M. Beyond the gouy–chapman model with heterodyne-detected second harmonic generation. *J. Phys. Chem. Lett.* **2019**, *10*, 2328-2334.

(30) Yan, E. C.; Liu, Y.; Eisenthal, K. B. New method for determination of surface potential of microscopic particles by second harmonic generation. *J. Phys. Chem. B* **1998**, *102*, 6331-6336.

(31) Liu, Y.; Yan, E. C.; Eisenthal, K. B. Effects of bilayer surface charge density on molecular adsorption and transport across liposome bilayers. *Biophys. J.* **2001**, *80*, 1004-1012.

(32) Hamal, P.; Nguyenhuu, H.; Subasinghege Don, V.; Kumal, R. R.; Kumar, R.; McCarley, R. L.; Haber, L. H. Molecular Adsorption and Transport at Liposome Surfaces Studied by Molecular Dynamics Simulations and Second Harmonic Generation Spectroscopy. *J. Phys. Chem. B* **2019**, *123*, 7722-7730.

(33) Kumal, R. R.; Nguyenhuu, H.; Winter, J. E.; McCarley, R. L.; Haber, L. H. Impacts of Salt, Buffer, and Lipid Nature on Molecular Adsorption and Transport in Liposomes As Observed by Second Harmonic Generation. *J. Phys. Chem. C* **2017**, *121*, 15851-15860.

(34) Zeng, J.; Eckenrode, H. M.; Dai, H.-L.; Wilhelm, M. J. Adsorption and transport of charged vs. neutral hydrophobic molecules at the membrane of murine erythroleukemia (MEL) cells. *Colloids Surf., B* **2015**, *127*, 122-129.

(35) Zeng, J.; Eckenrode, H. M.; Dounce, S. M.; Dai, H.-L. Time-resolved molecular transport across living cell membranes. *Biophys. J.* **2013**, *104*, 139-145.

(36) Alberts, B.; Johnson, A.; Lewis, J.; Raff, M.; Roberts, K.; Walter, P.: *Molecular Biology of the Cell*; New York: Garland Science, 2002.

(37) Stroberg, W.; Schnell, S. On the origin of non-membrane-bound organelles, and their physiological function. *Journal of theoretical biology* **2017**, *434*, 42-49.

(38) Wheeler, R. J.; Hyman, A. A. Controlling compartmentalization by non-membrane-bound organelles. *Philosophical Transactions of the Royal Society B: Biological Sciences* **2018**, *373*, 20170193.

(39) Heald, R.; Cohen-Fix, O. Morphology and function of membrane-bound organelles. *Current opinion in cell biology* **2014**, *26*, 79-86.

(40) Sharifian Gh, M.; Wilhelm, M. J.; Moore, M.; Dai, H.-L. Spatially Resolved Membrane Transport in a Single Cell Imaged by Second Harmonic Light Scattering. *Biochemistry* **2019**, *58*, 1841-1844.

(41) Domene, C.; Bond, P. J.; Sansom, M. S.: Membrane protein simulations: ion channels and bacterial outer membrane proteins. In *Adv. Protein Chem.*; Elsevier, 2003; Vol. 66; pp 159-193.

(42) Lindahl, E.; Sansom, M. S. Membrane proteins: molecular dynamics simulations. *Current opinion in structural biology* **2008**, *18*, 425-431.

(43) McCarley, R. L. Redox-responsive delivery systems. *Annu. Rev. Anal. Chem.* **2012**, *5*, 391-411.

(44) Ong, W.; Yang, Y.; Cruciano, A. C.; McCarley, R. L. Redox-triggered contents release from liposomes. *J. Am. Chem. Soc.* **2008**, *130*, 14739-14744.

(45) Charman, W. N. Lipids, lipophilic drugs, and oral drug delivery—some emerging concepts. *J. Pharm. Sci.* **2000**, *89*, 967-978.

(46) Escribá, P. V.; González-Ros, J. M.; Goñi, F. M.; Kinnunen, P. K.; Vigh, L.; Sánchez-Magraner, L.; Fernández, A. M.; Busquets, X.; Horváth, I.; Barceló-Coblijn, G. Membranes: a meeting point for lipids, proteins and therapies. *J Cell Mol Med.* **2008**, *12*, 829-875.

(47) Nguyen, T. T.; Conboy, J. C. High-throughput screening of drug–lipid membrane interactions via counter-propagating second harmonic generation imaging. *Anal. Chem.* **2011**, *83*, 5979-5988.

(48) Beloqui, A.; Solinís, M. Á.; Rodríguez-Gascón, A.; Almeida, A. J.; Préat, V. Nanostructured lipid carriers: promising drug delivery systems for future clinics. *Nanomedicine: Nanotechnology, Biology and Medicine* **2016**, *12*, 143-161.

(49) Goyal, P.; Goyal, K.; Kumar, S. V.; Singh, A.; Katare, O. P.; Mishra, D. N. Liposomal drug delivery systems–clinical applications. *Acta Pharm* **2005**, *55*, 1-25.

(50) Shrestha, H.; Bala, R.; Arora, S. Lipid-based drug delivery systems. *Journal of pharmaceutics* **2014**, *2014*.

(51) Marsh, D. Electron spin resonance in membrane research: protein–lipid interactions. *Methods* **2008**, *46*, 83-96.

(52) Aidley, D. J.; Stanfield, P. R.: *Ion channels: molecules in action*; Cambridge University Press, 1996.

(53) Austin, L. A.; Mackey, M. A.; Dreaden, E. C.; El-Sayed, M. A. The optical, photothermal, and facile surface chemical properties of gold and silver nanoparticles in biodiagnostics, therapy, and drug delivery. *Arch. Toxicol.* **2014**, *88*, 1391-1417.

(54) Goodman, A. M.; Hogan, N. J.; Gottheim, S.; Li, C.; Clare, S. E.; Halas, N. J. Understanding resonant light-triggered DNA release from plasmonic nanoparticles. *ACS nano* **2016**, *11*, 171-179.

(55) Hirsch, L. R.; Stafford, R. J.; Bankson, J. A.; Sershen, S. R.; Rivera, B.; Price, R.; Hazle, J. D.; Halas, N. J.; West, J. L. Nanoshell-mediated near-infrared thermal therapy of tumors under magnetic resonance guidance. *PNAS* **2003**, *100*, 13549-13554.

(56) Loo, C.; Lowery, A.; Halas, N.; West, J.; Drezek, R. Immunotargeted nanoshells for integrated cancer imaging and therapy. *Nano Lett.* **2005**, *5*, 709-711.

(57) Karam, T. E.; Smith, H. T.; Haber, L. H. Enhanced photothermal effects and excited-state dynamics of plasmonic size-controlled gold–silver–gold core–shell–shell nanoparticles. *The Journal of Physical Chemistry C* **2015**, *119*, 18573-18580.

(58) Abu-Laban, M.; Hamal, P.; Arrizabalaga, J. H.; Forghani, A.; Dikkumbura, A. S.; Kumal, R. R.; Haber, L. H.; Hayes, D. J. Combinatorial Delivery of miRNA-Nanoparticle Conjugates in Human Adipose Stem Cells for Amplified Osteogenesis. *Small* **2019**.

(59) Kumal, R. R.; Karam, T. E.; Haber, L. H. Determination of the surface charge density of colloidal gold nanoparticles using second harmonic generation. *J. Phys. Chem. C* **2015**, *119*, 16200-16207.

(60) Kumal, R. R.; Landry, C. R.; Abu-Laban, M.; Hayes, D. J.; Haber, L. H. Monitoring the photocleaving dynamics of colloidal microrna-functionalized gold nanoparticles using second harmonic generation. *Langmuir* **2015**, *31*, 9983-9990.

(61) Haber, L. H.; Kwok, S. J.; Semeraro, M.; Eisenthal, K. B. Probing the colloidal gold nanoparticle/aqueous interface with second harmonic generation. *Chem. Phys. Lett.* **2011**, *507*, 11-14.

(62) Langevin, D.: *Light scattering by liquid surfaces and complementary techniques*; M. Dekker, 1992.

(63) Wang, H.; Yan, E. C.; Liu, Y.; Eisenthal, K. B. Energetics and population of molecules at microscopic liquid and solid surfaces. *J. Phys. Chem. B* **1998**, *102*, 4446-4450.

(64) Srivastava, A.; Eisenthal, K. B. Kinetics of molecular transport across a liposome bilayer. *Chem. Phys. Lett.* **1998**, *292*, 345-351.

(65) Dadap, J. I.; Shan, J.; Eisenthal, K. B.; Heinz, T. F. Second-harmonic Rayleigh scattering from a sphere of centrosymmetric material. *Phys. Rev. Lett.* **1999**, *83*, 4045.
(66) de Beer, A. G.; Roke, S. Nonlinear Mie theory for second-harmonic and sum-frequency scattering. *Phys. Rev. B* **2009**, *79*, 155420.

(67) Tran, R. J.; Sly, K. L.; Conboy, J. C. Applications of surface second harmonic generation in biological sensing. *Annu. Rev. Anal. Chem.* **2017**, *10*, 387-414.

(68) Rao, Y.; Kwok, S. J.; Lombardi, J.; Turro, N. J.; Eisenthal, K. B. Label-free probe of HIV-1 TAT peptide binding to mimetic membranes. *PNAS* **2014**, *111*, 12684-12688.

(69) Geiger, F. M. Second harmonic generation, sum frequency generation, and χ (3): dissecting environmental interfaces with a nonlinear optical Swiss Army knife. *Annu. Rev. Phys. Chem.* **2009**, *60*, 61-83.

(70) Hayes, P. L.; Malin, J. N.; Jordan, D. S.; Geiger, F. M. Get charged up: Nonlinear optical voltammetry for quantifying the thermodynamics and electrostatics of metal cations at aqueous/oxide interfaces. *Chem. Phys. Lett.* **2010**, *499*, 183-192.

(71) Ohno, P.; Saslow, S.; Wang, H.-f.; Geiger, F.; Eisenthal, K.: Phase-referenced nonlinear spectroscopy of the α-quartz/water interface Nat. Commun, 2016.

(72) Troiano, J. M.; McGeachy, A. C.; Olenick, L. L.; Fang, D.; Liang, D.; Hong, J.; Kuech, T. R.; Caudill, E. R.; Pedersen, J. A.; Cui, Q.; Geiger, F. M. Quantifying the electrostatics of polycation–lipid bilayer interactions. *J. Am. Chem. Soc.* **2017**, *139*, 5808-5816.

(73) Gonella, G.; Lütgebaucks, C.; De Beer, A. G.; Roke, S. Second harmonic and sum-frequency generation from aqueous interfaces is modulated by interference. *J. Phys. Chem. C* **2016**, *120*, 9165-9173.

(74) Dreier, L. B.; Bernhard, C.; Gonella, G.; Backus, E. H.; Bonn, M. Surface Potential of a Planar Charged Lipid–Water Interface. What Do Vibrating Plate Methods, Second Harmonic and Sum Frequency Measure? *J. Phys. Chem. Lett.* **2018**, *9*, 5685-5691.

Chapter 2. Molecular Adsorption and Transport at Liposome Surfaces Studied by Molecular Dynamics Simulations and Second Harmonic Generation Spectroscopy

2.1 Introduction

A critical property of cell membranes is their ability to allow ions and drug molecules to translocate by passive transport processes.[1-9] This translocation can be characterized by the adsorption and time-resolved transport kinetics of ions and small molecules in the cell membrane, which is composed mainly of lipid bilayers and membrane proteins.[10-13] Liposomes are tiny spherical vesicles composed of phospholipid membranes and can be used for fundamental studies as model cell membranes.[14] Stimuli-responsive liposome phospholipids have also been used to increase the efficacy of drug delivery.[11,14] For liposome-based systems, it is essential to understand the transport properties of drug molecules, the associated energetics, and the determination of key factors that govern molecular binding at the membrane surface. Our recent investigation described these associated processes for the drug-like molecule, malachite green (MG), in different liposome, buffer, and electrolyte conditions using the surface-specific nonlinear spectroscopy, second harmonic generation (SHG).[15] Our prior work demonstrated that several factors impact molecular adsorption and transport across the membranes, including electrostatic interactions between the adsorbate molecule and the liposome surface, the lipid headgroup structure, electrolyte adsorption, ion-pairing, and hydration properties of the molecular ions.[15]

Sum frequency generation (SFG) and SHG are powerful nonlinear spectroscopic techniques used for investigating the physical and chemical properties of colloidal liposome samples in a manner that is noninvasive, nondestructive, and surface-sensitive.[15-20] Recently, SHG has been utilized to study interfacial dynamics of different colloidal nanoparticle systems.[21-29] In the SHG process, two incident photons of frequency ω add coherently to generate a third photon with a frequency of 2ω. SHG is dipole forbidden in centrosymmetric media, such as bulk solution, but it can be generated at the surface of nanoparticles where the symmetry is broken. Therefore, SHG measurements are sensitive to molecular adsorption at colloidal interfaces and can be used for studying dynamics at the liposome surface in water.[15,19,30-33]

The SHG electric field E_{SHG} depends on the second-order and third-order nonlinear optical susceptibilities, $\chi^{(2)}$ and $\chi^{(3)}$, respectively. The SHG electric field can be expressed as[24,34-39]

$$E_{SHG} = \sqrt{I_{SHG}} = \chi^{(2)} E_\omega E_\omega + \chi^{(3)} E_\omega E_\omega \phi_0 \qquad (2.1)$$

where, I_{SHG} is the SHG intensity, E_ω is the incident optical electric field at frequency ω, and ϕ_0 is the electrostatic surface potential arising from the nanoparticle surface charge density. The second-order nonlinear susceptibility $\chi^{(2)}$ term for SHG is from the two-photon spectroscopy of the surface and is dependent on several factors, such as the associated transition dipole moments and the orientational distributions,[39,40] with possible resonant enhancement if the second harmonic frequency is resonant with a molecular optical transition. Additionally, the static electric field created by the charged interface results in the third-order nonlinear susceptibility $\chi^{(3)}$ term for SHG caused by bulk solvent

molecules that have a distance-dependent net alignment with respect to the nanoparticle surface due to the electrostatic potential.[23,32,34,35] For liposome membrane systems with a bilayer thickness of approximately 5 nm, the SHG signal of the dye molecules adsorbed on the outer membrane/water interface is approximately equal and opposite to that of dye molecules adsorbed on the inner water/membrane interface.[19] By virtue of symmetry, the SHG signals from molecules at the outer and inner membrane surfaces effectively cancel out, so the SHG signal is approximately proportional to the population difference of dye molecules adsorbed at the liposome bilayer outer and inner surfaces.[19,41-46]

In this study, the SHG signal from the drug-like molecule, malachite green isothiocyanate (MGITC), is measured in real time in various liposome samples for fundamental studies of molecular interactions at lipid bilayers in water. The time-dependent SHG results from liposomes composed of dioleoylphosphatidyl-glycerol (DOPG), dioleoylphosphoserine (DOPS), dioleoylphosphocholine (DOPC), and quinonepropionic acid dioleoylphospho-ethanolamine (QPADOPE) in citrate buffer provide measurements of the molecular transport time, as well as the adsorption free energy and adsorption site concentration. These liposomes are selected as representations of different phospholipid types that are present in cell membranes, including singly-charged lipids, zwitterionic lipids, and lipids with multiple charged groups, as well as specialized lipids with a bulky hydrophobic headgroup. Additionally, the results are directly compared to our previous work using the similar dye molecule, malachite green, with these same liposomes. For additional analysis of the complex interactions at the different liposome surfaces, molecular dynamics (MD) simulations are carried out for MG and MGITC with DOPG and DOPC bilayers, and the simulation results show

excellent agreement with the SHG experimental observations. These combined SHG and MD studies provide crucial insights into the factors that determine molecular adsorption and transport properties in phospholipid membranes for developing models for drug-delivery applications. A key finding demonstrates the important role of chemical functional groups, such as isothiocyanate, in controlling molecular translocation across the membrane/water interface.

2.2 Experimental Section

2.2.1 Synthesis and Characterization.

Large unilamellar vesicles (LUVs) or liposomes of each lipid were prepared by extrusion, following the reported protocol.[15,47] The QPADOPE lipid synthesis has been described previously.[47,48] DOPC, DOPE, DOPG, and DOPS were purchased from Avanti Polar lipids, Inc. in a powder form stored in glass vials. Citric acid monohydrate (≥99.0%) and potassium hydroxide purified pellets (≥85%) were purchased from Sigma-Aldrich. MGITC was purchased from Setareh Biotech. Approximately, 4-6 mg of dry lipid film is hydrated at room temperature with 1.0 mL of 5.0 mM citrate buffer for 1 hour with regular vortexing, followed by six freeze-thaw cycles. The suspensions are subjected to 19 cycles of extrusion through a 200-nm pore Whatman Nucleopore polycarbonate track-etched membrane using a hand-held Mini-Extruder (Avanti Polar Lipids, Alabaster, AL). The total lipid concentration is determined using a Bartlett assay, as described in the Appendix A. The liposomes are roughly 150 nm in diameter with a polydispersity index (PDI) less than 0.1, as characterized by dynamic light scattering (DLS) measurements. Representative DLS size distributions are shown in Figure A.2. The zeta potentials of different liposomes in pH 4.0, 5 mM citrate buffer are −73.2 ± 1.1 mV (DOPG), −74.8 ± 1.7 mV (DOPS), −67.3

± 1.5 mV (QPADOPE), and −21.7 ± 2.3 mV (DOPC), and are listed in Table A.1. DOPG, DOPS and QPADOPE have comparable zeta potential values. However, the zeta potential of DOPC is significantly lower in magnitude due to its zwitterionic structure.

2.2.2 Second Harmonic Generation Setup.

The experimental setup for the SHG has been described previously.[15] The setup consists of an ultrafast laser system, an optical system, and high-sensitivity charge-coupled device (CCD) detector connected to a monochromator spectrograph. The Titanium:sapphire oscillator laser is centered at 800 nm with 75 fs pulses at 80 MHz repetition rate. The average laser power is attenuated to 1.0 W using a neutral density filter. The laser beam is focused to the sample in a 1 cm quartz cuvette to generate SHG signal which is detected in the forward direction with a high sensitivity spectrophotometer. Optical filters are used to remove any residual SHG signal from the laser beam before hitting the sample and to remove the fundamental 800 nm light after the sample. An integrated computer program controls a beam block and a magnetic stir bar in synchronization with automated data acquisition for background-subtracted time-dependent SHG measurements. For each time scan, 5 background spectra and 10 SHG spectra are acquired with 1 second acquisitions with the laser blocked and unblocked, respectively, in sequential and repeated measurements for statistical analysis of the SHG signal as a function of time.

2.2.3 Molecular Dynamics Simulations Details

Molecular dynamics simulations are carried out using the LAMMPS program (version 05 Sep 2014)[49] with the all-atom general AMBER force field (GAFF).[50] The partial

charges of the optimized structures are calculated by the RESP fitting technique[51,52] using the HF/6-31G* method in Gaussian 09 suite of programs.[53] Four different molecule-lipid systems (MG in DOPC, MGITC in DOPC, MG in DOPG and MGITC in DOPG) are simulated. The energy of each system is minimized, followed by equilibration in the isothermal-isobaric (NPT) and canonical (NVT) ensembles. The final simulation box dimensions are approximately 95.5 × 48.0 × 120.0 $Å^3$ for the DOPC system and 94.5 × 50.0 × 115.0 $Å^3$ for the DOPG system. The membrane/water interface is perpendicular to the z-axis for each system. Additional details regarding the four systems and the simulation setup are discussed in Appendix A.

The free energy profile of bringing the different dye molecules to the DOPC and DOPG membranes are determined by the umbrella sampling method.[54] The collective variable is taken to be the distance in the z-direction between the center of mass (COM) of the lipid bilayer and the COM of the dye molecule. For each system, 20 umbrella sampling windows are generated with a 18 ns simulation time per window and with a spacing of 1.5 Å along the z-axis. The potential of mean force is calculated using the weighted histogram analysis method (WHAM)[55,56] with the data from the last 14 ns of each umbrella sampling window. The statistical error of the potential mean force is calculated using the block averaging method with 3.5 ns of data for each block. In order to determine the relevant interactions that play a role in the adsorption and transport of the two dyes, the orientation of each dye molecule at the surface of the two membranes are analyzed and compared. Specifically, the distribution of the z-direction distance between two specific atom types in each dye molecule, namely the two amine N atoms and a C atom of the phenyl ring without the amine (see Appendix A) and the COM of the

membrane are calculated. The details of these calculations and distributions of the distances for each system are summarized in the Appendix A.

2.3 Results and Discussion

Representative SHG spectra of the DOPC liposomes at 50 μM lipid concentration with and without added 5 μM MGITC in 5.0 mM citrate buffer at pH 4.0 are shown in Figure 2.1a. The molecular structure of MGITC is shown in the inset of Figure 2.1a. MGITC is a hydrophobic, drug-like cation with an optical transition near 400 nm, as shown in Appendix A, proving resonance enhancement of the SHG signal for sensitive detection at the liposome surface. The SHG signal of the DOPC liposomes in 5.0 mM citrate buffer without MGITC is shown to have a very small SHG signal which is comparable to the SHG signal from buffer alone. When adding 5 μM MGITC to the liposomes, a large SHG peak is observed and is centered at 400 nm, with a full width half maximum of approximately 4.5 nm. These results are compared to the corresponding spectrum from 5 μM MGITC in 5.0 mM citrate buffer alone, without liposomes present, where the 400 nm signal originates from hyper Rayleigh scattering (HRS).[15,37,57] The SHG signal of MGITC in DOPC liposomes is ~3 times greater than the HRS from MGITC alone due to adsorption of MGITC at the liposome surface, in general agreement with our previous observations using MG.[15] The SHG spectra in Figure 1b shows the SHG signal from 5 μM MGITC added to the DOPC liposomes decreasing as a function of time, caused by the ensemble transport of MGITC molecules across the phospholipid liposome bilayer.[15,19] All SHG studies of the different liposomes presented here are performed in 5.0 mM citrate buffer at pH 4.0 for direct comparison and to ensure stability of the MGITC dye. In contrast, our previous studies on the similar molecular cation MG demonstrated

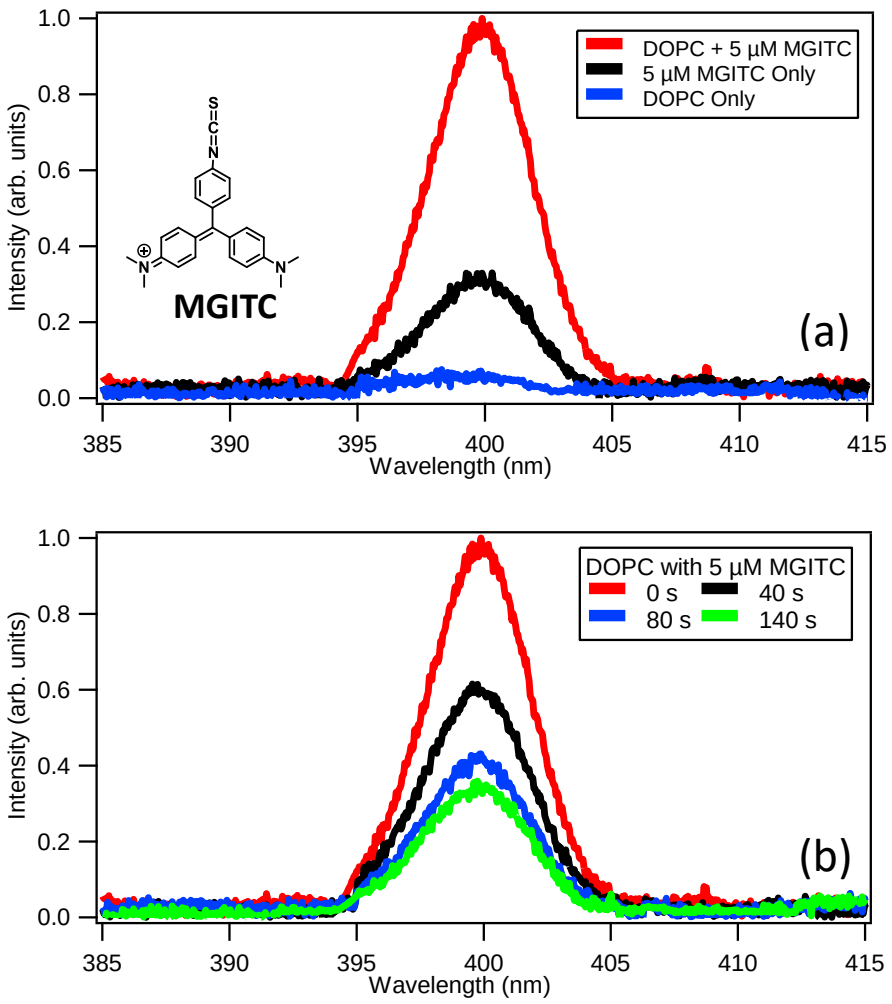

Figure 2.1. (a) SHG spectra of DOPC liposomes in the presence of 0 μM and 5 μM MGITC compared to 5 μM MGITC alone. Inset shows MGITC molecular structure. (b) SHG spectra of DOPC liposomes at various times after the addition of 5 μM MGITC. All samples are in 5.0 mM citrate buffer at pH 4.0.

no adsorption or transport in DOPC liposomes.[15] These results suggest that MGITC adsorbs and transports through the liposome membrane more efficiently than MG due to the added isothiocyanate group. These observations are in accord with expectations from distribution coefficients D and polar surface areas. At pH 4.0, MG has a $\log D$ value of 0.66 while MGITC has a $\log D$ value of 1.67, indicating a better lipophilic character for MGITC.[58] Additionally, a higher polar surface area of MGITC (18.61 A^2) in comparison to

MG (6.25 A^2) points to an anticipated stronger adsorption with the liposome surface, as discussed later.[59]

The time-dependent SHG intensities of MGITC added to DOPG, DOPS, and DOPC liposomes in citrate buffer at various dye concentrations are shown in Figure 2.2. The SHG intensities are all normalized with respect to the DOPS liposome sample upon addition of 4.75 μM MGITC. For all liposome samples, the abrupt rise in SHG intensity at time zero occurs when MGITC is added, followed by the gradual decay in intensity as the dye molecules transport through the liposome membrane until reaching equilibrium. The observed SHG intensities of MGITC added to liposomes are significantly higher than corresponding intensities of MG with these same liposomes,[15] where the presence of the isothiocyanate group in MGITC changes the orientational distribution of molecules on the liposome surface, resulting in altered molecular tilt angles and higher corresponding SHG intensities, as discussed later in greater detail from MD simulations. Additionally, the added isothiocyanate group may increase the hyperpolarizability leading to an increased $\chi^{(2)}$ term. The SHG intensity of MGITC with DOPS is higher than with DOPG, which is similar to our previous work with MG and DOPS and DOPG liposomes.[15]

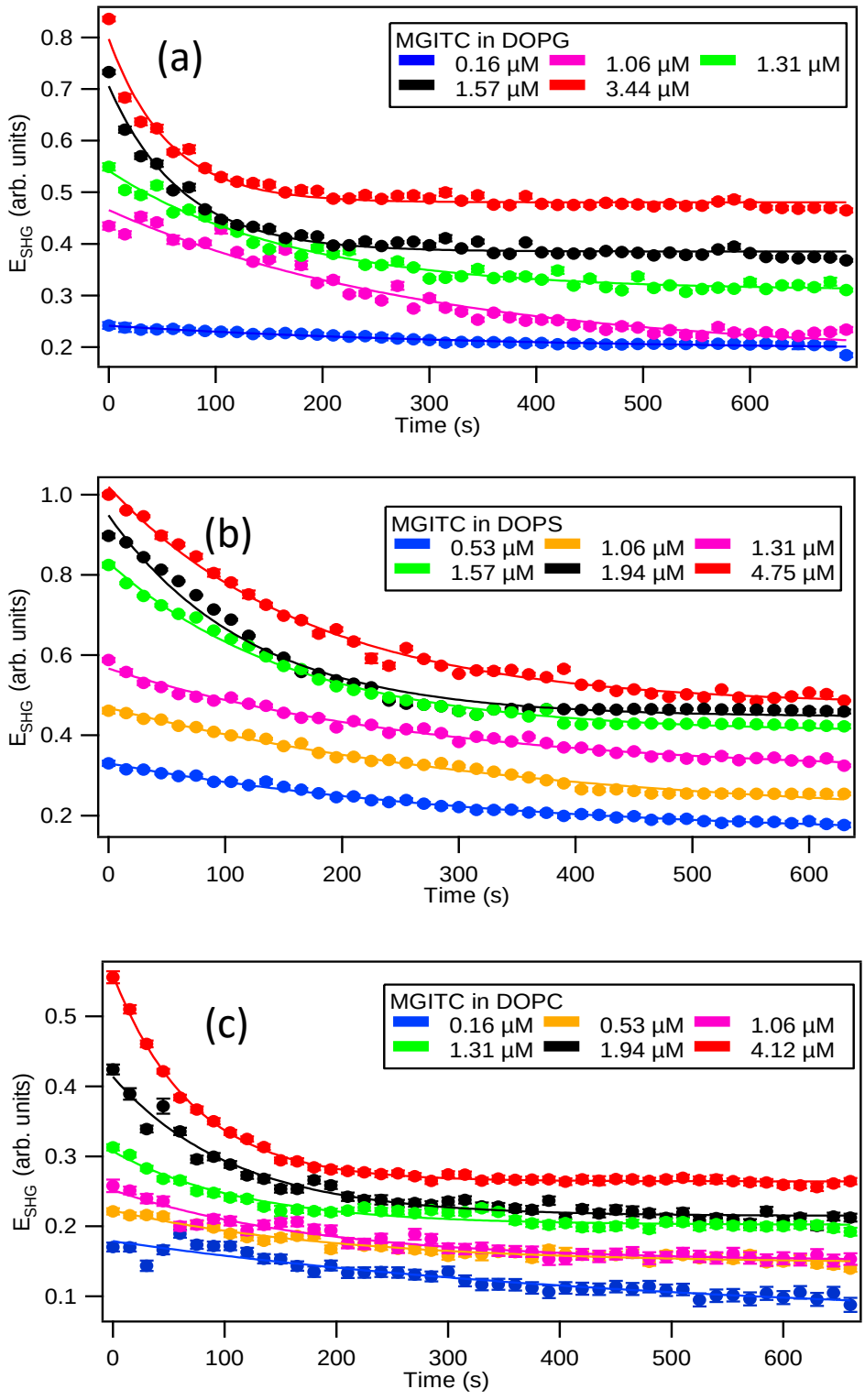

Figure 2.2. SHG time profiles upon addition of various concentrations of MGITC to (a) DOPG, (b) DOPS, and (c) DOPC liposomes in 5.0 mM citrate buffer at pH 4.0. Solid lines are best fits.

The molecular adsorption of MGITC at the liposome membrane surface is characterized using SHG adsorption isotherm measurements. The sudden rise in SHG signal upon MGITC addition to the liposome sample occurs due to the adsorption of MGITC ions to the outer membrane surface, corresponding to time zero. By plotting the intensity of the SHG signal at time zero as a function of added MGITC concentration, the adsorption isotherm is obtained. The results are fit using the modified Langmuir model to determine the adsorption site density and the free energy of adsorption of MGITC for each liposome surface in pH 4.0 citrate buffer. The modified Langmuir model is an extended form of the Langmuir model, which accounts for bulk depletion of the adsorbate due to a large cumulative liposome surface area. This model is based on the assumption of freely adsorbing molecules that form a single monolayer with a corresponding maximum adsorbate site density at the nanoparticle surface. The fits are given by[22,41]

$$I_{SHG} = A\left(\frac{N}{N_{max}}\right)^2 + B + M\alpha \tag{2.2}$$

and

$$\frac{N}{N_{max}} = \frac{\left(C+N_{max}+\frac{55.5}{K}\right)-\sqrt{\left(C+N_{max}+\frac{55.5}{K}\right)^2-4CN_{max}}}{2N_{max}} \tag{2.3}$$

where N is the concentration of dye molecules adsorbed, N_{max} is the maximum adsorption site concentration, *A* is the SHG intensity at saturation, *B* is the baseline offset, *M* is the concentration of free dye molecules in solution, *α* is the slope obtained from the plot of SHG intensity of dye alone as a function of concentration *C*, 55.5 is the molar concentration of water, and *K* is the adsorption equilibrium constant. The free energy of adsorption is obtained using $\Delta G = -RT\ln K$. The *α* term is discussed in more detail in Appendix A. Figure 2.3 shows the SHG adsorption isotherm measurements for MGITC

to the different liposome samples, where each data point corresponds to a fresh liposome sample at that added MGITC concentration. The molecular structures of DOPG, DOPS, and DOPC are shown as insets in Figure 2.3. The corresponding variables and fitting parameters are summarized in Table 2.1. The R^2 values for these fits are listed in Appendix A.

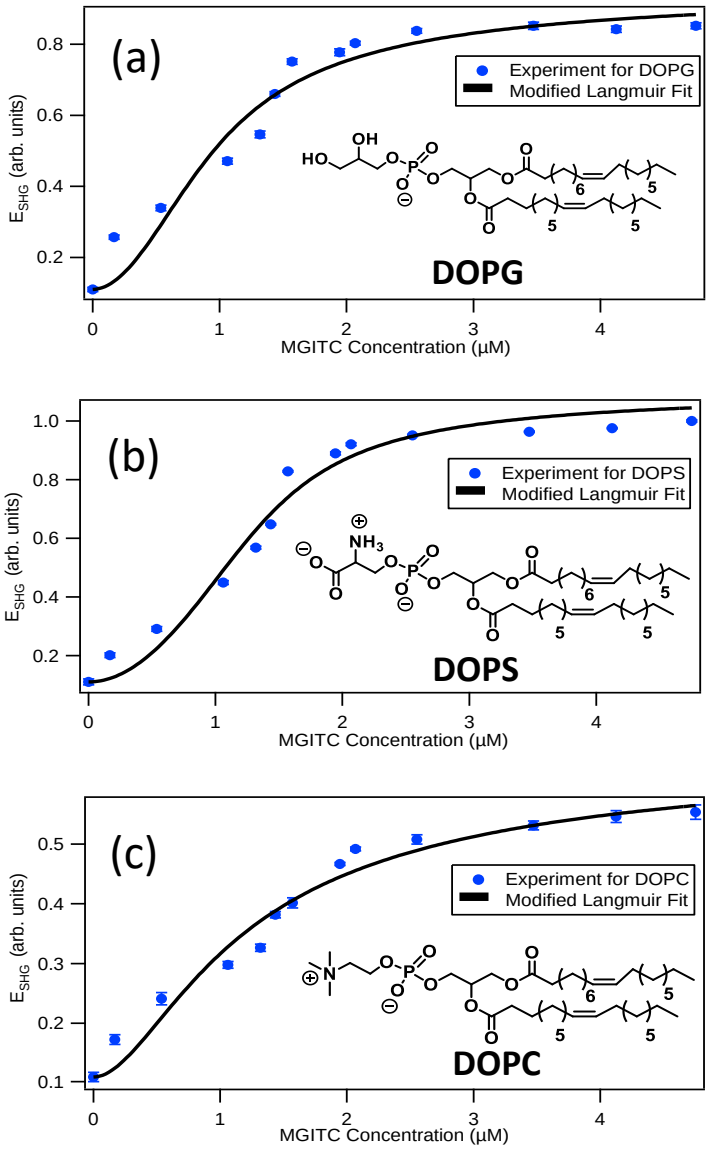

Figure 2.3. SHG-determined adsorption isotherms for MGITC with (a) DOPG, (b) DOPS, and (c) DOPC liposomes, respectively, in 5.0 mM citrate buffer at pH 4.0. Solid lines are best fits. Insets show molecular structures of DOPG, DOPS, and DOPC, respectively.

The adsorption equilibrium constants and free energy of adsorption magnitudes are larger in DOPG and DOPS, whereas these values are smaller for DOPC, in agreement with the zeta potential measurements. The larger value of the equilibrium constants in DOPG and DOPS is caused by the higher electrostatic attractions of the MGITC cations towards the more negative surface potentials. In comparison to MG,[15] the free energy of adsorption for MGITC to both DOPG and DOPS is more negative, indicating a stronger interaction between the MGITC dye molecules and the liposome surfaces. These findings are also in agreement with our molecular dynamics simulations results, as discussed later. The maximum adsorption site concentration and the corresponding number of lipid molecules per adsorption site provide key insights on the molecular interactions at the liposome bilayer. The SHG intensity at saturation is higher for DOPS and DOPG than for DOPC. Similarly, the obtained N_{max} values are higher for DOPS followed by DOPG. Compared to MG, the results suggest higher dye-dye repulsion and low ion-pair formation between MGITC and citrate at the liposome surfaces, leading to lower N_{max} values for MGITC than for MG in both DOPG and DOPS. The lower electrostatic interaction of MGITC with the zwitterionic DOPC surface is consistent with lower N_{max} values in DOPC than in DOPG and DOPS. These results for MGITC are in agreement with general trends from our previous work on MG and provide new insights that show the important influence of surface charge density, functional group interactions, and ion-pairing at the liposome surface.[15,44]

Table 2.1. List of Variables and Fitting Parameters Obtained from Modified Langmuir Model

	DOPG	**DOPS**	**DOPC**
K (10^9)	2.3 ± 1.2	3.7 ± 2.9	0.35 ± 0.04
N_{max} (μM)	1.8 ± 0.1	2.0 ± 0.1	1.5 ± 0.1
−ΔG (kcal/mol)	12.8 ± 0.3	13.1 ± 0.5	11.6 ± 0.1
Lipid/Site	27.7 ± 1.5	24.4 ± 1.8	45.4 ± 1.9
A	0.8 ± 0.01	1.0 ± 0.03	0.5 ± 0.01

The experimentally obtained SHG intensities are plotted versus time and are fit to single exponential functions given by

$$E_{SHG}(t) = a_0 + a_1 e^{-t/\tau} \tag{2.4}$$

to measure the molecular transport dynamics and the transport times τ. For each liposome and MGITC concentration, the fits from Equation 2.4 are displayed in Figure 2.2, showing excellent agreement with the data. The R^2 values for these fits are listed in Appendix A. The obtained transport times are plotted against concentration for each liposome sample, as shown in Figure 2.4. In the case of DOPG, shown in Figure A.5a, the MGITC transport rate $1/\tau$, displays a general linear relationship with dye concentration, in agreement with previous work on MG.[15,44] Additionally, previous SHG studies of MG in liposomes show decreased transport rates in higher added salt concentrations, where MG ion-pairing with counterions inhibits molecular transport kinetics.[15,44] The transport rate of MGITC in DOPC liposomes is much slower than in DOPG liposomes, possibly due to weaker electrostatic interactions at the zwitterionic surface and increased ion-pairing between MGITC and counterions. However, there is no clear linear trend of transport time versus concentration for MGITC in DOPS liposomes,

as shown in Figure 2.4b, and the transport rate is observed to have much less variation. These findings are also consistent with our previous studies for MG with DOPS liposomes, which suggests that the two additional charge centers of carboxylate and ammonium in the lipid head group suppress the formation of ion pairing.[15] As in MG, the transport of MGITC in the DOPS bilayer proceeds in accordance with Fick's law, caused by the concentration gradient across the membrane[60] and is less affected by ion pairing or changes in electrostatic surface potential.

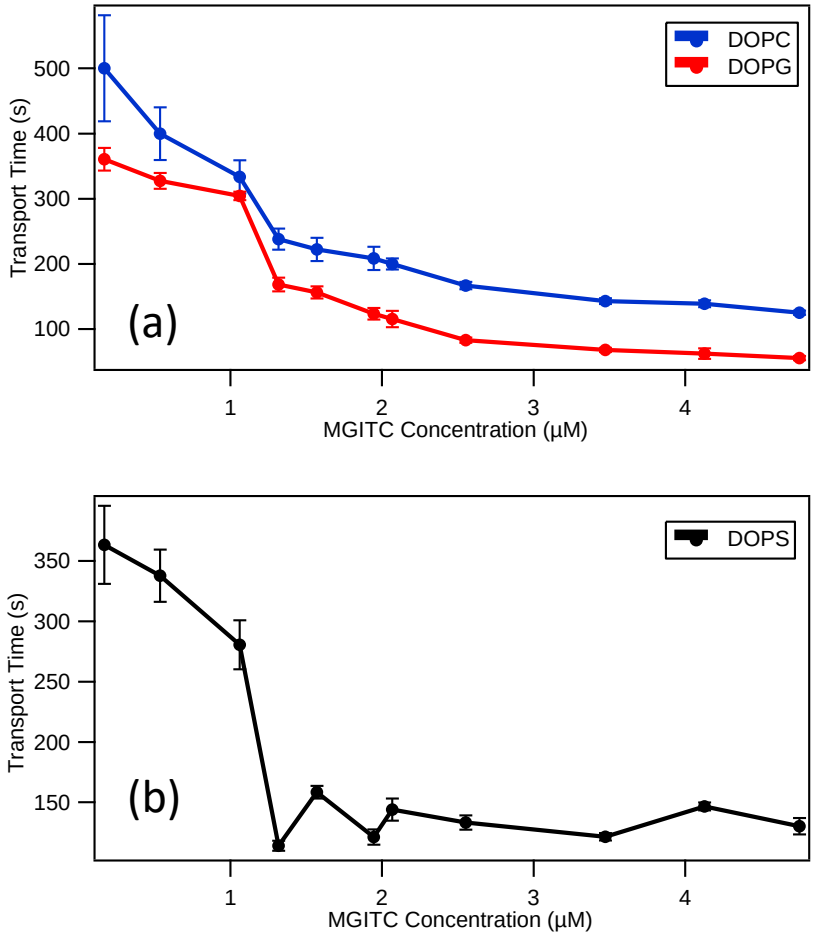

Figure 2.4. Transport times as a function of MGITC concentration in 5 mM citrate buffer of pH 4.0 for (a) DOPG, DOPC, and (b) DOPS liposomes.

Molecular dynamics simulations are performed for detailed comparisons on chemical and physical interactions of MG and MGITC with the liposome bilayers. Our previous investigations determined that MG neither adsorbs to nor transports through DOPC liposomes due to the zwitterionic surface that leads to greatly decreased electrostatic attraction.[15,44] In contrast, as shown in Figure 2.2 and 2.3, MGITC both adsorbs and transports efficiently in DOPC liposomes. This is consistent with our molecular dynamics simulations results as well, where the free energy profile for MG and MGITC as a function of distance from the center of mass (COM) of the DOPC and DOPG membranes are displayed in Figure 2.5.

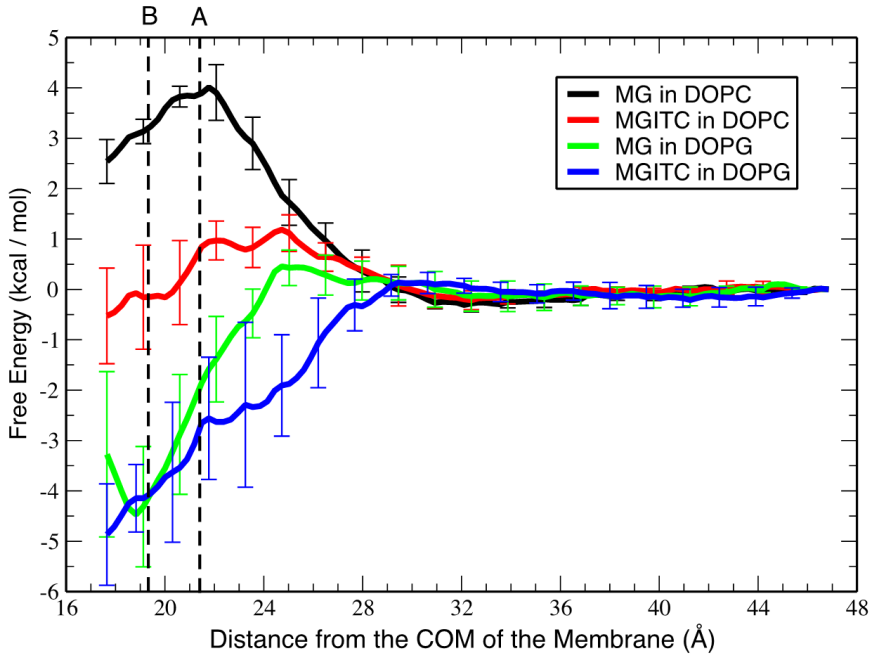

Figure 2.5. Free energy profile, as a function of the distance in the z-direction between the center of mass (COM) of the lipid bilayer and the COM of the dye molecule, for the transport processes of MG and MGITC dye molecules in DOPC and DOPG lipid bilayers. The vertical dotted black lines represent the average interface for (A) DOPC and (B) DOPG lipid bilayers. (Note: The membrane-water interface is perpendicular to the z-axis.)

The results show that the MGITC has a smaller energy barrier ~1 kcal/mol (~4.2 kJ/mol) for the insertion in the DOPC membrane as compared to MG ~4 kcal/mol (~16.8 kJ/mol). This indicates that MGITC transports more easily through the DOPC membrane than MG, in agreement with the SHG experimental

Figure 2.6a and Figure 2.6b show representative snapshots of the MG dye and the MGITC dye in the DOPC membrane, respectively. The NCS group of the MGITC molecule is preferentially directed towards the DOPC membrane. In contrast, one of the amine N atoms is preferentially directed toward the membrane for MG. The dipole moments of the two dye molecules, calculated using the Gaussian 09 suite of programs, are determined to be 2.28 and 10.59 Debye for MG and MGITC, respectively (see Appendix A for the details of the calculations). Therefore, the MGITC dipole moment is ~4 times higher than the MG dipole moment, due to the NCS group of the MGITC molecule. The lower energy barrier for MGITC as compared to the MG in DOPC membranes can be attributed to stronger dipole-dipole interactions between the NCS group and the neutral zwitterionic DOPC molecules. The positive charge of the amine group can also interact with the zwitterionic dipole, but given the delocalization of this positive charge, the charge-dipole interaction is not strong enough to overcome the barrier. Similarly, the free energy barriers for MG and MGITC molecules in anionic DOPG membranes are both much lower than the neutral zwitterionic DOPC membrane. The transport of MGITC through DOPG membranes is essentially barrier-less, whereas MG has a small barrier ~0.5 kcal/mol (~2.1 kJ/mol) owing to the strong Coulombic interaction between the dye and anionic liposome surface. Additionally, the most probable orientation of MG on DOPG is with both the amine groups pointing towards the membrane, while for

MGITC, one amine group and the NCS group are directed toward the DOPG membrane, as shown in Figure 2.6c and Figure 2.6d.

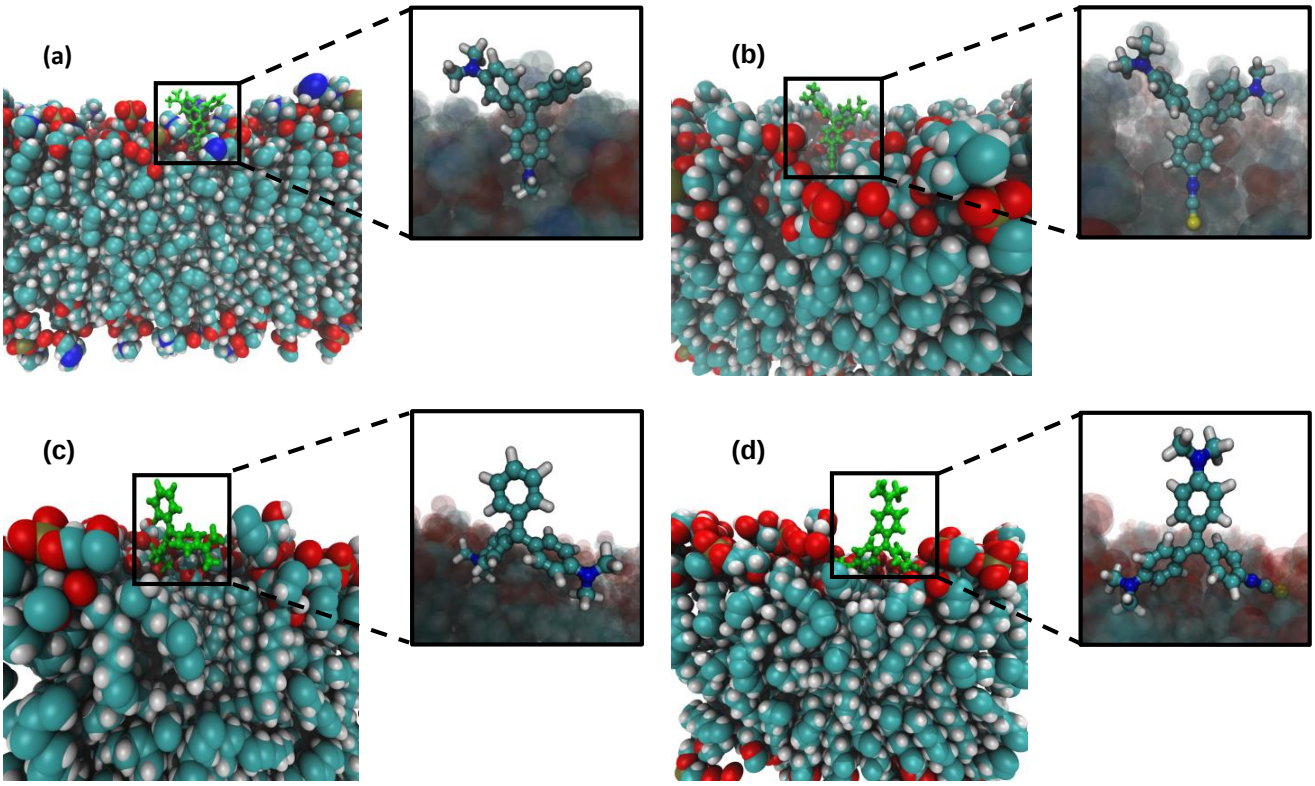

Figure 2.6. Snapshots showing the orientation of the dye molecules at the surface of each lipid bilayer and a zoomed-in view for (a) MG in DOPC, (b) MGITC in DOPC, (c) MG in DOPG, and (d) MGITC in DOPG. The atoms of carbon are represented in cyan, oxygen in red, sulfur in yellow, nitrogen in blue, and hydrogen in white.

Although the charge on the dye molecule is delocalized for MG, the interaction with the charged DOPG membrane is stronger than the weak charge-dipole interaction in the DOPC case. Similarly, the average orientation of MG at the DOPG membrane suggests that the electrostatic interactions between the positively-charged amine groups in the dye molecule and the negatively-charged DOPG membrane favor the adsorption process

from charge-charge interactions as compared to the neutral zwitterionic DOPC membrane from weak dipole-charge interactions. In the MGITC case, the strong dipole-charge interaction between the NCS dipole and the charged membrane competes with the electrostatic interactions between the positively charged amine groups of the dye and the negatively charge membrane, resulting in an average orientation with both the NCS and one amine group directed towards the membrane.

Molecular interactions are also studied between MGITC and the anionic QPADOPE liposomes using SHG measurements. QPADOPE liposomes are negatively charged with zeta potential values that are similar to those of the DOPG and DOPS liposomes at approximately −70 mV. However, the SHG intensities of different concentrations of MGITC alone in 5 mM citrate buffer are approximately equal to the corresponding SHG intensities of MGITC dye added to the QPADOPE liposomes, to within experimental uncertainty, indicating no adsorption. The SHG time profiles are also constant in time, showing that no transport of MGITC dye through the liposome bilayer occurs. Our previous work showed that MG also does not adsorb or transport in QPADOPE liposomes due to the location of the charged phosphate site, which is buried further from the liposome surface.[15] The bulky quinone group has strong hydrophobic interactions producing a dense shielding layer that prevents MGITC from approaching close to the charged phosphate center, decreasing the electrostatic Coulombic attraction. As a result, MGITC neither adsorbs nor transports in QPADOPE liposomes, as demonstrated in Appendix A.

These time-resolved SHG studies, combined with molecular dynamics simulations, clearly demonstrate that liposome-based ion transport and drug delivery

systems depend on many factors. A dominant factor is the electrostatic interaction between the ions and membrane. But other factors, such as dipole-dipole interactions, the molecular structure of the hydrophilic head groups, and the resulting locations of charged groups in the membrane, all play critical roles in the complex interactions that characterize molecular translocation in different liposome samples. A key finding is the importance of the functional group isothiocyanate in improving molecular adsorption and transport kinetics in phospholipid bilayers.

2.4 Conclusion

Time-dependent SHG measurements in combination with molecular dynamics simulations are used for investigations of molecular interactions of the small cationic dye malachite green isothiocyanate in different colloidal liposome samples. The experimental results are used to characterize the adsorption isotherms at the liposome surfaces and the corresponding transport kinetics across the different bilayers. These studies are also compared to our previous work on malachite green in these liposomes. The molecular transport of MGITC is found to be more rapid in the negatively-charged liposomes DOPG and DOPS compared to the zwitterionic liposome DOPC. The SHG results are consistent with corresponding molecular dynamics simulations that demonstrate that the energy barrier is lower for MGITC and MG in the anionic liposome DOPG than in the neutral zwitterionic liposome DOPC. Additionally, MGITC has stronger dipole-dipole interactions with the liposome surfaces than MG due to the added isothiocyanate functional group, leading to larger free energy of adsorption magnitudes. As a result, MGITC both adsorbs and transports in DOPC while MG does not. However, MGITC shows no adsorption and no transport with QPADOPE liposomes due to the bulky hydrophobic quinone shielding

layer. The collective behavior observed for molecular interactions at the liposome interface indicates that adsorption and transport kinetics are driven by many factors including electrostatic interactions from chemical functional groups, ion-pair formation, and more complicated hydrophobic and hydrophilic forces.

2.5. Notes

(1) Finkelstein, A. Water and nonelectrolyte permeability of lipid bilayer membranes. *J. Gen. Physiol.* **1976**, *68*, 127-135.

(2) Camenisch, G.; Folkers, G.; van de Waterbeemd, H. Review of theoretical passive drug absorption models: historical background, recent developments and limitations. *Pharm. Acta Helv.* **1996**, *71*, 309-327.

(3) Higuchi, W. I. Diffusional models useful in biopharmaceutics: drug release rate processes. *J. Pharm. Sci.* **1967**, *56*, 315-324.

(4) Schanker, L. Mechanisms of drug absorption and distribution. *Annu. Rev. Pharmacol.* **1961**, *1*, 29-45.

(5) Smith, D.; Artursson, P.; Avdeef, A.; Di, L.; Ecker, G. F.; Faller, B.; Houston, J. B.; Kansy, M.; Kerns, E. H.; Kramer, S. D. Passive lipoidal diffusion and carrier-mediated cell uptake are both important mechanisms of membrane permeation in drug disposition. *Mol. pharmaceutics* **2014**, *11*, 1727-1738.

(6) Van Meer, G.; Voelker, D. R.; Feigenson, G. W. Membrane lipids: where they are and how they behave. *Nat Rev Mol Cell Biol.* **2008**, *9*, 112.

(7) Escribá, P. V.; González-Ros, J. M.; Goñi, F. M.; Kinnunen, P. K.; Vigh, L.; Sánchez-Magraner, L.; Fernández, A. M.; Busquets, X.; Horváth, I.; Barceló-Coblijn, G. Membranes: a meeting point for lipids, proteins and therapies. *J Cell Mol Med.* **2008**, *12*, 829-875.

(8) Alberts, B.; Johnson, A.; Lewis, J.; Raff, M.; Roberts, K.; Walter, P.: *Molecular Biology of the Cell*; New York: Garland Science, 2002.

(9) Holthuis, J. C.; Menon, A. K. Lipid landscapes and pipelines in membrane homeostasis. *Nature* **2014**, *510*, 48.

(10) Pang, K. S. Modeling of intestinal drug absorption: roles of transporters and metabolic enzymes (for the Gillette Review Series). *Drug Metab. Dispos.* **2003**, *31*, 1507-1519.

(11) Liu, X.; Testa, B.; Fahr, A. Lipophilicity and its relationship with passive drug permeation. *Pharm. Res.* **2011**, *28*, 962-977.

(12) Walter, A.; Gutknecht, J. Permeability of small nonelectrolytes through lipid bilayer membranes. *J. Membr. Biol.* **1986**, *90*, 207-217.

(13) Hannesschlaeger, C.; Horner, A.; Pohl, P. Intrinsic Membrane Permeability to Small Molecules. *Chem. Rev.* **2019**, *119*, 5922-5953.

(14) McCarley, R. L. Redox-responsive delivery systems. *Annu. Rev. Anal. Chem.* **2012**, *5*, 391-411.

(15) Kumal, R. R.; Nguyenhuu, H.; Winter, J. E.; McCarley, R. L.; Haber, L. H. Impacts of Salt, Buffer, and Lipid Nature on Molecular Adsorption and Transport in Liposomes As Observed by Second Harmonic Generation. *J. Phys. Chem. C* **2017**, *121*, 15851-15860.

(16) Chen, X.; Yang, T.; Kataoka, S.; Cremer, P. S. Specific ion effects on interfacial water structure near macromolecules. *J. Am. Chem. Soc.* **2007**, *129*, 12272-12279.

(17) Troiano, J. M.; McGeachy, A. C.; Olenick, L. L.; Fang, D.; Liang, D.; Hong, J.; Kuech, T. R.; Caudill, E. R.; Pedersen, J. A.; Cui, Q.; Geiger, F. M. Quantifying the electrostatics of polycation–lipid bilayer interactions. *J. Am. Chem. Soc.* **2017**, *139*, 5808-5816.

(18) Liu, W.; Wang, Z.; Fu, L.; Leblanc, R. M.; Yan, E. C. Lipid compositions modulate fluidity and stability of bilayers: characterization by surface pressure and sum frequency generation spectroscopy. *Langmuir* **2013**, *29*, 15022-15031.

(19) Srivastava, A.; Eisenthal, K. B. Kinetics of molecular transport across a liposome bilayer. *Chem. Phys. Lett.* **1998**, *292*, 345-351.

(20) Wang, H.; Yan, E. C.; Liu, Y.; Eisenthal, K. B. Energetics and population of molecules at microscopic liquid and solid surfaces. *J. Phys. Chem. B* **1998**, *102*, 4446-4450.

(21) Khoury, R. A.; Ranasinghe, J. C.; Dikkumbura, A. S.; Hamal, P.; Kumal, R. R.; Karam, T. E.; Smith, H. T.; Haber, L. H. Monitoring the Seed-Mediated Growth of Gold Nanoparticles using In-Situ Second Harmonic Generation and Extinction Spectroscopy. *J. Phys. Chem. C* **2018**, *122*, 244400-224406.

(22) Haber, L. H.; Kwok, S. J.; Semeraro, M.; Eisenthal, K. B. Probing the colloidal gold nanoparticle/aqueous interface with second harmonic generation. *Chem. Phys. Lett.* **2011**, *507*, 11-14.

(23) Kumal, R. R.; Karam, T. E.; Haber, L. H. Determination of the surface charge density of colloidal gold nanoparticles using second harmonic generation. *J. Phys. Chem. C* **2015**, *119*, 16200-16207.

(24) Eisenthal, K. B. Second harmonic spectroscopy of aqueous nano-and microparticle interfaces. *Chem. Rev.* **2006**, *106*, 1462-1477.

(25) Kumal, R. R.; Abu-Laban, M.; Landry, C. R.; Kruger, B.; Zhang, Z.; Hayes, D. J.; Haber, L. H. Plasmon-enhanced photocleaving dynamics in colloidal microRNA-functionalized silver nanoparticles monitored with second harmonic generation. *Langmuir* **2016**, *32*, 10394-10401.

(26) Kumal, R. R.; Abu-Laban, M.; Hamal, P.; Kruger, B.; Smith, H. T.; Hayes, D. J.; Haber, L. H. Near-Infrared Photothermal Release of siRNA from the Surface of Colloidal Gold–Silver–Gold Core–Shell–Shell Nanoparticles Studied with Second-Harmonic Generation. *J. Phys. Chem. C* **2018**, *122*, 19699-19704.

(27) Wilhelm, M. J.; Sharifian Gh, M.; Dai, H.-L. Chemically Induced Changes to Membrane Permeability in Living Cells Probed with Nonlinear Light Scattering. *Biochemistry* **2015**, *54*, 4427-4430.

(28) Gh, M. S.; Wilhelm, M. J.; Dai, H.-L. Azithromycin-Induced Changes to Bacterial Membrane Properties Monitored in vitro by Second-Harmonic Light Scattering. *ACS Med. Chem. Lett.* **2018**, *9*, 569-574.

(29) Sharifian Gh, M.; Wilhelm, M. J.; Moore, M.; Dai, H.-L. Spatially Resolved Membrane Transport in a Single Cell Imaged by Second Harmonic Light Scattering. *Biochemistry* **2019**, *58*, 1841-1844.

(30) Wilhelm, M. J.; Sheffield, J. B.; Gonella, G.; Wu, Y.; Spahr, C.; Zeng, J.; Xu, B.; Dai, H.-L. Real-time molecular uptake and membrane-specific transport in living cells by optical microscopy and nonlinear light scattering. *Chem. Phys. Lett.* **2014**, *605*, 158-163.

(31) Liu, J.; Subir, M.; Nguyen, K.; Eisenthal, K. B. Second harmonic studies of ions crossing liposome membranes in real time. *J. Phys. Chem. B* **2008**, *112*, 15263-15266.

(32) Liu, Y.; Yan, E. C.; Zhao, X.; Eisenthal, K. B. Surface potential of charged liposomes determined by second harmonic generation. *Langmuir* **2001**, *17*, 2063-2066.

(33) Yan, E. C.; Eisenthal, K. B. Effect of cholesterol on molecular transport of organic cations across liposome bilayers probed by second harmonic generation. *Biophys. J.* **2000**, *79*, 898-903.

(34) Rao, Y.; Kwok, S. J.; Lombardi, J.; Turro, N. J.; Eisenthal, K. B. Label-free probe of HIV-1 TAT peptide binding to mimetic membranes. *PNAS* **2014**, *111*, 12684-12688.

(35) Hayes, P. L.; Malin, J. N.; Jordan, D. S.; Geiger, F. M. Get charged up: Nonlinear optical voltammetry for quantifying the thermodynamics and electrostatics of metal cations at aqueous/oxide interfaces. *Chem. Phys. Lett.* **2010**, *499*, 183-192.

(36) Yan, E. C.; Liu, Y.; Eisenthal, K. B. New method for determination of surface potential of microscopic particles by second harmonic generation. *J. Phys. Chem. B* **1998**, *102*, 6331-6336.

(37) Roke, S.; Gonella, G. Nonlinear light scattering and spectroscopy of particles and droplets in liquids. *Annu. Rev. Phys. Chem.* **2012**, *63*, 353-378.

(38) Dadap, J. I.; Shan, J.; Heinz, T. F. Theory of optical second-harmonic generation from a sphere of centrosymmetric material: small-particle limit. *J. Opt. Soc. Am. B: Opt. Phys.* **2004**, *21*, 1328-1347.

(39) Gonella, G.; Dai, H.-L. Second harmonic light scattering from the surface of colloidal objects: theory and applications. *Langmuir* **2013**, *30*, 2588-2599.

(40) Jen, S.-H.; Dai, H.-L.; Gonella, G. The effect of particle size in second harmonic generation from the surface of spherical colloidal particles. II: The nonlinear Rayleigh− Gans− Debye model. *J. Phys. Chem. C* **2010**, *114*, 4302-4308.

(41) Zeng, J.; Eckenrode, H. M.; Dai, H.-L.; Wilhelm, M. J. Adsorption and transport of charged vs. neutral hydrophobic molecules at the membrane of murine erythroleukemia (MEL) cells. *Colloids Surf., B* **2015**, *127*, 122-129.

(42) Sharifian Gh, M.; Wilhelm, M. J.; Dai, H.-L. Label-free optical method for quantifying molecular transport across cellular membranes in vitro. *J. Phys. Chem. Lett.* **2016**, *7*, 3406-3411.

(43) Shang, X.; Liu, Y.; Yan, E.; Eisenthal, K. B. Effects of counterions on molecular transport across liposome bilayer: probed by second harmonic generation. *J. Phys. Chem. B* **2001**, *105*, 12816-12822.

(44) Liu, Y.; Yan, E. C.; Eisenthal, K. B. Effects of bilayer surface charge density on molecular adsorption and transport across liposome bilayers. *Biophys. J.* **2001**, *80*, 1004-1012.

(45) Wilhelm, M. J.; Sharifian Gh, M.; Dai, H.-L. Influence of molecular structure on passive membrane transport: A case study by second harmonic light scattering. *J. Chem. Phys.* **2019**, *150*, 104705.

(46) Zeng, J.; Eckenrode, H. M.; Dounce, S. M.; Dai, H.-L. Time-resolved molecular transport across living cell membranes. *Biophys. J.* **2013**, *104*, 139-145.

(47) Ong, W.; Yang, Y.; Cruciano, A. C.; McCarley, R. L. Redox-triggered contents release from liposomes. *J. Am. Chem. Soc.* **2008**, *130*, 14739-14744.

(48) McCarley, R. L.; Forsythe, J. C.; Loew, M.; Mendoza, M. F.; Hollabaugh, N. M.; Winter, J. E. Release rates of liposomal contents are controlled by kosmotropes and chaotropes. *Langmuir* **2013**, *29*, 13991-13995.

(49) Plimpton, S. Fast parallel algorithms for short-range molecular dynamics. *J. Comput. Phys.* **1995**, *117*, 1-19.

(50) Wang, J.; Wolf, R. M.; Caldwell, J. W.; Kollman, P. A.; Case, D. A. Development and testing of a general amber force field. *J. Comput. Chem.* **2004**, *25*, 1157-1174.

(51) Bayly, C. I.; Cieplak, P.; Cornell, W.; Kollman, P. A. A well-behaved electrostatic potential based method using charge restraints for deriving atomic charges: the RESP model. *J. Phys. Chem.* **1993**, *97*, 10269-10280.

(52) Cieplak, P.; Cornell, W. D.; Bayly, C.; Kollman, P. A. Application of the multimolecule and multiconformational RESP methodology to biopolymers: Charge derivation for DNA, RNA, and proteins. *J. Comput. Chem.* **1995**, *16*, 1357-1377.

(53) Frisch, M. J.; Trucks, G. W.; Schlegel, H. B.; Scuseria, G. E.; Robb, M. A.; Cheeseman, J. R.; Scalmani, G.; Barone, V.; Petersson, G. A.; Nakatsuji, H.; Li, X.; Caricato, M.; Marenich, A. V.; Bloino, J.; Janesko, B. G.; Gomperts, R.; Mennucci, B.; Hratchian, H. P.; Ortiz, J. V.; Izmaylov, A. F.; Sonnenberg, J. L.; Williams; Ding, F.; Lipparini, F.; Egidi, F.; Goings, J.; Peng, B.; Petrone, A.; Henderson, T.; Ranasinghe, D.; Zakrzewski, V. G.; Gao, J.; Rega, N.; Zheng, G.; Liang, W.; Hada, M.; Ehara, M.; Toyota, K.; Fukuda, R.; Hasegawa, J.; Ishida, M.; Nakajima, T.; Honda, Y.; Kitao, O.; Nakai, H.; Vreven, T.; Throssell, K.; Montgomery Jr., J. A.; Peralta, J. E.; Ogliaro, F.; Bearpark, M. J.; Heyd, J. J.; Brothers, E. N.; Kudin, K. N.; Staroverov, V. N.; Keith, T. A.; Kobayashi, R.; Normand, J.; Raghavachari, K.; Rendell, A. P.; Burant, J. C.; Iyengar, S. S.; Tomasi, J.; Cossi, M.; Millam, J. M.; Klene, M.; Adamo, C.; Cammi, R.; Ochterski, J. W.; Martin, R. L.; Morokuma, K.; Farkas, O.; Foresman, J. B.; Fox, D. J.: Gaussian 16 Rev. B.01. Wallingford, CT, 2016.

(54) Kästner, J. Umbrella sampling. *WIREs Comput Mol Sci* **2011**, *1*, 932-942.

(55) Kumar, S.; Rosenberg, J. M.; Bouzida, D.; Swendsen, R. H.; Kollman, P. A. The weighted histogram analysis method for free-energy calculations on biomolecules. I. The method. *J. Comput. Chem.* **1992**, *13*, 1011-1021.

(56) Souaille, M.; Roux, B. t. Extension to the weighted histogram analysis method: combining umbrella sampling with free energy calculations. *Comput. Phys. Commun.* **2001**, *135*, 40-57.

(57) Rao, Y.; Guo, X.-m.; Tao, Y.-S.; Wang, H.-f. Observation of the direct S 2→ S 0 two-photon fluorescence between 370 and 480 nm and the hyperpolarizability of crystal violet (CV) from spectrally resolved hyper-Rayleigh scattering measurement. *J. Phys. Chem. A* **2004**, *108*, 7977-7982.

(58) Klopman, G.; Li, J.-Y.; Wang, S.; Dimayuga, M. Computer automated log P calculations based on an extended group contribution approach. *J. Chem. Inf. Model.* **1994**, *34*, 752-781.

(59) Ertl, P.; Rohde, B.; Selzer, P. Fast calculation of molecular polar surface area as a sum of fragment-based contributions and its application to the prediction of drug transport properties. *J. Med. Chem.* **2000**, *43*, 3714-3717.

(60) Friedman, M. H.: *Principles and models of biological transport*; Springer Science & Business Media, 2008.

Chapter 3. Influence of Temperature on Molecular Adsorption and Transport at Liposome Surfaces Studied by Molecular Dynamics Simulations and Second Harmonic Generation Spectroscopy

3.1 Introduction

Cellular membranes are constructed from a complex system of lipid species and membrane proteins for the regulation of molecular exchange with the surrounding environment.[1-3] A comprehensive study of cellular membranes, including their organization and chemical interactions, is critically important in describing signaling, metabolic functions, and the translocation of molecules.[4,5] Translocation can be characterized by molecular adsorption to the membrane surface and transport through the lipid bilayer.[6-8] Liposomes are small vesicles of phospholipids and are considered to be models for studying simplified biological membranes.[9-11] In this respect, it is crucial to investigate the effect of temperature on the properties of molecular translocation across the phospholipid bilayer in aqueous solution. The thermodynamics and kinetics related to molecular adsorption and transport at liposome surfaces provide detailed information that is relevant for understanding chemical interactions between small molecules and biological membranes. Recent work has investigated the effect of temperature on molecular transport of small molecules through the liposome membrane.[12,13] However, a complete characterization of molecular adsorption and transport in lipid bilayer systems, including the associated kinetics and thermodynamics, has not been studied in detail.

Second harmonic generation (SHG) spectroscopy has been widely used as an experimental method to probe the interfacial properties of colloidal nanoparticle systems.[10,14-20] SHG is a nonlinear optical process where two photons with a frequency

of ω add coherently to form a third photon with a frequency of 2ω. SHG is noninvasive, nondestructive, and surface-sensitive.[16,17] The second harmonic response from isotropic, centrosymmetric bulk media is dipole forbidden, resulting in no coherent signal.[21,22] However, SHG signal is allowed at surfaces and interfaces where the symmetry is broken.[14,15,20,23-26] SHG has been used extensively to study the molecular adsorption and transport of small cationic molecules, such as malachite green (MG)[19,27-30] and malachite green isothiocyanate (MGITC),[11] at liposome surfaces in aqueous solution. The adsorption of these dye molecules to the outer lipid bilayer produces an enhanced SHG signal,[27,31,32] followed by a decrease in SHG signal as the dye molecules transport through the membrane.[16,18,27,29,31-37] In our previous work, we investigated the molecular adsorption and transport properties of MG in liposomes with different lipids, buffers, and electrolyte conditions using time-dependent SHG.[10] We also studied the molecular interactions in different liposomes with the similar triphenylmethane dye molecule MGITC to interrogate the impact of chemical functional groups in these complicated translocation processes.[11] A fundamental understanding of the factors affecting lipid-based delivery systems can lead to potential clinical applications where the release of drug molecules from a liposome can be influenced by the surface chemistry and changes in the local environment.

In this chapter, we extend our investigations of chemical interactions at model biological membranes using time-dependent SHG spectroscopy combined with molecular dynamics (MD) simulations to study the molecular adsorption and transport of the small, drug-like cationic molecule, malachite green, with DOPG liposomes under varying sample temperatures. Measuring the temperature-dependent adsorption isotherms using SHG

provides for the determination of the free energies of adsorption and the adsorbate site concentrations, which further allows for the changes in enthalpy and entropy of the associated adsorption process to be obtained. Additionally, the kinetics of MG transport through the DOPG bilayer is measured, with the transport time decreasing as the temperature is increased, in agreement with previous studies.[13] Corresponding temperature-dependent MD simulations calculate the free energy profiles of bringing the MG molecule to the DOPG membrane, as well as the orientational distribution of MG at the bilayer surface, showing excellent agreement with the experimental results. By combining temperature-dependent and time-dependent SHG spectroscopy with MD simulations, the complicated chemical interactions occurring at the lipid bilayer interface in water are carefully studied for developing a greater understanding of biologically-relevant molecular translocation at model cellular membranes.

3.2 Experimental Section

3.2.1 Experimental Setup

The experimental set up for the SHG measurements has been described previously.[10,11,38] A titanium:sapphire oscillator laser, centered at 800 nm with a 75 fs pulse duration and 80 MHz repetition rate, is attenuated to an average power of 1.0 W and is focused to the sample contained in a 1 cm × 1 cm quartz cuvette to produce the SHG signal. The cuvette is wrapped with heating tape to control the sample temperature while measuring the time-dependent SHG intensity in the forward direction using a high-sensitivity charge-coupled device (CCD) detector connected to a monochromator spectrograph. A magnetic stir bar is used for automated stirring and a computer-controlled beam block is employed for measuring the background-subtracted SHG spectrum as a

function of time for each liposome sample at each temperature and added MG concentration.

3.2.2 Synthesis of Liposomes

The synthesis of large unilamellar vesicles (LUV) or liposomes of DOPG lipids has been previously reported[39,40] and is discussed in more detail in the Appendix B. DOPG was purchased from Avanti Polar lipids, Inc. in powder form. Citric acid monohydrate (≥99.0%), potassium hydroxide purified pellets (≥85%), and malachite green chloride were purchased from Sigma-Aldrich. The colloidal liposomes are characterized using dynamic light scattering (DLS) and zeta-potential measurements using a Zetasizer Nano ZS from Malvern Instruments Inc., UK. The average diameter of the DOPG lipids in 5 mM citrate buffer with pH 4.0 is measured to be 137 ± 42 nm with a polydispersity index of 0.07. Similarly, the corresponding zeta potential is determined to be −73.2 ± 1.1 mV.

3.2.3 Molecular Dynamics Simulations

Molecular dynamics simulations are carried out with the all-atom general AMBER force field (GAFF)[41] using the LAMMPS (version 05 Sep 2014)[42] software. The molecular structures of the molecules are optimized and the partial charges of the structures are calculated by the RESP fitting technique[43,44] using the HF/6-31G* method in the Gaussian 09 suite of programs.[45] The dye molecule-lipid system of MG with DOPG is simulated at two different temperatures of 303 K and 313 K. The equilibration simulations are carried out under isothermal-isobaric (NPT) conditions followed by simulations in the canonical (NVT) ensembles. The final simulation box dimensions are approximately 94.5 Å × 50.0 Å × 115.0 Å for the system simulated at 303 K and 94.0 Å × 50.0 Å × 117.5 Å for the

system simulated at 313 K. The membrane/water interface is perpendicular to the z-axis for each system. Additional details regarding the two systems and the simulation setup are discussed in the Appendix B. Using the umbrella sampling method,[46] the free energy profiles of bringing the MG molecule onto the DOPG membrane at the two different temperatures are determined. The displacement along the z-direction between the center of mass (COM) of the lipid bilayer and the COM of the dye molecule is used as the collective variable for the umbrella sampling. For both systems, 32 umbrella sampling windows are generated with an 18 ns simulation time per window and with a spacing of 1.5 Å along the z-axis. Using the weighted histogram analysis method (WHAM)[47,48] the potential of mean force of the adsorption process is calculated using the last 14 ns of each umbrella sampling window. The statistical error of the potential of mean force is determined using the block averaging method with 3.5 ns of data for each block. The orientation of the dipole moment of the MG molecule with respect to the DOPG membrane as the dye approaches the membrane is analyzed and compared for the two temperatures. In addition, the number of water molecules within 3.5 Å in the z-direction of the average surface of the DOPG molecules, as defined using the outermost oxygen atoms of the DOPG molecules, is calculated for each umbrella sampling window for both temperatures to determine the number of water molecules displaced as the MG molecule penetrates the membrane. Additional details of these calculations and analysis for each temperature are summarized in the Appendix B.

3.3. Results and Discussion

Time-dependent SHG measurements under varying sample temperature and MG concentration provide crucial information on the molecular transport through the lipid

bilayer. The SHG signal I_{SHG} is observed to rise abruptly upon the addition of MG into the colloidal DOPG liposome sample, due to MG adsorption to the outer surface of the bilayer, followed by a gradual, time-dependent exponential decrease in SHG signal caused by the MG transport through the liposome bilayer. These general observations are in agreement with previous studies.[10,11,27,29,49] The transport kinetics of MG crossing the DOPG lipid bilayer are analyzed by fitting the time-dependent SHG electric field, where $E_{SHG} = \sqrt{I_{SHG}}$, using the exponential function, $E_{SHG}(t) = a_0 + a_1 e^{-t/\tau}$, to obtain the molecular transport time τ under different MG concentrations and bulk temperatures. Here, t is the experimental time after MG addition. These exponential fits are plotted as solid lines for each temperature and MG concentration, as shown in Figure 3.1. For a direct comparison, all SHG intensities are normalized with respect to the DOPG liposomes immediately upon addition of 15 μM MG at 25 °C. Representative SHG spectra and calculated R^2 values for the exponential fits are included in the Appendix B. The bulk temperatures used are all above the transition temperature, −18 °C for DOPG, where the ordered gel phase changes to the more disordered liquid crystalline phase.[27]

The obtained transport times τ are plotted as a function of MG concentration for each temperature, as displayed in Figure 3.2a. The rate of molecular transport is significantly faster at higher temperatures. Applying heat to a lipid bilayer leads to increased hydrocarbon chain motion, less hydrogen bonding between adjacent acyl

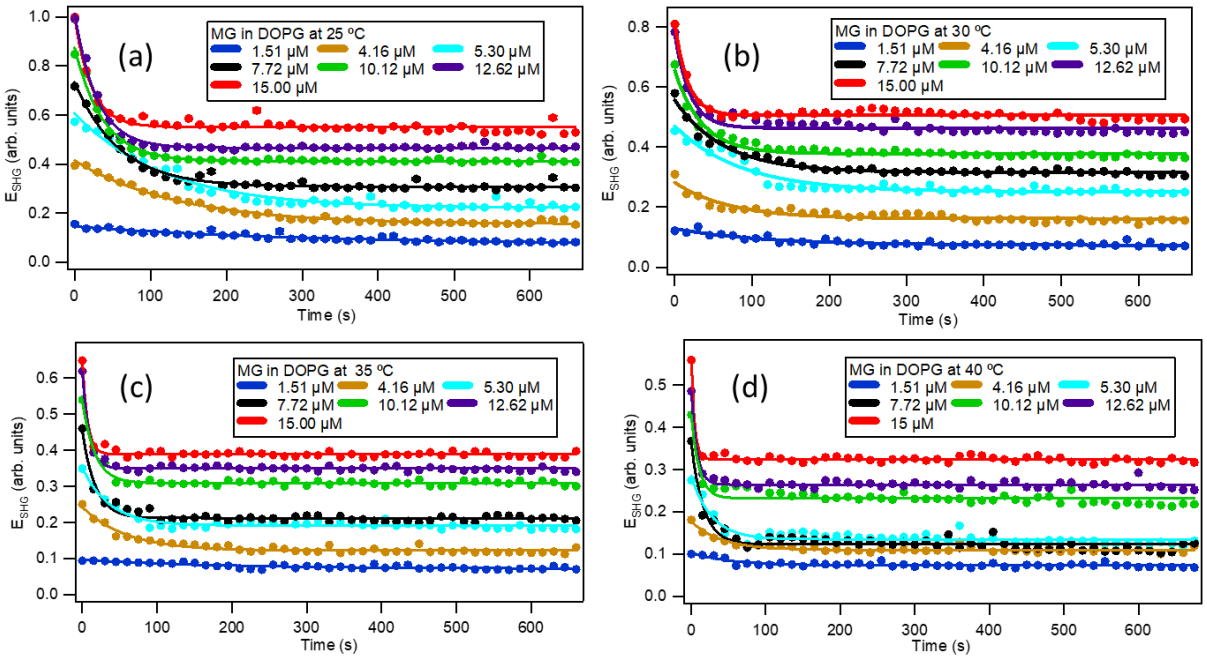

Figure 3.1. SHG time profiles upon addition of various concentrations of MG to DOPG liposomes at (a) 25 °C, (b) 30 °C, (c) 35 °C, and (d) 40 °C, respectively. Solid lines are best fits.

groups, and a larger volume of the overall non-polar region.[50,51] Similarly, the membrane fluidity is also increased at higher temperatures, which aids the rate of transport.[52,53] These findings are consistent with our SHG results, where increased temperature leads to the observed decrease in the MG transport time. These results are also in general agreement with previous studies.[12,13] Additionally, the obtained rate constants from the fits are shown to vary linearly as a function of MG concentration for each temperature, and the corresponding slopes are observed to vary linearly with temperature, as shown in the Appendix B. The linear dependence of the rate constant with respect to temperature is analogous to the related process of temperature-dependent diffusion described by the Stokes-Einstein equation.[54]

Adsorption isotherm measurements are performed by measuring the SHG intensity as a function of MG concentration to obtain the adsorption site density and

adsorption free energy for each sample temperature. For these isotherms, the SHG intensity is measured directly upon MG addition at t = 0 using a fresh liposome sample for each MG concentration and temperature. The experimentally obtained isotherms are fit using the modified Langmuir isotherm model to account for the reduction of the bulk concentration of the adsorbate molecules due to the large cumulative surface area of the colloidal liposome sample. The modified Langmuir model is given by[20,37]

$$I_{SHG} = A\left(\frac{N}{N_{max}}\right)^2 + B + M\alpha \tag{3.1}$$

and

$$\frac{N}{N_{max}} = \frac{\left(C+N_{max}+\frac{55.5}{K}\right)-\sqrt{\left(C+N_{max}+\frac{55.5}{K}\right)^2-4CN_{max}}}{2N_{max}} \tag{3.2}$$

where, N_{max} is the maximum adsorption site concentration, K is the adsorption equilibrium constant, A is the SHG intensity at saturation, and C is the added dye concentration. Additionally, N is the concentration of dye molecules adsorbed, B is the baseline offset, M is the concentration of free dye molecules in solution, and α is the slope obtained from free dye molecules alone in solution as a function of C. The fits of the modified Langmuir model to the experimental results are shown in Figure 3.2b and the corresponding fit parameters are listed in Table 3.1. The adsorption equilibrium constant K is observed to decrease as temperature is increased. This may be a consequence of increased counterion adsorption to the Stern layer under higher temperatures leading to decreased the electrostatic attraction of MG to the bilayer surface. Additionally, the adsorption site densities are found to have an opposite behavior, where higher temperatures have increased maximum adsorption site concentration N_{max} values. This is attributed to the increased mobility of counterions and the increase in area of the lipid

headgroups at higher temperatures.[52,53] Increased counterion concentration at the bilayer surface at higher temperatures also shields adsorbate-adsorbate repulsion, contributing to the higher N_{max} values.[10]

The free energy of adsorption, obtained from $\Delta G = -RT \ln K$, is plotted as a function of temperature, as shown in Figure 3.2c. The results are fit to a line with $\Delta G = \Delta H - T\Delta S$ to provide the thermodynamic properties of the molecular adsorption to the liposome surface, where ΔH is the change in adsorption enthalpy, ΔS is the change in adsorption entropy, and T is the temperature. The calculated ΔH from the y-intercept is −4.685 ± 0.248 kcal/mol, indicating that the net change in adsorption enthalpy represents an exothermic process. The calculated ΔS from the linear slope is 0.021 ± 0.001 kcal/K·mol. This change in entropy is a full accounting of the adsorption process, including the change in entropy of the adsorbate molecules as well as the overall liposome surface. The molecular adsorption by itself should have a negative change in entropy as the dye molecules are more ordered when adsorbed to the liposome surface. However, the adsorbate molecules replace water molecules and counterions that were originally at the liposome surface. Since each MG adsorbate molecule replaces numerous water molecules and counterions due to their relative sizes, an overall increase of entropy occurs upon adsorption when given a full account of all substituents. Our MD simulations indicate that approximately 70 water molecules are replaced by each MG molecule upon adsorption, as discussed in more detail in the Appendix B. Here, since ΔH is negative and ΔS is positive, the process of MG adsorption to the DOPG liposome surface is expected to be spontaneous at all aqueous temperatures. A comparative study of MG adsorption to colloidal polystyrene sulfate microspheres in water using temperature-

dependent SHG measurements is included in the Appendix B, demonstrating the general applicability of this technique for determining the thermodynamics of adsorption for a wide variety of colloidal systems.

Molecular dynamics simulations are used to obtain additional information about the interactions of MG molecules at the DOPG bilayer surface at two different temperatures. The free energy profile for the adsorption of MG as a function of distance in the z-direction between the COM of the MG molecule and the COM of the DOPG membrane at the two different temperatures are displayed in Figure 3.3. According to the free energy profile, at 313 K this adsorption process is essentially barrier-less, whereas at 303 K there is a small energy barrier of ~0.5 kcal/mol (~2.1 kJ/mol) for the adsorption process. Although MG is thermodynamically more favored to be adsorbed on the membrane under both temperatures, the results in Figure 3.3 demonstrate that the stability of the MG molecule inside the membrane is greater at higher temperatures. In addition, during the initial equilibrium MD canonical simulations before performing the umbrella sampling simulation, the MG molecule is seen to rapidly adsorb and penetrate into the DOPG membrane at the higher temperature, whereas the adsorption process takes much longer and displays less penetration at the lower temperature simulation as discussed in the Appendix B. These results are consistent with the SHG experimental observations, where MG transports faster through the bilayer and the corresponding ΔG value is more negative as temperature increases.

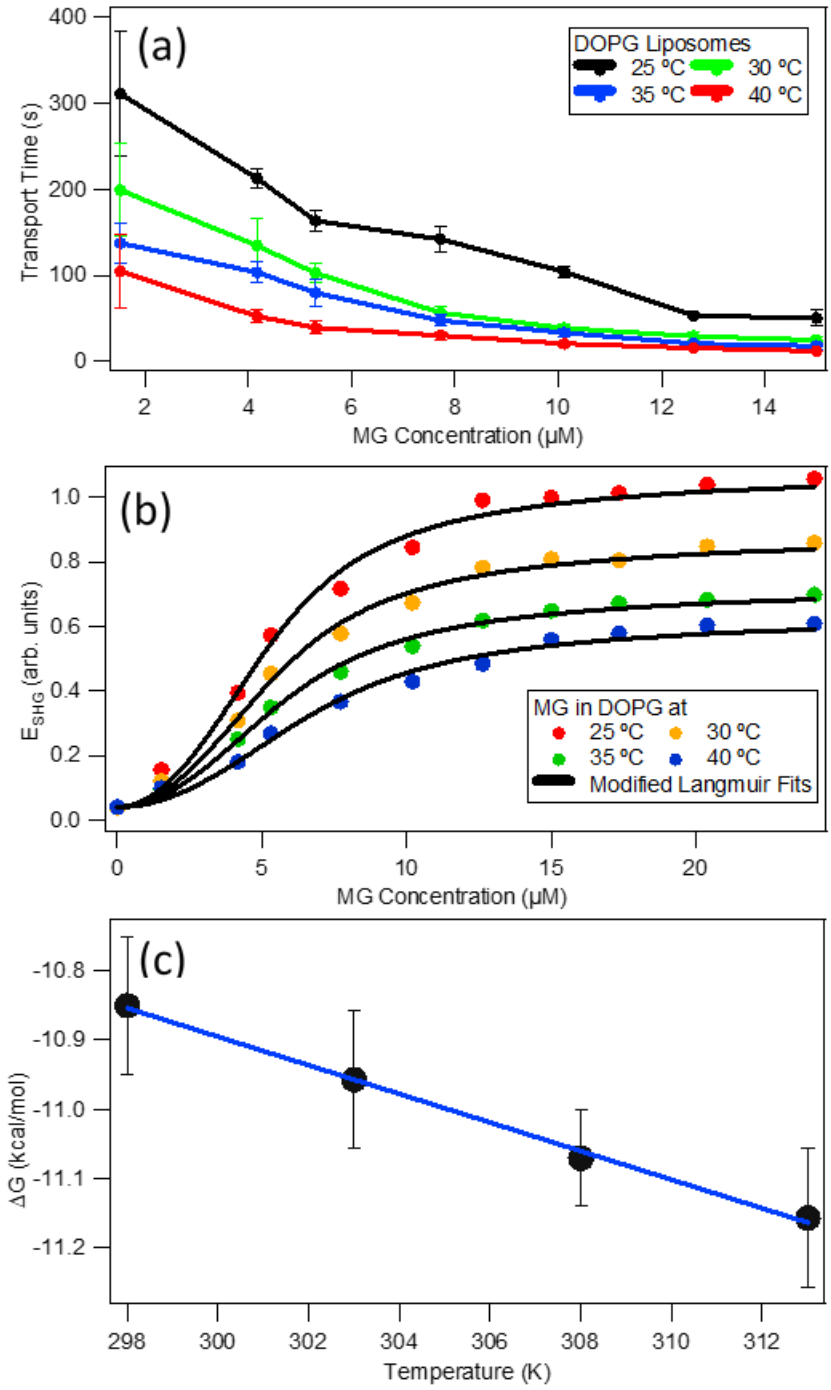

Figure 3.2 (a) Transport times as a function of MG concentration for DOPG liposomes at different temperatures. (b) SHG-determined adsorption isotherms for MG with DOPG liposomes in 5.0 mM citrate buffer at different temperatures. Solid lines are best fits. (c) Adsorption free energy for MG with DOPG liposomes as a function of temperature (black circles) with best linear fit (blue line).

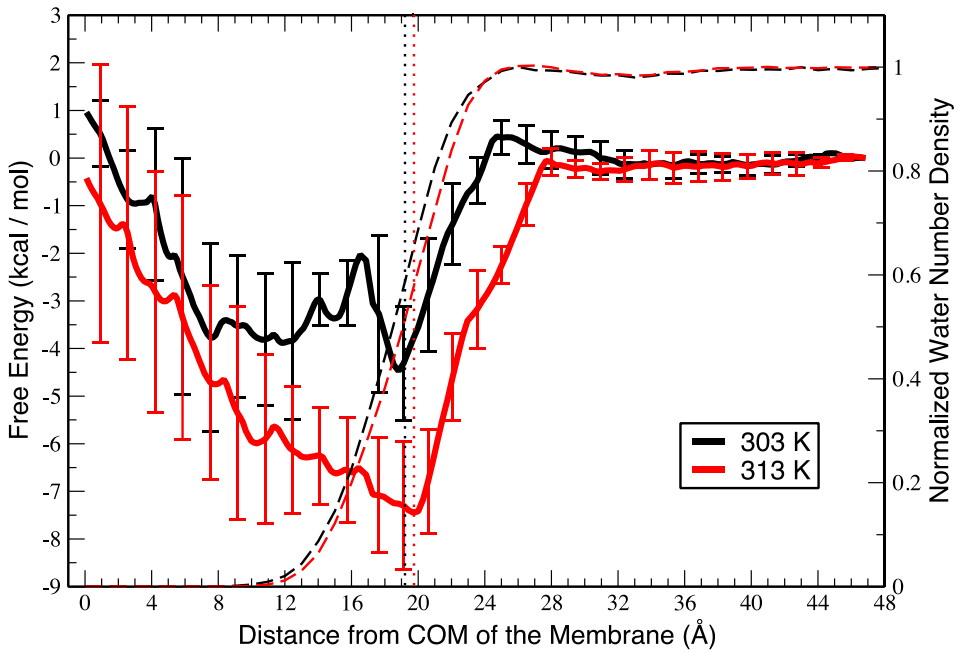

Figure 3.3. Potential of mean force curves for the adsorption process of MG molecule to DOPG lipid bilayer at temperatures of 303 K and 313 K as a function of distance along the z-axis (which is perpendicular to the membrane-water interface) between the center of mass of the membrane and the center of mass of the dye. The vertical dotted lines represent the average interface for 303 K (black) and 313 K (red). The dashed lines represent the normalized water number density calculated when the dye is far away from the interface for 303 K (black) and 313 K (red).

Table 3.1. Fitting Parameters and Free Energies Obtained from Modified Langmuir Model

	25 °C	30 °C	35 °C	40 °C
K (10^7)	9.1 ± 0.1	8.1 ± 0.2	7.2 ± 0.1	6.2 ± 0.3
N_{max} (μM)	5.4 ± 0.2	5.7 ± 0.4	6.0 ± 0.1	6.9 ± 0.3
A	1.0 ± 0.01	0.85 ± 0.01	0.69 ± 0.01	0.60 ± 0.01
−ΔG (kcal/mol)	10.8 ± 0.1	10.9 ± 0.1	11.1 ± 0.1	11.2 ± 0.1

These SHG and MD studies also give important insight regarding the adsorbate ordering and orientational distributions at the colloidal liposome surface in water. It is well established that the SHG signal from colloidal nanoparticles depends on the orientation angle of adsorbates, as well as the scattering angle and polarization configuration.[25,55-57] For our study, the SHG intensity at saturation A depends on both N_{max} and orientational distribution of adsorbed MG at the liposome surface.[10,29,58] Our experimental results show that A decreases as the temperature is increased, even as N_{max} is observed to increase. This suggests that the orientational distribution should also change as a function of temperature, leading to the lower measured SHG signals. Our MD simulation results are in excellent agreement with these observations, where the orientational distribution of the dipole moment of adsorbed MG molecule broadens significantly at the higher temperature, leading to decreased ordering and lower SHG signals, as discussed in greater detail in the Appendix B. Previous studies on MG in DOPG liposomes showed a more constant time-zero SHG signal under varying temperatures.[13] However, these measurements were conducted at 90º collection angle, while our measurements are performed in the forward direction, where different relative signal strengths from changes in N_{max} and orientational distribution could explain the deviation in these experimental observations. Overall, the SHG studies of MG adsorption and transport in DOPG liposomes under varying temperature provides detailed information on fundamental chemical interactions at a lipid bilayer in water that is complementary and consistent with the corresponding MD simulations.

3.4. Conclusion

The adsorption and transport of the small, cationic drug-like molecule, malachite green, at the DOPG liposome surface in water is investigated using molecular dynamics simulations and time-dependent second harmonic generation spectroscopy. The MD simulations results are in excellent agreement with the experimental results, demonstrating that the rate of transport is faster at higher temperatures. Additionally, the SHG adsorption isotherm measurements indicate that the adsorbate concentration increases while the free energy of adsorption becomes more negative as the temperature is increased. By plotting the free energy as a function of temperature, the changes in enthalpy and entropy are obtained, showing that the adsorption process is exothermic with increasing entropy when taking a full account of all substituents. The MD simulations also determine the temperature-dependent free energy curves of adsorption, the orientational distributions of the adsorbate at the surface, and the number of water molecules displaced upon adsorption, which all provide important context for interpreting the SHG results. In summary, this study shows that temperature is a critical and sensitive factor in quantifying chemical interactions with lipid bilayers, providing fundamental insight that can help in developing potential membrane-based drug-delivery applications.

3.5. Notes

(1) Escribá, P. V.; González-Ros, J. M.; Goñi, F. M.; Kinnunen, P. K.; Vigh, L.; Sánchez-Magraner, L.; Fernández, A. M.; Busquets, X.; Horváth, I.; Barceló-Coblijn, G. Membranes: a meeting point for lipids, proteins and therapies. *J Cell Mol Med.* **2008**, *12*, 829-875.

(2) Van Meer, G.; Voelker, D. R.; Feigenson, G. W. Membrane lipids: where they are and how they behave. *Nat Rev Mol Cell Biol.* **2008**, *9*, 112.

(3) Alberts, B.; Johnson, A.; Lewis, J.; Raff, M.; Roberts, K.; Walter, P.: *Molecular Biology of the Cell*; New York: Garland Science, 2002.

(4) Holthuis, J. C.; Menon, A. K. Lipid landscapes and pipelines in membrane homeostasis. *Nature* **2014**, *510*, 48.

(5) Schanker, L. Mechanisms of drug absorption and distribution. *Annu. Rev. Pharmacol.* **1961**, *1*, 29-45.

(6) Pang, K. S. Modeling of intestinal drug absorption: roles of transporters and metabolic enzymes (for the Gillette Review Series). *Drug Metab. Dispos.* **2003**, *31*, 1507-1519.

(7) Liu, X.; Testa, B.; Fahr, A. Lipophilicity and its relationship with passive drug permeation. *Pharm. Res.* **2011**, *28*, 962-977.

(8) Walter, A.; Gutknecht, J. Permeability of small nonelectrolytes through lipid bilayer membranes. *J. Membr. Biol.* **1986**, *90*, 207-217.

(9) McCarley, R. L. Redox-responsive delivery systems. *Annu. Rev. Anal. Chem.* **2012**, *5*, 391-411.

(10) Kumal, R. R.; Nguyenhuu, H.; Winter, J. E.; McCarley, R. L.; Haber, L. H. Impacts of Salt, Buffer, and Lipid Nature on Molecular Adsorption and Transport in Liposomes As Observed by Second Harmonic Generation. *J. Phys. Chem. C* **2017**, *121*, 15851-15860.

(11) Hamal, P.; Nguyenhuu, H.; Subasinghege Don, V.; Kumal, R. R.; Kumar, R.; McCarley, R. L.; Haber, L. H. Molecular Adsorption and Transport at Liposome Surfaces Studied by Molecular Dynamics Simulations and Second Harmonic Generation Spectroscopy. *J. Phys. Chem. B* **2019**, *123*, 7722-7730.

(12) Varshney, G.; Kintali, S.; Das, K. Effect of Curcumin Addition on the Adsorption and Transport of a Cationic Dye across DPPG-POPG Liposomes Probed by Second Harmonic Spectroscopy. *Langmuir* **2017**, *33*, 8302-8310.

(13) Kim, J.; Kim, M.-W. Temperature effect on the transport dynamics of a small molecule through a liposome bilayer. *Eur. Phys. J. E* **2007**, *23*, 313-317.

(14) Khoury, R. A.; Ranasinghe, J. C.; Dikkumbura, A. S.; Hamal, P.; Kumal, R. R.; Karam, T. E.; Smith, H. T.; Haber, L. H. Monitoring the Seed-Mediated Growth of Gold Nanoparticles using In-Situ Second Harmonic Generation and Extinction Spectroscopy. *J. Phys. Chem. C* **2018**, *122*, 244400-224406.

(15) Kumal, R. R.; Abu-Laban, M.; Hamal, P.; Kruger, B.; Smith, H. T.; Hayes, D. J.; Haber, L. H. Near-Infrared Photothermal Release of siRNA from the Surface of Colloidal Gold–Silver–Gold Core–Shell–Shell Nanoparticles Studied with Second-Harmonic Generation. *J. Phys. Chem. C* **2018**, *122*, 19699-19704.

(16) Eisenthal, K. B. Second harmonic spectroscopy of aqueous nano-and microparticle interfaces. *Chem. Rev.* **2006**, *106*, 1462-1477.

(17) Wang, H.; Yan, E. C.; Liu, Y.; Eisenthal, K. B. Energetics and population of molecules at microscopic liquid and solid surfaces. *J. Phys. Chem. B* **1998**, *102*, 4446-4450.

(18) Gh, M. S.; Wilhelm, M. J.; Dai, H.-L. Azithromycin-Induced Changes to Bacterial Membrane Properties Monitored in vitro by Second-Harmonic Light Scattering. *ACS Med. Chem. Lett.* **2018**, *9*, 569-574.

(19) Wilhelm, M. J.; Sharifian Gh, M.; Dai, H.-L. Chemically Induced Changes to Membrane Permeability in Living Cells Probed with Nonlinear Light Scattering. *Biochemistry* **2015**, *54*, 4427-4430.

(20) Haber, L. H.; Kwok, S. J.; Semeraro, M.; Eisenthal, K. B. Probing the colloidal gold nanoparticle/aqueous interface with second harmonic generation. *Chem. Phys. Lett.* **2011**, *507*, 11-14.

(21) Gan, W.; Gonella, G.; Zhang, M.; Dai, H.-L. Reactions and adsorption at the surface of silver nanoparticles probed by second harmonic generation. *J. Chem. Phys.* **2011**, *134*, 041104.

(22) Gonella, G.; Dai, H.-L. Second harmonic light scattering from the surface of colloidal objects: theory and applications. *Langmuir* **2013**, *30*, 2588-2599.

(23) Abu-Laban, M.; Hamal, P.; Arrizabalaga, J. H.; Forghani, A.; Dikkumbura, A. S.; Kumal, R. R.; Haber, L. H.; Hayes, D. J. Combinatorial Delivery of miRNA-Nanoparticle Conjugates in Human Adipose Stem Cells for Amplified Osteogenesis. *Small* **2019**, *15*, 1902864.

(24) Ranasinghe, J. C.; Dikkumbura, A. S.; Hamal, P.; Chen, M.; Khoury, R. A.; Smith, H. T.; Lopata, K.; Haber, L. H. Monitoring the growth dynamics of colloidal gold-silver core-shell nanoparticles using in situ second harmonic generation and extinction spectroscopy. *J. Chem. Phys.* **2019**, *151*, 224701.

(25) Jen, S.-H.; Gonella, G.; Dai, H.-L. The effect of particle size in second harmonic generation from the surface of spherical colloidal particles. I: Experimental observations. *J. Phys. Chem. A* **2009**, *113*, 4758-4762.

(26) Rao, Y.; Kwok, S. J.; Lombardi, J.; Turro, N. J.; Eisenthal, K. B. Label-free probe of HIV-1 TAT peptide binding to mimetic membranes. *PNAS* **2014**, *111*, 12684-12688.

(27) Srivastava, A.; Eisenthal, K. B. Kinetics of molecular transport across a liposome bilayer. *Chem. Phys. Lett.* **1998**, *292*, 345-351.

(28) Liu, J.; Subir, M.; Nguyen, K.; Eisenthal, K. B. Second harmonic studies of ions crossing liposome membranes in real time. *J. Phys. Chem. B* **2008**, *112*, 15263-15266.

(29) Liu, Y.; Yan, E. C.; Eisenthal, K. B. Effects of bilayer surface charge density on molecular adsorption and transport across liposome bilayers. *Biophys. J.* **2001**, *80*, 1004-1012.

(30) Shang, X.; Liu, Y.; Yan, E.; Eisenthal, K. B. Effects of counterions on molecular transport across liposome bilayer: probed by second harmonic generation. *J. Phys. Chem. B* **2001**, *105*, 12816-12822.

(31) Wilhelm, M. J.; Dai, H. L. Molecule-Membrane Interactions in Biological Cells Studied with Second Harmonic Light Scattering. *Chemistry–An Asian Journal* **2019**.

(32) Wilhelm, M. J.; Sharifian Gh, M.; Dai, H.-L. Influence of molecular structure on passive membrane transport: A case study by second harmonic light scattering. *J. Chem. Phys.* **2019**, *150*, 104705.

(33) Liu, J.; Shang, X.; Pompano, R.; Eisenthal, K. B. Antibiotic assisted molecular ion transport across a membrane in real time. *Faraday Discuss.* **2005**, *129*, 291-299.

(34) Yan, E. C.; Eisenthal, K. B. Effect of cholesterol on molecular transport of organic cations across liposome bilayers probed by second harmonic generation. *Biophys. J.* **2000**, *79*, 898-903.

(35) Sharifian Gh, M.; Wilhelm, M. J.; Moore, M.; Dai, H.-L. Spatially Resolved Membrane Transport in a Single Cell Imaged by Second Harmonic Light Scattering. *Biochemistry* **2019**, *58*, 1841-1844.

(36) Wilhelm, M. J.; Sheffield, J. B.; Gonella, G.; Wu, Y.; Spahr, C.; Zeng, J.; Xu, B.; Dai, H.-L. Real-time molecular uptake and membrane-specific transport in living cells by optical microscopy and nonlinear light scattering. *Chem. Phys. Lett.* **2014**, *605*, 158-163.

(37) Zeng, J.; Eckenrode, H. M.; Dai, H.-L.; Wilhelm, M. J. Adsorption and transport of charged vs. neutral hydrophobic molecules at the membrane of murine erythroleukemia (MEL) cells. *Colloids Surf., B* **2015**, *127*, 122-129.

(38) Kumal, R. R.; Karam, T. E.; Haber, L. H. Determination of the surface charge density of colloidal gold nanoparticles using second harmonic generation. *J. Phys. Chem. C* **2015**, *119*, 16200-16207.

(39) McCarley, R. L.; Forsythe, J. C.; Loew, M.; Mendoza, M. F.; Hollabaugh, N. M.; Winter, J. E. Release rates of liposomal contents are controlled by kosmotropes and chaotropes. *Langmuir* **2013**, *29*, 13991-13995.

(40) Ong, W.; Yang, Y.; Cruciano, A. C.; McCarley, R. L. Redox-triggered contents release from liposomes. *J. Am. Chem. Soc.* **2008**, *130*, 14739-14744.

(41) Wang, J.; Wolf, R. M.; Caldwell, J. W.; Kollman, P. A.; Case, D. A. Development and testing of a general amber force field. *J. Comput. Chem.* **2004**, *25*, 1157-1174.

(42) Plimpton, S. Fast parallel algorithms for short-range molecular dynamics. *J. Comput. Phys.* **1995**, *117*, 1-19.

(43) Bayly, C. I.; Cieplak, P.; Cornell, W.; Kollman, P. A. A well-behaved electrostatic potential based method using charge restraints for deriving atomic charges: the RESP model. *J. Phys. Chem.* **1993**, *97*, 10269-10280.

(44) Cieplak, P.; Cornell, W. D.; Bayly, C.; Kollman, P. A. Application of the multimolecule and multiconformational RESP methodology to biopolymers: Charge derivation for DNA, RNA, and proteins. *J. Comput. Chem.* **1995**, *16*, 1357-1377.

(45) M. J. Frisch, G. W. T., H. B. Schlegel, G. E. Scuseria, M. A. Robb, J. R. Cheeseman, G. Scalmani, V. Barone, B. Mennucci, G. A. Petersson, H. Nakatsuji, M. Caricato, X. Li, H. P. Hratchian, A. F. Izmaylov, J. Bloino, G. Zheng, J. L. Sonnenberg, M. Hada, M. Ehara, K. Toyota, R. Fukuda, J. Hasegawa, M. Ishida, T. Nakajima, Y. Honda, O. Kitao, H. Nakai, T. Vreven, J. A. Montgomery Jr., J. E. Peralta, F. Ogliaro, M. J. Bearpark, J. Heyd, E. N. Brothers, K. N. Kudin, V. N. Staroverov, R. Kobayashi, J. Normand, K. Raghavachari, A. P. Rendell, J. C. Burant, S. S. Iyengar, J. Tomasi, M. Cossi, N. Rega, N. J. Millam, M. Klene, J. E. Knox, J. B. Cross, V. Bakken, C. Adamo, J. Jaramillo, R. Gomperts, R. E. Stratmann, O. Yazyev, A. J. Austin, R. Cammi, C. Pomelli, J. W. Ochterski, R. L. Martin, K. Morokuma, V. G. Zakrzewski, G. A. Voth, P. Salvador, J. J. Dannenberg, S. Dapprich, A. D. Daniels, O¨. Farkas, J. B. Foresman, J. V. Ortiz, J. Cioslowski and D. J. Fox. *Gaussian 09, Revision A.02* **2009**.

(46) Kästner, J. Umbrella sampling. *WIREs Comput Mol Sci* **2011**, *1*, 932-942.

(47) Kumar, S.; Rosenberg, J. M.; Bouzida, D.; Swendsen, R. H.; Kollman, P. A. The weighted histogram analysis method for free-energy calculations on biomolecules. I. The method. *J. Comput. Chem.* **1992**, *13*, 1011-1021.

(48) Souaille, M.; Roux, B. t. Extension to the weighted histogram analysis method: combining umbrella sampling with free energy calculations. *Comput. Phys. Commun.* **2001**, *135*, 40-57.

(49) Sharifian Gh, M.; Wilhelm, M. J.; Dai, H.-L. Label-free optical method for quantifying molecular transport across cellular membranes in vitro. *J. Phys. Chem. Lett.* **2016**, *7*, 3406-3411.

(50) Mouritsen, O.; Boothroyd, A.; Harris, R.; Jan, N.; Lookman, T.; MacDonald, L.; Pink, D.; Zuckermann, M. Computer simulation of the main gel–fluid phase transition of lipid bilayers. *J. Chem. Phys.* **1983**, *79*, 2027-2041.

(51) Lewis, R. N.; McElhaney, R. N. Calorimetric and spectroscopic studies of the thermotropic phase behavior of lipid bilayer model membranes composed of a homologous series of linear saturated phosphatidylserines. *Biophys. J.* **2000**, *79*, 2043-2055.

(52) Szekely, P.; Dvir, T.; Asor, R.; Resh, R.; Steiner, A.; Szekely, O.; Ginsburg, A.; Mosenkis, J.; Guralnick, V.; Dan, Y. Effect of temperature on the structure of charged membranes. *J. Phys. Chem. B* **2011**, *115*, 14501-14506.

(53) Kučerka, N.; Nieh, M.-P.; Katsaras, J. Fluid phase lipid areas and bilayer thicknesses of commonly used phosphatidylcholines as a function of temperature. *Biochim. Biophys. Acta* **2011**, *1808*, 2761-2771.

(54) Miller, C. C. The Stokes-Einstein law for diffusion in solution. *Proceedings of the Royal Society of London. Series A, Containing Papers of a Mathematical and Physical Character* **1924**, *106*, 724-749.

(55) Gonella, G.; Dai, H.-L. Determination of adsorption geometry on spherical particles from nonlinear Mie theory analysis of surface second harmonic generation. *Phys. Rev. B* **2011**, *84*, 121402.

(56) Jen, S.-H.; Dai, H.-L.; Gonella, G. The effect of particle size in second harmonic generation from the surface of spherical colloidal particles. II: The nonlinear Rayleigh− Gans− Debye model. *J. Phys. Chem. C* **2010**, *114*, 4302-4308.

(57) Roke, S.; Gonella, G. Nonlinear Light Scattering and Spectroscopy of Particles and Droplets in Liquids. *Annual review of physical chemistry* **2012**, *63*, 353-378.

(58) Karam, T. E.; Haber, L. H. Molecular adsorption and resonance coupling at the colloidal gold nanoparticle interface. *J. Phys. Chem. C* **2014**, *118*, 642-649.

Chapter 4. Monitoring Molecular Interactions with Cell Membranes Using Time-Dependent Second Harmonic Generation Microscopy

4.1 Introduction

Cell membranes regulate critical interactions between cells and their external environment through both passive and active transport of ions and small molecules.[1-10] A fundamental understanding about relevant physio-chemical interactions, like molecular adsorption and transport, between molecules and biological membranes can provide critical insights on mechanisms of molecular transport in cells.[11-14] Additionally, gaining information about the role of environmental and intermolecular interactions on the translocation of molecules through cell membranes is important for the development of drug-delivery systems.[15-18] In this regard, it is crucial to design new experimental techniques that can characterize these complicated interactions in real time. In recent years, time-resolved second harmonic generation (SHG) spectroscopy has been successfully implemented as a label-free technique to interrogate the interfacial molecular interactions at liposome surfaces and at cellular membranes.[15,17,19-29] Our previous research demonstrated the use of SHG spectroscopy to study the impact of electrolytes,[30] chemical functional groups,[31] and temperature on adsorption and transport in cell membrane models using liposomes composed of different phospholipids. Here, we report the versatility of SHG microscopy to monitor molecular adsorption and transport in both living and fixed (dead) human nonsmall adenosquamous lung cancer (H596) cells.

Second harmonic generation is a powerful, nonlinear optical technique for studying buried interfaces such as biological membranes[19-22,32-34] and colloidal nanoparticles.[35-38] In SHG, two coherent photons of frequency ω add to form a third photon with a frequency

of 2ω. The second-harmonic response from an ensemble of bulk molecules in an isotropic distribution is zero for symmetry reasons.[32,39,40] However, SHG is allowed at the surface of nanoparticles and microparticles where the symmetry is broken. Thus, SHG microscopy is a surface-sensitive technique for studying systems such as protein networks,[41,42] surface potentials,[43] and drug-binding interactions.[44]

SHG has been developed as an effective technique for characterizing molecular adsorption and transport of drug-like molecules at bio-membranes. Cationic molecules, such as malachite green (MG) and malachite green isothiocyanate (MGITC), adsorb to the negatively-charged, outer bilayer surface of the membrane and subsequently transport to the inner bilayer.[22,26,30,31] For membrane-based systems, the SHG signal of the molecules adsorbed onto outer and inner hydrophilic membrane are approximately equal and opposite. Thus, SHG signal decreases as a function of time and the generated signal is approximately equal to the population difference of dye molecules attached to outer and inner membrane layer respectively.[16,17,19-21,23,26-29,32,33,45] Recently, SHG spectroscopy has been used to study the surface charge density of colloidal nanoparticles,[46] chemical reactions and growth dynamics at nanoparticle surfaces,[36,38] molecular adsorption to colloidal plasmonic nanoparticles,[47] and the release of miRNA molecules from monometallic and bimetallic nanostructures.[35,37,48-50] Additionally, SHG spectroscopy has also been used to investigated the enhanced nonlinear signals from molecular-based nanomaterials[51] as well as electronic and structural properties at buried interfaces of thin films.[52]

In this chapter, SHG microscopy is utilized to investigate the adsorption and transport kinetics of the positively-charged triphenylmethane molecules, malachite green

and malachite green isothiocyanate, across the plasma membrane of human nonsmall adenosquamous lung cancer cells. H596 lung cancer cells are selected as a model for investigating the translocation of cationic drug-like molecules through a human small-cell cancerous cell.[54] The time-dependent SHG microscopy results provide direct information about the molecular binding and associated transport kinetics. The molecular interactions are compared between MG and MGITC to demonstrate the role of chemical functional groups in these complicated processes. Additionally, the dynamics are also compared between living and fixed cells to gain more information about the molecular transport dynamics. The results indicate that these complicated chemical interactions at biological membranes are influenced by several factors including electrostatic interactions, chemical functional groups, and cell integrity.

4.2 Experimental Section

4.2.1 Cell Culture

H596 cells are provided by Dr. Molly Silvers and Dr. David Boothman at the Simmons Cancer Center of the UT Southwest Medical Center.[53] Cell culture media, fetal bovine serum albumin and all other supplements are purchased from American Type Culture Collection (ATCC; manassas, VA). H596 cells are cultured in RPMI-1640 medium supplemented with 10% fetal bovine serum, 10 IU mL^{-1} penicillin, 10 $\mu g\, mL^{-1}$ streptomycin (Life Technologies), and Normocin (Invivogen, Fisher Scientific). Cells are incubated in 75 cm^{-2} treated tissue culture flasks in the dark at 37 °C under 5% CO_2 and 95% air in a humidified incubator. Upon reaching 70% confluency, cells are tryspinized and counted. Cells are then seeded into Delta T dishes (Bioptechs) at 100,000 cells per dish. After cells are seeded into the dish, they are incubated in the dark at 37 °C under

5% CO_2 and 95% air in a humidified incubator for 24 hours before being used in the microscopy experiments.

4.2.2 Experimental setup

The experimental setup consists of an ultrafast laser system, a resonant scanning multiphoton confocal inverted microscope (Leica Microsystem SP5), and a highly sensitive non-descanned modular type photomultiplier tube (PMT) detector. The titanium:sapphire oscillator laser is centered at 850 nm with 70 fs pulses at an 84 MHz repetition rate. The laser beam is collimated to and attenuated to approximately 10 mW at the objective focus in the SHG imaging experiments. The laser beam is focused onto a cell specimen through a 100X 1.47 NA oil, high numerical aperture objective (Olympus) for imaging cells. The SHG emission is collected in the backward direction using the same objective by selecting a filter cube (680 nm Short Pass filter) equipped with 320-430 nm range band-pass filter and detected by sensitive PMT. LAS X software (Leica Microsystems) is employed for laser scanning control and image acquisition. Image sizes are of 1024 X 1024 pixels captured at 400 Hz pixel rate and an acquisition time of 30 seconds is used between successive frames. The cell samples are deposited on Delta T dishes with 1.5 mL of 10 mM phosphate-buffered saline solution at pH 7.4. All experiments are performed by closing the microscope box for carbon dioxide regulation and temperature control at 37 ºC to ensure live cell imaging.

4.3 Results and Discussion

Figure 4.1 shows time-dependent SHG microscopy images of 0.1 μM MGITC added to a H596 cell sample. At time zero, when MGITC is added to the cell sample, the

SHG image initially shows only a very low amount of background signal. However, after waiting 25 minutes, a clear SHG image of the cell is observed. This indicates the adsorption of dye molecules onto the outer surface of the cell membrane. The electrostatic and dipole-dipole interaction between the MGITC dye molecule and negatively-charged membrane surface results in an ordered arrangement of the SHG-active MGITC molecules at the cell membrane interface, leading to significant enhancement of the SHG signal. The SHG intensity becomes stronger at 34 minutes indicating increased MGITC adsorption to the outer cell membrane surface. However, at 45 minutes the SHG image intensity decreases due to the transport of dye molecules from outer surface to inner surface of living H596 cell membrane. Additionally, at 80 minutes, the SHG image almost completely disappears, resembling the SHG image from time zero before MGITC adsorption takes place, due to approximately equal MGITC populations at the inner and outer membrane surface at equilibrium and the resulting cancellation of the SHG signal.

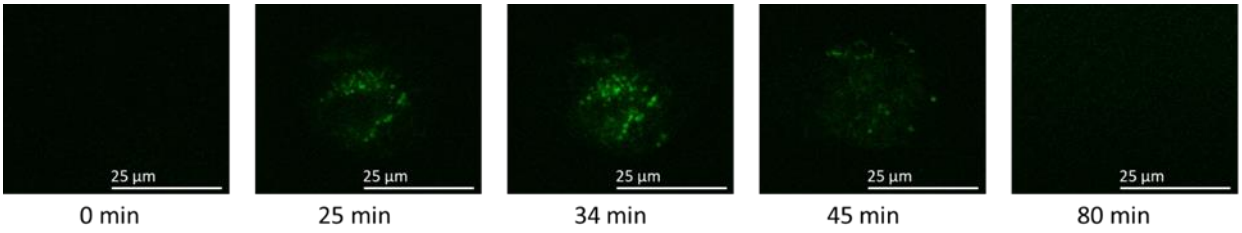

Figure 4.1. Time-dependent SHG microscopy images of 0.1 μM MGITC added to living H596 cells.

Similarly, Figure 4.2 displays the time-dependent SHG microscopy images of 0.1 μM MG added to the H596 cell sample. The obtained results have a similar trend, where no clear SHG image is observed at 0 minutes, immediately after MG addition to the cell

sample. The SHG intensity then slowly grows over time, where a bright image of the cell is clearly observed at 75 minutes, due to MG adsorption to the outer membrane surface. The SHG intensity then slowly decreases as a function of time from the ensemble molecular transport of the dye molecules. At 120 minutes, the SHG image has a very low SHG intensity, indicating almost complete cancellation of the signal. Control experiments with cells alone and dye molecules alone also show very small SHG signal, as displayed in Appendix C. The experiments with cells alone or dye alone do not show any time-dependent dynamics from surface-specific SHG signals.

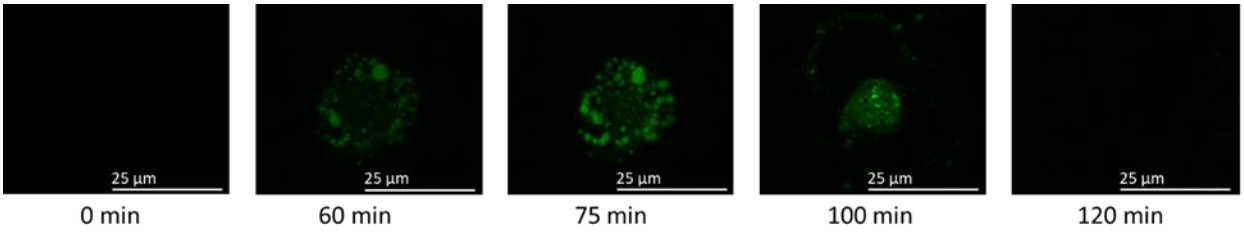

Figure 4.2. Time-dependent SHG microscopy images of 0.1 μM MG added to living H596 cells.

H596 cells fixed with 4% formaldehyde are also studied to investigate the difference in molecular interactions between living and fixed cells. Figure 4.3 shows the time-dependent SHG microscopy images after addition of 0.1 μM MGITC dye in a sample of fixed H596 cells. The time-resolved images demonstrate the same general trend seen in Figures 4.1 and 4.2 due to molecular adsorption and transport. However, the appearance of living and fixed H596 are found to be considerably different. Living cells are circular, with an approximate size of 25 μm, whereas fixed cells are noticeably elongated as these cells are adhered to the surface, in general agreement with the previous H596 imaging studies.[54] The time required for MGITC molecules to reach

maximum SHG intensity in fixed cells is approximately 33 minutes. Additional observations, such as the decay time and heterogeneity of SHG signals in the fixed cells are described with comparisons to the living cells later in the Chapter. A similar SHG microscopy measurement with MGITC added to the fixed H596 cell sample under the same experimental conditions is presented in Appendix C, showing general agreement and reproducibility.

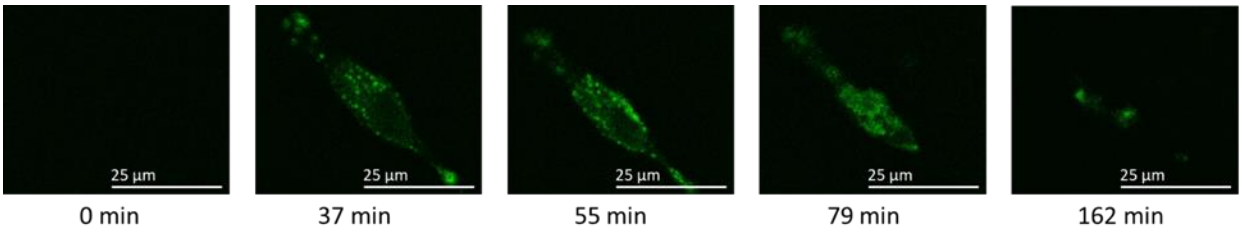

Figure 4.3. Time-dependent SHG microscopy images of 0.1 μM MGITC added to fixed H596 cells.

The time-resolved SHG microscopy results are analyzed in greater detail by focusing on different regions of interest (ROIs) for additional information regarding the variation of the SHG intensity as a function of time. Figures 4.4 and 4.5 show the 0.1 μM MGITC and 0.1 μM MG results, respectively, analyzed at different ROIs in the living cell samples. Five distinct ROIs with areas of 3.2 x 3.2 μm^2 are compared for each experiment, where the ROI locations are indicated in Figures 4.4a and 4.5a, respectively, and the corresponding SHG intensity time profiles are shown in Figures 4.4b and 4.5b, respectively. The average of the five ROIs is plotted as a function of time for MGITC and MG added to the H596 cell samples, as shown in Figures 4.4c and 4.5c, respectively. The results demonstrate that MGITC takes approximately 34 minutes to reach peak SHG intensity while MG adsorption occurs more slowly, taking approximately 75 minutes to

reach peak SHG intensity in the living H596 cells. This indicates a stronger molecule-membrane interaction with MGITC as compared to MG. Our previous studies with different phospholipid liposomes determined that the free energy of adsorption is more negative for MGITC than for MG, in agreement with these SHG microscopy results on cells.[31]

The SHG decay profile is fitted with a single exponential function given by

$$E_{SHG}(t) = a_0 + a_1 e^{-t/\tau} \quad (4.2)$$

to obtain the corresponding transport lifetime τ for MGITC and MG in the living cells. These best fits are shown as solid black lines in Figures 4.4c and 4.5c. The transport lifetime is approximately 2.5 times faster for MGITC in comparison to MG, with the values of 8 ± 1 minutes and 21 ± 4 minutes, respectively. MG and MGITC have similar chemical structures and spectroscopic properties.[31] However, the added isothiocyanate group in MGITC enhances the interactions with the lipid bilayer, as discussed in our previous study of colloidal liposomes.[31] The faster transport lifetime for MGITC as compared to that of MG is in agreement with our previous work on liposomes, which includes molecular dynamics simulations. The calculated dipole moment of MGITC is approximately 4 times greater than that of MG, and MGITC has a larger distribution coefficient and polar surface area than MG.[30,31] These factors make MGITC more lipophilic than MG, while also having much larger dipole-dipole interactions with the lipid bilayer, contributing to the observed faster molecular transport. Additionally, previous results in the literature from SHG microscopy of MG in human dermal fibroblast cells is measured with a transport lifetime of approximately 20 ± 1 minutes, in general agreement with our results.[16]

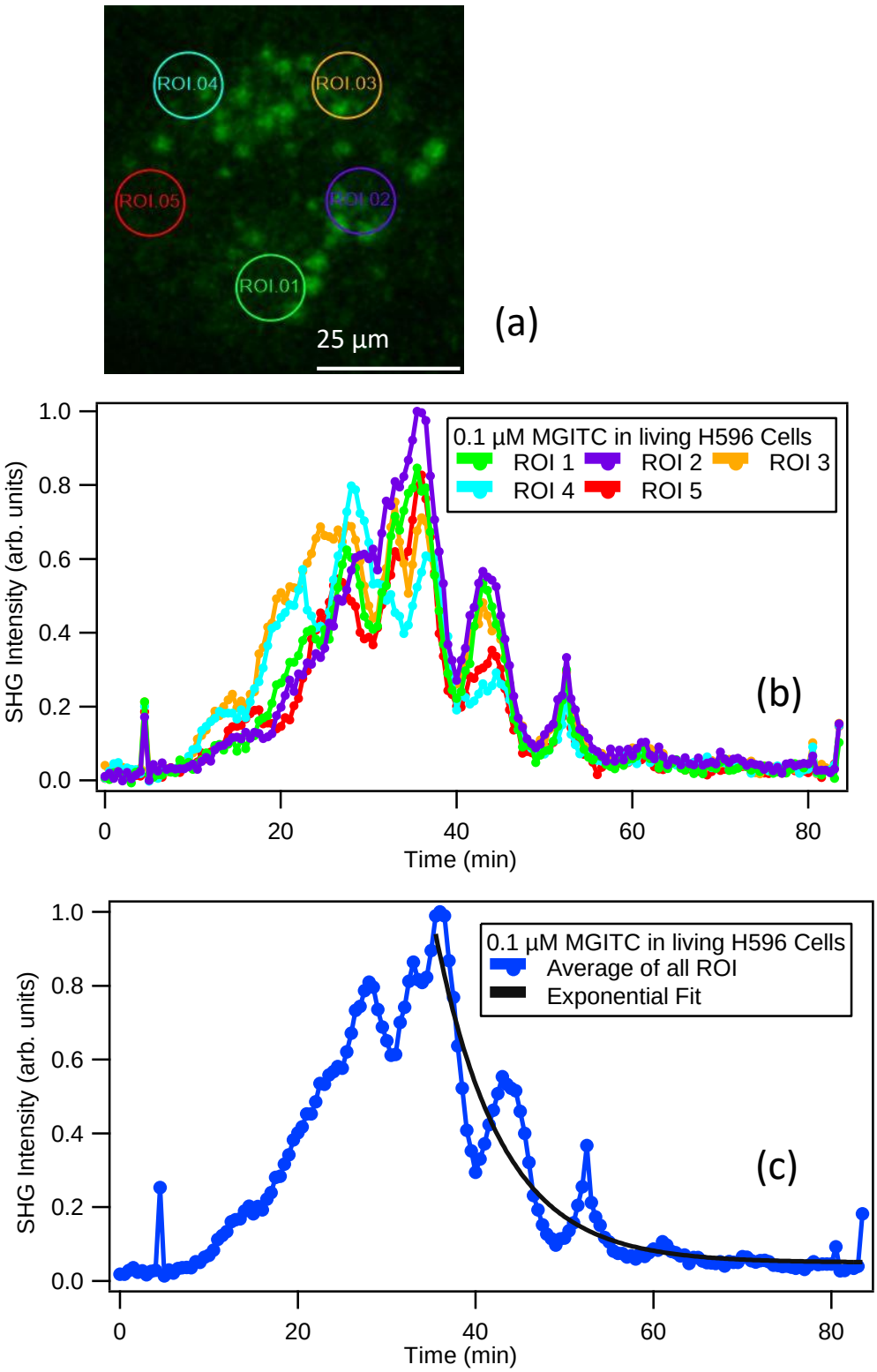

Figure 4.4. (a) Representative zoomed SHG image for 0.1 μM MGITC added to living H596 cells at 33 minutes, showing different ROIs. Time profiles for molecular adsorption and transport for 0.1 μM MGITC added to living H596 cells (b) at different ROIs and (c) using the average of all ROIs. The black solid line is best fit.

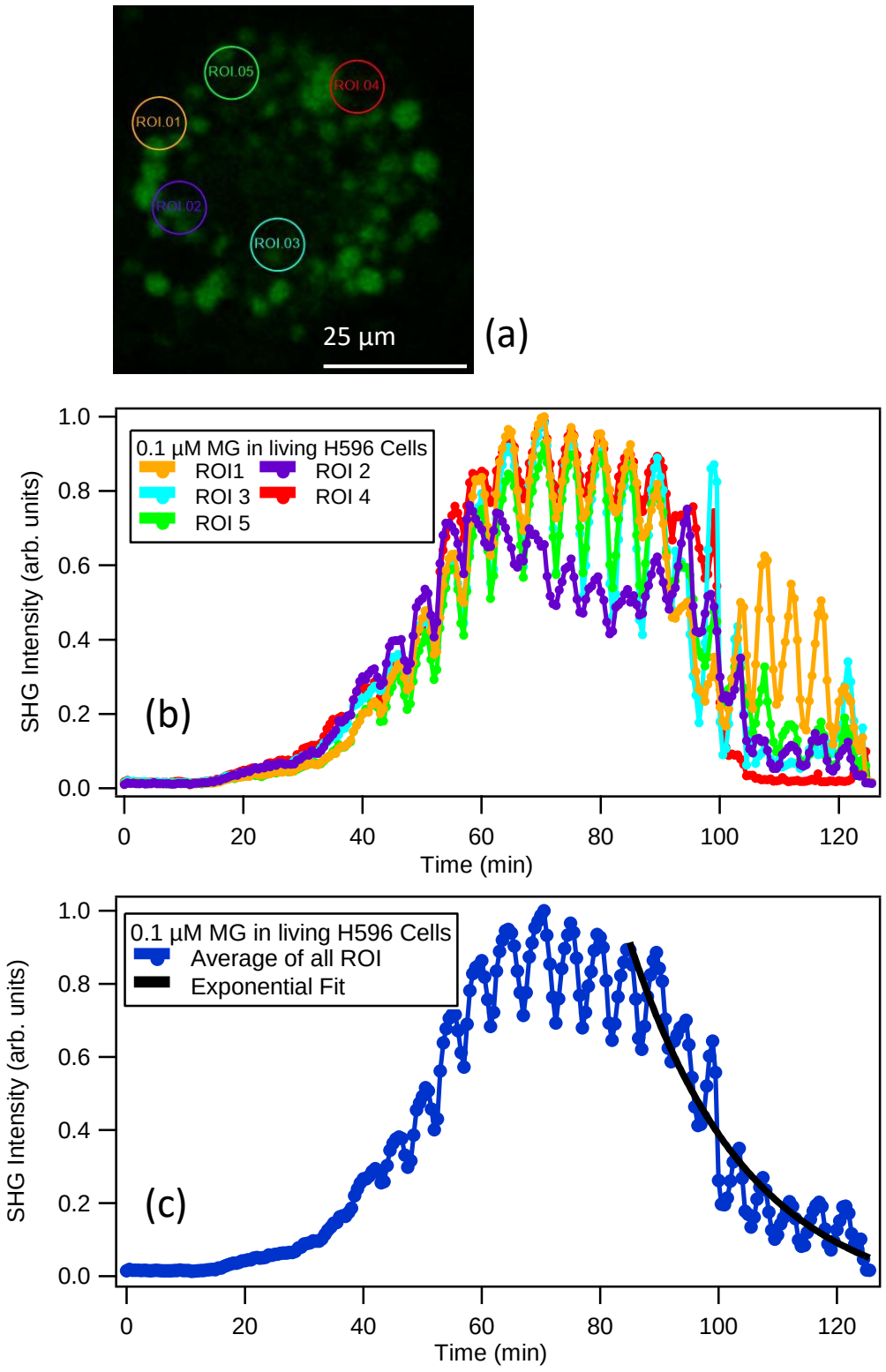

Figure 4.5. (a) Representative zoomed SHG image for 0.1 μM MG added to living H596 cells at 75 minutes, showing different ROIs. Time profiles for molecular adsorption and transport for 0.1 μM MGITC added to living H596 cells (b) at different ROIs and (c) using the average of all ROIs. The black solid line is best fit.

Interestingly, the time-resolved results for living H596 cells show clear the oscillations in SHG signal for both MGITC and MG molecules, as shown in Figure 4.4 and 4.5. These oscillatory behaviors were not seen in our previous studies with liposomes. These oscillations may be the result of active transport taking place in the living cells which might be linked to complicated changes in the electrostatic surface potential of the membrane during the molecular translocation process. This will be discussed in greater detail later in the Chapter.

The SHG time profiles from five ROIs from 0.1 μM MGITC added to the fixed H596 cell sample are shown in Figure 4.6 for direct comparison with living H596 cells. The SHG intensity time profiles show greater heterogeneity at different locations of the membrane for fixed H596 cells. The transport lifetime is determined from the exponential fit of the decay from the average of the ROI signals, which is shown with the black line in Figure 4.6c. The transport lifetime of MGITC is approximately 2 times faster in living cells in comparison to fixed cells with the values of 8 ± 1 minutes and 17 ± 1 minutes, respectively. Correspondingly, the time to reach peak SHG signal is approximately 34 minutes and 55 minutes for living and fixed cells, respectively. Cell regulation process, where ion channels try to rebalance the perturbed electrostatic potential of the cell membrane because of molecule adsorption, could contribute to the faster transport. The living cells can also have higher membrane permeability in comparison to the fixed cells leading to faster transport times. More work is needed to fully understand these interactions in greater detail.

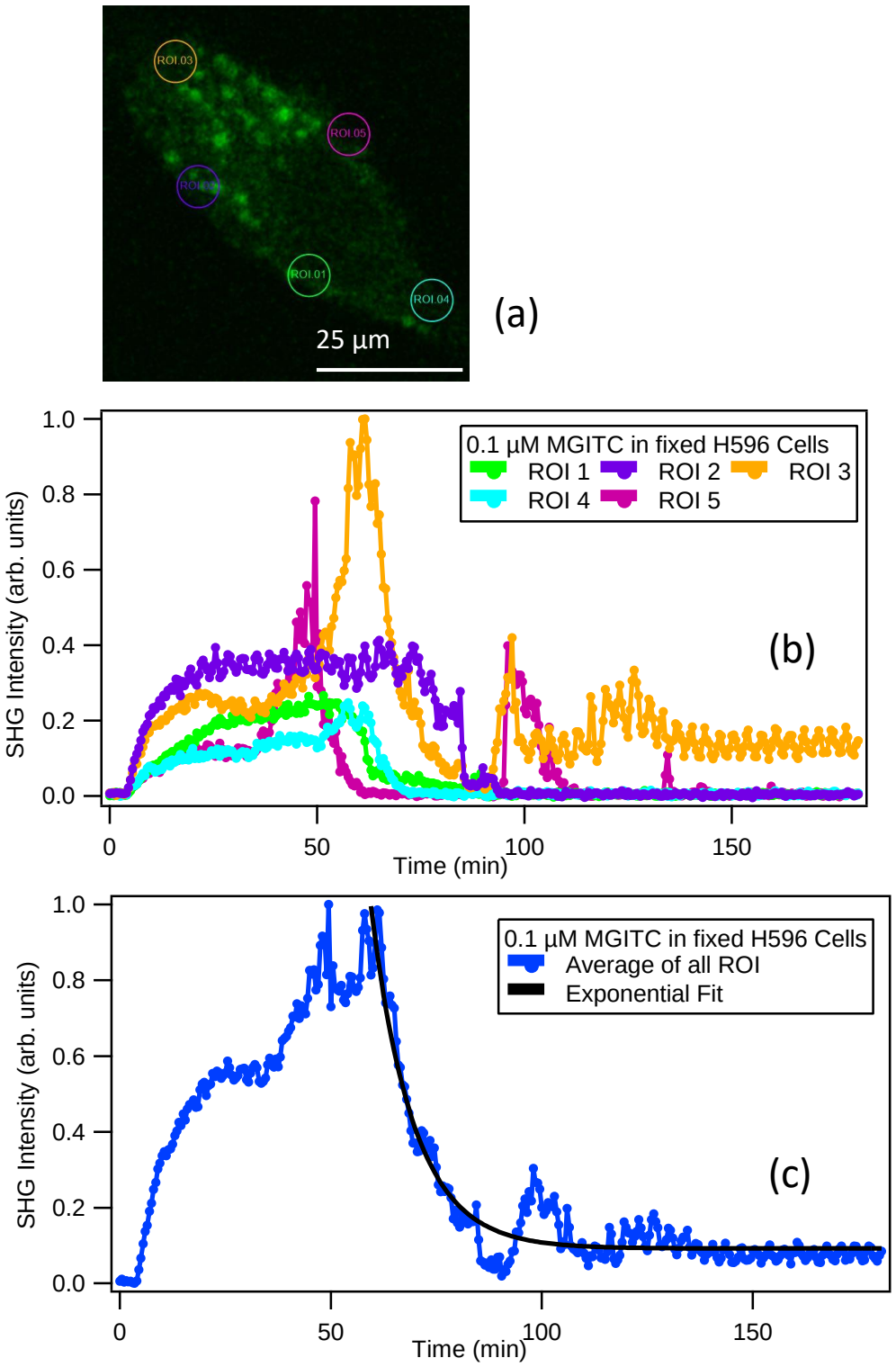

Figure 4.6 (a) Representative zoomed SHG image for 0.1 μM MGITC added to fixed H596 cells at 55 minutes, showing different ROIs. Time profiles for molecular adsorption and transport for 0.1 μM MGITC added to fixed H596 cells (b) at different ROIs and (c) using the average of all ROIs. The black solid line is best fit.

The time-dependent SHG results for 0.1 μM MGITC dye added to fixed H596 cells shows significant heterogeneity in signals. Previous work has demonstrated that molecular translocation can vary as a function of location on the cell membrane, as we observe in our studies.[16] Membranes have heterogeneous lipid compositions[55-58] where the cationic dye molecules could adsorb rapidly in some locations while having slower or no adsorption in other locations due to variations in surface charge and chemical structure near the membrane surface. The fixed cells can also have a lower degree of membrane integrity leading to increased dye aggregation, which can also lead to the observed variations in signal.

The time-resolved SHG microscopy analysis, shown in Figures 4.4 and 4.5, demonstrate that the SHG intensities decay with pronounced fluctuations in the living H596 cell samples. However, the corresponding results for fixed H596 cells show considerably less fluctuation. The average frequency of oscillation, determined from the difference of peak oscillation times, is $0.0021 \pm 0.0004\ s^{-1}$ and $0.0036 \pm 0.0004\ s^{-1}$ for MGITC and MG, respectively. These fluctuations in living cells may be caused by active transport where the cell uses its energy to pump ions[8,59] such as Na^+, K^+, Ca^{2+}, or H^+ into and out of the cell in order to balance the sudden changes in pH and electrostatic surface potential at the cell membrane as the dye molecules adsorb and transport through the bilayer. These sudden changes could lead to the observed fluctuations in SHG signal caused by resulting changes in the $\chi^{(2)}$ and $\chi^{(3)}$ terms of the overall nonlinear susceptibility.[32,40,46,60,61] Additionally, the cycles of rising and falling SHG intensities could be attributed to dynamic imbalances in molecular concentrations, surface charge, and pH as the cell attempts to regulate its cell membrane surface chemistry as the dye adsorption

and passive transport processes take place. For the fixed cells, no active transport is occurring so clear oscillations in the SHG intensity are not observed. This difference between living and fixed cells could also indicate a defensive mechanism in living cells in response to the foreign dye molecules. Different cell lines could have different responses and types of oscillatory SHG signals, which will be explored in future studies. The time traces integrated over the entire cells are also shown in Appendix C.

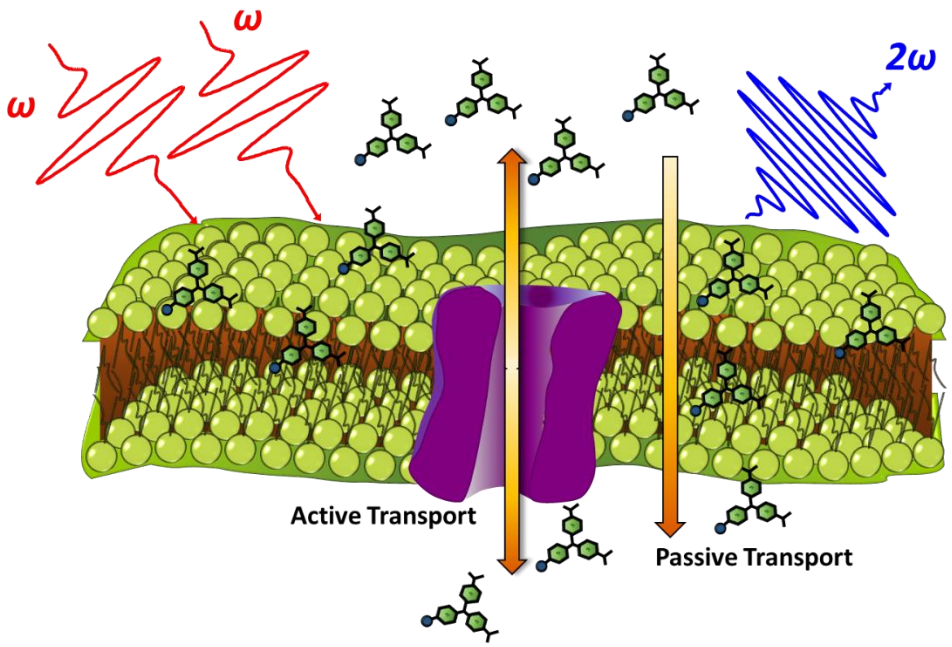

Figure 4.7. Schematic representation of active and passive transport occurring in H596 cells studied using SHG microscopy.

A key concept describing the utilization of SHG microscopy to study active and passive transport at the cell membrane is represented schematically in Figure 4.7. Molecular adsorption of MG or MGITC molecules to the outer cell membrane occurs followed by passive transport through the lipid bilayer. Concurrently, ion channels pump different ions into and out of the cell in order to regulate the cell membrane electrostatic

potential and local pH, which can lead to deviations in the adsorption and transport dynamics as well as the observed oscillatory behaviors. The changes in the adsorbate populations at the inner and outer membrane surfaces are probed in real time using SHG microscopy during the molecular adsorption and transport process until an overall final state of equilibrium is reached. This technique is demonstrated to be a powerful framework for future studies where these adsorption and transport dynamics can be studied under varying experimental conditions that include the buffer and electrolyte concentrations as well as the sample temperature. Similarly, these experiments can be repeated under different dye concentrations to better understand the mechanism of the associated active and passive transport that occurs. Future molecular translocation investigations with different cell lines, such as human dermal fibroblasts or murine erythroleukemia cells, can be performed with comparisons to previous SHG studies.[16,28] Similarly, different types of ion pumps and their roles in translocation can be studied for developing fundamental characterizations of active and passive transport occurring in cellular membranes using different SHG-active chemical probes.

4.4 Conclusion

In summary, SHG microscopy is demonstrated to be a powerful technique for studying the physiochemical interactions of different cationic dyes with H596 cells. The experimental results are analyzed to determine associated information on transport kinetics across the cell membrane. MGITC is shown to have stronger binding and faster translocation in comparison to MG in the cell membrane, in excellent agreement with our previous work on liposomes. Additionally, the molecular interactions are stronger and faster in living cells in comparison to the fixed cells. Clear oscillations in the SHG signal

are observed in the living cells but not in fixed cells which are attributed to more complicated processes involving active transport for cell membrane regulation of pH and electrostatic potential. These results show that time-dependent SHG microscopy is an excellent technique for investigating the surface-sensitive molecular interactions at cell membranes in living and fixed cells for advancing potential drug-delivery applications.

4.5. Notes

(1) Van Meer, G.; Voelker, D. R.; Feigenson, G. W. Membrane lipids: where they are and how they behave. *Nat Rev Mol Cell Biol.* **2008**, *9*, 112.

(2) Escribá, P. V.; González-Ros, J. M.; Goñi, F. M.; Kinnunen, P. K.; Vigh, L.; Sánchez-Magraner, L.; Fernández, A. M.; Busquets, X.; Horváth, I.; Barceló-Coblijn, G. Membranes: a meeting point for lipids, proteins and therapies. *J Cell Mol Med.* **2008**, *12*, 829-875.

(3) Alberts, B.; Johnson, A.; Lewis, J.; Raff, M.; Roberts, K.; Walter, P.: *Molecular Biology of the Cell*; New York: Garland Science, 2002.

(4) Holthuis, J. C.; Menon, A. K. Lipid landscapes and pipelines in membrane homeostasis. *Nature* **2014**, *510*, 48.

(5) Finkelstein, A. Water and nonelectrolyte permeability of lipid bilayer membranes. *J. Gen. Physiol.* **1976**, *68*, 127-135.

(6) Schanker, L. Mechanisms of drug absorption and distribution. *Annu. Rev. Pharmacol.* **1961**, *1*, 29-45.

(7) Smith, D.; Artursson, P.; Avdeef, A.; Di, L.; Ecker, G. F.; Faller, B.; Houston, J. B.; Kansy, M.; Kerns, E. H.; Kramer, S. D. Passive lipoidal diffusion and carrier-mediated cell uptake are both important mechanisms of membrane permeation in drug disposition. *Mol. pharmaceutics* **2014**, *11*, 1727-1738.

(8) Shih, Y.-L.; Huang, L.-T.; Tu, Y.-M.; Lee, B.-F.; Bau, Y.-C.; Hong, C. Y.; Lee, H.-l.; Shih, Y.-P.; Hsu, M.-F.; Lu, Z.-X. Active Transport of Membrane Components by Self-Organization of the Min Proteins. *Biophys. J.* **2019**, *116*, 1469-1482.

(9) Albers, R. Biochemical aspects of active transport. *Annu. Rev. Biochem* **1967**, *36*, 727-756.

(10) Bennett, H. S. The concepts of membrane flow and membrane vesiculation as mechanisms for active transport and ion pumping. *The Journal of biophysical and biochemical cytology* **1956**, *2*, 99.

(11) Pang, K. S. Modeling of intestinal drug absorption: roles of transporters and metabolic enzymes (for the Gillette Review Series). *Drug Metab. Dispos.* **2003**, *31*, 1507-1519.

(12) Liu, X.; Testa, B.; Fahr, A. Lipophilicity and its relationship with passive drug permeation. *Pharm. Res.* **2011**, *28*, 962-977.

(13) Walter, A.; Gutknecht, J. Permeability of small nonelectrolytes through lipid bilayer membranes. *J. Membr. Biol.* **1986**, *90*, 207-217.

(14) Hannesschlaeger, C.; Horner, A.; Pohl, P. Intrinsic Membrane Permeability to Small Molecules. *Chem. Rev.* **2019**, *119*, 5922-5953.

(15) Gh, M. S.; Wilhelm, M. J.; Dai, H.-L. Azithromycin-Induced Changes to Bacterial Membrane Properties Monitored in vitro by Second-Harmonic Light Scattering. *ACS Med. Chem. Lett.* **2018**, *9*, 569-574.

(16) Sharifian Gh, M.; Wilhelm, M. J.; Moore, M.; Dai, H.-L. Spatially Resolved Membrane Transport in a Single Cell Imaged by Second Harmonic Light Scattering. *Biochemistry* **2019**, *58*, 1841-1844.

(17) Zeng, J.; Eckenrode, H. M.; Dai, H.-L.; Wilhelm, M. J. Adsorption and transport of charged vs. neutral hydrophobic molecules at the membrane of murine erythroleukemia (MEL) cells. *Colloids Surf., B* **2015**, *127*, 122-129.

(18) Sharma, A.; Sharma, U. S. Liposomes in drug delivery: progress and limitations. *Int. J. Pharm.* **1997**, *154*, 123-140.

(19) Liu, J.; Subir, M.; Nguyen, K.; Eisenthal, K. B. Second harmonic studies of ions crossing liposome membranes in real time. *J. Phys. Chem. B* **2008**, *112*, 15263-15266.

(20) Liu, Y.; Yan, E. C.; Eisenthal, K. B. Effects of bilayer surface charge density on molecular adsorption and transport across liposome bilayers. *Biophys. J.* **2001**, *80*, 1004-1012.

(21) Shang, X.; Liu, Y.; Yan, E.; Eisenthal, K. B. Effects of counterions on molecular transport across liposome bilayer: probed by second harmonic generation. *J. Phys. Chem. B* **2001**, *105*, 12816-12822.

(22) Srivastava, A.; Eisenthal, K. B. Kinetics of molecular transport across a liposome bilayer. *Chem. Phys. Lett.* **1998**, *292*, 345-351.

(23) Yan, E. C.; Eisenthal, K. B. Effect of cholesterol on molecular transport of organic cations across liposome bilayers probed by second harmonic generation. *Biophys. J.* **2000**, *79*, 898-903.

(24) Fang, H.; Xu, B.; Li, X.; Kuhn, D. L.; Zachary, Z.; Tian, G.; Chen, V.; Chu, R.; DeLacy, B. G.; Rao, Y.; Dai, H.-L. Effects of molecular structure and solvent polarity on adsorption of carboxylic anchoring dyes onto TiO2 particles in aprotic solvents. *Langmuir* **2017**, *33*, 7036-7042.

(25) Wilhelm, M. J.; Dai, H. L. Molecule-Membrane Interactions in Biological Cells Studied with Second Harmonic Light Scattering. *Chemistry–An Asian Journal* **2019**.

(26) Wilhelm, M. J.; Sharifian Gh, M.; Dai, H.-L. Chemically Induced Changes to Membrane Permeability in Living Cells Probed with Nonlinear Light Scattering. *Biochemistry* **2015**, *54*, 4427-4430.

(27) Wilhelm, M. J.; Sharifian Gh, M.; Dai, H.-L. Influence of molecular structure on passive membrane transport: A case study by second harmonic light scattering. *J. Chem. Phys.* **2019**, *150*, 104705.

(28) Wilhelm, M. J.; Sheffield, J. B.; Gonella, G.; Wu, Y.; Spahr, C.; Zeng, J.; Xu, B.; Dai, H.-L. Real-time molecular uptake and membrane-specific transport in living cells by optical microscopy and nonlinear light scattering. *Chem. Phys. Lett.* **2014**, *605*, 158-163.

(29) Zeng, J.; Eckenrode, H. M.; Dounce, S. M.; Dai, H.-L. Time-resolved molecular transport across living cell membranes. *Biophys. J.* **2013**, *104*, 139-145.

(30) Kumal, R. R.; Nguyenhuu, H.; Winter, J. E.; McCarley, R. L.; Haber, L. H. Impacts of Salt, Buffer, and Lipid Nature on Molecular Adsorption and Transport in Liposomes As Observed by Second Harmonic Generation. *J. Phys. Chem. C* **2017**, *121*, 15851-15860.

(31) Hamal, P.; Nguyenhuu, H.; Subasinghege Don, V.; Kumal, R. R.; Kumar, R.; McCarley, R. L.; Haber, L. H. Molecular Adsorption and Transport at Liposome Surfaces Studied by Molecular Dynamics Simulations and Second Harmonic Generation Spectroscopy. *J. Phys. Chem. B* **2019**, *123*, 7722-7730.

(32) Eisenthal, K. B. Second harmonic spectroscopy of aqueous nano-and microparticle interfaces. *Chem. Rev.* **2006**, *106*, 1462-1477.

(33) Liu, J.; Shang, X.; Pompano, R.; Eisenthal, K. B. Antibiotic assisted molecular ion transport across a membrane in real time. *Faraday Discuss.* **2005**, *129*, 291-299.

(34) Liu, Y.; Yan, E. C.; Zhao, X.; Eisenthal, K. B. Surface potential of charged liposomes determined by second harmonic generation. *Langmuir* **2001**, *17*, 2063-2066.

(35) Abu-Laban, M.; Hamal, P.; Arrizabalaga, J. H.; Forghani, A.; Dikkumbura, A. S.; Kumal, R. R.; Haber, L. H.; Hayes, D. J. Combinatorial Delivery of miRNA-Nanoparticle Conjugates in Human Adipose Stem Cells for Amplified Osteogenesis. *Small* **2019**.

(36) Khoury, R. A.; Ranasinghe, J. C.; Dikkumbura, A. S.; Hamal, P.; Kumal, R. R.; Karam, T. E.; Smith, H. T.; Haber, L. H. Monitoring the Seed-Mediated Growth of Gold Nanoparticles using In-Situ Second Harmonic Generation and Extinction Spectroscopy. *J. Phys. Chem. C* **2018**, *122*, 244400-224406.

(37) Kumal, R. R.; Abu-Laban, M.; Hamal, P.; Kruger, B.; Smith, H. T.; Hayes, D. J.; Haber, L. H. Near-Infrared Photothermal Release of siRNA from the Surface of Colloidal Gold–Silver–Gold Core–Shell–Shell Nanoparticles Studied with Second-Harmonic Generation. *J. Phys. Chem. C* **2018**, *122*, 19699-19704.

(38) Ranasinghe, J. C.; Dikkumbura, A. S.; Hamal, P.; Chen, M.; Khoury, R. A.; Smith, H. T.; Lopata, K.; Haber, L. H. Monitoring the growth dynamics of colloidal gold-silver core-shell nanoparticles using in situ second harmonic generation and extinction spectroscopy. *J. Chem. Phys.* **2019**, *151*, 224701.

(39) Haber, L. H.; Kwok, S. J.; Semeraro, M.; Eisenthal, K. B. Probing the colloidal gold nanoparticle/aqueous interface with second harmonic generation. *Chem. Phys. Lett.* **2011**, *507*, 11-14.

(40) Wang, H.; Yan, E. C.; Borguet, E.; Eisenthal, K. B. Second harmonic generation from the surface of centrosymmetric particles in bulk solution. *Chem. Phys. Lett.* **1996**, *259*, 15-20.

(41) Freund, I.; Deutsch, M. Second-harmonic microscopy of biological tissue. *Opt. Lett.* **1986**, *11*, 94-96.

(42) Campagnola, P. J.; Loew, L. M. Second-harmonic imaging microscopy for visualizing biomolecular arrays in cells, tissues and organisms. *Nat. Biotechnol.* **2003**, *21*, 1356-1360.

(43) Macias-Romero, C.; Nahalka, I.; Okur, H. I.; Roke, S. Optical imaging of surface chemistry and dynamics in confinement. *Science* **2017**, *357*, 784-788.

(44) Nguyen, T. T.; Conboy, J. C. High-throughput screening of drug–lipid membrane interactions via counter-propagating second harmonic generation imaging. *Anal. Chem.* **2011**, *83*, 5979-5988.

(45) Sharifian Gh, M.; Wilhelm, M. J.; Dai, H.-L. Label-free optical method for quantifying molecular transport across cellular membranes in vitro. *J. Phys. Chem. Lett.* **2016**, *7*, 3406-3411.

(46) Kumal, R. R.; Karam, T. E.; Haber, L. H. Determination of the surface charge density of colloidal gold nanoparticles using second harmonic generation. *J. Phys. Chem. C* **2015**, *119*, 16200-16207.

(47) Karam, T. E.; Haber, L. H. Molecular adsorption and resonance coupling at the colloidal gold nanoparticle interface. *J. Phys. Chem. C* **2014**, *118*, 642-649.

(48) Abu-Laban, M.; Kumal, R. R.; Casey, J.; Becca, J.; LaMaster, D.; Pacheco, C. N.; Sykes, D. G.; Jensen, L.; Haber, L. H.; Hayes, D. J. Comparison of thermally actuated retro-diels-alder release groups for nanoparticle based nucleic acid delivery. *J. Colloid Interface Sci.* **2018**, *526*, 312-321.

(49) Kumal, R. R.; Abu-Laban, M.; Landry, C. R.; Kruger, B.; Zhang, Z.; Hayes, D. J.; Haber, L. H. Plasmon-enhanced photocleaving dynamics in colloidal microRNA-functionalized silver nanoparticles monitored with second harmonic generation. *Langmuir* **2016**, *32*, 10394-10401.

(50) Kumal, R. R.; Landry, C. R.; Abu-Laban, M.; Hayes, D. J.; Haber, L. H. Monitoring the photocleaving dynamics of colloidal microrna-functionalized gold nanoparticles using second harmonic generation. *Langmuir* **2015**, *31*, 9983-9990.

(51) Karam, T. E.; Siraj, N.; Zhang, Z.; Ezzir, A. F.; Warner, I. M.; Haber, L. H. Ultrafast and nonlinear spectroscopy of brilliant green-based nanoGUMBOS with enhanced near-infrared emission. *J. Chem. Phys.* **2017**, *147*, 144701.

(52) Zhao, K.; Taylor, J. E.; Haber, L. H.; Zhang, J.; Plummer, E. W.; Saghayezhian, M. Probing the interfacial symmetry using rotational second-harmonic generation in oxide heterostructures. *The Journal of Physical Chemistry C* **2019**, *123*, 23000-23006.

(53) Bey, E. A.; Bentle, M. S.; Reinicke, K. E.; Dong, Y.; Yang, C.-R.; Girard, L.; Minna, J. D.; Bornmann, W. G.; Gao, J.; Boothman, D. A. An NQO1-and PARP-1-mediated cell death pathway induced in non-small-cell lung cancer cells by β-lapachone. *PNAS* **2007**, *104*, 11832-11837.

(54) Silvers, W. C.; Prasai, B.; Burk, D. H.; Brown, M. L.; McCarley, R. L. Profluorogenic reductase substrate for rapid, selective, and sensitive visualization and detection of human cancer cells that overexpress NQO1. *J. Am. Chem. Soc.* **2013**, *135*, 309-314.

(55) Marsh, D. Lipid-protein interactions and heterogeneous lipid distribution in membranes. *Molecular Membrane Biology* **1995**, *12*, 59-64.

(56) Pike, L. J. Lipid rafts: heterogeneity on the high seas. *Biochem. J* **2004**, *378*, 281-292.

(57) Semrau, S.; Schmidt, T. Membrane heterogeneity–from lipid domains to curvature effects. *Soft Matter* **2009**, *5*, 3174-3186.

(58) Sezgin, E.; Levental, I.; Mayor, S.; Eggeling, C. The mystery of membrane organization: composition, regulation and roles of lipid rafts. *Nature reviews Molecular cell biology* **2017**, *18*, 361.

(59) Fewtrell, C. Ca2+ oscillations in non-excitable cells. *Annual Review of Physiology* **1993**, *55*, 427-454.

(60) Wang, H.; Yan, E. C.; Liu, Y.; Eisenthal, K. B. Energetics and population of molecules at microscopic liquid and solid surfaces. *J. Phys. Chem. B* **1998**, *102*, 4446-4450.

(61) Yan, E. C.; Liu, Y.; Eisenthal, K. B. New method for determination of surface potential of microscopic particles by second harmonic generation. *J. Phys. Chem. B* **1998**, *102*, 6331-6336.

Chapter 5. Plasmon-Resonant Light-Triggered Photothermal Release of miRNA from the Surface of Colloidal Gold and Silver Nanoparticles Studied with Second Harmonic Generation Spectroscopy

5.1 Introduction

Thermally-labile linkers enable the development of nanoparticle-based delivery systems for the spatiotemporal release of "cargo" molecules into selected target sites.[1-5] Nanoparticle-based systems like liposomes,[6-8] hydrogels,[9-11] and micelles[4,12,13] rely upon changes in local environment to induce the delivery of cargo molecules, such as pharmaceuticals, oligonucleotides, or chemotherapeutics agents. However, the controlled and precise release of the cargo molecules can be achieved by applying external-based triggers like light,[14,15] magnetic fields,[16,17] or electric fields.[18,19] Here, we demonstrate the use of surface-specific second harmonic generation (SHG) spectroscopy to study the interfacial dynamics at different colloidal plasmonic nanoparticles functionalized with microRNA (miRNA) mimics using a furan-malemide based Diels-Alder adduct for light-triggered photothermal release of miRNA molecules at their corresponding plasmonic resonances. Plasmonic nanoparticles like gold nanoparticles (GNPs) and silver nanoparticles (SNPs) are promising candidates for a wide variety of biomedical applications.[15,20-25] These nanoparticles offer low toxicity, excellent biocompatibility, and chemical control of surface functionalities. Additionally, gold and silver nanoparticles have localized surface plasmon resonances (LSPRs) characterized by the coherent and collective oscillation of free electrons excited by

electromagnetic radiation.[23,26-31] LSPR properties depend on the shape, size, composition, and surrounding medium of the nanoparticles.[20,22-24,29,30,32] These plasmon resonances can cause optical field enhancements leading to applications in noninvasive bioimaging, biolabeling, and enhanced nonlinear spectroscopy, while also providing the origin of high plasmonic photothermal efficiencies.[15,33-35] The photothermal efficiency in plasmonic nanoparticles is defined as the percentage of light energy that is converted to heat energy, which is highly dependent on both absorption and scattering cross sections.[36-38] Recently, bimetallic nanoparticles in core-shell configurations have offered unique tailored optical properties extending to the near-infrared region (NIR).[15,22,28] Nanoparticles with optical properties in the NIR biological window are advantageous for potential applications in nanomedicine,[34] photothermal cancer therapy,[33] and gene-silencing applications[25] due to the extended optical penetration and decreased harmful effects using NIR light as compared to the visible or ultraviolet regions.

Second harmonic generation is a noninvasive, nondestructive, surface-sensitive, nonlinear spectroscopy for characterizing physical and chemical properties at colloidal nanoparticle interfaces.[29,31,39-42] In the SHG process, two incident photons of frequency ω add coherently to generate a third photon with a frequency of 2ω. SHG is dipole forbidden in centrosymmetric media, like bulk solution, but it can be generated at the surface of nanoparticles where the symmetry is broken. Recently, SHG has been used as an accurate method to determine molecular adsorption and chemical reactions at nanoparticle surfaces,[30,43] ion-transport processes in liposomes,[40,44-50] and the release of oligonucleotides from the surface of plasmonic nanoparticles.[21-24,51]

The SHG electric field E_{SHG} depends on the second-order and third-order nonlinear optical susceptibilities, $\chi^{(2)}$ and $\chi^{(3)}$, respectively. The SHG electric field can be expressed as

$$E_{SHG} = \sqrt{I_{SHG}} = \chi^{(2)} E_\omega E_\omega + \chi^{(3)} E_\omega E_\omega \phi_0 \quad (5.1)$$

where, I_{SHG} is the SHG intensity, E_ω is the incident optical electric field at frequency ω, and ϕ_0 is the electrostatic surface potential arising from the nanoparticle surface charge density.[29,31,39,41,52-55] The second-order nonlinear susceptibility $\chi^{(2)}$ term for SHG is from the two-photon spectroscopy of the surface.[39,52] Additionally, the static electric field created by the charged interface results in the third-order nonlinear susceptibility $\chi^{(3)}$ term for SHG caused by bulk solvent molecules that have a distance-dependent net alignment with respect to the nanoparticle surface due to the electrostatic potential.[54-56]

In our group's previous studies, we have investigated the photocleaving kinetics of miRNA from the surface of gold and silver nanoparticle with nitrobenzyl linkers using SHG spectroscopy under ultraviolet irradiation.[23,24] Recently, we also used SHG to study the retro-Diels-Alder photothermal release of miRNA from the surface of silver nanoparticles under different temperatures.[21] The current study described in this chapter focuses on comparing the efficiency of the photothermal release of miRNA from different plasmonic nanoparticles at their corresponding plasmon resonances. The experimental setup uses a probe laser at 800 nm to generate SHG signals from the colloidal nanoparticle solution. A second laser is tuned in wavelength to the nanoparticle plasmon resonance to trigger the photothermal cleaving of the Diels-Alder linker that attaches the miRNA to the nanoparticle surface. Colloidal gold, silver, and gold-silver-gold core-shell-shell

(Au@Ag@Au CSS) nanoparticles are synthesized and functionalized with miRNA molecules using Diels-Alder chemistry of furfuryl mercaptan with 6-maleimidohexanoic acid. Upon photothermal excitation at the plasmon resonance, a retro-Diels-Alder reaction is initiated when the local temperature around the nanoparticle surface reaches approximately 60 ºC or greater,[21,57] releasing the miRNA into the surrounding solution. The fluorophore Alexa350 is attached to the end of the miRNA for fluorescence quantification measurements. The Scheme 5.1. shows the schematic representation of miRNA attachment and release from a CSS nanoparticle using Diels-Alder chemistry.

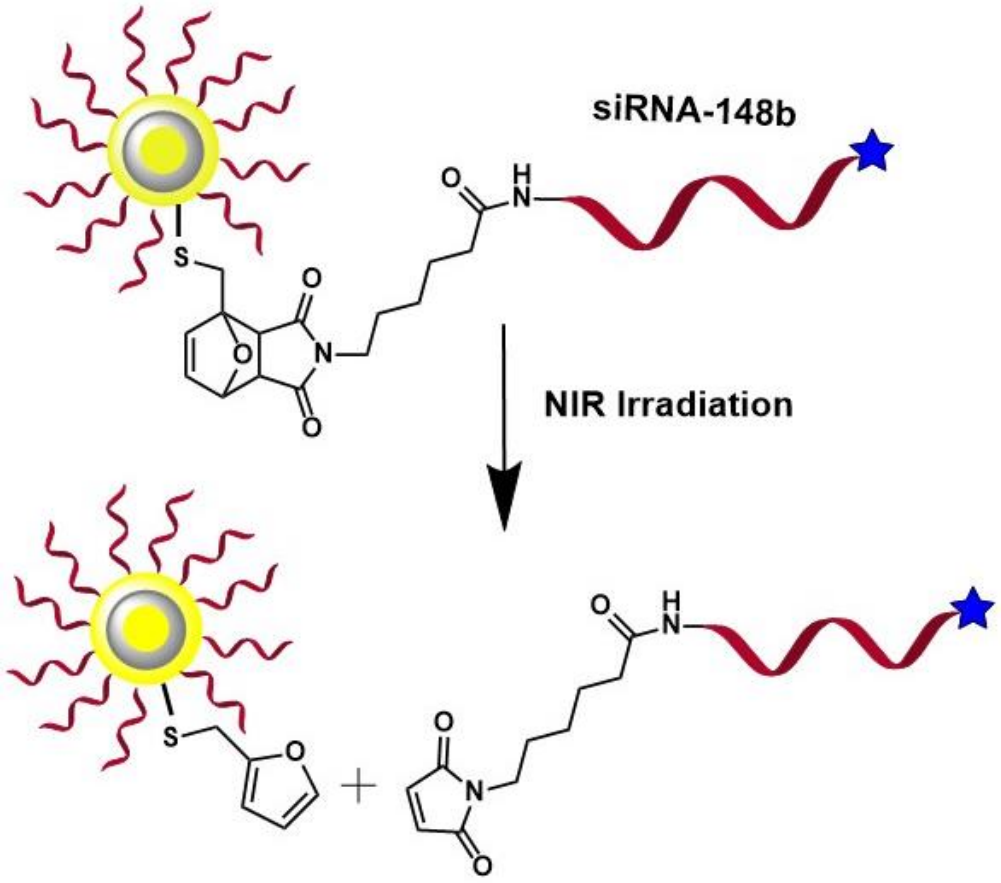

Scheme 5.1. The miRNA is attached to the surface of gold-silver-gold core-shell-shell nanoparticles using Diels-Alder chemistry. NIR irradiation causes photothermal cleaving and miRNA release.

5.2 Experimental Section

5.2.1 Synthesis and Characterization of Plasmonic nanoparticles

The gold and silver nanoparticles are prepared in colloidal aqueous suspension using chemical reduction of chloroauric acid and silver nitrate, respectively.[28,31,58,59] All chemicals are purchased from Alfa Aesar and used without further purification in ultrapure water. The colloidal gold nanoparticle sample is prepared by a seeded-growth method using hydroquinone and sodium citrate as reducing agents. Briefly, an aqueous solution of 300 μL of 25 mM chloroauric acid in 30 mL of ultrapure water is brought to reflux under vigorous stirring conditions, followed by the addition of 900 μL of 34 mM sodium citrate to synthesize gold seeds. The colloidal gold seed solution undergoes a color change from pale yellow to deep red after 15 min and is then removed from heating and cooled to room temperature (RT). For the seeded-growth synthesis of gold nanoparticles, 200 μL of prepared gold seeds and 100 μL of 25 mM chloroauric acid are added to 10 mL of water, followed by the addition of 30 μL of 34 mM sodium citrate, and 100 μL of 30 mM hydroquinone at RT under vigorous stirring conditions for 60 min. For the silver nanoparticle synthesis, an aqueous solution is first made by mixing 250 μL of 59 mM silver nitrate, 1 mL of 34 mM sodium citrate, 30 μL of 98 μM potassium iodide, and 1.25 mL of ultrapure water. This solution is added to 100 μL of 100 mM ascorbic acid solution in 47.5 mL of boiling water and the mixture is refluxed for 60 min under vigorous stirring conditions to prepare the silver nanoparticles.

For the synthesis of colloidal Au@Ag@Au CSS nanoparticles, a three step procedure is followed.[22,28] Briefly, an aqueous solution of 300 μL of 25 mM chloroauric acid in 30 mL of ultrapure water is brought to reflux under vigorous stirring conditions,

followed by the addition of 900 μL of 34 mM sodium citrate to synthesize GNPs. Three aliquots of 60 μL of 100 mM ascorbic acid, 15 μL of 100 mM silver nitrate, and 75 μL of 100 mM sodium hydroxide are added to 10 mL of water containing 300 μL of Au seeds at RT under vigorous stirring conditions to synthesize Au@Ag CS NPs. The last gold shell is grown by adding 100 μL of 25 mM chloroauric acid, followed by the addition of 25 μL of 34 mM sodium citrate and 10 uL of 30 mM hydroquinone at RT under vigorous stirring conditions.

The synthesized nanoparticles are functionalized with miRNA molecules. GNPs and CSS nanoparticles are functionalized with the miR-148b whereas SNPs are functionalized with miR-21. The sequences of these miRNA are 3' C6-NH2 2'OMe CAA CAC CAG UCG AUG GGC UGU Cy3 5' for miR-21 and 5' C6-NH2 2'OMe UCA GUG CAU CAC AGA ACU UUG U 6-FAM 3' for miR-148b. The surfaces are first conjugated with thiol- and carboxyl- terminated Diels-Alder cycloadducts. Briefly, 2.11 g of 6-maleimidohexanoic acid and 0.5 g of 2-furanmethanethiol are mixed in 20 mL of 1:1 methanol and dichloromethane for 7 days. The linkers are then mixed with the nanoparticles at approximately 8 x 10^9 particles/mL in 1 mL aliquots for 24 h at RT to allow for surface attachment through thiol linkage. For oligonucleotide addition, the nanoparticles are first centrifuged at 10,000 g for 10 min, removing the supernatant and resuspending in isopropanol three successive times, followed by mixing with 100 μL of 100 mM 1-ethyl-3-(3-dimethylaminopropyl) carbodiimide hydrochloride/N-hydroxysuccinimide (EDC/NHS) and the respective 5'-amine miRNA mimics (4 μM, 30 μL) for 24 h at RT to allow for covalent coupling. Verification of conjugation is tested after centrifugation and resuspension in diethyl pyrocarbonate (DEPC) water, by displacing the

ligands with 10 μL tris(2-carboxyethyl) phosphine hydrochloride solution (TCEP) treatment, and measuring supernatant fluorescence at 525 nm for FAM, and 575 nm for Cy3. Additional details on these fluorescent labels FAM and Cy3 are included in Appendix D.

The representative transmission electron microscopy images for GNPs seeds, GNPs, and SNPs are shown in Figure 5.1. Similarly, representative TEM images for colloidal Au@Ag@Au CSS nanoparticle are shown in Figure 5.2. The nanoparticles are highly monodisperse and spherical. The measured sizes for the GNP seeds, GNPs, and SNPs are 14 ± 1 nm, 68 ± 1 nm, 50 ± 6 nm, respectively, which are shown in Figure 5.1. The measured sizes for the GNP seeds, Au@Ag CS nanoparticles, and Au@Ag@Au CSS nanoparticles are 14 ± 1 nm, 60 ± 10 nm, and 109 ± 5 nm, respectively, which are shown in Figure 5.2. The dynamic light scattering (DLS) measurements for the miRNA-functionalized nanoparticles are shown in Appendix D. For each case, the average hydrodynamic size of nanoparticle sample is found to increase after attaching the miRNA to the nanoparticle surface, in agreement with our previous studies.[23,24] Additionally, the corresponding zeta potentials of the nanoparticles alone and miRNA-functionalized nanoparticles are shown in Appendix D. The surface charge density of the nanoparticle interface increases after miRNA functionalization, which correspondingly increases the magnitude of the zeta potential for nanoparticles with miRNA in comparison to nanoparticles without miRNA. Figure 5.3 shows the representative extinction spectra for GNPs and SNPs with and without miRNA. The extinction spectra show a slight red-shifting as nanoparticles are functionalized with miRNA. Additional details on extinction spectroscopy results before and after release of miRNA are discussed in Appendix D. For

the CSS nanoparticles, the plasmon peak blue shifts on addition of the silver shell and then red shifts on addition of the outer gold shell. The optical properties of CSS nanoparticles are located in the NIR region. The NIR region is better suited for light-triggered biological applications as deep tissue penetration and minimal tissue damage occur using this optical irradiation.[33,34]

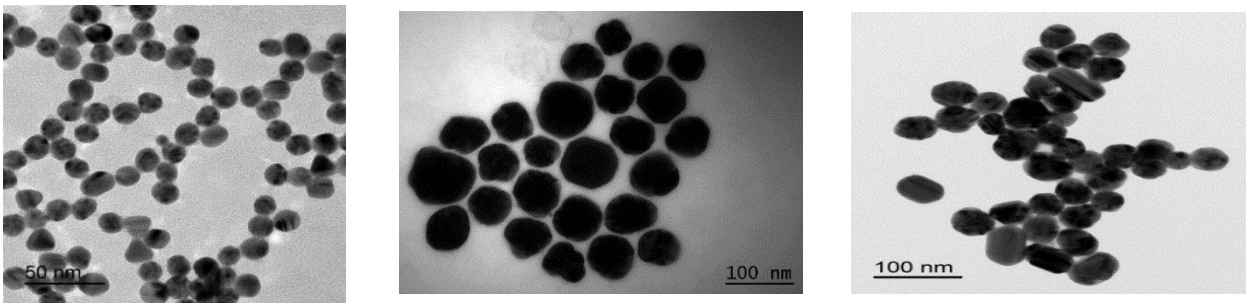

Figure 5.1. Representative TEM images of (a) GNPs seeds, (b) GNPs, and (c) SNPs, respectively.

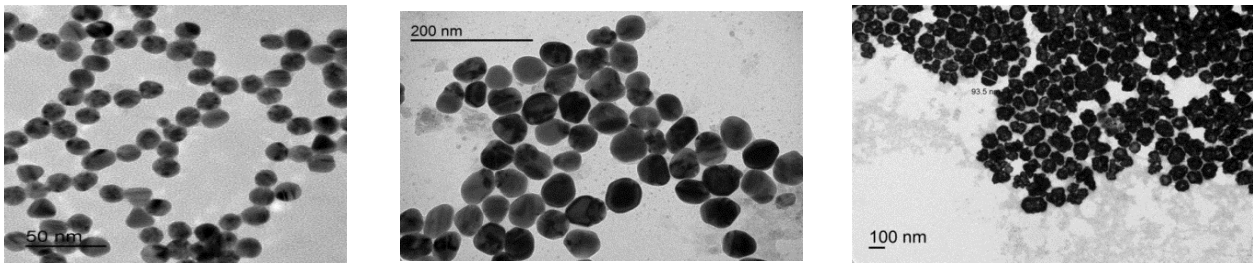

Figure 5.2. Representative TEM images of (a) GNPs seeds, (b) Au@Ag core-shell nanoparticles, and (c) Au@Ag@Au core-shell-shell nanoparticles, respectively.

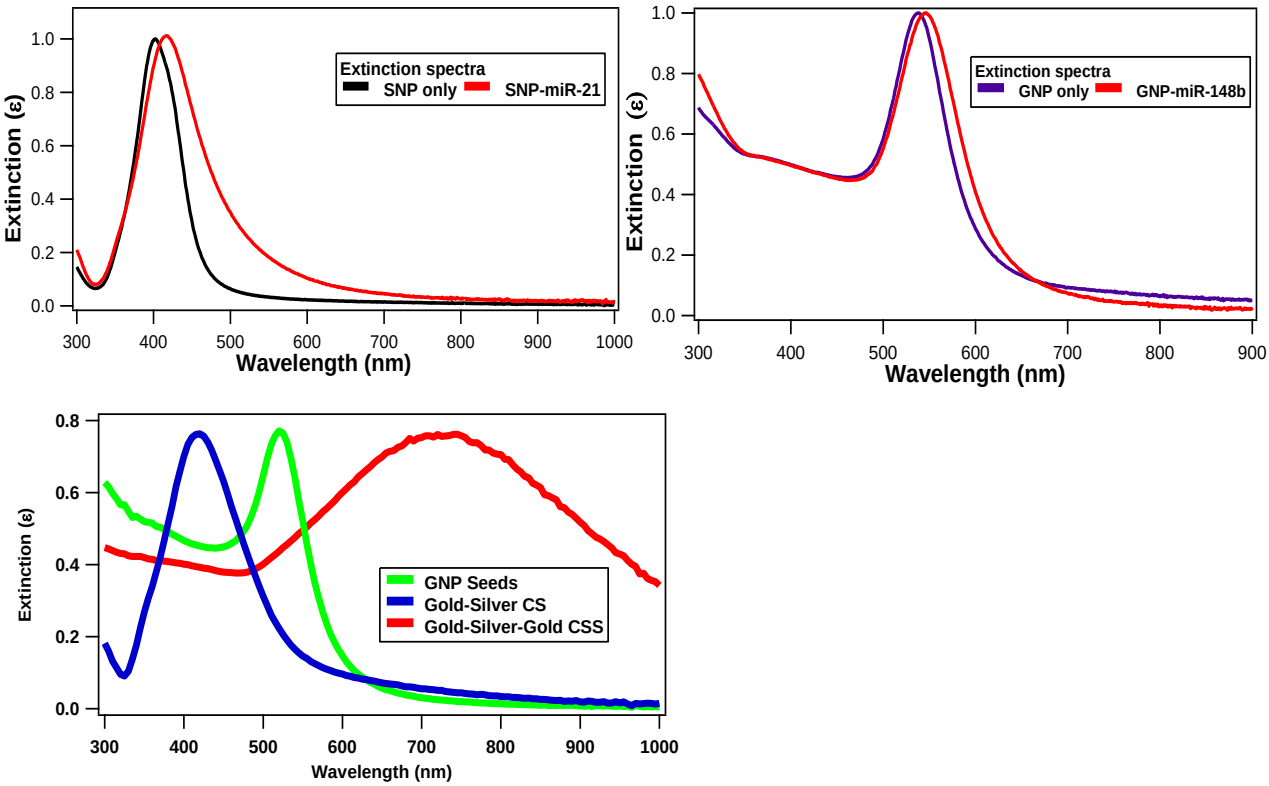

Figure 5.3. Representative extinction spectra of (a) SNPs and (b) GNPs before and after miRNA functionalization. (c) Extinction spectra of GNP seeds, Au@Ag core-shell nanoparticles, and Au@Ag@Au core-shell-shell nanoparticles.

5.2.2 Experimental setup

The experimental setup for the second harmonic generation (SHG), which consists of an ultrafast laser system, an optical setup, and a high-sensitivity spectroscopy detector, has been described previously.[21,22,25] A portion of the Titanium:sapphire oscillator laser beam, centered at 800 nm with 75 fs pulses at 80 MHz repetition rate and an average power of 2.6 W, is used to seed the amplifier laser which pumps an optical parametric amplifier (OPA) for tunable-wavelength laser light. The beam from the OPA is used for irradiation studies at 400 nm and 530 nm, corresponding to the plasmon resonances of the silver and gold nanoparticles, respectively. However for the CSS nanoparticles, the

laser beam produced from the amplifier laser at 800 nm is used directly for the irradiation studies, corresponding to the CSS plasmon resonance. For SHG measurements, the remaining portion of the 800 nm oscillator laser is attenuated to an average power of 790 mW and is focused to a 1 cm quartz cuvette containing the nanoparticle sample. An integrated data acquisition program controls a magnetic stir bar and a beam block to open and shut every 20 s for collecting the SHG and background spectra in order to measure the background-subtracted SHG signal as a function of time.

5.3 Results and Discussion

The release of miRNA from the surface of gold and silver plasmonic nanoparticles is measured in real time using surface-specific SHG spectroscopy. Representative SHG spectra, centered at 400 nm with a full width half-maximum of approximately 4.5 nm, of nanoparticles and miRNA complex are shown in Figure 5.4. The miRNA-functionalized nanoparticles have higher SHG intensities than the corresponding nanoparticles without miRNA functionalization due to the increased surface charge density through the $\chi^{(3)}$ effect, in agreement with our previous results.[21-25] Upon irradiation at the nanoparticle's plasmon resonance, the nanoparticle absorbs energy, which leads to the cleaving of the linker and the subsequent release of miRNA into solution, resulting in a lower SHG intensity, as shown in Figure 5.4. These cleaving dynamics are caused by a photothermal response of the plasmonic nanoparticles or by generated hot electrons from the plasmon resonance leading to cleaving of the linker, or by a combination of these two processes.

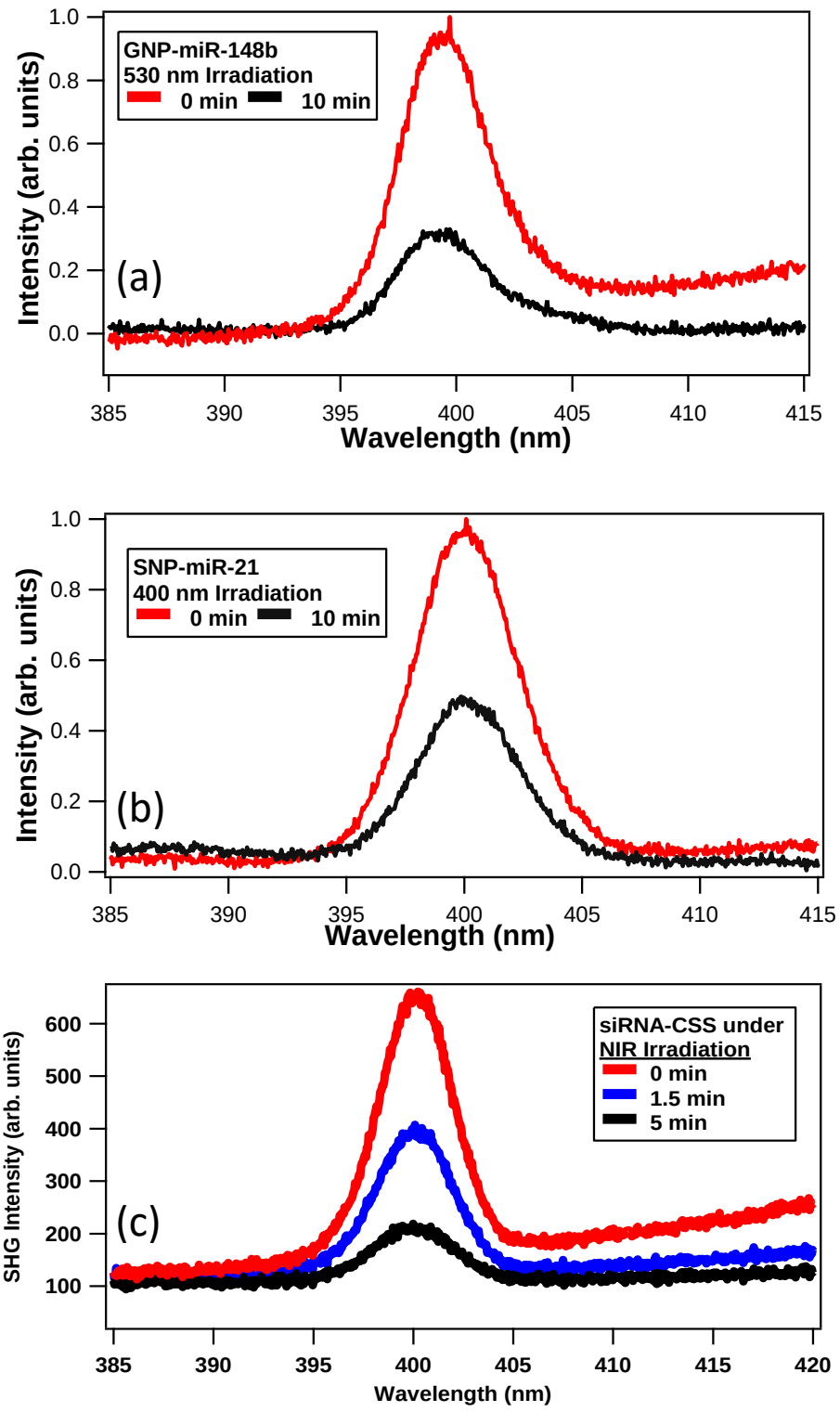

Figure 5.4. Representative SHG spectra of (a) SNPs, (b) GNPs, and (c) CSS nanoparticles at different irradiation times at their corresponding plasmon resonances.

The time-dependent SHG experiments for three sets of nanoparticles are analyzed using power-dependent fits. Higher irradiation powers lead to faster and more complete photothermal cleaving, as shown in Figure 5.5. The experimentally obtained results are fit to a pseudo first-order exponential function given by $E_{SHG} = A + B\ e^{-kt}$ where k is the cleaving rate and A and B are proportionality constants. The values of the fit parameters are summarized in Appendix D. Figure 5.5c displays the obtained rate constants k plotted as a function of laser power for the gold and silver nanoparticles, with corresponding linear fits. The obtained slopes from the fits are (0.007 ± 0.001) s^{-1} mW^{-1} and (0.011 ± 0.001) s^{-1} mW^{-1} for the gold and silver nanoparticles, respectively. Similarly, the obtained y-intercepts from the fits are (0.471 ± 0.166) s^{-1} and (0.366 ± 0.147) s^{-1} for the gold and silver nanoparticles, respectively. The nonzero y-intercepts are caused by a small amount of cleaving caused by the 800 nm laser needed for the SHG measurements. These experimental results indicate that the photothermal release of miRNA at the corresponding plasmon resonance is approximately 1.5 times more efficient for silver nanoparticles. This result can be attributed to a higher concentration of hot electron formation in silver nanoparticles leading to higher cleaving efficiencies,[60] although more research is needed to study this process in greater detail. Additionally, control experiments show that the SNP-miR-21 complex has only minimal cleaving upon irradiation with 530 nm, as displayed in Figure 5.5a. In contrast, the GNP-miR-148b complex has a greater amount of cleaving upon irradiation at 400 nm, as shown in Figure 5.5b. The gold nanoparticle plasmon peak is centered near 530 nm; however, the gold nanoparticles still have significant absorption near 400 nm, as displayed in Figure 5.3b. This absorption at 400 nm can raise the local temperature of the gold nanoparticle surface

leading to the photothermal release of miRNA and the corresponding decrease in the SHG intensity that is observed.

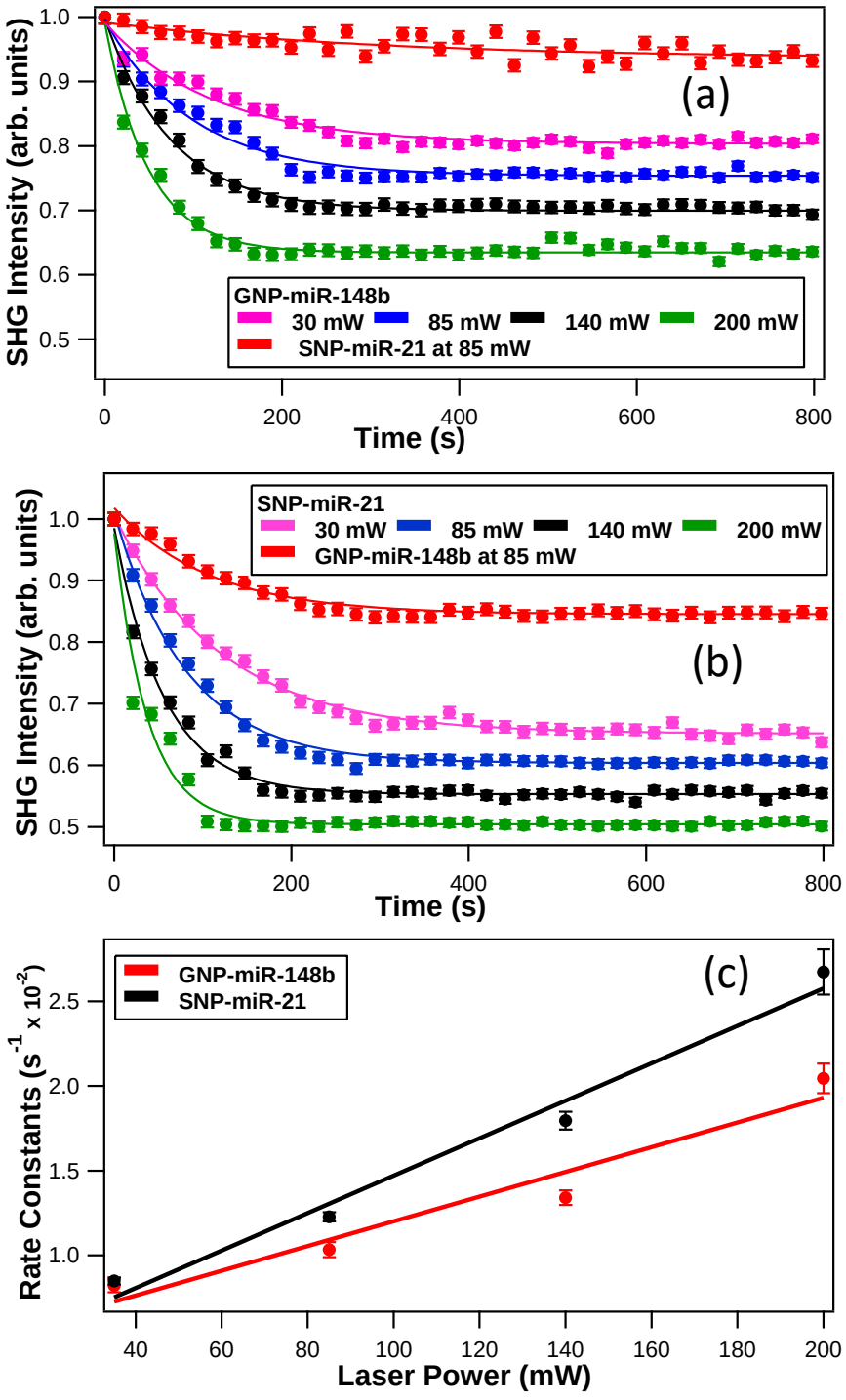

Figure 5.5. SHG intensity of the miRNA-functionalized (a) silver and (b) gold nanoparticles as a function of time under varying laser irradiation powers using 400 nm and 530 nm, respectively. (c) Rate constants plotted as a function of laser power.

Figure 5.7a shows the power-dependent analysis of the photothermal release of miRNA from CSS nanoparticle systems. The time-resolved results have a similar behavior as gold and silver nanoparticle where miRNA molecules are releasing from CSS nanoparticle surface leading to a decrease in SHG intensity. Additionally, Figure 5.7b shows the obtained rate constants plotted as a function of irradiation laser power. Interestingly, in comparison to gold and silver nanoparticles, CSS nanoparticles have a different behavior where the rate constant values plateau after approximately 100 mW, indicating the complete release of miRNA above this irradiation power is not limited by the laser power but is instead limited by the diffusion of nanoparticles through the aqueous solution through the laser focus. For SNPs and GNPs, 200 mW of irradiation still shows increasing cleaving rates, where a plateau is not observed. This result indicates that the CSS nanoparticles have a higher photothermal response, which could be attributed to a faster phonon-phonon relaxation lifetime. The phonon-phonon relaxation lifetime of GNPs and SNPs are approximately 100 ps[28,61] and 85 ps,[61] respectively. However, the phonon-phonon relaxation lifetime of CSS nanoparticles is approximately 24 ps,[28] leading to enhanced photothermal properties. However, more work is needed to fully characterize the photothermal response of each plasmonic nanoparticle sample.

Additional characterizations techniques such as extinction spectroscopy, fluorescence spectroscopy, zeta-potential measurements, and confocal imaging results are presented in Appendix D and are in general agreement with these SHG observations. In summary, these studies demonstrate the potential of plasmonic nanoparticles for photothermal release of small biological “cargo” molecules in real time. These investigations of release kinetics of miRNA molecules from plasmonic nanoparticles using

SHG spectroscopy provide detailed information for developing targeted drug-delivery applications.

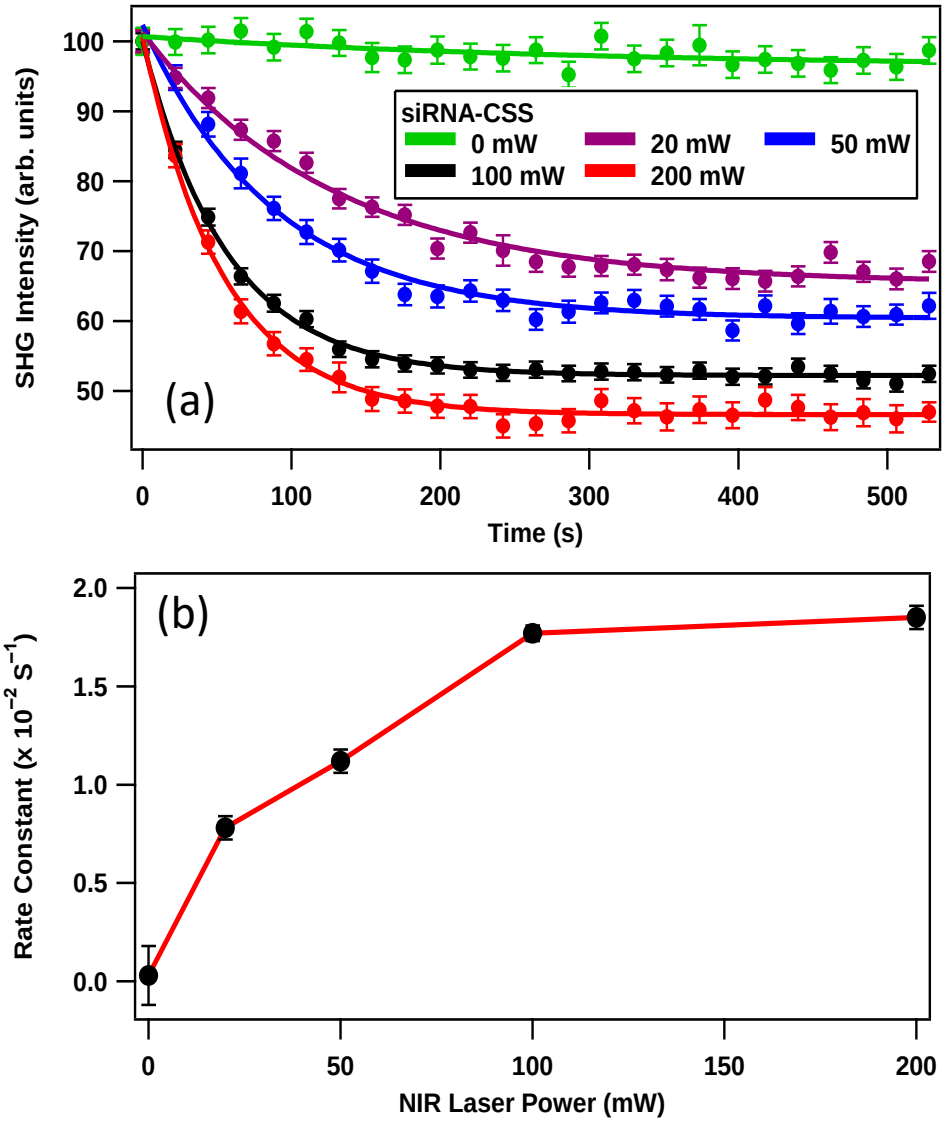

Figure 5.7. (a) SHG intensity of the miRNA-functionalized CSS nanoparticles as a function of time under varying laser irradiation powers under NIR irradiation. (b) Rate constants plotted as a function of laser irradiation power.

5.4 Conclusion

The photothermal release of miRNA from colloidal plasmonic nanoparticles are investigated at their corresponding plasmon resonances using time-dependent SHG spectroscopy. The miRNA is attached to the nanoparticle surface using a thermally-cleavable linker prepared from Diels-Alder chemistry. The complete release of miRNA occurs at lower power for CSS nanoparticle in comparison to GNPs and SNPs indicating greater photothermal response of CSS nanoparticle at its corresponding plasmon resonance. Additionally, the results from extinction spectroscopy, fluorescence spectroscopy, zeta-potential measurements, and confocal microscopy imaging agrees with the general observations from SHG measurements. These results provide a framework for developing potential nanoparticle-based light-triggered drug-delivery applications.

5.5. Notes

(1) Cobley, C. M.; Au, L.; Chen, J.; Xia, Y. Targeting gold nanocages to cancer cells for photothermal destruction and drug delivery. *Expert opinion on drug delivery* **2010**, *7*, 577-587.

(2) Mura, S.; Nicolas, J.; Couvreur, P. Stimuli-responsive nanocarriers for drug delivery. *Nature materials* **2013**, *12*, 991-1003.

(3) Rossin, R.; van Duijnhoven, S. M.; Ten Hoeve, W.; Janssen, H. M.; Kleijn, L. H.; Hoeben, F. J.; Versteegen, R. M.; Robillard, M. S. Triggered drug release from an antibody–drug conjugate using fast “click-to-release” chemistry in mice. *Bioconjugate Chem.* **2016**, *27*, 1697-1706.

(4) Salma, S. A.; Patil, M. P.; Kim, D. W.; Le, C. M. Q.; Ahn, B.-H.; Kim, G.-D.; Lim, K. T. Near-infrared light-responsive, diselenide containing core-cross-linked micelles prepared by the Diels–Alder click reaction for photocontrollable drug release application. *Polymer Chemistry* **2018**, *9*, 4813-4823.

(5) Brown, P. K.; Qureshi, A. T.; Moll, A. N.; Hayes, D. J.; Monroe, W. T. Silver nanoscale antisense drug delivery system for photoactivated gene silencing. *ACS nano* **2013**, *7*, 2948-2959.

(6) Balazs, D. A.; Godbey, W. Liposomes for use in gene delivery. *Journal of drug delivery* **2011**, *2011*.

(7) Charman, W. N. Lipids, lipophilic drugs, and oral drug delivery—some emerging concepts. *J. Pharm. Sci.* **2000**, *89*, 967-978.

(8) Sharma, A.; Sharma, U. S. Liposomes in drug delivery: progress and limitations. *Int. J. Pharm.* **1997**, *154*, 123-140.

(9) Gupta, P.; Vermani, K.; Garg, S. Hydrogels: from controlled release to pH-responsive drug delivery. *Drug Discovery Today* **2002**, *7*, 569-579.

(10) He, C.; Kim, S. W.; Lee, D. S. In situ gelling stimuli-sensitive block copolymer hydrogels for drug delivery. *J. Controlled Release* **2008**, *127*, 189-207.

(11) Kim, S. W.; Bae, Y. H.; Okano, T. Hydrogels: swelling, drug loading, and release. *Pharm. Res.* **1992**, *9*, 283-290.

(12) Gong, J.; Chen, M.; Zheng, Y.; Wang, S.; Wang, Y. Polymeric micelles drug delivery system in oncology. *J. Controlled Release* **2012**, *159*, 312-323.

(13) Gaucher, G.; Dufresne, M.-H.; Sant, V. P.; Kang, N.; Maysinger, D.; Leroux, J.-C. Block copolymer micelles: preparation, characterization and application in drug delivery. *J. Controlled Release* **2005**, *109*, 169-188.

(14) Bakhtiari, A. B. S.; Hsiao, D.; Jin, G.; Gates, B. D.; Branda, N. R. An efficient method based on the photothermal effect for the release of molecules from metal nanoparticle surfaces. *Angew. Chem. Int. Ed.* **2009**, *48*, 4166-4169.

(15) Goodman, A. M.; Hogan, N. J.; Gottheim, S.; Li, C.; Clare, S. E.; Halas, N. J. Understanding resonant light-triggered DNA release from plasmonic nanoparticles. *ACS nano* **2016**, *11*, 171-179.

(16) Chen, G.-J.; Wang, L.-F. Design of magnetic nanoparticles-assisted drug delivery system. *Current pharmaceutical design* **2011**, *17*, 2331-2351.

(17) Thibaudau, F. Ultrafast photothermal release of DNA from gold nanoparticles. *The journal of physical chemistry letters* **2012**, *3*, 902-907.

(18) Ge, J.; Neofytou, E.; Cahill III, T. J.; Beygui, R. E.; Zare, R. N. Drug release from electric-field-responsive nanoparticles. *ACS nano* **2012**, *6*, 227-233.

(19) Zhu, Y.; Liu, H.; Li, F.; Ruan, Q.; Wang, H.; Fujiwara, M.; Wang, L.; Lu, G. Dipolar molecules as impellers achieving electric-field-stimulated release. *J. Am. Chem. Soc.* **2010**, *132*, 1450-1451.

(20) Austin, L. A.; Mackey, M. A.; Dreaden, E. C.; El-Sayed, M. A. The optical, photothermal, and facile surface chemical properties of gold and silver nanoparticles in biodiagnostics, therapy, and drug delivery. *Arch. Toxicol.* **2014**, *88*, 1391-1417.

(21) Abu-Laban, M.; Kumal, R. R.; Casey, J.; Becca, J.; LaMaster, D.; Pacheco, C. N.; Sykes, D. G.; Jensen, L.; Haber, L. H.; Hayes, D. J. Comparison of thermally actuated retro-diels-alder release groups for nanoparticle based nucleic acid delivery. *J. Colloid Interface Sci.* **2018**, *526*, 312-321.

(22) Kumal, R. R.; Abu-Laban, M.; Hamal, P.; Kruger, B.; Smith, H. T.; Hayes, D. J.; Haber, L. H. Near-Infrared Photothermal Release of siRNA from the Surface of Colloidal Gold–Silver–Gold Core–Shell–Shell Nanoparticles Studied with Second-Harmonic Generation. *J. Phys. Chem. C* **2018**, *122*, 19699-19704.

(23) Kumal, R. R.; Abu-Laban, M.; Landry, C. R.; Kruger, B.; Zhang, Z.; Hayes, D. J.; Haber, L. H. Plasmon-enhanced photocleaving dynamics in colloidal microRNA-functionalized silver nanoparticles monitored with second harmonic generation. *Langmuir* **2016**, *32*, 10394-10401.

(24) Kumal, R. R.; Landry, C. R.; Abu-Laban, M.; Hayes, D. J.; Haber, L. H. Monitoring the photocleaving dynamics of colloidal microrna-functionalized gold nanoparticles using second harmonic generation. *Langmuir* **2015**, *31*, 9983-9990.

(25) Abu-Laban, M.; Hamal, P.; Arrizabalaga, J. H.; Forghani, A.; Dikkumbura, A. S.; Kumal, R. R.; Haber, L. H.; Hayes, D. J. Combinatorial Delivery of miRNA-Nanoparticle Conjugates in Human Adipose Stem Cells for Amplified Osteogenesis. *Small* **2019**, *15*, 1902864.

(26) Haes, A. J.; Hall, W. P.; Chang, L.; Klein, W. L.; Van Duyne, R. P. A localized surface plasmon resonance biosensor: First steps toward an assay for Alzheimer's disease. *Nano Lett.* **2004**, *4*, 1029-1034.

(27) Pattnaik, P. Surface plasmon resonance. *Appl. Biochem. Biotechnol.* **2005**, *126*, 79-92.

(28) Karam, T. E.; Smith, H. T.; Haber, L. H. Enhanced photothermal effects and excited-state dynamics of plasmonic size-controlled gold–silver–gold core–shell–shell nanoparticles. *The Journal of Physical Chemistry C* **2015**, *119*, 18573-18580.

(29) Haber, L. H.; Kwok, S. J.; Semeraro, M.; Eisenthal, K. B. Probing the colloidal gold nanoparticle/aqueous interface with second harmonic generation. *Chem. Phys. Lett.* **2011**, *507*, 11-14.

(30) Khoury, R. A.; Ranasinghe, J. C.; Dikkumbura, A. S.; Hamal, P.; Kumal, R. R.; Karam, T. E.; Smith, H. T.; Haber, L. H. Monitoring the Seed-Mediated Growth of Gold Nanoparticles using In-Situ Second Harmonic Generation and Extinction Spectroscopy. *J. Phys. Chem. C* **2018**, *122*, 244400-224406.

(31) Kumal, R. R.; Karam, T. E.; Haber, L. H. Determination of the surface charge density of colloidal gold nanoparticles using second harmonic generation. *J. Phys. Chem. C* **2015**, *119*, 16200-16207.

(32) Karam, T. E.; Haber, L. H. Molecular adsorption and resonance coupling at the colloidal gold nanoparticle interface. *J. Phys. Chem. C* **2014**, *118*, 642-649.

(33) Hirsch, L. R.; Stafford, R. J.; Bankson, J. A.; Sershen, S. R.; Rivera, B.; Price, R.; Hazle, J. D.; Halas, N. J.; West, J. L. Nanoshell-mediated near-infrared thermal therapy of tumors under magnetic resonance guidance. *PNAS* **2003**, *100*, 13549-13554.

(34) Loo, C.; Lowery, A.; Halas, N.; West, J.; Drezek, R. Immunotargeted nanoshells for integrated cancer imaging and therapy. *Nano Lett.* **2005**, *5*, 709-711.

(35) Rastinehad, A. R.; Anastos, H.; Wajswol, E.; Winoker, J. S.; Sfakianos, J. P.; Doppalapudi, S. K.; Carrick, M. R.; Knauer, C. J.; Taouli, B.; Lewis, S. C. Gold nanoshell-localized photothermal ablation of prostate tumors in a clinical pilot device study. *PNAS* **2019**, *116*, 18590-18596.

(36) Chen, H.; Shao, L.; Ming, T.; Sun, Z.; Zhao, C.; Yang, B.; Wang, J. Understanding the photothermal conversion efficiency of gold nanocrystals. *small* **2010**, *6*, 2272-2280.

(37) Raji, V.; Kumar, J.; Rejiya, C.; Vibin, M.; Shenoi, V. N.; Abraham, A. Selective photothermal efficiency of citrate capped gold nanoparticles for destruction of cancer cells. *Experimental cell research* **2011**, *317*, 2052-2058.

(38) Ali, M. R.; Wu, Y.; El-Sayed, M. A. Gold-nanoparticle-assisted plasmonic photothermal therapy advances toward clinical application. *The Journal of Physical Chemistry C* **2019**, *123*, 15375-15393.

(39) Eisenthal, K. B. Second harmonic spectroscopy of aqueous nano-and microparticle interfaces. *Chem. Rev.* **2006**, *106*, 1462-1477.

(40) Hamal, P.; Nguyenhuu, H.; Subasinghege Don, V.; Kumal, R. R.; Kumar, R.; McCarley, R. L.; Haber, L. H. Molecular Adsorption and Transport at Liposome Surfaces Studied by Molecular Dynamics Simulations and Second Harmonic Generation Spectroscopy. *J. Phys. Chem. B* **2019**, *123*, 7722-7730.

(41) Gonella, G.; Dai, H.-L. Second harmonic light scattering from the surface of olloidal objects: theory and applications. *Langmuir* **2013**, *30*, 2588-2599.

(42) Karam, T. E.; Siraj, N.; Zhang, Z.; Ezzir, A. F.; Warner, I. M.; Haber, L. H. Ultrafast and nonlinear spectroscopy of brilliant green-based nanoGUMBOS with enhanced near-infrared emission. *J. Chem. Phys.* **2017**, *147*, 144701.

(43) Ranasinghe, J. C.; Dikkumbura, A. S.; Hamal, P.; Chen, M.; Khoury, R. A.; Smith, H. T.; Lopata, K.; Haber, L. H. Monitoring the growth dynamics of colloidal gold-silver core-shell nanoparticles using in situ second harmonic generation and extinction spectroscopy. *J. Chem. Phys.* **2019**, *151*, 224701.

(44) Kumal, R. R.; Nguyenhuu, H.; Winter, J. E.; McCarley, R. L.; Haber, L. H. Impacts of Salt, Buffer, and Lipid Nature on Molecular Adsorption and Transport in Liposomes As Observed by Second Harmonic Generation. *J. Phys. Chem. C* **2017**, *121*, 15851-15860.

(45) Gh, M. S.; Wilhelm, M. J.; Dai, H.-L. Azithromycin-Induced Changes to Bacterial Membrane Properties Monitored in vitro by Second-Harmonic Light Scattering. *ACS Med. Chem. Lett.* **2018**, *9*, 569-574.

(46) Zeng, J.; Eckenrode, H. M.; Dounce, S. M.; Dai, H.-L. Time-resolved molecular transport across living cell membranes. *Biophys. J.* **2013**, *104*, 139-145.

(47) Liu, J.; Shang, X.; Pompano, R.; Eisenthal, K. B. Antibiotic assisted molecular ion transport across a membrane in real time. *Faraday Discuss.* **2005**, *129*, 291-299.

(48) Liu, J.; Subir, M.; Nguyen, K.; Eisenthal, K. B. Second harmonic studies of ions crossing liposome membranes in real time. *J. Phys. Chem. B* **2008**, *112*, 15263-15266.

(49) Liu, Y.; Yan, E. C.; Eisenthal, K. B. Effects of bilayer surface charge density on molecular adsorption and transport across liposome bilayers. *Biophys. J.* **2001**, *80*, 1004-1012.

(50) Srivastava, A.; Eisenthal, K. B. Kinetics of molecular transport across a liposome bilayer. *Chem. Phys. Lett.* **1998**, *292*, 345-351.

(51) Abu-Laban, M.; Hamal, P.; Arrizabalaga, J. H.; Forghani, A.; Dikkumbura, A. S.; Kumal, R. R.; Haber, L. H.; Hayes, D. J. Combinatorial Delivery of miRNA-Nanoparticle Conjugates in Human Adipose Stem Cells for Amplified Osteogenesis. *Small* **2019**.

(52) Wang, H.; Yan, E. C.; Borguet, E.; Eisenthal, K. B. Second harmonic generation from the surface of centrosymmetric particles in bulk solution. *Chem. Phys. Lett.* **1996**, *259*, 15-20.

(53) Wang, H.; Yan, E. C.; Liu, Y.; Eisenthal, K. B. Energetics and population of molecules at microscopic liquid and solid surfaces. *J. Phys. Chem. B* **1998**, *102*, 4446-4450.

(54) Yan, E. C.; Liu, Y.; Eisenthal, K. B. New method for determination of surface potential of microscopic particles by second harmonic generation. *J. Phys. Chem. B* **1998**, *102*, 6331-6336.

(55) Hayes, P. L.; Malin, J. N.; Jordan, D. S.; Geiger, F. M. Get charged up: Nonlinear optical voltammetry for quantifying the thermodynamics and electrostatics of metal ations at aqueous/oxide interfaces. *Chem. Phys. Lett.* **2010**, *499*, 183-192.

(56) Rao, Y.; Kwok, S. J.; Lombardi, J.; Turro, N. J.; Eisenthal, K. B. Label-free probe of HIV-1 TAT peptide binding to mimetic membranes. *PNAS* **2014**, *111*, 12684-12688.

(57) Yamashita, S.; Fukushima, H.; Niidome, Y.; Mori, T.; Katayama, Y.; Niidome, T. Controlled-release system mediated by a retro Diels–Alder reaction induced by the photothermal effect of gold nanorods. *Langmuir* **2011**, *27*, 14621-14626.

(58) Perrault, S. D.; Chan, W. C. Synthesis and surface modification of highly monodispersed, spherical gold nanoparticles of 50− 200 nm. *J. Am. Chem. Soc.* **2009**, *131*, 17042-17043.

(59) Li, H.; Xia, H.; Wang, D.; Tao, X. Simple synthesis of monodisperse, quasi-spherical, citrate-stabilized silver nanocrystals in water. *Langmuir* **2013**, *29*, 5074-5079.

(60) Hartland, G. V.; Besteiro, L. V.; Johns, P.; Govorov, A. O. What's so hot about electrons in metal nanoparticles? *ACS Energy Lett.* **2017**, *2*, 1641-1653.

(61) Link, S.; Burda, C.; Wang, Z. L.; El-Sayed, M. A. Electron dynamics in gold and gold–silver alloy nanoparticles: The influence of a nonequilibrium electron distribution and the size dependence of the electron–phonon relaxation. *J. Chem. Phys.* **1999**, *111*, 1255-1264.

Chapter 6. Concluding Remarks

6.1. Summary

Nanoparticle-based drug-delivery systems have long been an intriguing focus of study and an enormous amount of knowledge has been obtained through experimental and theoretical investigations. In this thesis, I have used the nonlinear optical technique of second harmonic generation to study two different types of nanoparticle systems; biological membranes and plasmonic nanoparticles.

Membrane-based liposome systems are studied using second harmonic generation spectroscopy for drug-like cationic molecules to determine adsorption free energies, adsorbate concentrations, and molecular transport lifetimes. These molecule-membrane interactions are influenced by electrolytes, chemical functional groups, temperature, and the local environment.[1] Additionally, second harmonic generation microscopy is used for imaging and characterization of molecular adsorption and transport in living and dead H596 cells. The results are consistent with the general concepts of molecular translocation developed in our liposome studies. The results also show an interesting trend of time-dependent oscillations in the SHG signal in living cells but not in fixed, dead cells, which is attributed to dynamic cycles of active transport of ions by the cells in order to regulate membrane potential and local pH. Similarly, the investigations are in agreement with our liposome work, where chemical functional groups such as isothiocyanate is demonstrated to have a huge influence on molecule-membrane interactions in H596 cells.

Plasmonic nanoparticles are synthesized and functionalized with drug-like miRNA molecules to study the photothermal release kinetics in colloidal gold, silver, and gold-silver-gold core-shell-shell plasmonic nanoparticles under irradiation at their corresponding plasmon resonances with monitoring using time-dependent second harmonic generation spectroscopy.[2,3] The research demonstrates a higher photothermal efficiency for gold-silver-gold core-shell-shell plasmonic nanoparticles, which has its plasmon resonance in the near-infrared biological window.

In summary, surface-specific second harmonic generation is shown to be a very promising platform to study several microparticle-based and nanoparticle-based systems for developing potential drug-delivery applications.

6.2. Ultrafast and Nonlinear Spectroscopy of Nanomaterials

A minor part of my graduate career also focused on using ultrafast pump-probe reflectivity to study heating and melting dynamics in aluminum thin film samples of different thicknesses deposited on silica substrates. The results indicate that nanomaterial thin films becomes bulk-like as the thickness increases past the characteristic heat penetration depth, which is estimated to be approximately 170 nm for aluminum. Additionally, optical microscopy images are taken for samples before and after laser irradiation to further characterize the laser-induced heating and melting. The results suggest the important influence of power-dependent and thickness-dependent heating and melting dynamics for aluminum thin films. Broadly, this work can give fundamental information for improving selective laser melting and 3D printing of metals. A manuscript is currently in preparation on this work, for which I am a co-author.

Additionally, I also had the great opportunity to work on *in situ* characterizations of plasmonic nanoparticle growth dynamics in aqueous solution. The changes in nanoparticle size and surface morphology are investigated using our home-built setup that combines time-dependent extinction spectroscopy and second harmonic generation spectroscopy simultaneously to monitor the nanoparticle growth in real time under varying reaction conditions. Using this setup, our group has studied growth dynamics of colloidal gold nanoparticles, gold-silver core-shell nanoparticles, and silver-gold core-shell nanoparticles.[4,5] The utilization of linear and nonlinear spectroscopy to study nanoparticle growth captures changes in the nanomaterial bulk and surface during reaction times, providing crucial information about short-lived intermediates, associated growth kinetics, and surface modifications. This *in situ* characterization technique provides new approaches for tailoring plasmonic nanoengineering and associated applications.

6.3. Future Work

The surface-specific second harmonic generation technique can be applied to study a variety of fundamental molecule-membrane interactions. In future work, new triphenylmethane dyes can be used to study liposomes and cells. For example, a malachite green molecular scaffold with an added NO_2 that has a larger dipole moment than malachite green and malachite green isothiocyanate can be investigated. Additionally, malachite green with added hydrophilic or hydrophobic groups like chlorine or benzene can be studied in different liposome samples or cell samples, along with molecular dynamics simulations, to investigate the role of chemical modifications in improving drug delivery. This work can lead towards ambitious aspirations that would functionalize existing drug molecules like doxorubicin or paclitaxel with isothiocyanate or

other targeted functional groups, then study the molecular binding and transport in liposomes and cells. Similarly, the basic principles discussed in Chapters 2, 3, and 4 can be applied to bacterial cells to determine which factors, including chemical functional groups and the local environment, can be utilized for enhancing molecular translocation through bacterial cell membranes while identifying universal and specialized concepts for improving drug delivery. Additionally, the cell work discussed in Chapter 4 can be further extended using healthy cell lines for direct comparison between cancerous cells and healthy cells to reveal potential new insights on molecule-membrane interactions involving both passive and active transport.

Photothermal applications of gold and hybrid plasmonic nanoparticles in tumor therapy has shown remarkable promise over the past 15 years. In this regard, the Haber Lab has been extensively working on the characterization of novel gold-silver-gold core-shell-shell nanoparticles and their wavelength-dependent photothermal efficiencies. In future work, we can continue these studies by measuring photothermal efficiencies of novel gold-silver-gold core-shell-shell nanoparticles with continuous lasers, oscillator lasers, and amplifier lasers to study the influence of pulse power, pulse duration, and repetition rate. Similarly, we can extend these investigations where colloidal suspensions of tumor cells can be added to gold-silver-gold core-shell-shell nanoparticles in solution then irradiated with different types of laser light. Additionally, light-triggered release of miRNA can be investigated with rough and smooth gold-silver-gold core-shell-shell nanoparticles, at its corresponding plasmon resonance, to understand the effect of plasmonic hot spots in photothermal drug-delivery systems.

In summary, second harmonic generation is demonstrated to be a promising and powerful technique for time-dependent and surface-sensitive investigations of colloidal nanoparticle-based drug-delivery systems.

6.4. Notes

(1) Hamal, P.; Nguyenhuu, H.; Subasinghege Don, V.; Kumal, R. R.; Kumar, R.; McCarley, R. L.; Haber, L. H. Molecular Adsorption and Transport at Liposome Surfaces Studied by Molecular Dynamics Simulations and Second Harmonic Generation Spectroscopy. *J. Phys. Chem. B* **2019**, *123*, 7722-7730.

(2) Abu-Laban, M.; Hamal, P.; Arrizabalaga, J. H.; Forghani, A.; Dikkumbura, A. S.; Kumal, R. R.; Haber, L. H.; Hayes, D. J. Combinatorial Delivery of miRNA-Nanoparticle Conjugates in Human Adipose Stem Cells for Amplified Osteogenesis. *Small* **2019**, *15*, 1902864.

(3) Kumal, R. R.; Abu-Laban, M.; Hamal, P.; Kruger, B.; Smith, H. T.; Hayes, D. J.; Haber, L. H. Near-Infrared Photothermal Release of siRNA from the Surface of Colloidal Gold–Silver–Gold Core–Shell–Shell Nanoparticles Studied with Second-Harmonic Generation. *J. Phys. Chem. C* **2018**, *122*, 19699-19704.

(4) Khoury, R. A.; Ranasinghe, J. C.; Dikkumbura, A. S.; Hamal, P.; Kumal, R. R.; Karam, T. E.; Smith, H. T.; Haber, L. H. Monitoring the Seed-Mediated Growth of Gold Nanoparticles using In-Situ Second Harmonic Generation and Extinction Spectroscopy. *J. Phys. Chem. C* **2018**, *122*, 244400-224406.

(5) Ranasinghe, J. C.; Dikkumbura, A. S.; Hamal, P.; Chen, M.; Khoury, R. A.; Smith, H. T.; Lopata, K.; Haber, L. H. Monitoring the growth dynamics of colloidal gold-silver core-shell nanoparticles using in situ second harmonic generation and extinction spectroscopy. *J. Chem. Phys.* **2019**, *151*, 224701.

Appendix A. Supplementary Material for Chapter 2

A.1 Lipid Concentration Determination and Liposome Size Distributions

The total lipid concentrations were determined by a modified Bartlett assay, which is based on the colorimetric determination of inorganic phosphate, and has been reported previously.[1] Briefly, phospholipids in liposomes were converted to inorganic phosphate by perchloric acid, followed by the formation of phosphor-molybdic acid after the addition of ammonium molybdate in an acidic condition. The phosphor-molybdic acid was then reduced by Fiske-Subbarow reducer, producing a blue solution, and its absorbance was measured at 800 nm. The calibration curve for the Bartlett assay, as shown in Figure A.1, is fit with a linear equation with a slope of 0.00326 ± 0.00004 and a *y*-intercept of −0.002 ± 0.003. The R^2 value for the fit is 0.9991. The zeta potentials of different liposomes at 5 mM citrate buffer of pH 4.0 is displayed in Table A.1. Similarly, the representative DLS size distributions are shown in Figure A.2. The representative sizes obtained are 137 ± 42 nm, 156 ± 58 nm, 151 ± 64 nm, and 158 ± 67 nm, respectively, for DOPG, DOPS, DOPC, and QPADOPE liposomes. Similarly, the polydispersity index (PDI) values are 0.07, 0.09, 0.10, and 0.20, respectively, for DOPG, DOPS, DOPC, and QPADOPE liposomes. Zeta potential and dynamic light scattering measurements are taken using a Zetasizer Nano ZS from Malvern Instruments Inc., UK. Absorption measurements are done using a UV−vis spectrometer from PerkinElmer, Boston, MA, U.S.A.

Table A.1. Zeta Potentials of Different Liposome Samples

Buffer (pH 4.0)	Zeta Potential (mV)			
	DOPG	DOPS	QPADOPE	DOPC
5.0 mM citrate	−73.2 ± 1.1	−74.8 ± 1.7	−67.3 ± 1.5	−21.7 ± 2.3

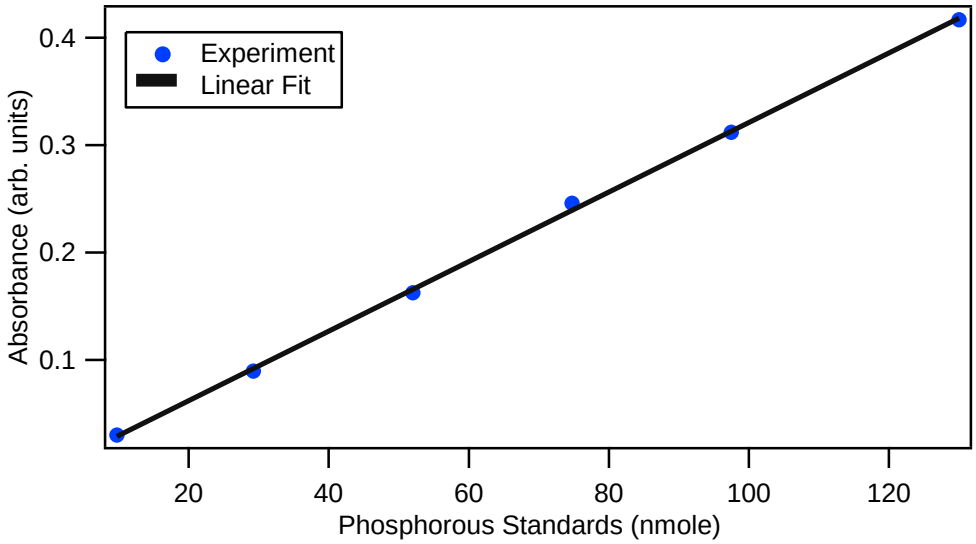

Figure A.1. Bartlett assay calibration for determining the lipid concentration.

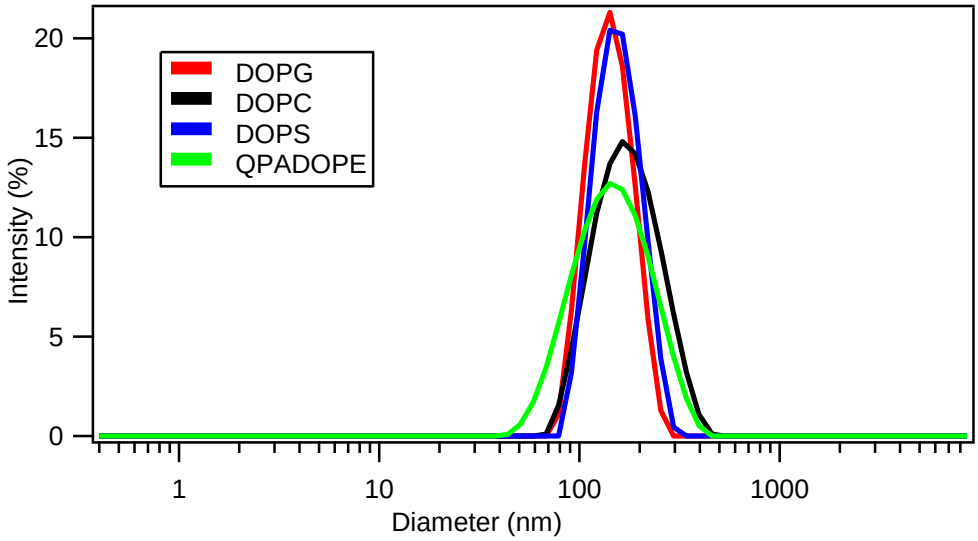

Figure A.2. Size distributions measured by dynamic light scattering for DOPG, DOPC, DOPS, and QPADOPE liposomes.

A.2 SHG Adsorption Isotherm to PSS Microparticles

Adsorption isotherms for malachite green isothiocyanate (MGITC) adsorbing to the surface of polystyrene sulfate (PSS) microspheres in aqueous colloidal suspension are determined using SHG measurements for comparison to the liposome results presented in the manuscript. The PSS microspheres are purchased from Polysciences and are diluted in nanopure water to a concentration of 1.8×10^{10} particles/mL. The experimental setup is the same as the one used for the liposome measurements, with the same data analysis procedure.[1,2] To our knowledge, no work has previously reported SHG measurements for MGITC adsorbing to polystyrene microspheres in water. MGITC shows an SHG signal that is approximately 12 times greater than from MG at the same concentration of 0.75 μM, as shown in Figure A.3a. The experimentally obtained isotherms are fit with the modified Langmuir isotherm model as displayed in Figure A.3b.

Using the modified Langmuir model, the corresponding adsorption free energy ΔG is −13.6 ± 0.05 kcal/mol with an equilibrium constant K value of (9.9 ± 0.9) × 10^9 and an N_{max} value of 0.2 ± 0.003 μM. The adsorption free energy of MGITC in PSS is stronger in comparison to liposomes and is in general agreement with the literature trends.[3] Similarly, the adsorption free energy also correlates that the electrostatic binding of MGITC in polystyrene sulfate microspheres is stronger than that of malachite green (MG). The reported value for the adsorption free energy of MG in polystyrene sulfate microspheres is −11.1 ± 0.1.[2,4] Interestingly, the reported N_{max} value of MG in polystyrene sulfate microspheres is 1.2 ± 0.2 μM[4], which is approximately 6 times larger than for MGITC.[1,2] A similar trend has been reported in the literature where a strong electrostatic attraction between triphenylmethane dye molecules and colloidal polystyrene microspheres leads to higher dye-dye repulsions, leading to diminished values of N_{max}.[2]

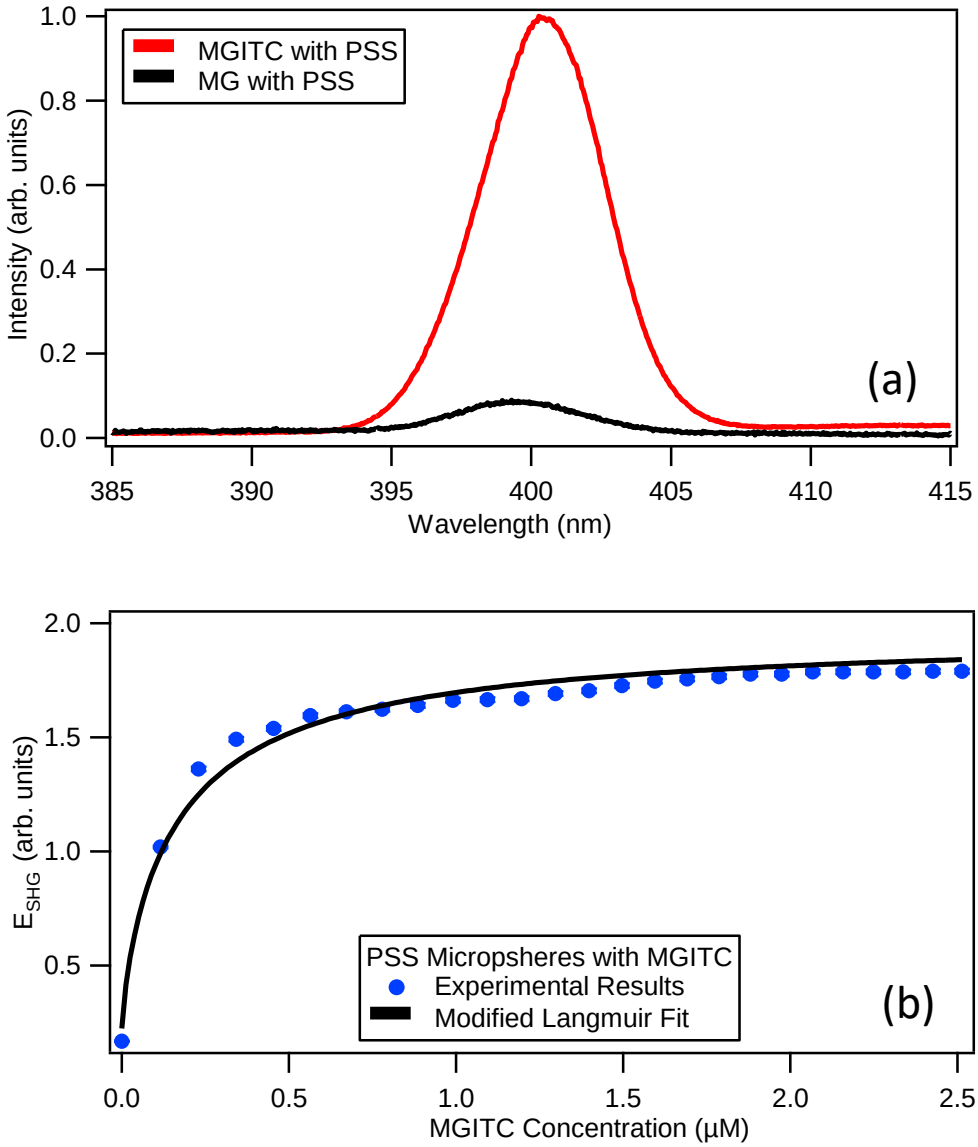

Figure A.3. (a) Representative SHG spectra of polystyrene sulfate microspheres with 0.75 μM of MGITC and MG. (b) SHG-determined adsorption isotherm of MGITC with polystyrene sulfate microspheres.

A.3 Additional Details on SHG Measurements of Molecular Interactions with Liposomes

Figure A.4a shows the extinction spectrum of MGITC in citrate buffer at pH 4.0 for different experimental times indicating the stability of the MGITC dye in solutions under these conditions. Additionally, a schematic energy level diagram of the MGITC dye is shown in Figure A.4b, where resonance enhancement at 2ω occurs corresponding to the transition from ground state S_0 to the vibrationally excited S_2 state. The transport times τ of MGITC through the bilayers of DOPG, DOPS and DOPC liposomes are listed in Table A.2. Similarly, the obtained rate constants (τ^{-1}) for liposomes also have a similar trend as the transport times, as shown in Figure A.5. The interaction of MGITC with the QPADOPE liposomes and with 5.0 mM citrate buffer of pH 4.0 is also studied using SHG measurements, as displayed in Figures A.6a and A.6b. These corresponding SHG intensities are plotted as a function of concentration with linear fits, as shown in Figures A.7a and A.7b. These SHG signal intensities are normalized consistently with Figures 2.2 and 2.3 in Chapter 2 as well as Figures A.6a and A.6b such that $I_{SHG} = E_{SHG}^2$. The obtained slopes from the fits are (0.017 ± 0.001) μM^{-1} and (0.015 ± 0.001) μM^{-1} for Figures A.7a and A7b, respectively. These corresponding SHG intensities are approximately equal indicating no observed adsorption to the QPADOPE liposomes, to within experimental uncertainty. Additionally, the SHG time traces in Figure A.6a do not change with time, confirming that no transport occurs. As described in Chapter 2, these signals are understood to be primarily from hyper Rayleigh scattering from MGITC. The value of the slope from Figure A.7b is used for α in the SHG fits described in Equation 2.2 of the Chapter 2.

In order to investigate the possible counterion effect, the transport kinetics of the MGITC dye molecule are studied with DOPG liposomes in 5.0 mM citrate buffer of pH 4.0 with no additional potassium perchlorate and with 5.0 mM additional potassium perchlorate (PP) at two different MGITC concentrations. The SHG time traces, shown in Figure A.8a only shift down slightly upon addition of PP, similar to our previous studies with MG and potassium chloride (KCl).[1,5] These results indicate that the perchlorate ion does not cause significant or unexpected counterion effects with MGITC. Additionally, there is no significant change in the MGITC spectrum upon addition of 5.0 mM PP, and the dye remains stable over time, as shown in the extinction spectra in Figure A.8b.

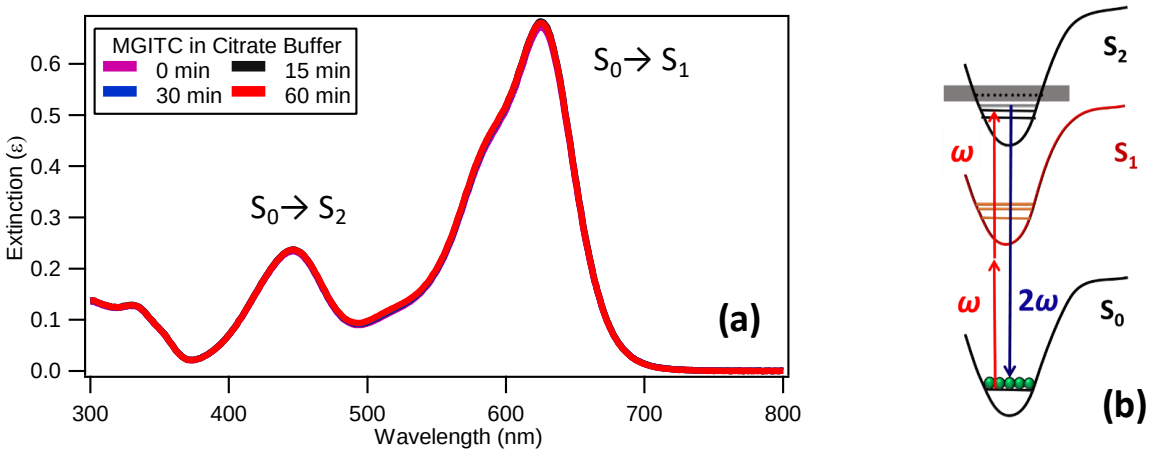

Figure A.4. (a) Extinction spectrum of MGITC in citrate buffer of pH 4.0 at various times. (b) Energy level diagram of MGITC dye molecule, showing resonance enhancement of SHG.

Table A.2. Transport times of MGITC in DOPC, DOPS and DOPG liposomes

MGITC (μM)	Transport Time (second)		
	DOPC	DOPS	DOPG
0.16	500 ± 81	364 ± 32	360 ± 17
0.53	400 ± 40	338 ± 21	327 ± 12
1.06	334 ± 25	280 ± 20	304 ± 6
1.31	238 ± 16	114 ± 4	168 ± 10
1.57	222 ± 17	158 ± 5	156 ± 9
1.94	208 ± 17	121 ± 6	123 ± 8
2.06	200 ± 8	143 ± 9	115 ± 12
2.55	167 ± 5	133 ± 5	83 ± 4
3.44	143 ± 4	121 ± 3	67 ± 3
4.75	125 ± 3	130 ± 6	55 ± 3

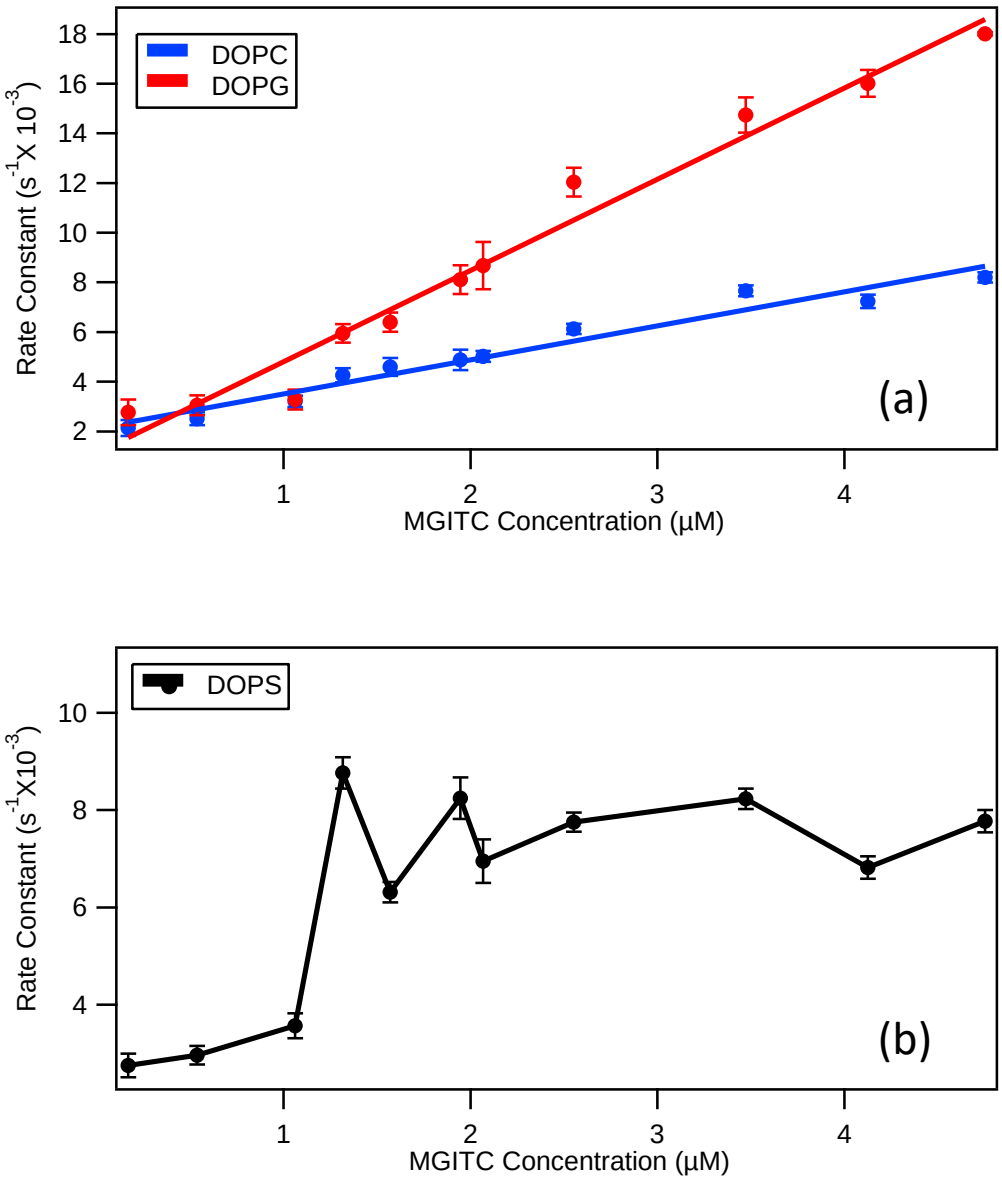

Figure A.5. Variation of the transport rate constant as a function of MGITC concentration for (a) DOPG, DOPC, and (b) DOPS liposomes in 5 mM citrate buffer of pH 4.0.

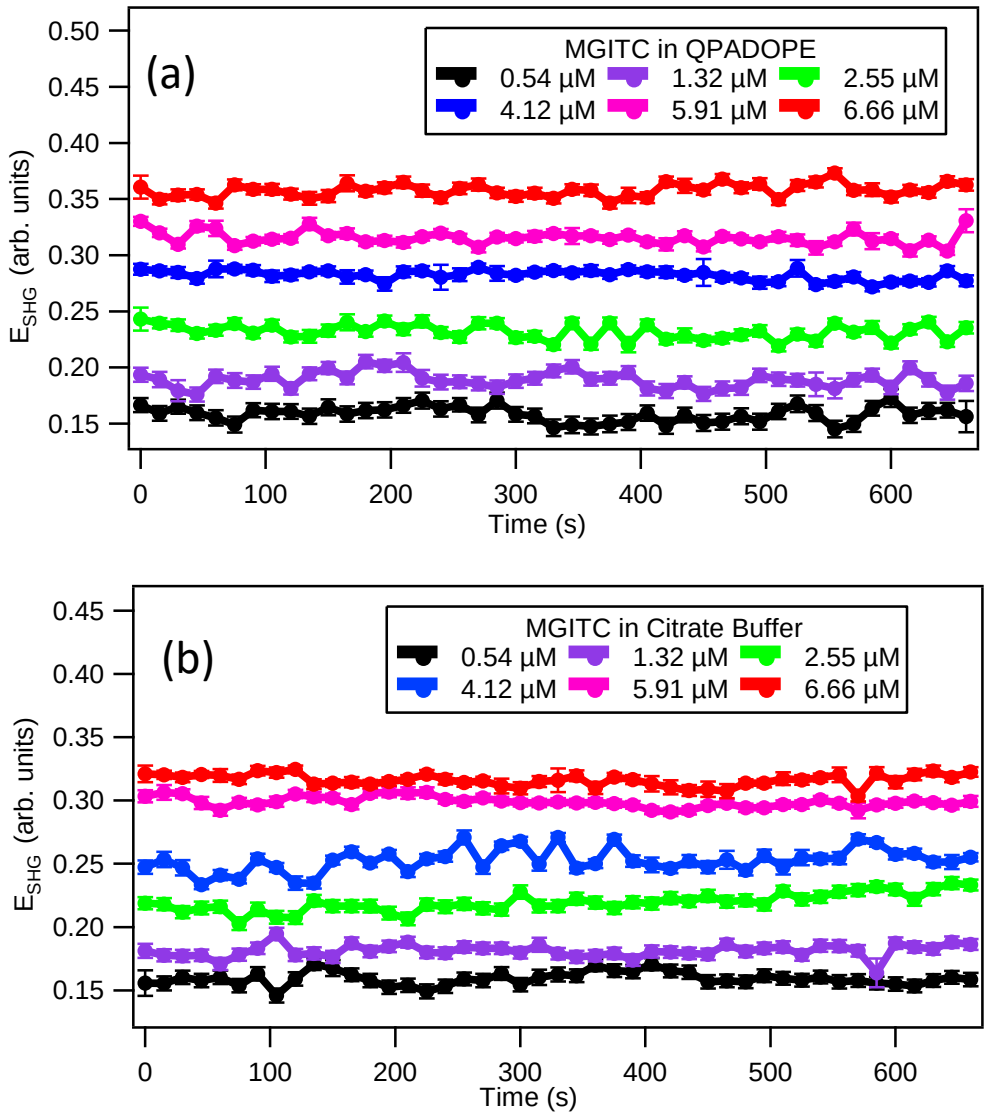

Figure A.6. SHG time profiles upon addition of various concentrations of MGITC to (a) QPADOPE liposomes and (b) 5 mM citrate buffer at pH 4.0.

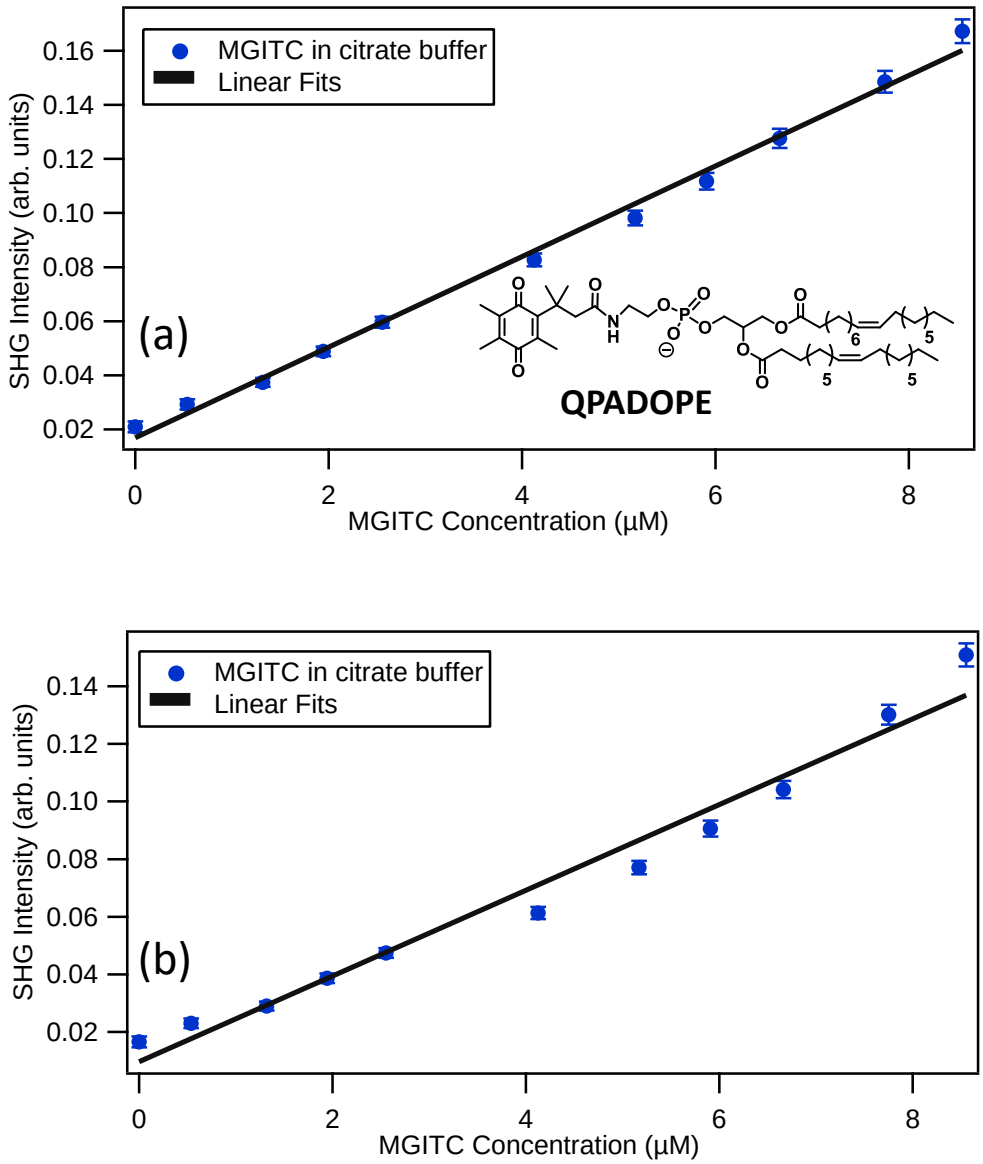

Figure A.7. SHG signal intensity of (a) QPADOPE liposomes and (b) citrate buffer as a function of added MGITC concentration (blue circles) compared to linear fits (black lines). The inset of (a) shows the molecular structure of QPADOPE.

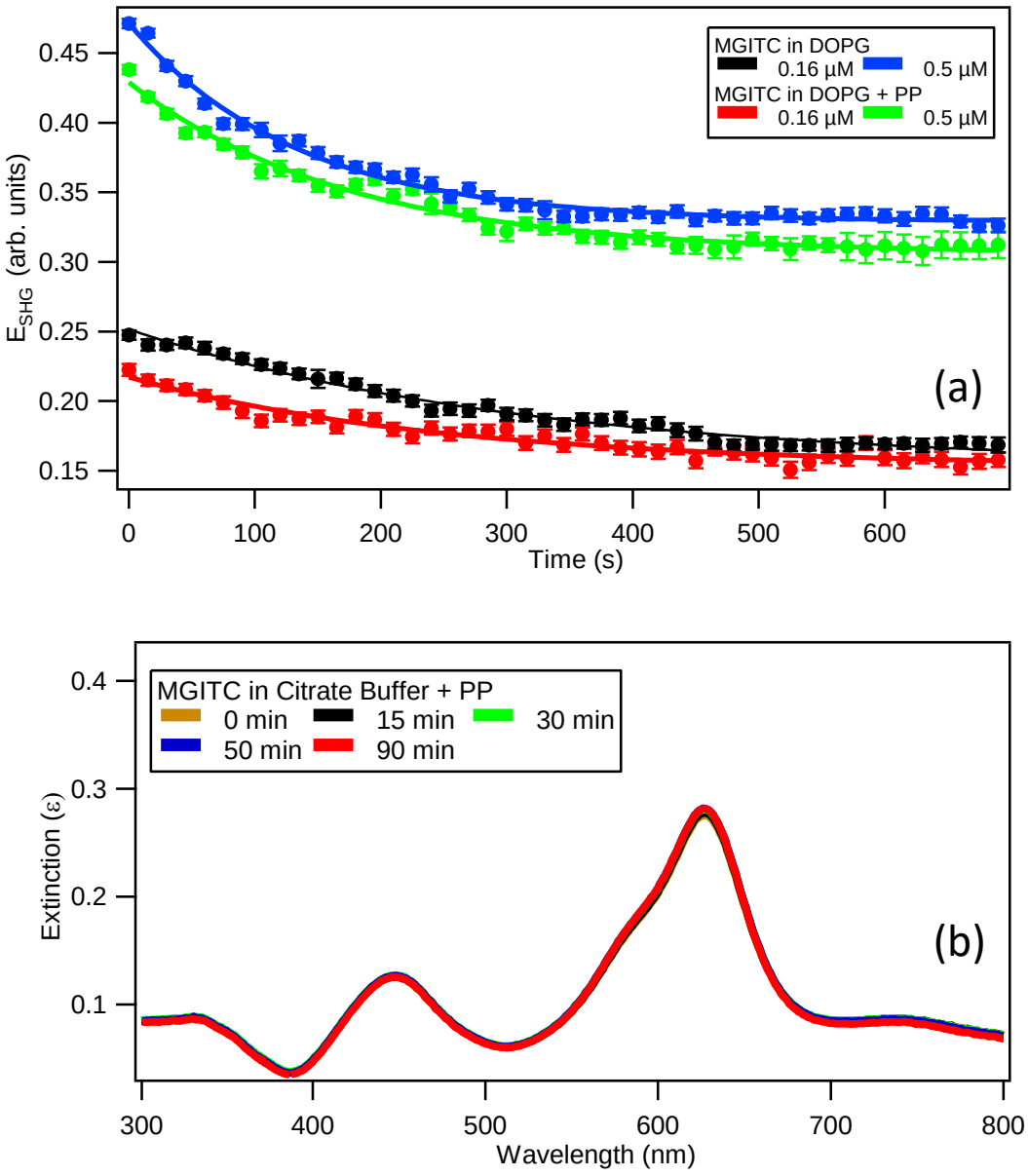

Figure A.8. (a) SHG time profiles upon addition of various concentrations of MGITC to DOPG liposomes at different buffer conditions. (b) Absorption spectra of malachite green isothiocyanate in citrate buffer with 5 mM potassium perchlorate at pH 4.0 at various times.

A.4 Molecular Dynamics Simulations Details

The CHARMM-GUI Membrane Builder[6,7] was used to build the initial structures of DOPC and DOPG membranes. Each bilayer initially had 72 phospholipid molecules. These bilayers were then solvated with 6075 SPC/E[8] water molecules using Packmol.[9] Since DOPG molecules are negatively charged, 72 K^+ ions were added to the DOPG system to neutralize the system charge. The box dimensions of the solvated membranes were approximately 59.0 × 62.0 × 126.0 $Å^3$ for DOPC, and 57.0 × 60.0 × 124.0 $Å^3$ for DOPG. Molecular dynamics simulations were carried out using LAMMPS program (version 05 Sep 2014)[10] with the all-atom general AMBER force field (GAFF).[11] The partial charges of the optimized structures were calculated by the RESP fitting technique[12,13] using the HF/6-31G* method in Gaussian 09 suite of programs.[14] The input files for the simulations were generated using the Moltemplate[15] package. The energies of these initial solvated DOPC and DOPG systems were minimized followed by a 5 ns simulation in the isothermal-isobaric (NPT) ensemble and then a 10 ns simulation in the canonical (NVT) ensemble. Both systems were then replicated along the x-axis and simulated for a further 5 ns in the NVT ensemble. The final simulation box dimensions were approximately 95.5 × 48.0 × 120.0 $Å^3$ for DOPC systems, and 94.5 × 50.0 × 115.0 $Å^3$ for DOPG systems.

The MG and MGITC structures were built using the Avogardo[16] package and the structures were optimized using Gaussian 09 suite of programs[14] with the HF/6-31G* method. The partial charges were calculated by the RESP fitting technique[12,13] using the HF/6-31G* method. Then four different systems were generated by inserting one molecule of either MG or MGITC with their respective counter ion (Cl^- for MG and ClO_4^-

for MGITC) into the solvated DOPC and DOPG membrane systems that were already equilibrated. Energy minimization was performed on all four systems, which were then equilibrated in the NPT ensemble for 1 ns. Each system was then simulated for a total of 10 ns. The Langevin thermostat[17] with a collision frequency of 1 ps^{-1} was applied to control the temperature at 303 K. The pressure of the system was controlled at 1 atm by applying the Berendsen barostat[18] with a damping time of 1 ps and an isothermal compressibility of 4.6×10^{-5} atm^{-1}. The pressure was controlled semi-isotropically (only along the z-component of the system) as has been used previously.[19] The SHAKE algorithm was used to constrain the bond lengths and bond angles for the water molecules and the periodic boundary condition was used for all four systems. Electrostatic interactions were calculated using the PPPM (particle-particle particle-mesh) method[20] and the non-bonded Lennard-Jones interactions were cutoff beyond 10 Å. The time step used for these simulations was 2 fs.

The umbrella sampling method[21] was used to determine the free energy profile of the adsorption of the two dyes on the two membranes. The starting structures for the umbrella sampling windows for each case were taken from the respective regular canonical simulations. The collective variable was the distance in the z-direction between the center of mass (COM) of the lipid bilayer and the COM of the dye molecule. For each system 20 umbrella sampling windows were simulated with a step-size of 1.5 Å and a harmonic force constant of 3 kcal/mol. The simulation time for each window was 18 ns. The weighted histogram analysis (WHAM) method[22,23] was used to derive the potential mean force for the adsorption processes of each dye molecules. Only the last 14 ns of each umbrella sampling window was used for this analysis. The calculation of the statistical error with

the potential mean force was calculated using the block averaging method with each block having 3.5 ns of simulation time.

The surface of the DOPC membrane was defined as the average z-coordinates of the nitrogen atom of each DOPC molecule on one side of the membrane. Similarly, the surface of the DOPG membrane was determined using the average z-coordinates of the oxygen atom of each DOPG's furthest hydroxyl group on one side of the membrane.

Orientation Analysis

In order to determine the orientation of each dye molecule when they are at the surface of the DOPC and DOPG membrane, the distribution of the distance in the z-direction between different reference atoms of the dye molecule and the COM of the lipid bilayer was used. The two nitrogen atoms of the amine group and the carbon atom in the third phenyl group in each dye molecule were used as the reference atoms for this analysis (See Figure A.9a and A.9b). All four distributions of the distances (Figures A.9c – A.9f) are shown for when the dye molecules are at the surface of the membranes. Specifically, for MG and MGITC in DOPC these distances were taken from the window with the collective variable set to 22.5 Å. The average distance (along the z-direction), D1, between the COM of the dye molecule and the surface was found to be 0.4 ± 0.2 Å for MG in DOPC. According to Figure S9c, one of the nitrogen atoms of the amine group is directed towards the membrane and the other two atoms (nitrogen and carbon) are directed away from the DOPC membrane. The average distance (along the z-direction), D1, between the COM of the dye molecule and the surface was found to be 0.7 ± 0.2 Å for MGITC in DOPC. From Figure A.9d it is clear that the carbon atom with the NCS group

is directed towards the membrane. Figures A.9e and A.9f show the orientations of the two dye molecules in the DOPG membrane. For the distance analyses, the window with the collective variable set to 19.5 Å was used. The average distance, D2, between the COM of the dye molecule and the surface was found to be 0.3 ± 0.2 Å for MG in DOPG and 0.2 ± 0.2 Å for MGITC in DOPG. In both of these systems an extra amine group nitrogen atom is also directed towards the DOPG membrane other than the group that was directed towards the DOPC membrane.

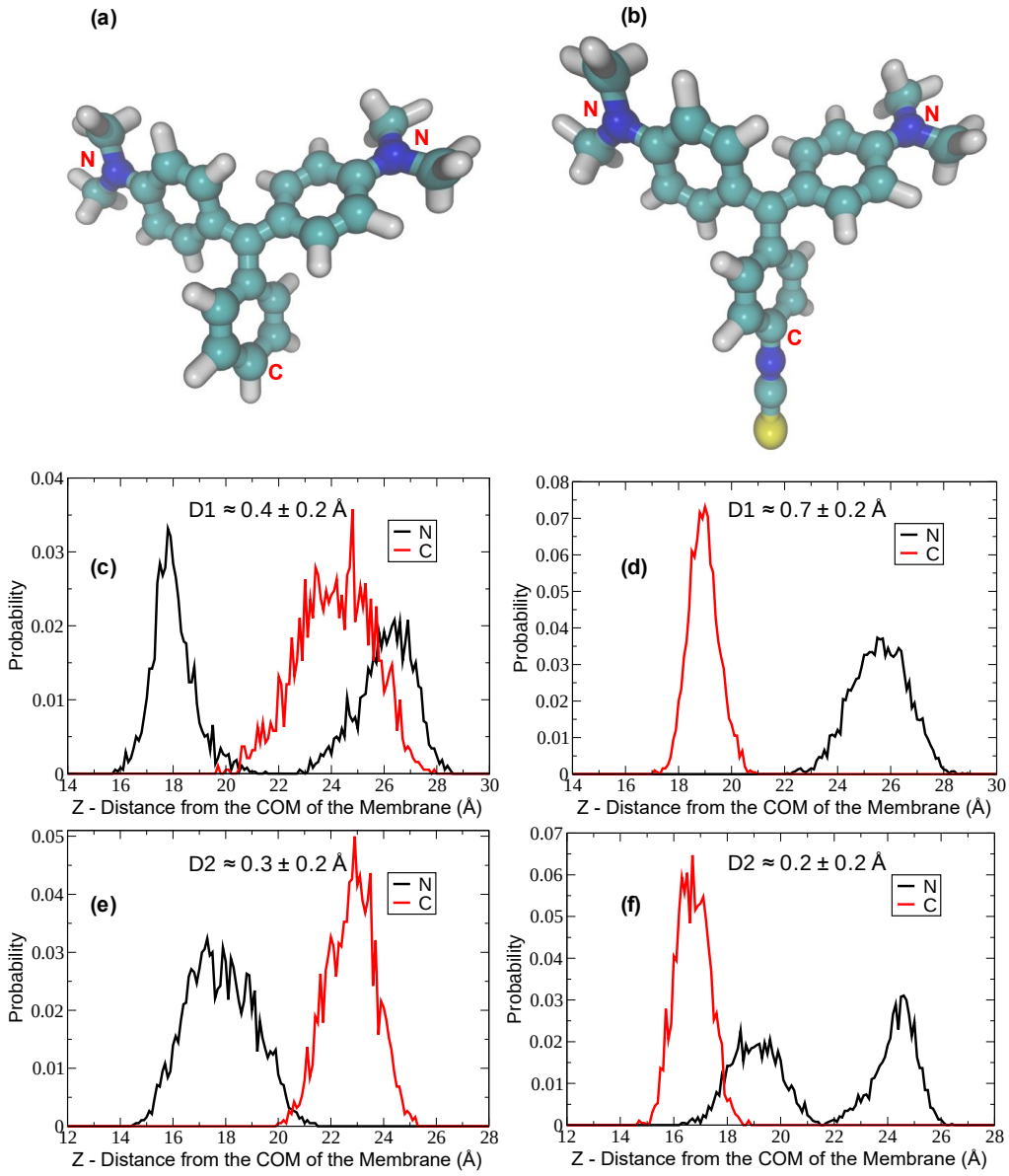

Figure A.9. N and C atoms used in the distance distribution (along the z-direction) calculations for (a) MG and (b) MGITC molecules, respectively. The carbon atoms are represented in cyan, sulfur atoms in yellow, nitrogen atoms in blue, and hydrogen in white. Distributions of the distances (along the z-direction) between the defined N and C atoms of the dye molecules in different lipid bilayer from (c) MG in DOPC, (d) MGITC in DOPC, (e) MG in DOPG, and (f) MGITC in DOPG. D1 is the distance between the COM of the dye and the surface of the DOPC membrane. D2 is the distance between the COM of the dye and the surface of the DOPG membrane.

Distribution of the Electron Density

Using the Gaussian 09 suite of programs[14] with the RESP fitting technique,[12,13] the electron density distribution maps of MG and MGITC dye molecules were obtained. For these calculations, HF/6-31G* method and basis set were used. The two electron density maps are shown in Figure A.10. Comparing the two electron density maps, the electron density is more negative on the NCS group of the MGITC molecule whereas the electron density of MG is distributed more evenly throughout the molecule, resulting in MGITC having a higher dipole moment of 10.59 Debye as compared to 2.28 Debye for MG.

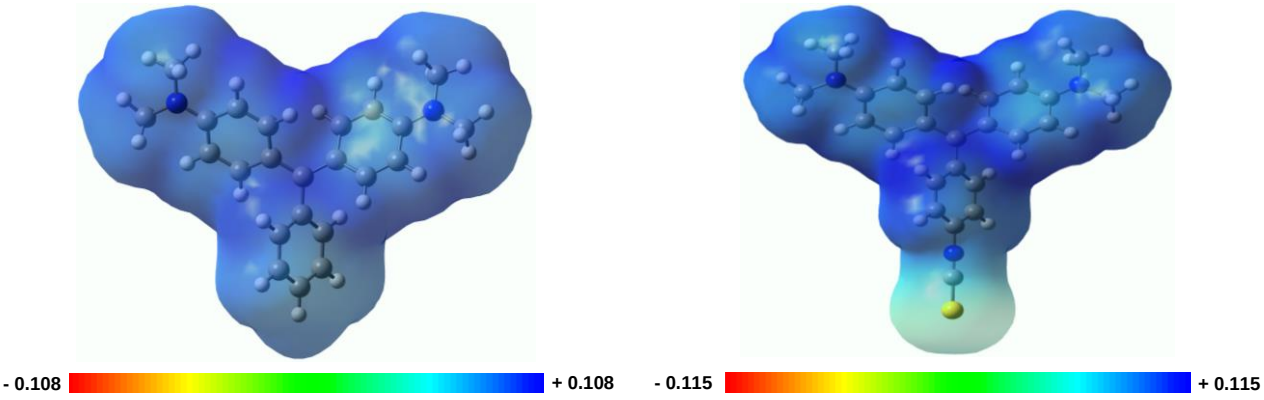

Figure A.10. Distribution of the electron density around the dye molecule for (a) MG and (b) MGITC. The carbon atoms are represented in ash, sulfur atoms in yellow, nitrogen atoms in blue, and hydrogen atoms in white.

A.5 Error Analysis of Fits

The R^2-values obtained for time-dependent exponential fits are summarized in Table A.3. Similarly, the R^2-values obtained for modified Langmuir fits are shown in Table A.4.

Table A.3. R^2-values of time-dependent exponential fits.

	R^2-Values of exponential fits		
MGITC (μM)	DOPG	DOPS	DOPC
0.16	0.93	0.89	0.89
0.53	0.99	0.99	0.95
1.06	0.96	0.98	0.93
1.31	0.97	0.99	0.95
1.57	0.97	0.93	0.97
1.94	0.99	0.75	0.97
3.44	0.96	0.97	0.99
4.12	0.96	0.99	0.99
4.75	0.99	0.99	0.99

Table A.4. R^2-Values of Modified Langmuir Fits

Liposome	DOPG	DOPS	DOPC
R^2-Value	0.955	0.974	0.969

A.6. Notes

(1) Kumal, R. R.; Nguyenhuu, H.; Winter, J. E.; McCarley, R. L.; Haber, L. H. Impacts of Salt, Buffer, and Lipid Nature on Molecular Adsorption and Transport in Liposomes As Observed by Second Harmonic Generation. *J. Phys. Chem. C* **2017**, *121*, 15851-15860.

(2) Karam, T. E.; Haber, L. H. Molecular adsorption and resonance coupling at the colloidal gold nanoparticle interface. *J. Phys. Chem. C* **2014**, *118*, 642-649.

(3) Zeng, J.; Eckenrode, H. M.; Dai, H.-L.; Wilhelm, M. J. Adsorption and transport of charged vs. neutral hydrophobic molecules at the membrane of murine erythroleukemia (MEL) cells. *Colloids Surf., B* **2015**, *127*, 122-129.

(4) Wang, H.; Yan, E. C.; Liu, Y.; Eisenthal, K. B. Energetics and population of molecules at microscopic liquid and solid surfaces. *J. Phys. Chem. B* **1998**, *102*, 4446-4450.

(5) Shang, X.; Liu, Y.; Yan, E.; Eisenthal, K. B. Effects of counterions on molecular transport across liposome bilayer: probed by second harmonic generation. *J. Phys. Chem. B* **2001**, *105*, 12816-12822.

(6) Jo, S.; Kim, T.; Iyer, V. G.; Im, W. CHARMM-GUI: a web-based graphical user interface for CHARMM. *J. Comput. Chem.* **2008**, *29*, 1859-1865.

(7) Wu, E. L.; Cheng, X.; Jo, S.; Rui, H.; Song, K. C.; Dávila-Contreras, E. M.; Qi, Y.; Lee, J.; Monje-Galvan, V.; Venable, R. M. CHARMM-GUI membrane builder toward realistic biological membrane simulations. *J. Comput. Chem.* **2014**, *35*, 1997-2004.

(8) Berendsen, H.; Grigera, J.; Straatsma, T. The missing term in effective pair potentials. *J. Phys. Chem.* **1987**, *91*, 6269-6271.

(9) Martínez, L.; Andrade, R.; Birgin, E. G.; Martínez, J. M. PACKMOL: a package for building initial configurations for molecular dynamics simulations. *J. Comput. Chem.* **2009**, *30*, 2157-2164.

(10) Plimpton, S. Fast parallel algorithms for short-range molecular dynamics. *J. Comput. Phys.* **1995**, *117*, 1-19.

(11) Wang, J.; Wolf, R. M.; Caldwell, J. W.; Kollman, P. A.; Case, D. A. Development and testing of a general amber force field. *J. Comput. Chem.* **2004**, *25*, 1157-1174.

(12) Bayly, C. I.; Cieplak, P.; Cornell, W.; Kollman, P. A. A well-behaved electrostatic potential based method using charge restraints for deriving atomic charges: the RESP model. *J. Phys. Chem.* **1993**, *97*, 10269-10280.

(13) Cieplak, P.; Cornell, W. D.; Bayly, C.; Kollman, P. A. Application of the multimolecule and multiconformational RESP methodology to biopolymers: Charge derivation for DNA, RNA, and proteins. *J. Comput. Chem.* **1995**, *16*, 1357-1377.

(14) M. J. Frisch, G. W. T., H. B. Schlegel, G. E. Scuseria, M. A. Robb, J. R. Cheeseman, G. Scalmani, V. Barone, B. Mennucci, G. A. Petersson, H. Nakatsuji, M. Caricato, X. Li, H. P. Hratchian, A. F. Izmaylov, J. Bloino, G. Zheng, J. L. Sonnenberg, M. Hada, M. Ehara, K. Toyota, R. Fukuda, J. Hasegawa, M. Ishida, T. Nakajima, Y. Honda, O. Kitao, H. Nakai, T. Vreven, J. A. Montgomery Jr., J. E. Peralta, F. Ogliaro, M. J. Bearpark, J. Heyd, E. N. Brothers, K. N. Kudin, V. N. Staroverov, R. Kobayashi, J. Normand, K. Raghavachari, A. P. Rendell, J. C. Burant, S. S. Iyengar, J. Tomasi, M. Cossi, N. Rega, N. J. Millam, M. Klene, J. E. Knox, J. B. Cross, V. Bakken, C. Adamo, J. Jaramillo, R. Gomperts, R. E. Stratmann, O. Yazyev, A. J. Austin, R. Cammi, C. Pomelli, J. W. Ochterski, R. L. Martin, K. Morokuma, V. G. Zakrzewski, G. A. Voth, P. Salvador, J. J. Dannenberg, S. Dapprich, A. D. Daniels, O¨. Farkas, J. B. Foresman, J. V. Ortiz, J. Cioslowski and D. J. Fox. *Gaussian 09, Revision A.02* **2009**.

(15) Jewett, A. I.; Zhuang, Z.; Shea, J.-E. Moltemplate a coarse-grained model assembly tool. *Biophys. J.* **2013**, *104*, 169a.

(16) Hanwell, M. D.; Curtis, D. E.; Lonie, D. C.; Vandermeersch, T.; Zurek, E.; Hutchison, G. R. Avogadro: an advanced semantic chemical editor, visualization, and analysis platform. *Journal of cheminformatics* **2012**, *4*, 17.

(17) Schneider, T.; Stoll, E. Molecular-dynamics study of a three-dimensional one-component model for distortive phase transitions. *Phys. Rev. B* **1978**, *17*, 1302.

(18) Berendsen, H. J.; Postma, J. v.; van Gunsteren, W. F.; DiNola, A.; Haak, J. R. Molecular dynamics with coupling to an external bath. *The Journal of chemical physics* **1984**, *81*, 3684-3690.

(19) Ding, W.; Palaiokostas, M.; Wang, W.; Orsi, M. Effects of lipid composition on bilayer membranes quantified by all-atom molecular dynamics. *The Journal of Physical Chemistry B* **2015**, *119*, 15263-15274.

(20) Hockney, R. W.; Eastwood, J. W.: *Computer simulation using particles*; crc Press, 1988.

(21) Kästner, J. Umbrella sampling. *WIREs Comput Mol Sci* **2011**, *1*, 932-942.

(22) Souaille, M.; Roux, B. t. Extension to the weighted histogram analysis method: combining umbrella sampling with free energy calculations. *Comput. Phys. Commun.* **2001**, *135*, 40-57.

(23) Kumar, S.; Rosenberg, J. M.; Bouzida, D.; Swendsen, R. H.; Kollman, P. A. The weighted histogram analysis method for free-energy calculations on biomolecules. I. The method. *J. Comput. Chem.* **1992**, *13*, 1011-1021.

Appendix B. Supplementary Material for Chapter 3

B.1. Lipid Synthesis, Concentration Determination, and Liposome Size Distributions

The 1,2-dioleoyl-sn-glycero-3phospho-(1'rac-glycerol) (DOPG) lipid synthesis protocol has been reported previously.[1-3] For determination of the lipid concentration, perchloric acid was used to convert phospholipids to inorganic phosphates. The addition of ammonium molybdate in an acidic condition leads to the formation of phosphor-molybdic acid, which was then reduced by Fiske-Subbarow reducer, producing a blue solution for absorbance measurements at 800 nm. Absorption measurements were done using a UV−vis spectrometer from PerkinElmer, Boston, MA, U.S.A. The calibration curve for the Bartlett assay, as shown in Figure B1, is fit with a linear equation with a slope of 0.00300 ± 0.00004, a *y*-intercept of −0.002 ± 0.003, and an R^2 value of 0.999 for the fit. The dynamic light scattering (DLS) size distribution is shown in Figure B2 with a size of 137 ± 42 nm and a polydispersity index of 0.07 for the DOPG liposomes in 5 mM citrate buffer with pH 4.0. The molecular structure of DOPG is shown in Figure B3.

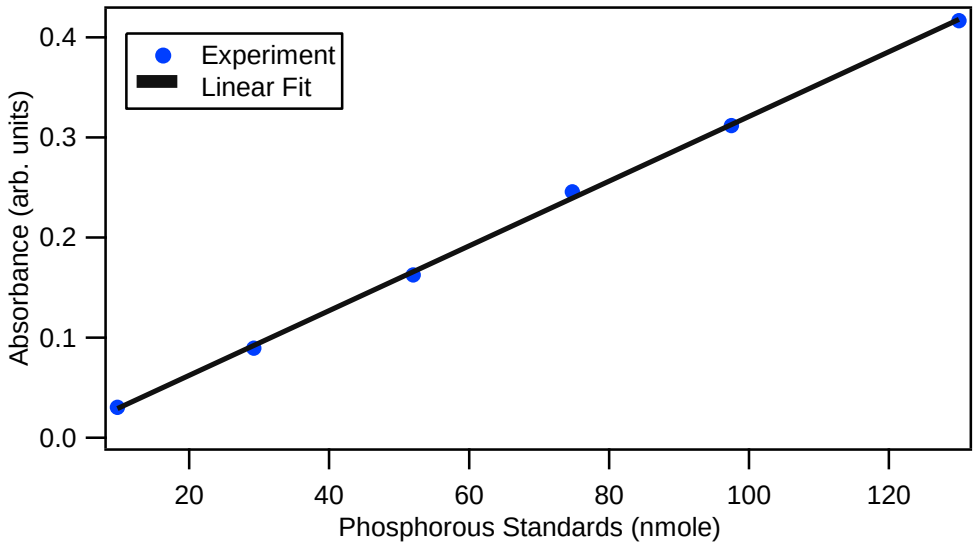

Figure B.1. Bartlett assay calibration for determining the lipid concentration.

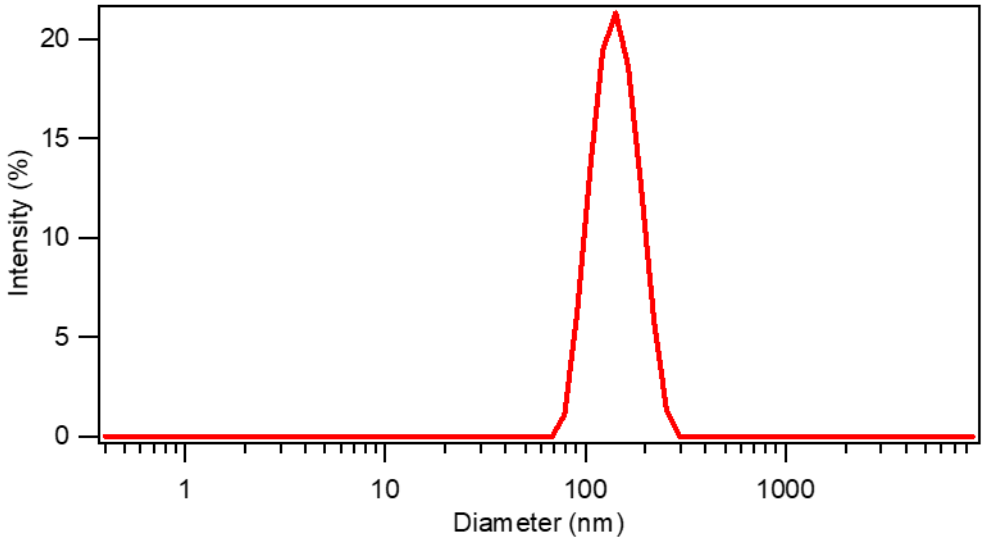

Figure B.2. Size distribution measured by DLS for the DOPG liposome sample.

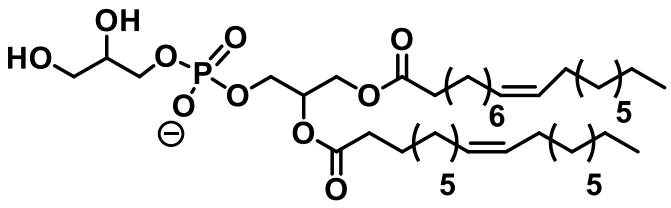

Figure B.3. Molecular structure of DOPG.

B.2. Additional Details on SHG Measurements of Molecular Interactions with Liposomes

Representative second harmonic generation (SHG) spectra of the liposome and malachite green (MG) samples are shown in Figure B4a. The SHG spectrum of the DOPG liposomes upon addition of 15 μM MG at 25 °C at 50 μM lipid concentration in 5.0 mM citrate buffer of pH 4.0 shows a strong SHG signal centered at 400 nm with a full width at half maximum of 4.5 nm. The small signal at wavelengths greater than 410 nm is due to two-photon fluorescence from MG,[2,4] and is clearly separated spectroscopically from the SHG signal. The SHG intensity is enhanced by approximately 2.5 times in comparison to the hyper-Raleigh scattering (HRS) signal generated from free dye molecules alone,[5,6] confirming molecular adsorption of MG to the liposome surface. In contrast, the SHG signal from the liposomes alone is much lower, in agreement with our previous studies.[2,3] For a direct comparison, all SHG intensities are normalized with respect to the DOPG liposomes upon addition of 15 μM MG at 25 °C. Figure B4b displays the SHG spectra of DOPG liposomes immediately after the addition of 15 μM MG under different temperatures ranging from 25 °C to 40 °C. The SHG intensity is found to decrease as temperature is increased, which is primarily attributed to the change in the orientational

distribution of the dipole moment of the adsorbed MG dye molecules at the liposome interface,[7] as discussed in greater detail in the Chapter 3 and later in this Appendix using results obtained from molecular dynamics (MD) simulations.

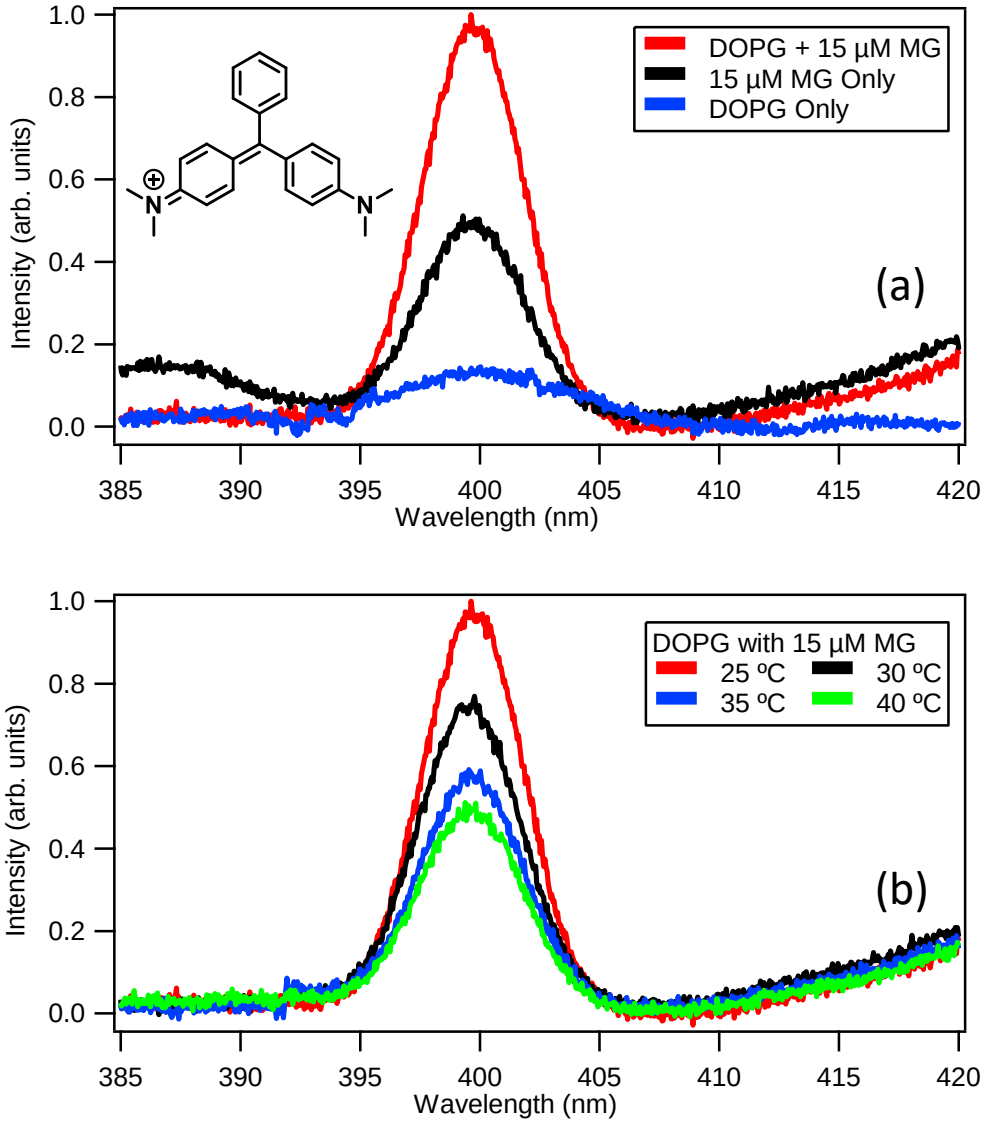

Figure B.4. (a) SHG spectra of DOPG liposomes in the presence of 0 μM and 15 μM MG compared to 15 μM MG alone. Inset shows MG molecular structure. (b) SHG spectra of DOPG liposomes immediately upon the addition of 15 μM MG at different temperatures. All samples are in 5.0 mM citrate buffer at pH 4.0.

The determined rate constants (τ^{-1}) for different temperatures are plotted as a function of MG concentration at different temperatures, as shown in Figure B5, with corresponding linear fits for each temperature. The slopes of obtained rate constants from Figure B5 are plotted as a function of temperature and are displayed in Figure B7. The transport times are also tabulated in Table B1. The HRS intensities obtained for different MG concentrations in 5 mM citrate buffer with pH 4.0 at 25 °C and 40 °C are shown in Figure B6 with corresponding linear fits. The HRS signal is from incoherent second-order scattering which arises from orientational and density fluctuations of molecules in the bulk solutions.[5] The HRS signal has the same spectra as the SHG signals, centered at 400 nm, and the same data acquisition and analysis procedures are used.

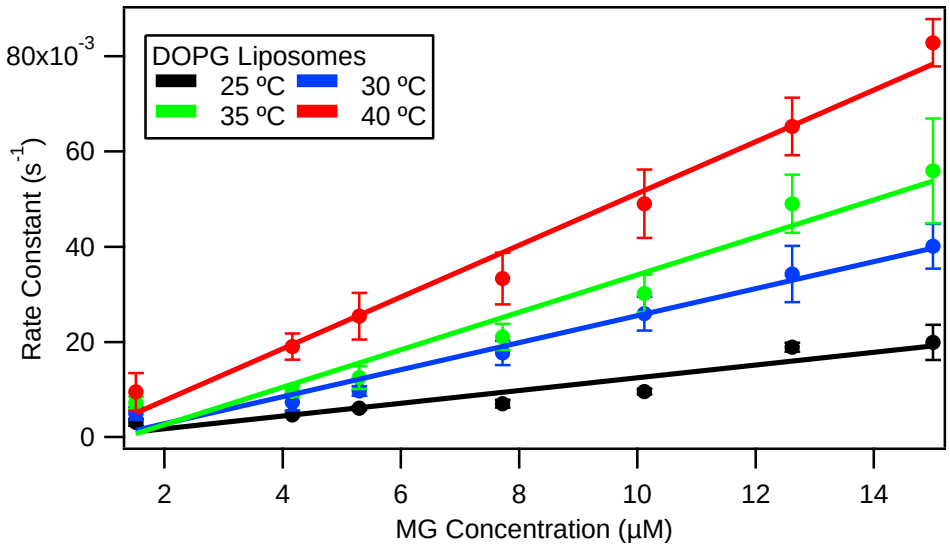

Figure B.5. Variation of the transport rate constant as a function of MG concentration for DOPG liposomes in 5.0 mM citrate buffer of pH 4.0 at different temperatures with corresponding linear fits.

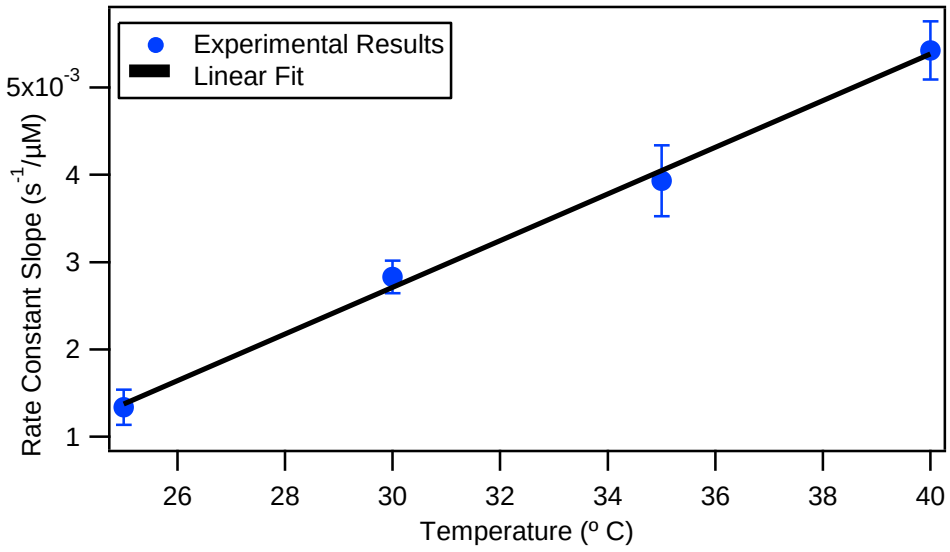

Figure B.6. Variation of the rate constant slope as a function of temperature (blue circles) with a linear fit (black line).

Table B1: Transport times of MG in DOPG liposomes at different temperatures

Transport Time (s)				
MG (μM)	**25 °C**	**30 °C**	**35 °C**	**40 °C**
1.51	311 ± 72	199 ± 54	137 ± 23	104 ± 43
4.16	213 ± 11	134 ± 31	103 ± 12	52 ± 7
5.30	163 ± 11	102 ± 10	79 ± 15	39 ± 7
7.72	141 ± 15	56 ± 8	47 ± 6	29 ± 4
10.12	104 ± 6	38 ± 5	33 ± 4	20 ± 2
12.62	52 ± 2	29 ± 5	20 ± 2	15 ± 1
15.00	50 ± 9	24 ± 3	17 ± 3	12 ± 1

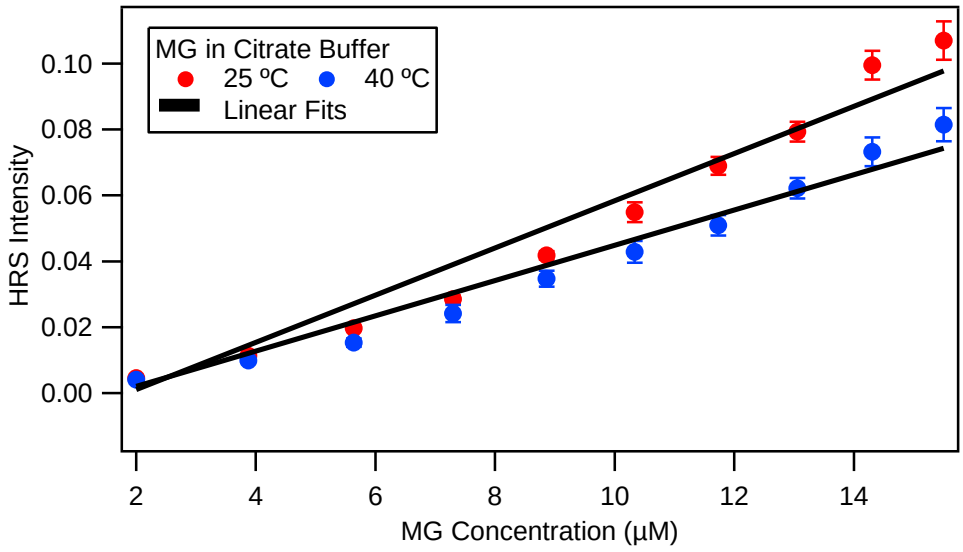

Figure B.7. HRS signal intensity of citrate buffer as a function of added MG concentration (blue and red circles) compared to linear fits (black lines) at 25 °C and 40 °C, respectively.

B.3. Second harmonic generation studies of colloidal polystyrene sulfate particles

Adsorption isotherms for MG adsorbing to the surface of polystyrene sulfate (PSS) microspheres in aqueous colloidal suspension are determined using SHG measurements for comparison to the liposome results presented in the manuscript. These results demonstrate the general applicability of temperature-dependent SHG adsorption isotherm measurements for determining enthalpy and entropy, while also providing relevant comparisons to the results from the DOPG liposomes. The PSS microspheres of diameter 1.06 ± 0.03 μm are purchased from Polysciences and are diluted in nanopure water to a concentration of 1.8×10^{10} particles/mL. The experimental setup is the same as the one used for the liposome measurements, with the same data analysis procedure. The adsorption of MG to polystyrene sulfate particles (PSSPs) in water is driven by the electrostatic force between the positively-charged amine group of MG and the negatively-charged sulfate group at the PSSP surface.[8,9] The SHG adsorption isotherms for this

system are studied as a function of temperature, with the results shown in Figure B8 for temperatures of 20 °C, 30 °C, 40 °C, 50 °C, and 60 °C. The experimentally obtained isotherms are fit using the modified Langmuir model, as described previously. The fitting parameters obtained from the modified Langmuir fits are listed in Table B2. The obtained equilibrium constant is a measure of the electrostatic interaction between the charged dye and microparticle interface. However, the value of the equilibrium constant does not change to within the experimental uncertainty for the temperature range studied here. The obtained adsorption equilibrium constants for 20 °C, 30 °C, 40 °C, 50 °C, and 60 °C are (2.37 ± 0.32) × 10^9, (1.9 ± 0.53) × 10^9, (2.49 ± 0.32) × 10^9, (2.81 ± 0.32) × 10^9, and (2.27 ± 0.54) × 10^9, respectively. In comparison to the liposome results presented in the manuscript, the obtained adsorption equilibrium constants are larger in magnitude indicating a stronger interaction between MG and PSSPs, in agreement with the previous studies.[3,10]

The free energy of adsorption, obtained from $\Delta G = -RT \ln K$, is plotted as a function of temperature, as shown in Figure B9. Here, the results are fit to a line with $\Delta G = \Delta H - T\Delta S$ to provide the thermodynamic properties of the molecular adsorption, where ΔH is the change in adsorption enthalpy, ΔS is the change in adsorption entropy, and T is the temperature. The calculated ΔH from the y-intercept is 0.45 ± 1.00 kcal/mol, indicating that the net change in adsorption enthalpy is approximately zero to within experimental uncertainty. The calculated ΔS from the linear slope is 0.044 ± 0.003 kcal/K·mol. This change in entropy is a full accounting of the adsorption process, including the change in entropy of the adsorbate molecules and the solvated microparticle surface. The adsorption process is described by free dye molecules adsorbing to “empty” adsorption

sites, which are then converted to “filled” adsorption sites.[2,4,11] The molecular adsorption of the MG adsorbates alone should have negative entropy as these MG molecules are more ordered when adsorbed to the nanoparticle surface. However, the adsorbate MG molecules are replacing water molecules and counterions that were originally at the nanoparticle surface. Since each MG adsorbate molecule will replace numerous water molecules and counterions due to their relative sizes, an overall increase of entropy occurs upon adsorption, when given a full account. For this particular case, where ΔH is approximately equal to zero to within the experimental uncertainty, the overall condition is $\Delta G \approx -T\Delta S$, so the molecular adsorption process is expected to be spontaneous at all aqueous temperatures.

The obtained values of N_{max} from the temperature-dependent SHG adsorption isotherms are 0.027 ± 0.001 μM, 0.070 ± 0.001 μM, 0.138 ± 0.016 μM, 0.162 ± 0.002 μM, and 0.237 ± 0.028 μM for 20 °C, 30 °C 40 °C, 50 °C, and 60 °C, respectively. The N_{max} values all increase with increasing temperature. This trend is in agreement with the liposomes results as well. It is important to point out that in comparison to PSSPs, liposomes systems are more complicated as both adsorption and transport takes place. Additionally, the N_{max} values increase approximately 10-fold as the temperature is increased from 20 °C to 60 °C indicating that the PSSP double layer is more susceptible to temperature changes than the lipid bilayer. As temperature increases, the collision frequency of MG and counterions at the surface increase. This may result in increased ion-pairing and decreased adsorbate-adsorbate repulsion as the temperature increases, leading to larger N_{max} values. The SHG intensities at the plateau region also increase as the temperature increases due to these larger N_{max} values. This trend is the opposite as

compared to results obtained with the liposomes, illustrating the importance of considering both N_{max} and orientation angle at the colloidal surface.

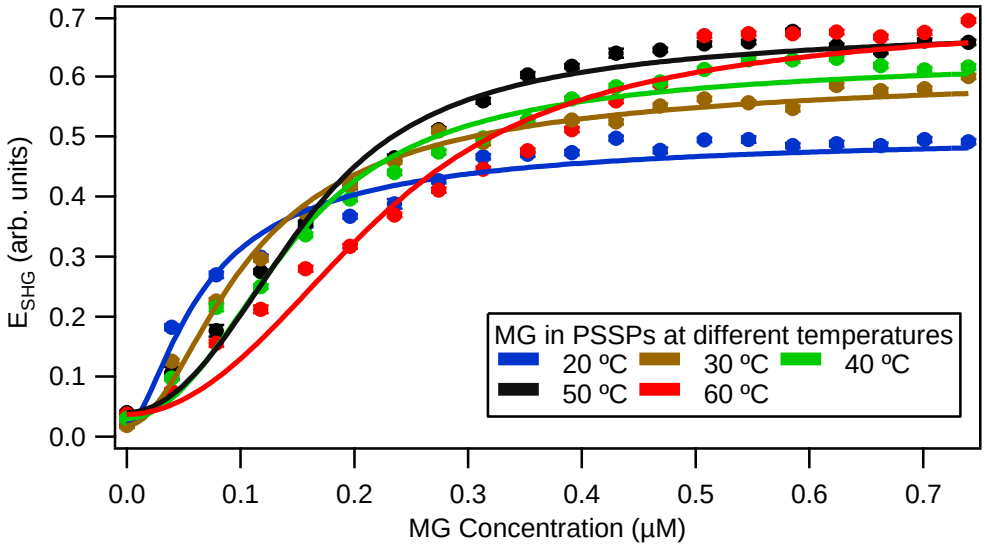

Figure B.8. SHG-determined adsorption isotherms for MG with PSSPs at different temperatures.

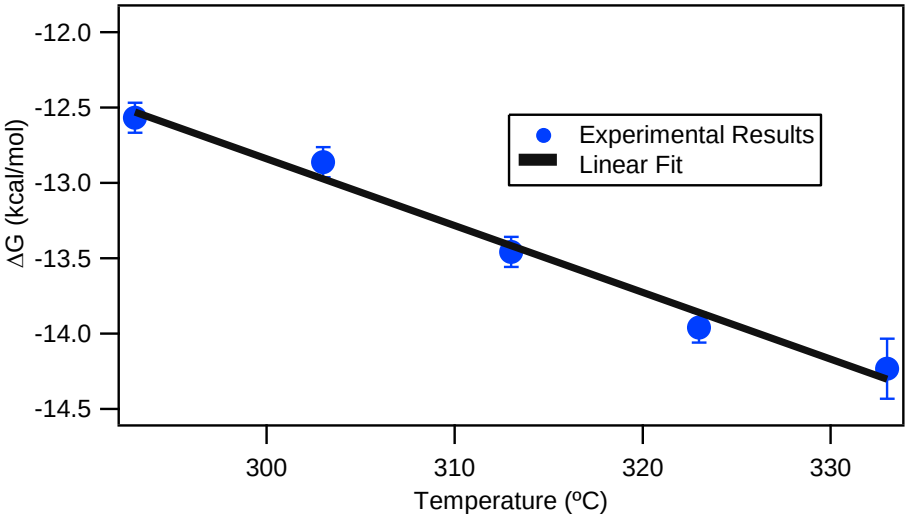

Figure B.9. Adsorption free energy for MG to the PSSPs surface in water under varying temperature.

Table B2. List of Variables and Fitting Parameters Obtained from the Modified Langmuir Isotherm Model for MG to PSSPs at Different Temperatures

Temperature		K (10^9)	N_{max} (μM)	-ΔG (kcal/mol)
293 K	20°C	2.37 ± 0.32	0.027 ± 0.001	12.6 ± 0.1
303 K	30°C	1.90 ± 0.53	0.070 ± 0.001	12.8 ± 0.1
313 K	40°C	2.49 ± 0.37	0.138 ± 0.016	13.4 ± 0.1
323 K	50°C	2.81 ± 0.33	0.162 ± 0.002	13.9 ± 0.1
333 K	60°C	2.27 ± 0.54	0.237 ± 0.028	14.2 ± 0.2

B.4. Additional details on estimating counterion concentrations

Using the Gouy-Chapman model, the relative percentage change of the citrate counterion concentration near the surface of the liposome is approximated at different temperatures.[12,13] Here, the citrate counterion concentration is calculated as a function of distance and is integrated from 0 A (the surface) to 20 A, as a reasonable estimate for the distance where ion-pairing with MG can occur near the liposome surface. The Debye length is approximated using the equation $k^{-1} = \sqrt{\frac{\epsilon_r \epsilon_0 k_B T}{2000 N_A I e^2}}$, where ϵ_r is the dielectric constant of water, ϵ_0 is the permittivity of free space, k_B is the Boltzmann constant, T is the bulk temperature, N_A is Avogadro's number, I is the ionic strength of 5 mM citrate buffer, and e is the elementary charge. Using this equation, the Debye length is calculated to be approximately 2.0 nm. Additionally, the potential is determined from 0 to 20 A using the equation, $\Phi_x = \Phi_0 e^{-kx}$,where Φ_0 is the potential at the surface, Φ_x is the distance dependent potential, k^{-1} is the debye length, and x is the distance from the surface. The zeta potential for our liposome sample is measured to be −70 mV. For this approximation,

the potential at the surface is assumed to be more negative than the measured zeta potential, with Φ_0 = −80 mV. The obtained potentials are used to determine the change in counterion concentration as a function of distance using the equation $Q_v(x) = F\Sigma z_j c_j e^{(-\frac{z_j F \Phi_x}{RT})}$,where Q_v is the volume charge density, F is Faraday's Constant, z_j is the charge of the j^{th} ion, c_j is the bulk concentration of the j^{th} ion, and R is the universal gas constant. Using these equations, we determine that there is a 13% increase in citrate counterion concentration over this distance range as the bulk temperature increases from 25 °C to 40 °C. This result is in general agreement with our observations from adsorption isotherm experiments where increased N_{max} values were attributed to increased counterion pairing at higher temperatures. Increased counterion pairing will decrease adsorbate-adsorbate repulsions leading to larger N_{max} values.

B.4. Molecular Dynamics Simulations Details

The initial lipid bilayer with 72 DOPG molecules is built using the CHARMM-GUI Membrane Builder[14,15] followed by the solvation of the system with 6075 SPC/E[16] water molecules and 72 K^+ ions to neutralize the system charge using the Packmol[17] software package. The partial charges of the optimized structures are calculated by the RESP fitting technique[18,19] using the HF/6-31G* method in Gaussian 09 suite of programs.[20] The initial box dimensions of the system are 57.0 Å × 60.0 Å × 124.0 Å. The Moltemplate[21] package is used to generate the input files for the molecular dynamics simulations. Using the LAMMPS program (version 05 Sep 2014)[22] molecular dynamics simulations are carried out with the all-atom general AMBER force field (GAFF)[23] at a temperature of 303 K. In order to equilibrate the system, an initial energy minimization followed by a 5 ns simulation in the isothermal-isobaric (NPT) ensemble and then a 10 ns simulation in the

canonical (NVT) ensemble are performed. The system is then replicated along the x-axis. This elongated system is further simulated for 5 ns in the canonical (NVT) ensemble making the final simulation box dimension approximately 94.5 Å × 50.0 Å × 112.0 Å.

The next steps of the simulation process are to introduce the MG molecule to the pre-equilibrated DOPG system followed by equilibration of the system at the two different temperatures. For this purpose the MG molecule is built using the Avogardo[24] package and the structure optimization and the partial charge calculations (by the RESP fitting technique[18,19]) are performed using the Gaussian 09[20] suite of programs with the HF/6-31G* method. The MG molecule is then added to a vacuum layer of length 15 Å in the z-direction of the pre-equilibrated DOPG membrane system. This system is then simulated at two different temperatures (303 K and 313 K). For each system, equilibration simulations in the isothermal-isobaric (NPT) ensemble for 5 ns and in the canonical (NVT) ensemble for 10 ns are performed. The final simulation box dimensions are approximately 94.5 Å × 50.0 Å × 115.0 Å for the system simulated at 303 K and 94.0 Å × 50.0 Å × 117.5 Å for the system simulated at 313 K. A simulation for another total of 10 ns follows these simulations. To maintain the temperatures at 303 K and 313 K, the Langevin thermostat[25] with a collision frequency of 1 ps^{-1} is applied. The pressure of the system is controlled semi-isotropically (only along the z-component of the system) which has been used previously by by Mario Orsi et al.[26] at 1 atm, using the Berendsen barostat[27] with a damping time of 1 ps and an isothermal compressibility of 4.6 × 10^{-5} atm^{-1} in both simulations. Periodic boundary conditions with the SHAKE algorithm are used for these simulations for the water molecules to restrain the structure of the water molecules. Electrostatic interactions are calculated using the particle-particle particle-mesh (PPPM)[28]

method and the non-bonded Lennard-Jones interactions are cutoff beyond 10 Å. A 1 fs time step is used for both the simulations at the two temperatures.

In order to obtain the free energy profile of the adsorption process of the MG molecule on to the DOPG membrane at the two different temperatures, an enhanced sampling technique, namely the umbrella sampling method,[29] is used. The final structures from the canonical simulations performed before are used as the starting configurations for the umbrella sampling windows. For these umbrella sampling simulations, the distance in the z-direction between the center of mass (COM) of the MG molecule and the COM of the DOPG membrane is used as the collective variable. For each system, 32 umbrella sampling windows (each with 18 ns) are simulated, with a step-size of 1.5 Å and a harmonic force constant of 3 kcal/mol. To derive the potential of mean force (free energy) from the umbrella sampling simulations, the weighted histogram analysis (WHAM)[30,31] method is used. For this process, only the last 14 ns of each umbrella sampling window is used. Using the block averaging method with 3.5 ns of simulation time for each block, the statistical error with the potential of mean force is calculated. The average surface of the DOPG membrane is determined using the average z-coordinates of the oxygen atom of each DOPG's furthest hydroxyl group on one side of the membrane. In addition, the change in the normalized water number density is used to determine the membrane-water interface. For this analysis the umbrella sampling window when the COM of the MG molecule is approximately 25 Å away from the average membrane surface is used. In order to obtain the water number density, the number of water molecules in a water layer with 1 Å thickness in the z-direction is counted and binned.

B.5. Canonical Simulations

Prior to the umbrella sampling simulations, 20 ns of canonical simulations are performed. Figure B10 shows the distance in the z-direction between the COM of the MG molecule and the COM of the DOPG membrane for the canonical simulations for the two different temperatures. The average surface of the DOPG membrane is determined using the average z-coordinates of the oxygen atom of each DOPG's furthest hydroxyl group on one side of the membrane and the interfacial region is determined using the normalized water number density.

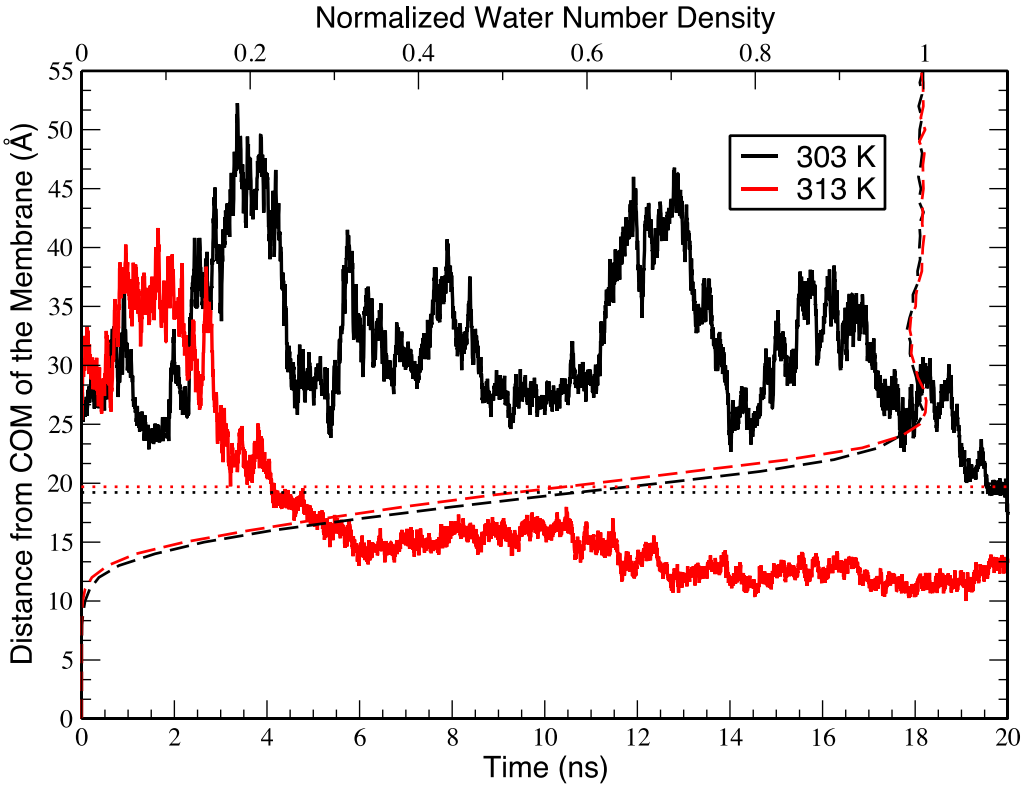

Figure B.10. The distance in the z-direction between the COM of the MG molecule and the COM of the DOPG membrane for 303 K and 313 K temperature for the canonical simulations. The horizontal dotted lines represent the average interface for 303 K (black) and 313 K (red). The dashed lines represent the normalized water number density for 303 K (black) and 313 K (red).

According to results in Figure B10, the MG molecule gets adsorbed more rapidly to the DOPG membrane at the higher temperature compared to the lower temperature simulation. Figure S11 shows a representative snapshot of the MG molecule adsorbed on to the DOPG membrane during the canonical simulation under 313 K temperature. The MG molecule at the lower temperature takes much longer to reach the interface and does not readily penetrate the membrane, unlike in the higher temperature case. This indicates that the higher energy barrier at the lower temperature simulation hinders the adsorption process of the MG molecule as compared to the higher temperature simulation.

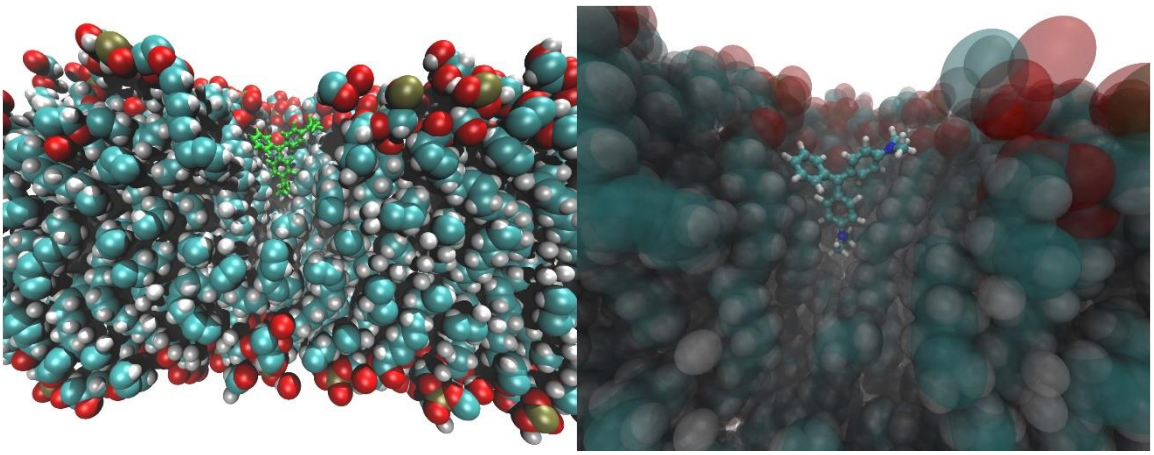

Figure B11. A representative snapshot of the MG molecule adsorbed on to the DOPG membrane during the canonical simulation under 313 K temperature (on the left) and the zoomed-in view of the snapshot. (on the right)

B.6. Orientation Calculations

In order to gain a molecular level understanding of the change of SHG intensities at different temperatures, the orientation angle θ (Figure B12a) between the dipole moment vector V_d of the MG molecule and the vector normal to the membrane surface V_s

pointing to the solvent side, with the MG molecule at different distances in the z-direction from the COM of the membrane is calculated. The results from this analysis is shown in Figure B12. This specific type of orientational distribution has been used to gain an understanding of molecular ordering at interfaces in previous MD studies.[32] Figure B12b shows that the dipole vector of the MG molecule always forms a narrow distribution at an angle greater than 90°, with the two amine groups of the MG molecule directed towards the membrane, at the lower temperature. This demonstrates that the orientation of the MG molecule is well ordered at the aqueous solution-membrane interface at the lower temperature, thereby enhancing the intensity of the SHG signal. In contrast, at the higher temperature, the angular distribution is much broader with a wider range of angles indicating a less-ordered interfacial structure due to the weakened interaction between the MG and the DOPG molecules, as shown in Figure B12c. This contributes to the lower observed SHG intensity at higher temperatures. The MD simulations are also used to study the displacement of the water solvent molecules caused by the MG molecular adsorption, as explained in greater detail in the section below. According to the results shown in Figure B13, approximately 50 – 70 water molecules are displaced when MG adsorbs to the DOPG membrane at both 303 K and 313 K. This is also in agreement with the SHG experimental results, where a positive change in entropy is observed due to adsorption from a large number of interfacial water molecules being displaced from every singular MG molecular adsorption event that occurs.

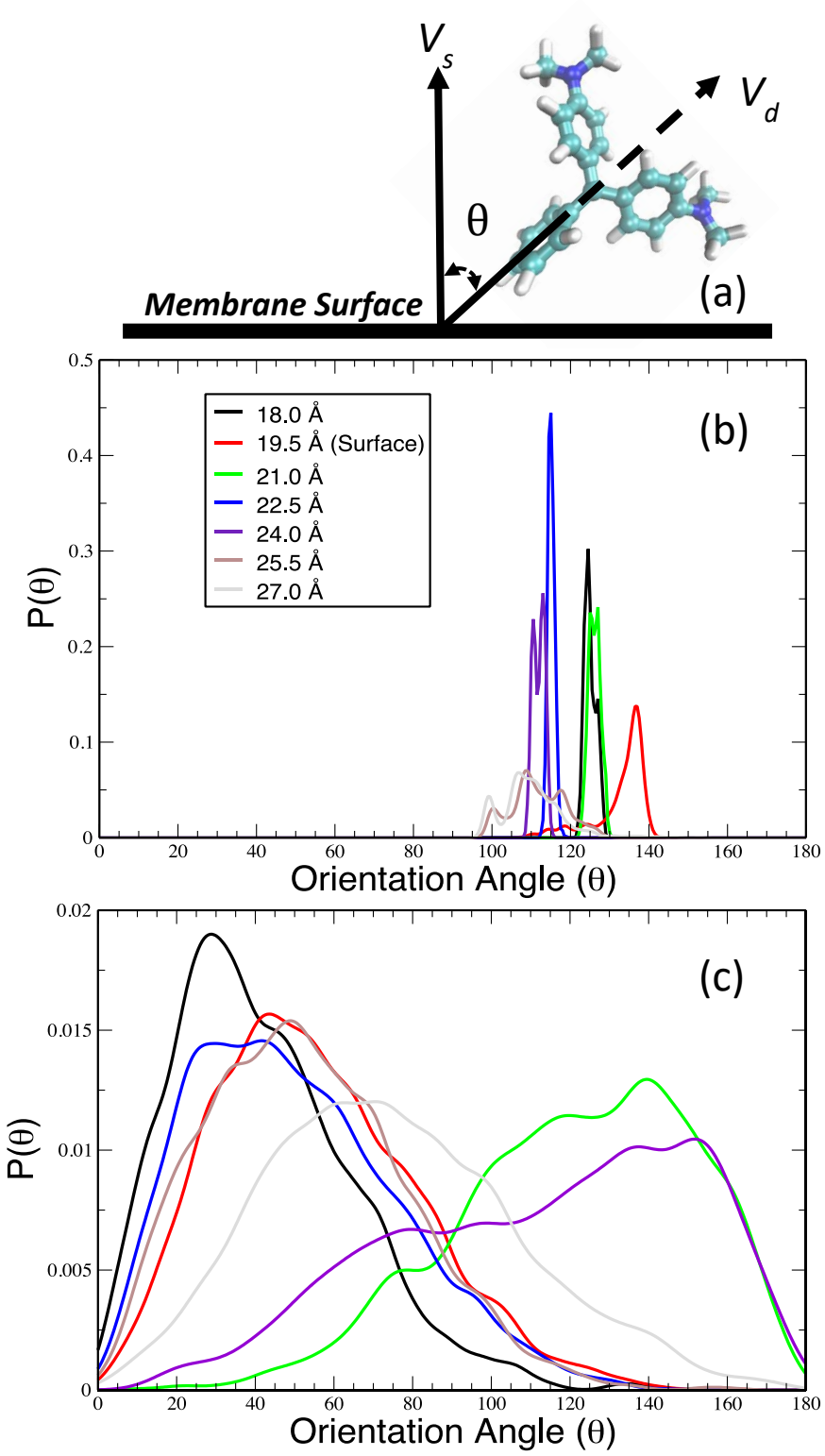

Figure B12. (a) Definition of the orientation angle θ of MG. V_d is the dipole vector of the MG molecule, and V_s is the vector normal to the DOPG membrane surface, pointing in the direction of the solvent side. The probability distribution of the angle θ for different umbrella sampling windows at (b) 303 K and (c) 313 K. The legend in (b) indicates the distance in the z-direction between the COM of the DOPG membrane and the COM of the MG molecule for both (b) and (c).

B.7. Water Displacement Calculations

In order to analyze the displacement of water molecules as the MG molecule adsorbs to the DOPG membrane, the change in the number of interfacial water molecules is calculated. This interfacial water layer is defined as the water molecules which are within 3.5 Å along the z-direction from the average surface of the membrane. The average surface of the DOPG membrane is determined using the z-coordinates of the oxygen atom of each DOPG's furthest hydroxyl group on one side of the membrane. Figure B13 shows the number of water molecules in the layer within 3.5 Å from the average surface of the membrane for different umbrella sampling windows calculated as a function of the separation in the z-direction between the MG molecule and COM of the membrane. According to these results, the number of water molecules decreases more rapidly at the higher temperature as the MG molecule approaches the membrane, as compared to the lower temperature case. This is consistent with the orientation angle distributions observed for the dye at two temperatures. For the higher temperature the orientation angle distribution is much broader and more random while it is more ordered in the lower temperature simulations. Since the dipole vector distribution is broader at higher temperature, the MG molecule clearly shows greater orientational variability during adsorption to the membrane, which results in more water molecules being displaced near the membrane surface at the higher temperature.

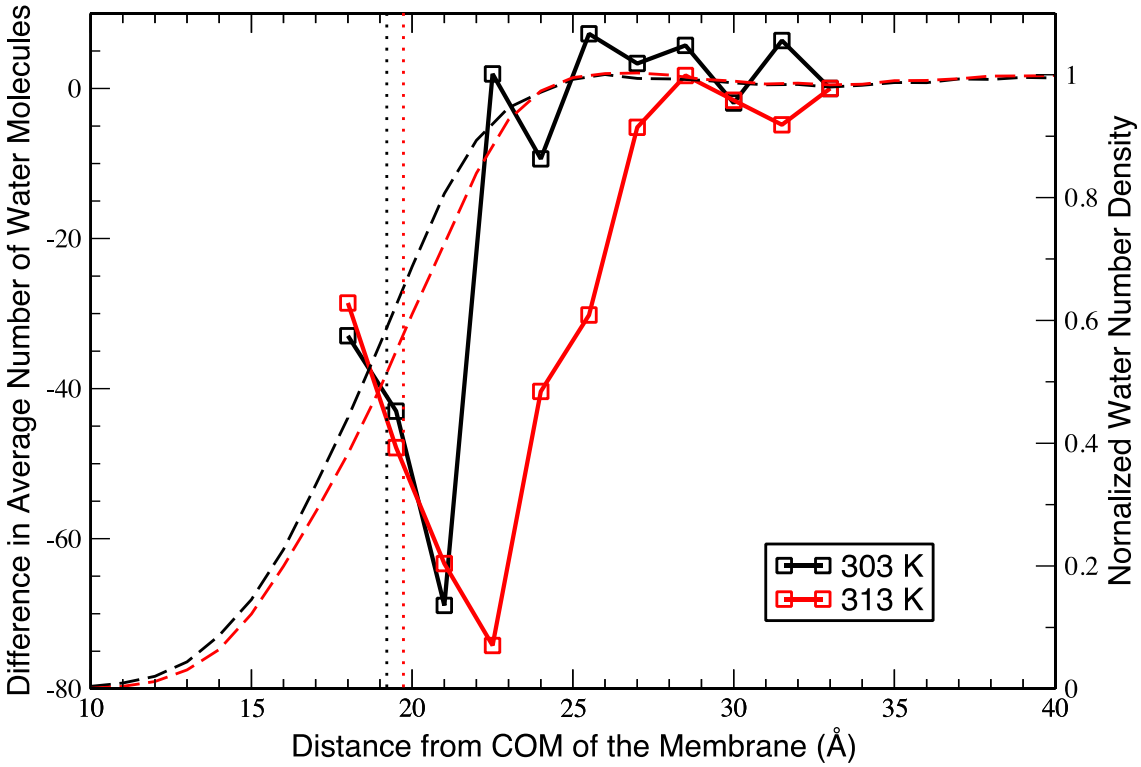

Figure B13. The number of water molecules in the first solvation layer of the membrane, when the MG molecule is at different separation distances in the z-direction from the COM of the DOPG membrane for temperatures of 303 K and 313 K. The vertical dotted lines represent the average interface for 303 K (black) and 313 K (red). The dashed lines represent the normalized water number density change for 303 K (black) and 313 K (red).

B.8. Error Analysis of Fits

The R^2-values obtained for time-dependent exponential fits of the SHG results from Figure 2 are summarized in Table B3. Similarly, the R^2-values obtained for the modified Langmuir fits of the SHG results for the liposomes and PSSPs are shown in Tables B4 and B5, respectively.

Table B3: R^2 values of time-dependent exponential fits of the SHG results

R^2-values of exponential fits				
MG (μM)	**25 °C**	**30 °C**	**35 °C**	**40 °C**
1.51	0.999	0.994	0.997	0.997
4.16	0.998	0.996	0.998	0.998
5.30	0.996	0.997	0.999	0.995
7.72	0.998	0.999	0.998	0.991
10.12	0.999	0.999	0.999	0.997
12.62	0.999	0.999	0.999	0.999
15.00	0.999	0.999	0.999	0.999

Table B4: R^2 values of modified Langmuir fits from SHG results for liposomes

Temperature	**25 °C**	**30 °C**	**35 °C**	**40 °C**
R^2 –value	0.989	0.993	0.995	0.989

Table B5: R^2 values of modified Langmuir fits from SHG results for PSSPs

Temperature	**20 °C**	**30 °C**	**40 °C**	**50 °C**	**60 °C**
R^2 –value	0.964	0.989	0.978	0.988	0.966

B.9. Notes

(1) Ong, W.; Yang, Y.; Cruciano, A. C.; McCarley, R. L. Redox-triggered contents release from liposomes. *J. Am. Chem. Soc.* **2008**, *130*, 14739-14744.

(2) Kumal, R. R.; Nguyenhuu, H.; Winter, J. E.; McCarley, R. L.; Haber, L. H. Impacts of Salt, Buffer, and Lipid Nature on Molecular Adsorption and Transport in Liposomes As Observed by Second Harmonic Generation. *J. Phys. Chem. C* **2017**, *121*, 15851-15860.

(3) Hamal, P.; Nguyenhuu, H.; Subasinghege Don, V.; Kumal, R. R.; Kumar, R.; McCarley, R. L.; Haber, L. H. Molecular Adsorption and Transport at Liposome Surfaces Studied by Molecular Dynamics Simulations and Second Harmonic Generation Spectroscopy. *J. Phys. Chem. B* **2019**, *123*, 7722-7730.

(4) Karam, T. E.; Haber, L. H. Molecular adsorption and resonance coupling at the colloidal gold nanoparticle interface. *J. Phys. Chem. C* **2014**, *118*, 642-649.

(5) Roke, S.; Gonella, G. Nonlinear light scattering and spectroscopy of particles and droplets in liquids. *Annu. Rev. Phys. Chem.* **2012**, *63*, 353-378.

(6) Rao, Y.; Guo, X.-m.; Tao, Y.-S.; Wang, H.-f. Observation of the direct S 2→ S 0 two-photon fluorescence between 370 and 480 nm and the hyperpolarizability of crystal violet (CV) from spectrally resolved hyper-Rayleigh scattering measurement. *J. Phys. Chem. A* **2004**, *108*, 7977-7982.

(7) Tran, R. J.; Sly, K. L.; Conboy, J. C. Applications of surface second harmonic generation in biological sensing. *Annu. Rev. Anal. Chem.* **2017**, *10*, 387-414.

(8) Wang, H.; Yan, E. C.; Liu, Y.; Eisenthal, K. B. Energetics and population of molecules at microscopic liquid and solid surfaces. *J. Phys. Chem. B* **1998**, *102*, 4446-4450.

(9) Gonella, G.; Dai, H.-L. Second harmonic light scattering from the surface of colloidal objects: theory and applications. *Langmuir* **2013**, *30*, 2588-2599.

(10) Zeng, J.; Eckenrode, H. M.; Dai, H.-L.; Wilhelm, M. J. Adsorption and transport of charged vs. neutral hydrophobic molecules at the membrane of murine erythroleukemia (MEL) cells. *Colloids Surf., B* **2015**, *127*, 122-129.

(11) Eisenthal, K. B. Second harmonic spectroscopy of aqueous nano-and microparticle interfaces. *Chem. Rev.* **2006**, *106*, 1462-1477.

(12) Kumal, R. R.; Karam, T. E.; Haber, L. H. Determination of the surface charge density of colloidal gold nanoparticles using second harmonic generation. *J. Phys. Chem. C* **2015**, *119*, 16200-16207.

(13) Yan, E. C.; Liu, Y.; Eisenthal, K. B. New method for determination of surface potential of microscopic particles by second harmonic generation. *J. Phys. Chem. B* **1998**, *102*, 6331-6336.

(14) Jo, S.; Kim, T.; Iyer, V. G.; Im, W. CHARMM-GUI: a web-based graphical user interface for CHARMM. *J. Comput. Chem.* **2008**, *29*, 1859-1865.
(15) Wu, E. L.; Cheng, X.; Jo, S.; Rui, H.; Song, K. C.; Dávila-Contreras, E. M.; Qi, Y.; Lee, J.; Monje-Galvan, V.; Venable, R. M. CHARMM-GUI membrane builder toward realistic biological membrane simulations. *J. Comput. Chem.* **2014**, *35*, 1997-2004.

(16) Berendsen, H.; Grigera, J.; Straatsma, T. The missing term in effective pair potentials. *J. Phys. Chem.* **1987**, *91*, 6269-6271.

(17) Martínez, L.; Andrade, R.; Birgin, E. G.; Martínez, J. M. PACKMOL: a package for building initial configurations for molecular dynamics simulations. *J. Comput. Chem.* **2009**, *30*, 2157-2164.

(18) Bayly, C. I.; Cieplak, P.; Cornell, W.; Kollman, P. A. A well-behaved electrostatic potential based method using charge restraints for deriving atomic charges: the RESP model. *J. Phys. Chem.* **1993**, *97*, 10269-10280.

(19) Cieplak, P.; Cornell, W. D.; Bayly, C.; Kollman, P. A. Application of the multimolecule and multiconformational RESP methodology to biopolymers: Charge derivation for DNA, RNA, and proteins. *J. Comput. Chem.* **1995**, *16*, 1357-1377.

(20) M. J. Frisch, G. W. T., H. B. Schlegel, G. E. Scuseria, M. A. Robb, J. R. Cheeseman, G. Scalmani, V. Barone, B. Mennucci, G. A. Petersson, H. Nakatsuji, M. Caricato, X. Li, H. P. Hratchian, A. F. Izmaylov, J. Bloino, G. Zheng, J. L. Sonnenberg, M. Hada, M. Ehara, K. Toyota, R. Fukuda, J. Hasegawa, M. Ishida, T. Nakajima, Y. Honda, O. Kitao, H. Nakai, T. Vreven, J. A. Montgomery Jr., J. E. Peralta, F. Ogliaro, M. J. Bearpark, J. Heyd, E. N. Brothers, K. N. Kudin, V. N. Staroverov, R. Kobayashi, J. Normand, K. Raghavachari, A. P. Rendell, J. C. Burant, S. S. Iyengar, J. Tomasi, M. Cossi, N. Rega, N. J. Millam, M. Klene, J. E. Knox, J. B. Cross, V. Bakken, C. Adamo, J. Jaramillo, R. Gomperts, R. E. Stratmann, O. Yazyev, A. J. Austin, R. Cammi, C. Pomelli, J. W. Ochterski, R. L. Martin, K. Morokuma, V. G. Zakrzewski, G. A. Voth, P. Salvador, J. J. Dannenberg, S. Dapprich, A. D. Daniels, O¨. Farkas, J. B. Foresman, J. V. Ortiz, J. Cioslowski and D. J. Fox. *Gaussian 09, Revision A.02* **2009**.

(21) Jewett, A. I.; Zhuang, Z.; Shea, J.-E. Moltemplate a coarse-grained model assembly tool. *Biophys. J.* **2013**, *104*, 169a.

(22) Plimpton, S. Fast parallel algorithms for short-range molecular dynamics. *J. Comput. Phys.* **1995**, *117*, 1-19.

(23) Wang, J.; Wolf, R. M.; Caldwell, J. W.; Kollman, P. A.; Case, D. A. Development and testing of a general amber force field. *J. Comput. Chem.* **2004**, *25*, 1157-1174.

(24) Hanwell, M. D.; Curtis, D. E.; Lonie, D. C.; Vandermeersch, T.; Zurek, E.; Hutchison, G. R. Avogadro: an advanced semantic chemical editor, visualization, and analysis platform. *Journal of cheminformatics* **2012**, *4*, 17.

(25) Schneider, T.; Stoll, E. Molecular-dynamics study of a three-dimensional one-component model for distortive phase transitions. *Phys. Rev. B* **1978**, *17*, 1302.

(26) Ding, W.; Palaiokostas, M.; Wang, W.; Orsi, M. Effects of lipid composition on bilayer membranes quantified by all-atom molecular dynamics. *The Journal of Physical Chemistry B* **2015**, *119*, 15263-15274.

(27) Berendsen, H. J.; Postma, J. v.; van Gunsteren, W. F.; DiNola, A.; Haak, J. R. Molecular dynamics with coupling to an external bath. *The Journal of chemical physics* **1984**, *81*, 3684-3690.

(28) Hockney, R. W.; Eastwood, J. W.: *Computer simulation using particles*; crc Press, 1988.

(29) Kästner, J. Umbrella sampling. *WIREs Comput Mol Sci* **2011**, *1*, 932-942.

(30) Souaille, M.; Roux, B. t. Extension to the weighted histogram analysis method: combining umbrella sampling with free energy calculations. *Comput. Phys. Commun.* **2001**, *135*, 40-57.

(31) Kumar, S.; Rosenberg, J. M.; Bouzida, D.; Swendsen, R. H.; Kollman, P. A. The weighted histogram analysis method for free-energy calculations on biomolecules. I. The method. *J. Comput. Chem.* **1992**, *13*, 1011-1021.

(32) Subasinghege Don, V.; David, R.; Du, P.; Milet, A.; Kumar, R. Interfacial Water at Graphene Oxide Surface: Ordered or Disordered? *J. Phys. Chem. B* **2019**, *123*, 1636-1649.

Appendix C. Supplementary Material for Chapter 4

C.1. Additional details on SHG microscopy experiments

Additional measurements of time-dependent second harmonic generation (SHG) microscopy for 0.1 μM malachite green isothiocyanate (MGITC) dye with fixed H596 cells are obtained and analyzed for determining the kinetics of adsorption and transport, with representative images displayed in Figure C.1. Here, the time-resolved results show that the peak SHG signal for this experiment is reached at approximately 55 minutes after adding the MGITC, in general agreement with the results presented in Chapter 4. The time-resolved SHG images are averaged over five regions of interest (ROIs), as shown in Figure C.2, and the signal decay after the maximum is fit to an exponential equation, as described in Chapter 4, to obtain the transport lifetime τ of 19 ± 1 minutes. This lifetime is in excellent agreement with the results shown in Chapter 4 for a different fixed cell using the same experimental conditions. As described in the Chapter, there is greater heterogeneity in SHG intensity over different ROIs in the fixed cells, which can be attributed to changes in lipid composition and a lack of membrane integrity that can lead to variations in dye adsorption and aggregation at different locations.

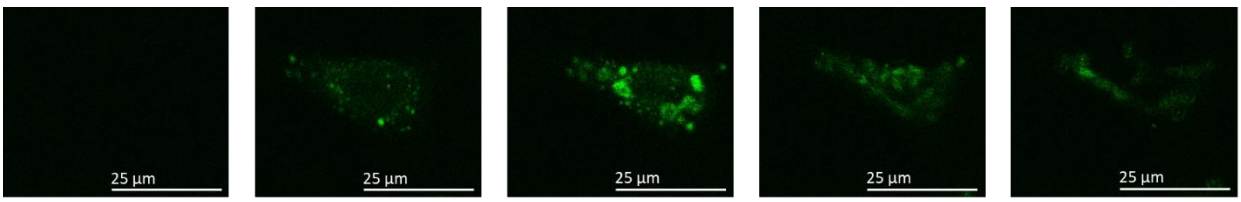

Figure C.1. Time-dependent images for 0.1 μM MGITC with fixed H596 cells.

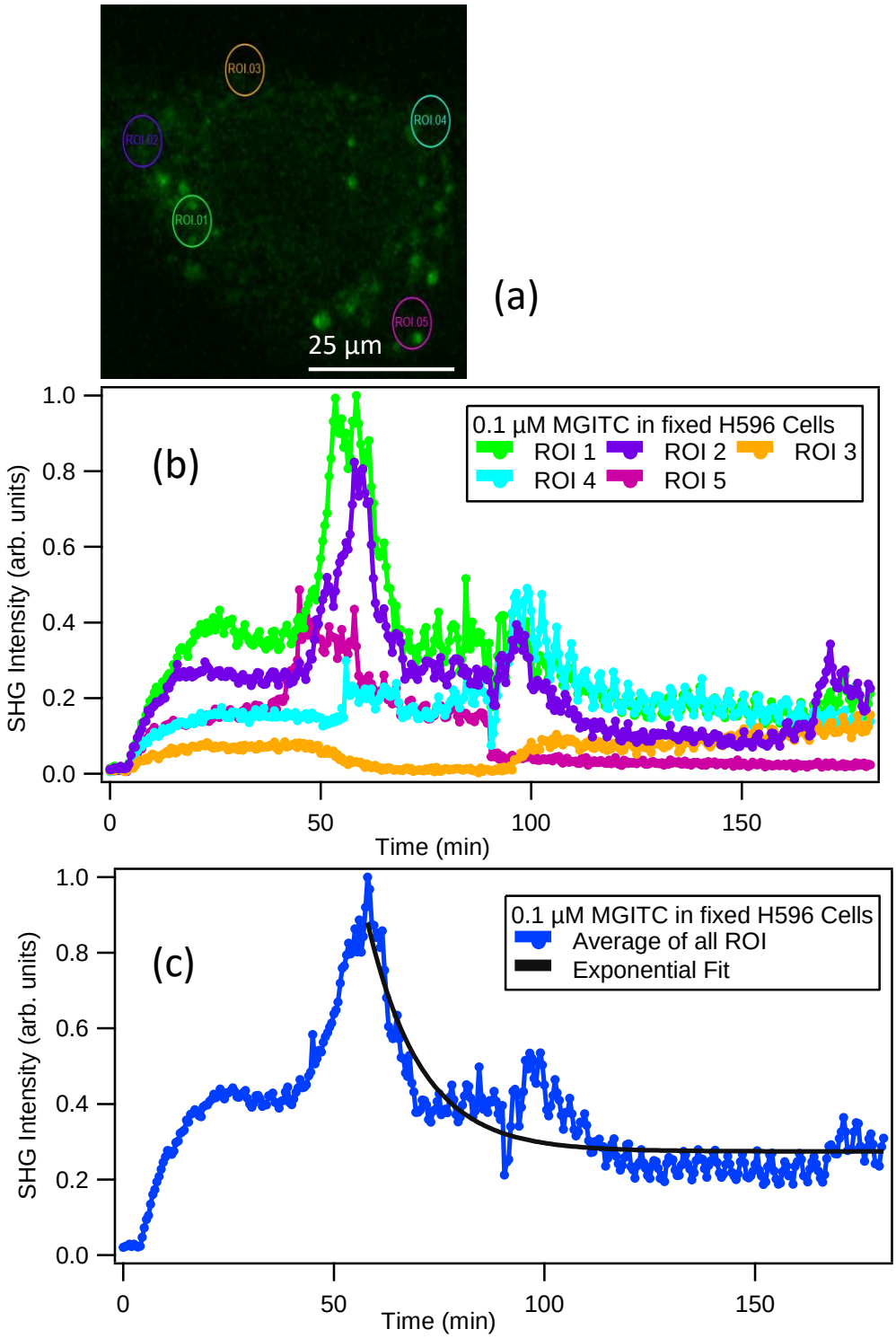

Figure C.2. (a) Representative zoomed SHG image for 0.1 μM MGITC added to fixed H596 cells at 57 minutes, showing different ROIs. Time profiles for molecular adsorption and transport for 0.1 μM MGITC added to fixed H596 cells at (b) different ROIs and (c) using the average of all ROIs. The solid black line is the best fit.

Interestingly, the SHG intensity time profiles for this experiment show that the signal does not go to zero at long times. This indicates a remaining difference in MGITC populations at the inner and outer membrane surface.

For additional analysis, the SHG time traces are also plotted for an individual ROI covering the entire cell. Figure C.3, and C.4 represents the SHG intensity profiles for 0.1 μM MGITC and 0.1 μM MG with living H596 cells, respectively. The ROIs in these experiments have areas of 12 x 13 μm^2 and 21 x 21 μm^2 for MGITC and MG, respectively. The oscillations in SHG intensity are very prominent even when the ROI covers the entire cell. Additionally, the results for 0.1 μM MGITC with fixed H596 cells are represented in Figure C.5 and C.6, respectively, with ROI areas of 63 x 12 μm^2 and 44 x 15 μm^2, respectively. The general trend for molecular adsorption and transport is observed for fixed cells as well; however, the SHG intensities have considerably less oscillations, in agreement with the observations described in Chapter 4.

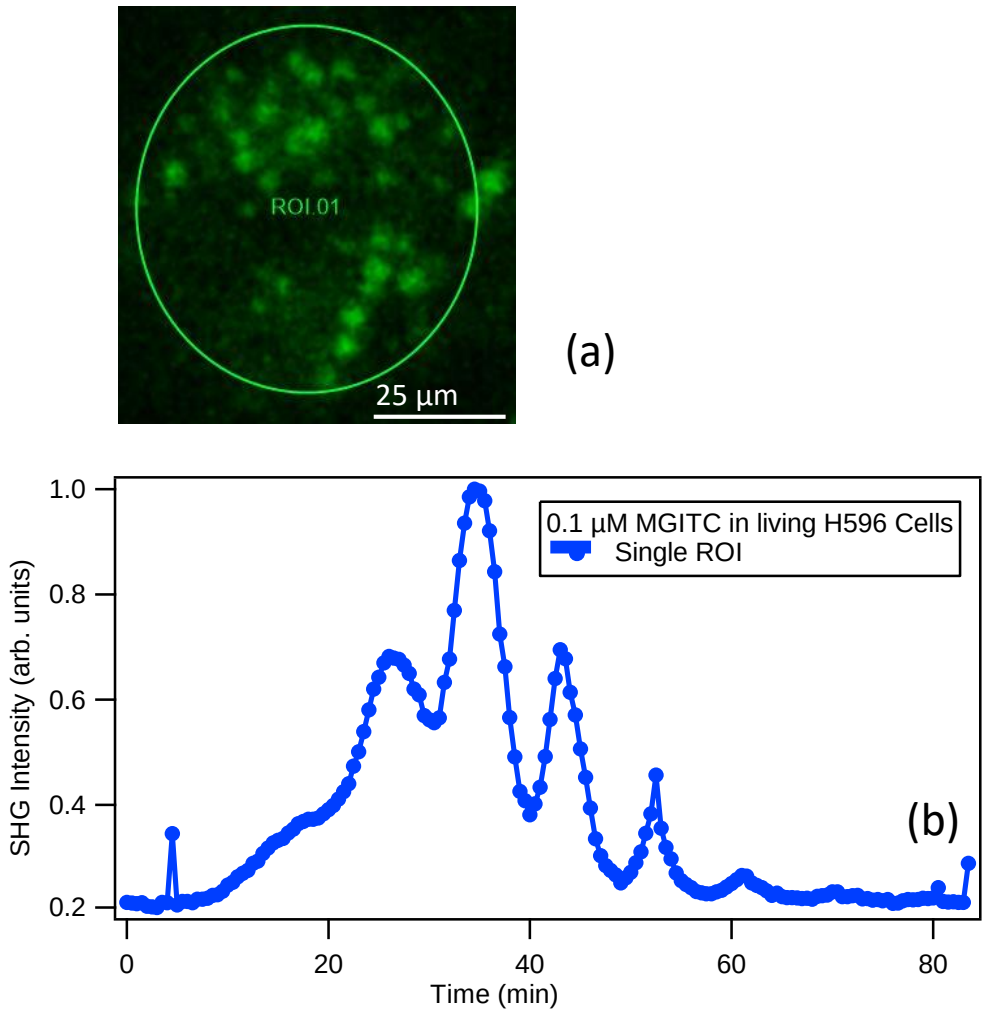

Figure C.3. (a) Representative zoomed SHG image for 0.1 μM MGITC added to living H596 cells at 34 minutes, showing a ROI covering the entire cell. (b) Time profiles for molecular adsorption and transport for 0.1 μM MGITC added to living H596 cells for this larger single-cell ROI.

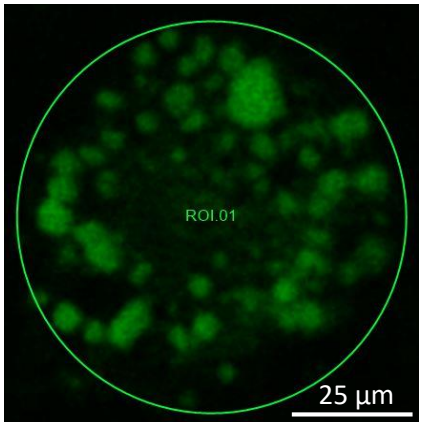

(a)

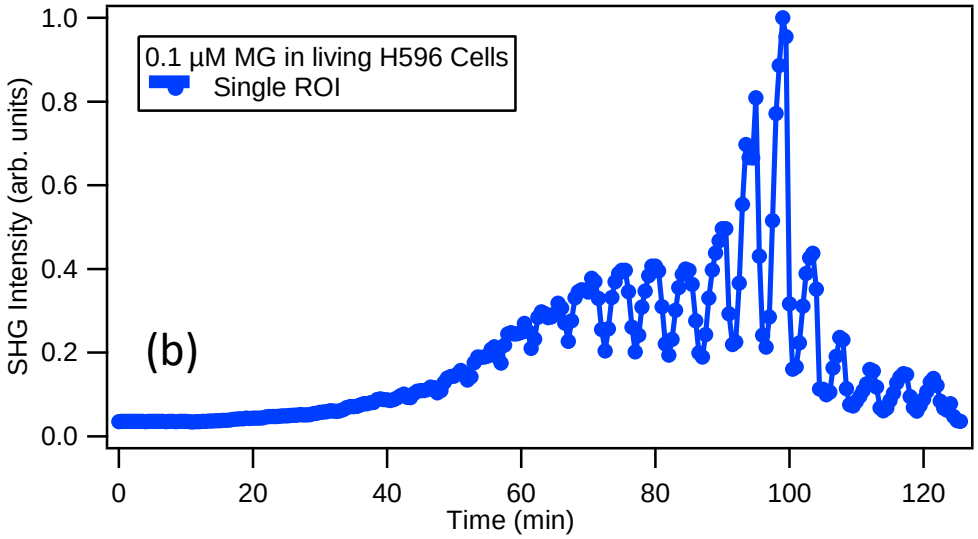

Figure C.4. (a) Representative zoomed SHG image for 0.1 μM MG added to living H596 cells at 75 minutes, showing a ROI covering the entire cell. (b) Time profiles for molecular adsorption and transport for 0.1 μM MG added to living H596 cells for this larger single-cell ROI.

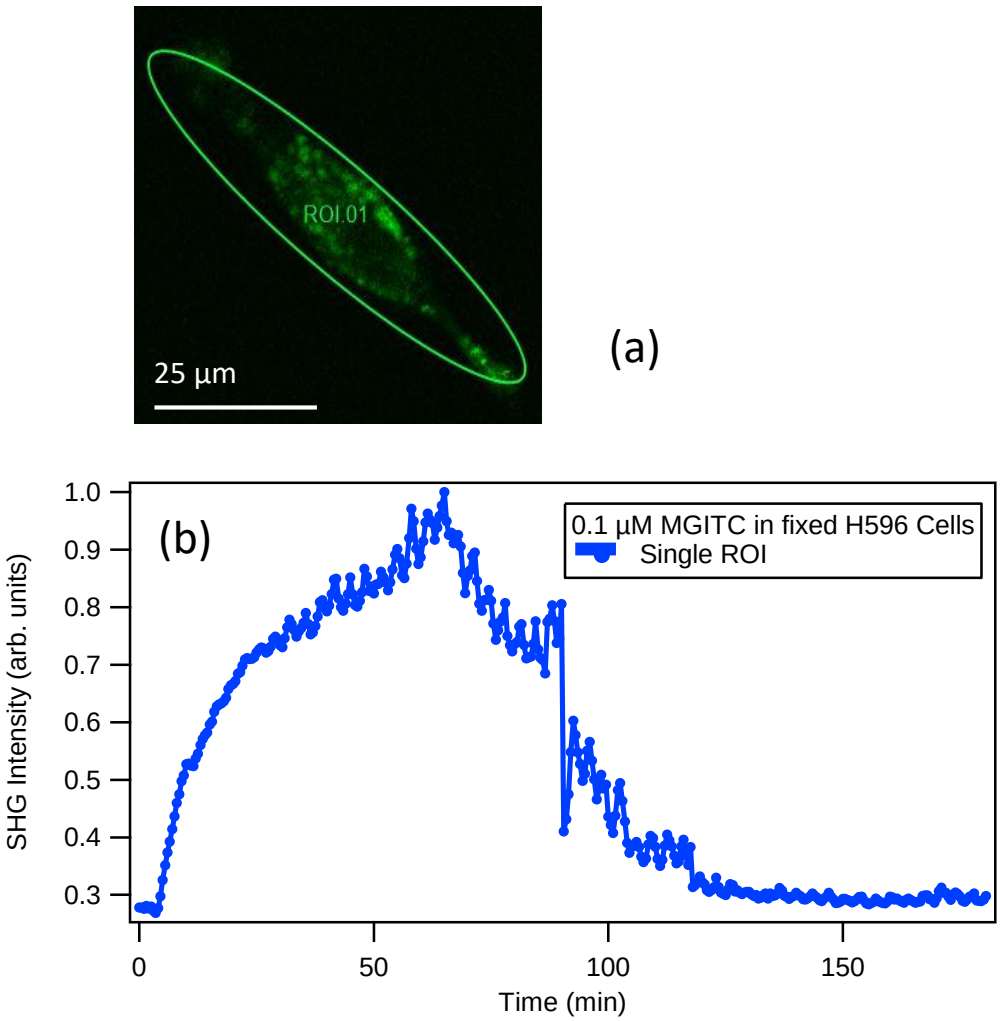

Figure C.5. (a) Representative zoomed SHG image for 0.1 μM MGITC added to fixed H596 cells at 55 minutes, showing a ROI covering the entire cell. (b) Time profiles for molecular adsorption and transport for 0.1 μM MGITC added to fixed H596 cells for this larger single-cell ROI.

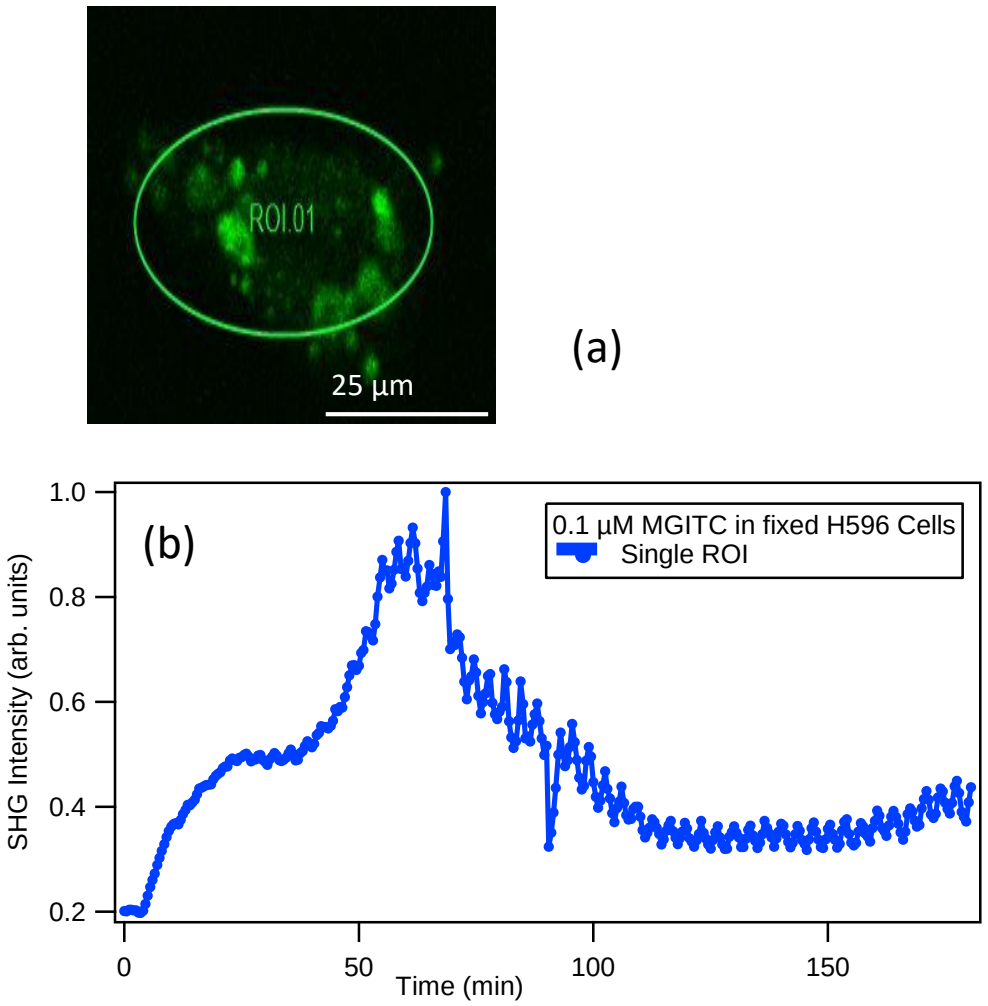

Figure C.6. (a) Representative zoomed SHG image for 0.1 μM MGITC added to fixed H596 cells at 55 minutes, showing ROI covering the entire cell. (b) Time profiles for molecular adsorption and transport for 0.1 μM MGITC added to fixed H596 cells for this larger single-cell ROI.

Figure C.7 shows SHG microscopy images for H596 cells only using the fundamental laser wavelength of 850 nm and 750 nm, respectively. Similarly, Figures C.8 displays SHG microscopy images for 4.0 μM MG dye only at different times. In both cases, the SHG intensities are very low and no time dependence in the SHG images are observed.

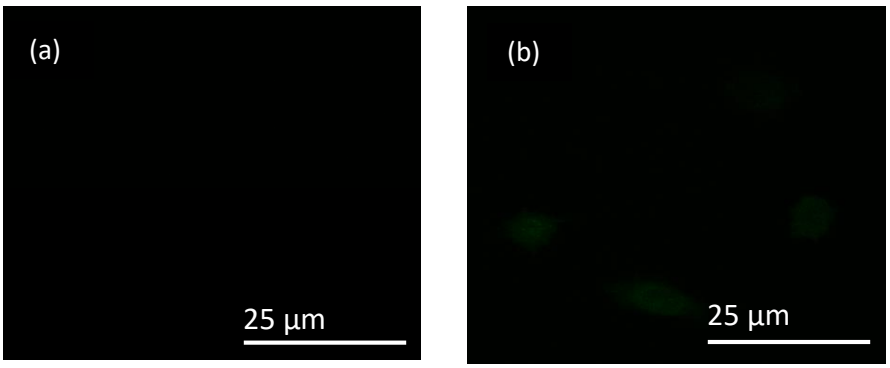

Figure C.7. SHG microscopy images for H596 cells only at (a) 850 nm and (b) 750 nm, respectively.

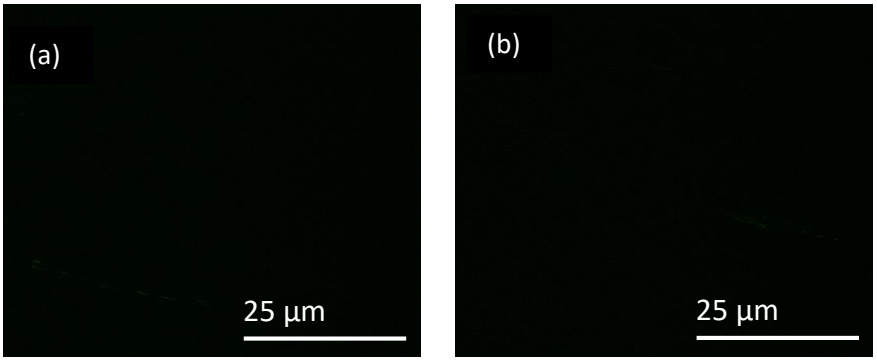

Figure C.8. SHG microscopy images for 4.0 μM MG dye only at (a) 5 min and (b) 8 min, respectively.

C.2. Cytotoxicity of Malachite Green

H596 cells are cultured in a 96 well plate at 15,000 cells/well and incubated overnight in the dark at 37 °C under 5% CO_2 and 95% air in a humidified incubator. After 24 hours, the wells are dosed with 2.8 mM, 1.4 mM, and 0.7 mM of malachite green (MG)

for 2 hours, 1 hour, and 30 minutes, respectively, with each concentration and time completed in triplicate for statistical analysis. After the cells are dosed with MG, 20 mL of CellTiter96®AQ$_{ueous}$ one solution reagent is added to each well containing 100 mL of culture medium. The plate is then incubated for 2 hours in the dark at 37°C under 5% CO_2 and 95% air in a humidified incubator. Following incubation, absorbance measurements are taken at 490 nm using an Eppendorf PlateReader AF2200 to determine the cell viability.[1]

Figure C.9. shows the cytotoxicity results for three different concentrations of MG dye. These concentrations are higher than the 0.1 μM concentration used in the SHG microscopy experiments. For 0.7 μM, we can observe that cell viability of MG approximately 100%, to within experimental uncertainty. These results indicate that the MG dye is not toxic for 2 hours under this concentration. However, the combination of the dye and the laser irradiation together may result in increased toxicity to these cells.

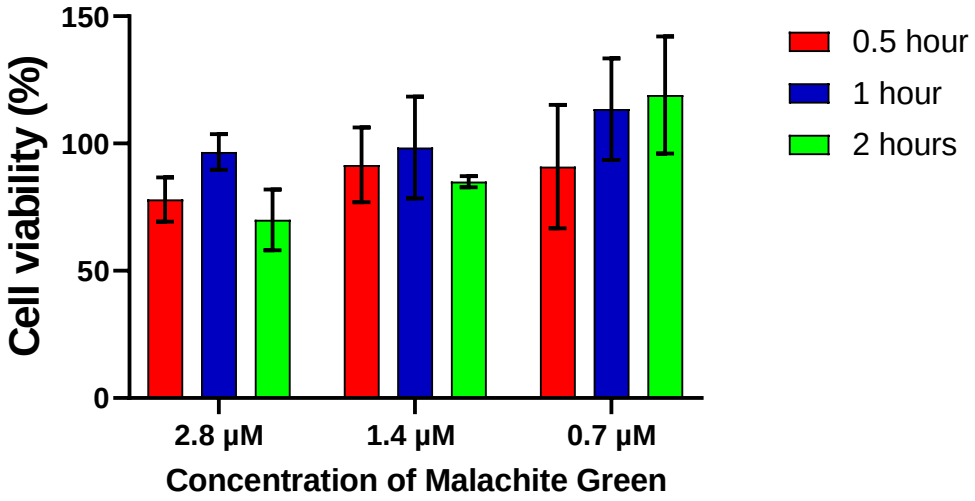

Figure C.9. Comparison of cytotoxicity percentage of H596 cells exposed to 2.8 μM, 1.4 μM, and 0.7 μM concentrations of malachite green over different times.

C.3. Error Analysis of Fits

The R^2-values obtained for time dependent exponential fits are summarized in Table S1.

Table S1: R^2-values of time-dependent exponential fits

Concentration of Dye	R^2-values
Experiment with living cell	
0.1 μM MG	0.900
0.1 μM MGITC	0.969
Experiment with fixed cell	
0.1 μM MGITC	0.978
0.1 μM MGITC	0.987

C.4. Notes

(1) Fontenete, S.; Leite, M.; Cappoen, D.; Santos, R.; Ginneken, C. V.; Figueiredo, C.; Wengel, J.; Cos, P.; Azevedo, N. F. Fluorescence in vivo hybridization (FIVH) for detection of Helicobacter pylori infection in a C57BL/6 mouse model. *PLoS One* **2016**, *11*, e0148353.

Appendix D. Supplementary Material for Chapter 5

D.1. Additional characterization for miRNA release

Figure D.1a. shows the zeta potentials of the nanoparticle samples at different light-emitting diode (LED) light energies at their respective plasmon wavelengths. To further investigate the extent of release at their plasmon wavelengths, fluorescence measurements of the released miRNA in the supernatant are taken after irradiation at 530 nm and 405 nm with increasing incident light exposure. These results are presented in Figure D.1b. In these samples, miR-21 on SNPs are tagged with Cy3 molecules, while miR-148b on GNPs are labelled with FAM. As shown, the photothermal release is achieved at each nanoparticle's plasmonic wavelength, while almost no release is observed upon reversal of the applied light wavelengths. Furthermore, at equal light energy outputs, the SNPs exhibits much more robust miRNA release as compared to the GNPs.

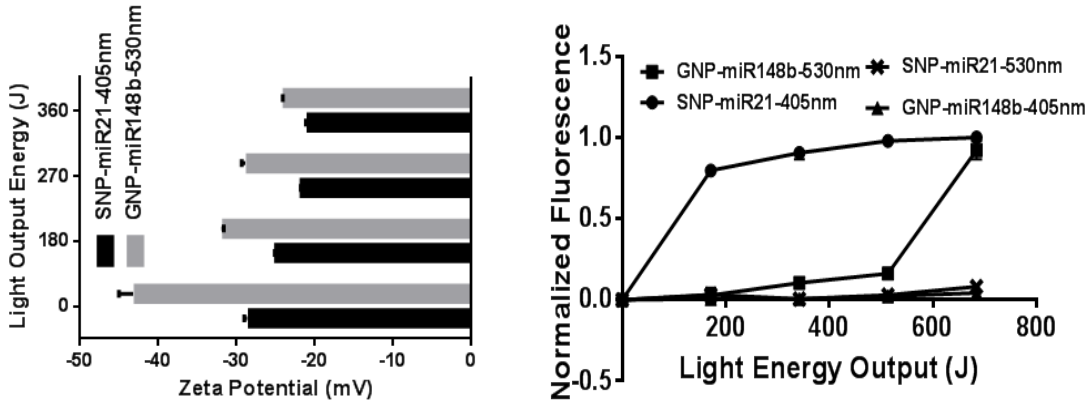

Figure D.1. (a) Zeta potential measurements of miRNA-nanoparticle conjugates for silver and gold surfaces with increasing doses of incident light. (b) Normalized fluorescence measurements of nanoparticle supernatant solutions, irradiated at 405 and 530 nm wavelengths. Gold nanoparticle surfaces in this experiment are modified with Diels-Alder linked miRNA mimic-FAM dye molecules, while silver nanoparticles are surface-modified similarly with Cy3-tagged dye molecules.

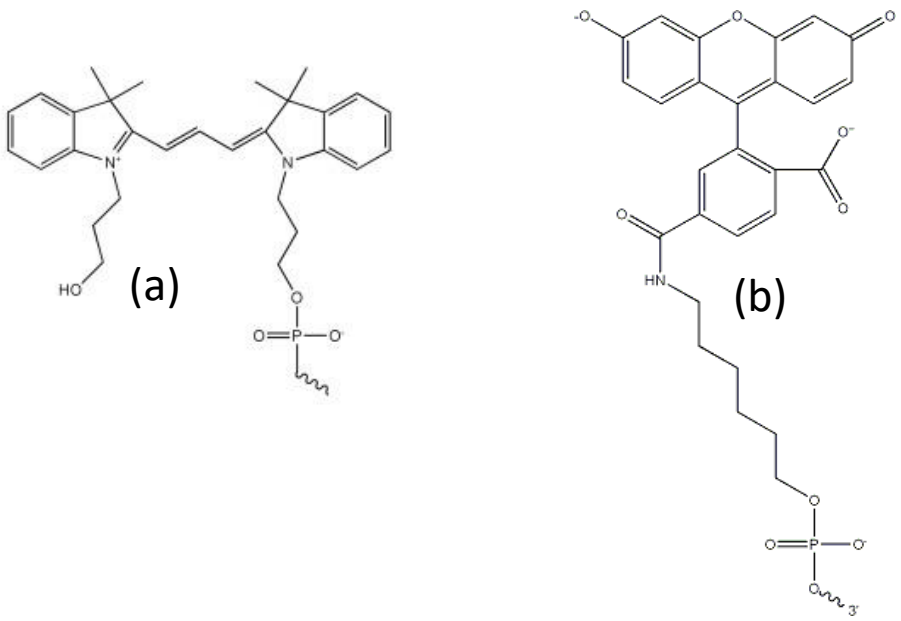

Figure D.2. Molecular structures of (a) Cy3 and (b) FAM molecules, respectively.[1,2]

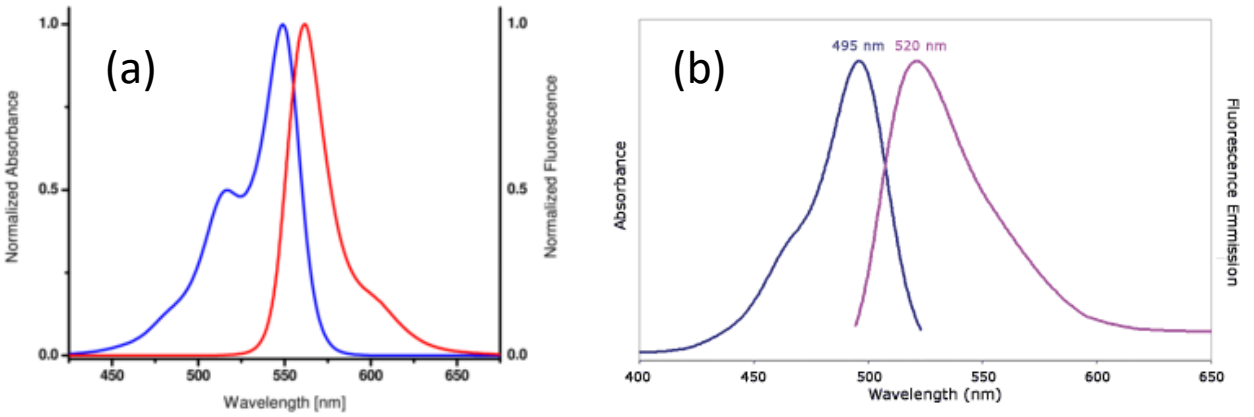

Figure D.3. Representative absorption and emission spectra's of (a) Cy3 and (b) FAM molecules.[1,2]

D.2. Additional Extinction Spectroscopy and Dynamic Light Scattering Measurements for Silver and Gold nanoparticles

The extinction spectra for miRNA-functionalized gold nanoparticles and miRNA-functionalized silver nanoparticles are shown in Figures D.4 and D.5, respectively. For both sets of nanoparticles, the extinction spectra has significant red-shifting upon miRNA functionalization. However, the extinction spectra are blue-shifted after irradiating the nanoparticles at their corresponding plasmon resonances. These results further indicate that the oligonucleotides have released from the surface of the gold and silver nanoparticles. The general trend obtained from extinction spectroscopy is in excellent agreement with the SHG observations shown in Chapter 4. Similarly, the nanoparticles functionalized with miRNA have larger hydrodynamic radii, as measured by dynamic light scattering, as shown in Figures D.6 and D.7, confirming the increase in size due to the added miRNA, which is in general agreement with our previous studies.[3-6]

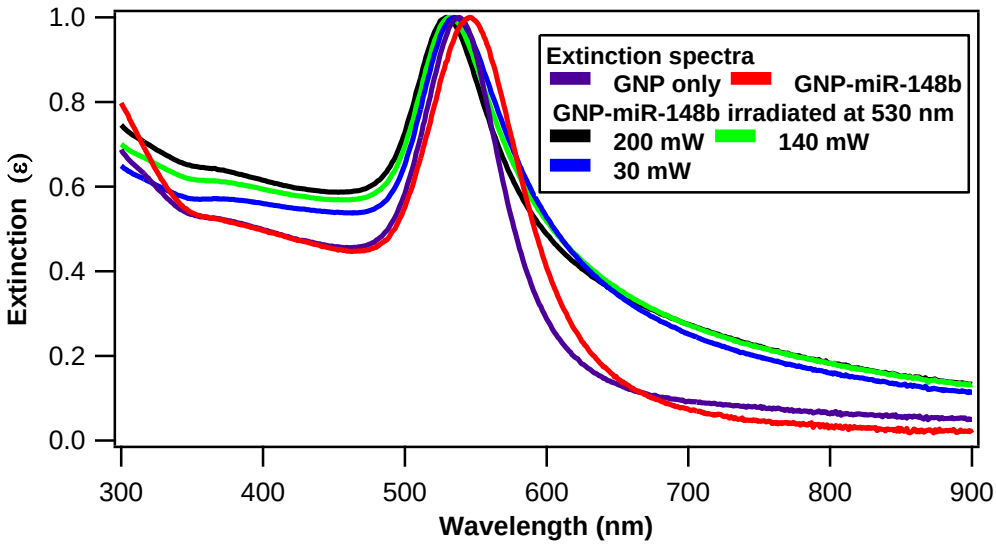

Figure D.4. Extinction spectra of the GNPS, the miRNA-functionalized GNPs, and the miRNA-functionalized GNPs after laser irradiation with 530 nm wavelength.

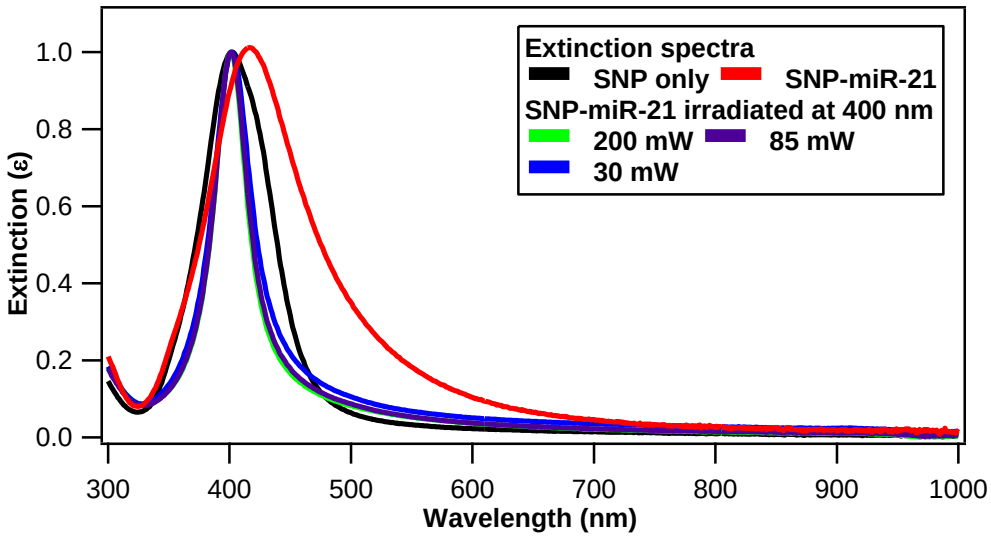

Figure D.5. Extinction spectra of the SNPs, the miRNA-functionalized SNPs, and the miRNA-functionalized SNPs after laser irradiation with 400 nm wavelength.

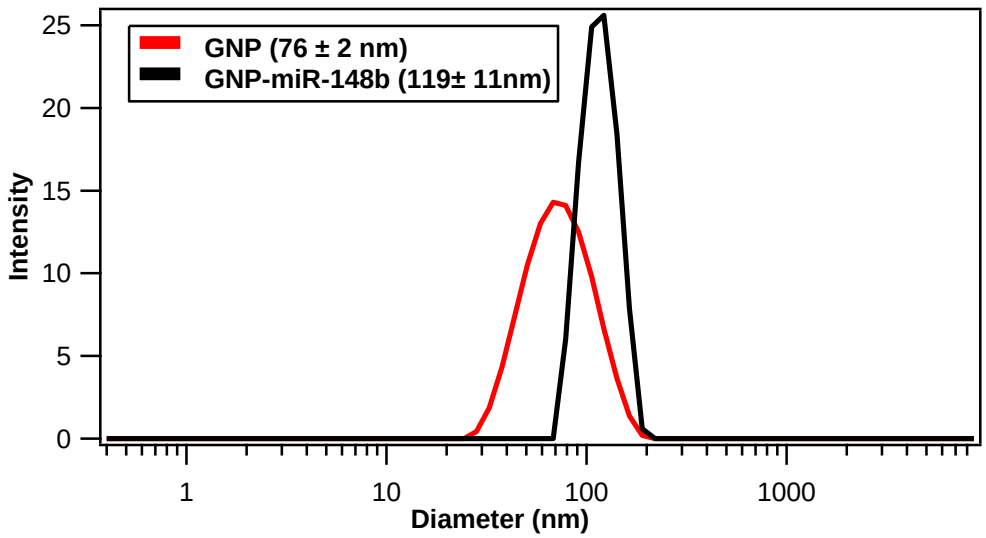

Figure D.6. Size distributions measured by dynamic light scattering for GNPs and the miRNA-functionalized GNPs.

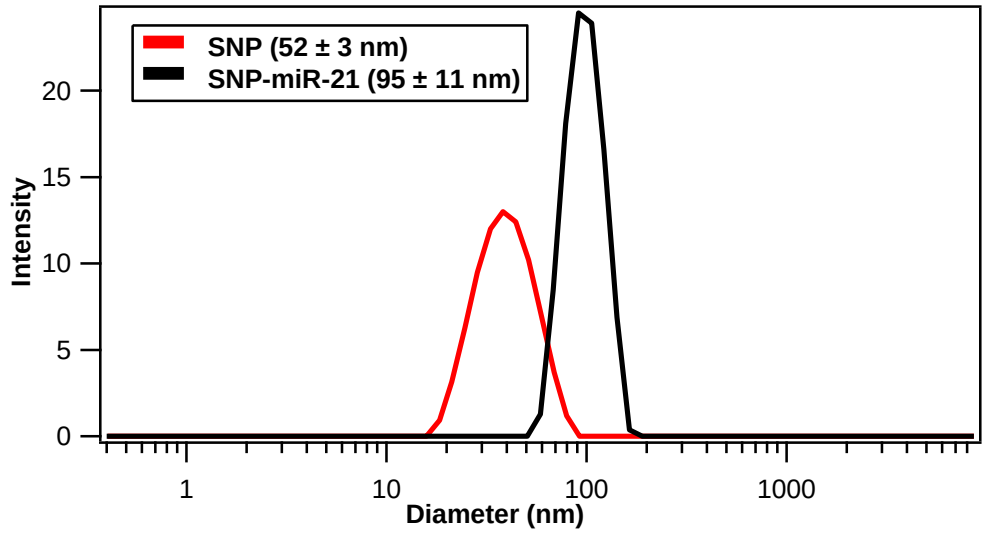

Figure D.7. Size distributions measured by dynamic light scattering for SNPs and the miRNA-functionalized SNPs.

The experimentally obtained SHG time-traces are fit with single exponential functions, as explained in Chapter 4. Tables D.1, D.2, and D.3 show the tabulated values for the fitting parameters for the silver, gold, and gold-silver-gold core-shell-shell nanoparticle systems, respectively.

Table D.1. Fit parameters obtained for the SNP-miR-21 nanoparticle system at different 400 nm laser powers

Power (mW)	Fit Parameters (SNP-miR-21)		
	A	B	k (10^{-2} s^{-1})
35	0.652 ± 0.001	0.353 ± 0.005	0.85 ± 0.02
85	0.603 ± 0.001	0.405 ± 0.005	1.23 ± 0.03
140	0.553 ± 0.001	0.432 ± 0.007	1.80 ± 0.05
200	0.504 ± 0.001	0.472 ± 0.012	2.67 ± 0.13

Table D.2. Fit parameters obtained for the GNP-miR-148b nanoparticle system at different 530 nm laser powers

Power (mW)	Fit Parameters (GNP-miR-148b)		
	A	B	k (10^{-2} s^{-1})
35	0.803 ± 0.001	0.188 ± 0.005	0.82 ± 0.04
85	0.754 ± 0.001	0.242 ± 0.006	1.03 ± 0.04
140	0.699 ± 0.001	0.298 ± 0.005	1.34 ± 0.04
200	0.635 ± 0.001	0.356 ± 0.008	2.04 ± 0.09

Table D.3. Fit parameters obtained for the CSS-miR-148b nanoparticle system at different 800 nm laser powers

Power (mW)	Fit Parameters (CSS-miR-148b)		
	A	B	k (10^{-2} s^{-1})
0	96.4 ± 2.3	4.3 ± 2.0	0.03 ± 0.15
20	65.4 ± 0.7	35.8 ± 1.1	0.78 ± 0.06
50	60.4 ± 0.5	41.9 ± 1.1	1.12 ± 0.06
100	52.2 ± 0.2	47.9 ± 0.6	1.77 ± 0.04
200	46.6 ± 0.3	54.0 ± 1.0	1.85 ± 0.06

D.3. In vitro photo-release of GNPs and SNPs using confocal imaging

Working in collaboration with Prof. Daniel Hayes and his research group at Penn State University, these miRNA-functionalized GNPs and miRNA-functionalized SNPs were used in confocal microscopy to investigate the photothermal release of the Diels-Alder linked and FAM-tagged oligonucleotides *in vitro* between the two sets of nanoparticles. The results are in general agreement with the SHG measurements where SNP shows higher release of FAM-tagged oligonucleotides. Figures D.6 and D.7 display the confocal imaging results obtained for two sets of nanoparticles at different wavelengths.

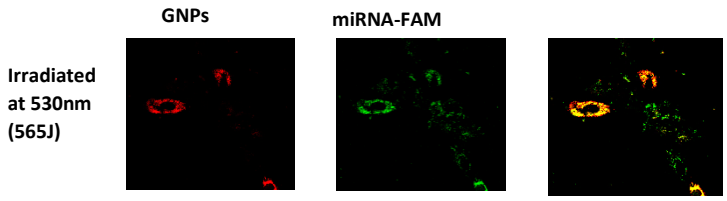

Figure D.8. Colocalization of GNPs (red) & conjugated FAM molecules (green) in hASCs. Irradiation at 400 nm (50 J) and 530 nm (565 nm).

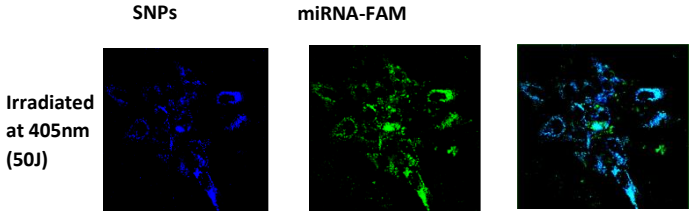

Figure D.9. Colocalization of SNPs (blue) & conjugated FAM molecules (green) in hASCs. Irradiation at 400 nm (50 J) and 530 nm (565 nm).

D.4. Notes

(1) https://www.idtdna.com/site/Catalog/Modifications/Product/1108.

(2) https://www.jenabioscience.com/probes-epigenetics/protein-labeling/labeling-of-purified-proteins/fluorescent-amine-labeling/fp-201-cy3-cy3-protein-labeling-kit.

(3) Abu-Laban, M.; Kumal, R. R.; Casey, J.; Becca, J.; LaMaster, D.; Pacheco, C. N.; Sykes, D. G.; Jensen, L.; Haber, L. H.; Hayes, D. J. Comparison of thermally actuated retro-diels-alder release groups for nanoparticle based nucleic acid delivery. *J. Colloid Interface Sci.* **2018**, *526*, 312-321.

(4) Kumal, R. R.; Abu-Laban, M.; Hamal, P.; Kruger, B.; Smith, H. T.; Hayes, D. J.; Haber, L. H. Near-Infrared Photothermal Release of siRNA from the Surface of Colloidal Gold–Silver–Gold Core–Shell–Shell Nanoparticles Studied with Second-Harmonic Generation. *J. Phys. Chem. C* **2018**, *122*, 19699-19704.

(5) Kumal, R. R.; Abu-Laban, M.; Landry, C. R.; Kruger, B.; Zhang, Z.; Hayes, D. J.; Haber, L. H. Plasmon-enhanced photocleaving dynamics in colloidal microRNA-functionalized silver nanoparticles monitored with second harmonic generation. *Langmuir* **2016**, *32*, 10394-10401.

(6) Kumal, R. R.; Landry, C. R.; Abu-Laban, M.; Hayes, D. J.; Haber, L. H. Monitoring the photocleaving dynamics of colloidal microrna-functionalized gold nanoparticles using second harmonic generation. *Langmuir* **2015**, *31*, 9983-9990.

Appendix E. Permissions

E.1. Permission to Reprint Article as Chapter 2

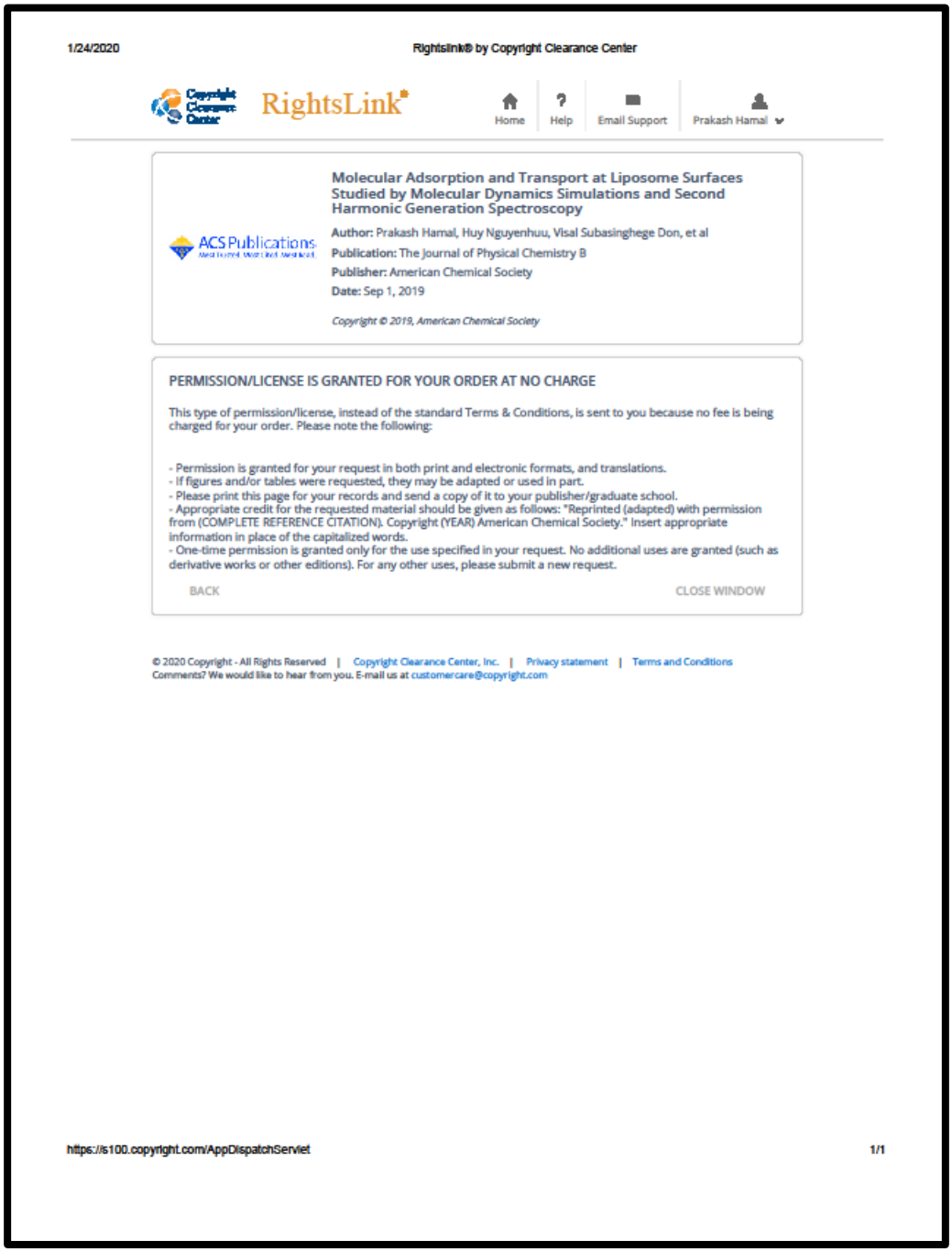

1/24/2020 Rightslink® by Copyright Clearance Center

RightsLink

Home | Help | Email Support | Prakash Hamal

Molecular Adsorption and Transport at Liposome Surfaces Studied by Molecular Dynamics Simulations and Second Harmonic Generation Spectroscopy

ACS Publications

Author: Prakash Hamal, Huy Nguyenhuu, Visal Subasinghege Don, et al
Publication: The Journal of Physical Chemistry B
Publisher: American Chemical Society
Date: Sep 1, 2019

Copyright © 2019, American Chemical Society

PERMISSION/LICENSE IS GRANTED FOR YOUR ORDER AT NO CHARGE

This type of permission/license, instead of the standard Terms & Conditions, is sent to you because no fee is being charged for your order. Please note the following:

- Permission is granted for your request in both print and electronic formats, and translations.
- If figures and/or tables were requested, they may be adapted or used in part.
- Please print this page for your records and send a copy of it to your publisher/graduate school.
- Appropriate credit for the requested material should be given as follows: "Reprinted (adapted) with permission from (COMPLETE REFERENCE CITATION). Copyright (YEAR) American Chemical Society." Insert appropriate information in place of the capitalized words.
- One-time permission is granted only for the use specified in your request. No additional uses are granted (such as derivative works or other editions). For any other uses, please submit a new request.

BACK CLOSE WINDOW

© 2020 Copyright - All Rights Reserved | Copyright Clearance Center, Inc. | Privacy statement | Terms and Conditions
Comments? We would like to hear from you. E-mail us at customercare@copyright.com

https://s100.copyright.com/AppDispatchServlet 1/1

E.2. Permission to Reuse this Article in Section 5.3

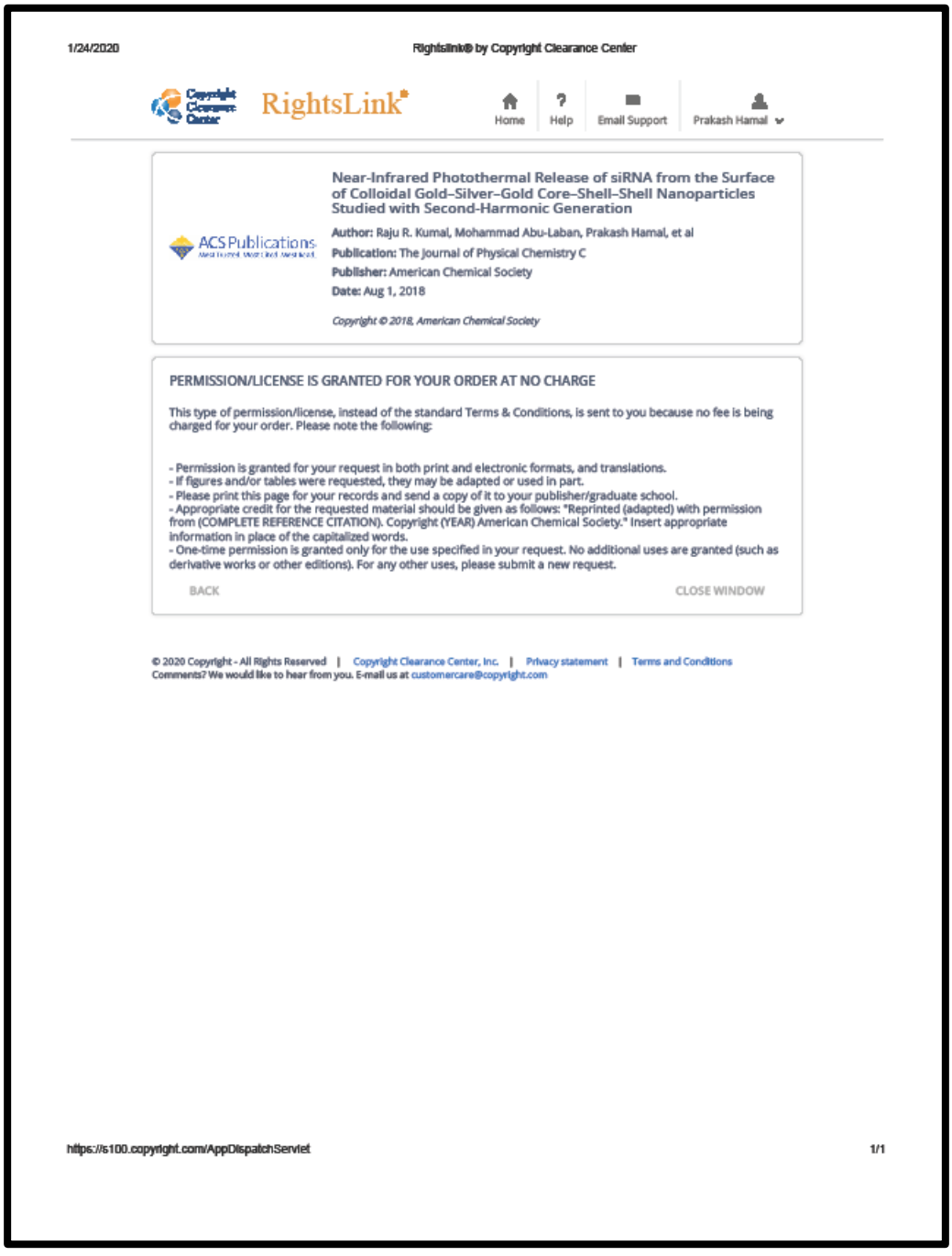

1/24/2020 Rightslink® by Copyright Clearance Center

RightsLink

Home | Help | Email Support | Prakash Hamal

Near-Infrared Photothermal Release of siRNA from the Surface of Colloidal Gold–Silver–Gold Core–Shell–Shell Nanoparticles Studied with Second-Harmonic Generation

ACS Publications

Author: Raju R. Kumal, Mohammad Abu-Laban, Prakash Hamal, et al
Publication: The Journal of Physical Chemistry C
Publisher: American Chemical Society
Date: Aug 1, 2018

Copyright © 2018, American Chemical Society

PERMISSION/LICENSE IS GRANTED FOR YOUR ORDER AT NO CHARGE

This type of permission/license, instead of the standard Terms & Conditions, is sent to you because no fee is being charged for your order. Please note the following:

- Permission is granted for your request in both print and electronic formats, and translations.
- If figures and/or tables were requested, they may be adapted or used in part.
- Please print this page for your records and send a copy of it to your publisher/graduate school.
- Appropriate credit for the requested material should be given as follows: "Reprinted (adapted) with permission from (COMPLETE REFERENCE CITATION). Copyright (YEAR) American Chemical Society." Insert appropriate information in place of the capitalized words.
- One-time permission is granted only for the use specified in your request. No additional uses are granted (such as derivative works or other editions). For any other uses, please submit a new request.

BACK CLOSE WINDOW

© 2020 Copyright - All Rights Reserved | Copyright Clearance Center, Inc. | Privacy statement | Terms and Conditions
Comments? We would like to hear from you. E-mail us at customercare@copyright.com

https://s100.copyright.com/AppDispatchServlet 1/1

E.3. Permission to Reuse this Article in Section 5.3

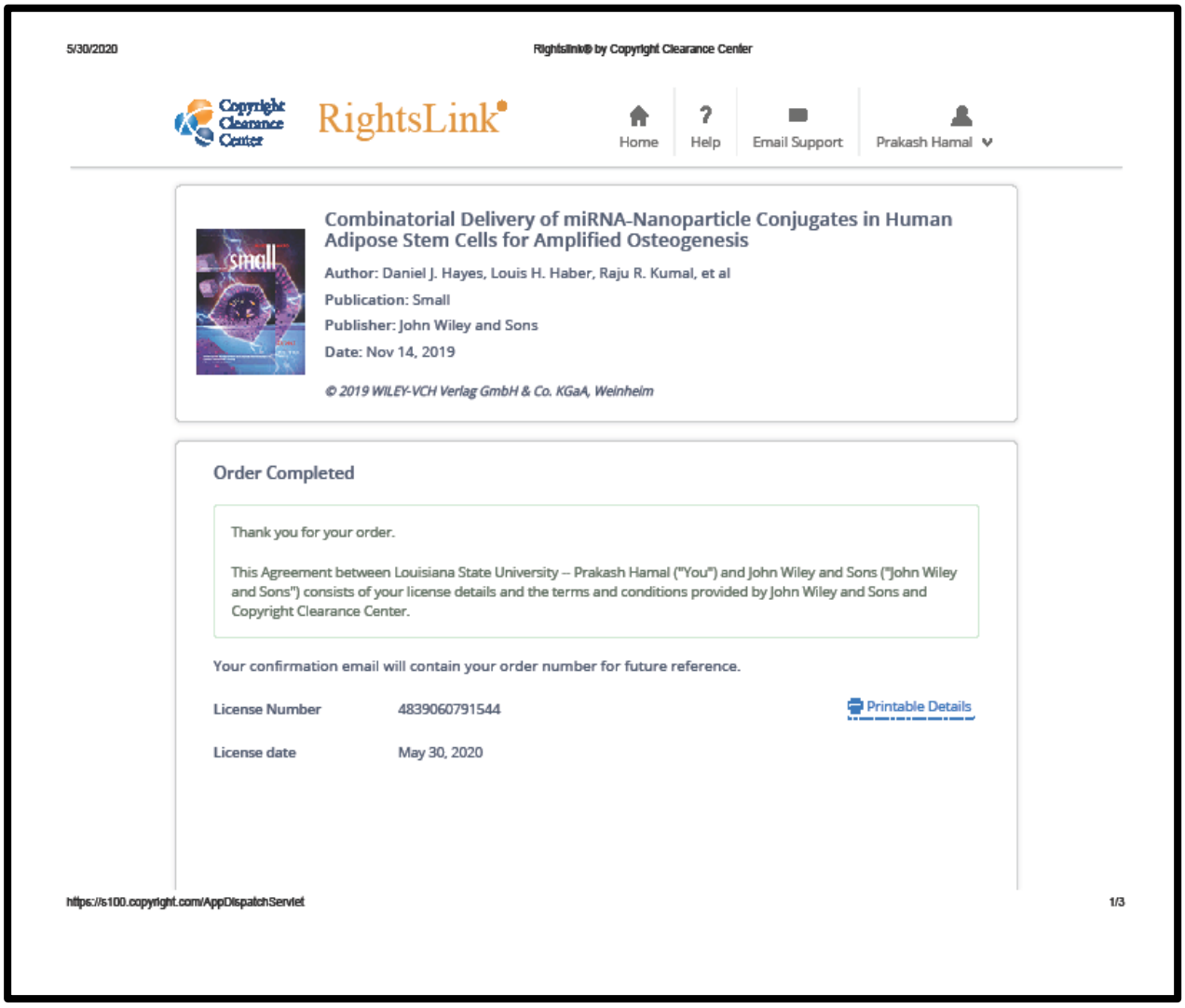

5/30/2020 RightsLink® by Copyright Clearance Center

Copyright Clearance Center RightsLink

Home | Help | Email Support | Prakash Hamal

Combinatorial Delivery of miRNA-Nanoparticle Conjugates in Human Adipose Stem Cells for Amplified Osteogenesis

Author: Daniel J. Hayes, Louis H. Haber, Raju R. Kumal, et al

Publication: Small

Publisher: John Wiley and Sons

Date: Nov 14, 2019

© 2019 WILEY-VCH Verlag GmbH & Co. KGaA, Weinheim

Order Completed

Thank you for your order.

This Agreement between Louisiana State University -- Prakash Hamal ("You") and John Wiley and Sons ("John Wiley and Sons") consists of your license details and the terms and conditions provided by John Wiley and Sons and Copyright Clearance Center.

Your confirmation email will contain your order number for future reference.

License Number	4839060791544	Printable Details
License date	May 30, 2020	

https://s100.copyright.com/AppDispatchServlet 1/3

List of References

Abu-Laban, M.; Hamal, P.; Arrizabalaga, J. H.; Forghani, A.; Dikkumbura, A. S.; Kumal, R. R.; Haber, L. H.; Hayes, D. J. Combinatorial Delivery of miRNA-Nanoparticle Conjugates in Human Adipose Stem Cells for Amplified Osteogenesis. *Small* **2019**.

Aidley, D. J.; Stanfield, P. R.: *Ion channels: molecules in action*; Cambridge University Press, 1996.

Albers, R. Biochemical aspects of active transport. *Annu. Rev. Biochem* **1967**, *36*, 727-756.

Alberts, B.; Johnson, A.; Lewis, J.; Raff, M.; Roberts, K.; Walter, P.: *Molecular Biology of the Cell*; New York: Garland Science, 2002.

Ali, M. R.; Wu, Y.; El-Sayed, M. A. Gold-nanoparticle-assisted plasmonic photothermal therapy advances toward clinical application. *The Journal of Physical Chemistry C* **2019**, *123*, 15375-15393.

Alivisatos, A. P. Semiconductor clusters, nanocrystals, and quantum dots. *science* **1996**, *271*, 933-937.

Antonietti, M.: *Colloid Chemistry II*; Springer, 2003; Vol. 227.

Austin, L. A.; Mackey, M. A.; Dreaden, E. C.; El-Sayed, M. A. The optical, photothermal, and facile surface chemical properties of gold and silver nanoparticles in biodiagnostics, therapy, and drug delivery. *Arch. Toxicol.* **2014**, *88*, 1391-1417.

Bakhtiari, A. B. S.; Hsiao, D.; Jin, G.; Gates, B. D.; Branda, N. R. An efficient method based on the photothermal effect for the release of molecules from metal nanoparticle surfaces. *Angew. Chem. Int. Ed.* **2009**, *48*, 4166-4169.

Balazs, D. A.; Godbey, W. Liposomes for use in gene delivery. *Journal of drug delivery* **2011**, *2011*.

Bayly, C. I.; Cieplak, P.; Cornell, W.; Kollman, P. A. A well-behaved electrostatic potential based method using charge restraints for deriving atomic charges: the RESP model. *J. Phys. Chem.* **1993**, *97*, 10269-10280.

Beloqui, A.; Solinís, M. Á.; Rodríguez-Gascón, A.; Almeida, A. J.; Préat, V. Nanostructured lipid carriers: promising drug delivery systems for future clinics. *Nanomedicine: Nanotechnology, Biology and Medicine* **2016**, *12*, 143-161.

Bennett, H. S. The concepts of membrane flow and membrane vesiculation as mechanisms for active transport and ion pumping. *The Journal of biophysical and biochemical cytology* **1956**, *2*, 99.

Bey, E. A.; Bentle, M. S.; Reinicke, K. E.; Dong, Y.; Yang, C.-R.; Girard, L.; Minna, J. D.; Bornmann, W. G.; Gao, J.; Boothman, D. A. An NQO1-and PARP-1-mediated cell death pathway induced in non-small-cell lung cancer cells by β-lapachone. *PNAS* **2007**, *104*, 11832-11837.

Brown, P. K.; Qureshi, A. T.; Moll, A. N.; Hayes, D. J.; Monroe, W. T. Silver nanoscale antisense drug delivery system for photoactivated gene silencing. *ACS nano* **2013**, *7*, 2948-2959.

Camenisch, G.; Folkers, G.; van de Waterbeemd, H. Review of theoretical passive drug absorption models: historical background, recent developments and limitations. *Pharm. Acta Helv.* **1996**, *71*, 309-327.

Campagnola, P. J.; Loew, L. M. Second-harmonic imaging microscopy for visualizing biomolecular arrays in cells, tissues and organisms. *Nat. Biotechnol.* **2003**, *21*, 1356-1360.

Charman, W. N. Lipids, lipophilic drugs, and oral drug delivery—some emerging concepts. *J. Pharm. Sci.* **2000**, *89*, 967-978.

Chen, G.-J.; Wang, L.-F. Design of magnetic nanoparticles-assisted drug delivery system. *Current pharmaceutical design* **2011**, *17*, 2331-2351.

Chen, H.; Shao, L.; Ming, T.; Sun, Z.; Zhao, C.; Yang, B.; Wang, J. Understanding the photothermal conversion efficiency of gold nanocrystals. *small* **2010**, *6*, 2272-2280.

Chen, X.; Yang, T.; Kataoka, S.; Cremer, P. S. Specific ion effects on interfacial water structure near macromolecules. *J. Am. Chem. Soc.* **2007**, *129*, 12272-12279.

Cieplak, P.; Cornell, W. D.; Bayly, C.; Kollman, P. A. Application of the multimolecule and multiconformational RESP methodology to biopolymers: Charge derivation for DNA, RNA, and proteins. *J. Comput. Chem.* **1995**, *16*, 1357-1377.

Cobley, C. M.; Au, L.; Chen, J.; Xia, Y. Targeting gold nanocages to cancer cells for photothermal destruction and drug delivery. *Expert opinion on drug delivery* **2010**, *7*, 577-587.

Dadap, J. I.; Shan, J.; Eisenthal, K. B.; Heinz, T. F. Second-harmonic Rayleigh scattering from a sphere of centrosymmetric material. *Phys. Rev. Lett.* **1999**, *83*, 4045.

de Beer, A. G.; Roke, S. Nonlinear Mie theory for second-harmonic and sum-frequency scattering. *Phys. Rev. B* **2009**, *79*, 155420.

Dixon, M. C. Quartz crystal microbalance with dissipation monitoring: enabling real-time characterization of biological materials and their interactions. *Journal of biomolecular techniques: JBT* **2008**, *19*, 151.

Domene, C.; Bond, P. J.; Sansom, M. S.: Membrane protein simulations: ion channels and bacterial outer membrane proteins. In *Adv. Protein Chem.*; Elsevier, 2003; Vol. 66; pp 159-193.

Dreier, L. B.; Bernhard, C.; Gonella, G.; Backus, E. H.; Bonn, M. Surface Potential of a Planar Charged Lipid–Water Interface. What Do Vibrating Plate Methods, Second Harmonic and Sum Frequency Measure? *J. Phys. Chem. Lett.* **2018**, *9*, 5685-5691.

Eisenthal, K. B. Second harmonic spectroscopy of aqueous nano-and microparticle interfaces. *Chem. Rev.* **2006**, *106*, 1462-1477.

Ertl, P.; Rohde, B.; Selzer, P. Fast calculation of molecular polar surface area as a sum of fragment-based contributions and its application to the prediction of drug transport properties. *J. Med. Chem.* **2000**, *43*, 3714-3717.

Escribá, P. V.; González-Ros, J. M.; Goñi, F. M.; Kinnunen, P. K.; Vigh, L.; Sánchez-Magraner, L.; Fernández, A. M.; Busquets, X.; Horváth, I.; Barceló-Coblijn, G. Membranes: a meeting point for lipids, proteins and therapies. *J Cell Mol Med.* **2008**, *12*, 829-875.

Evans, D. F.; Wennerström, H. The colloidal domain: where physics, chemistry, biology, and technology meet. **1999**.

Everett, D. H.: *Basic principles of colloid science*; Royal society of chemistry, 2007.
Fewtrell, C. Ca2+ oscillations in non-excitable cells. *Annual Review of Physiology* **1993**, *55*, 427-454.

Finkelstein, A. Water and nonelectrolyte permeability of lipid bilayer membranes. *J. Gen. Physiol.* **1976**, *68*, 127-135.

Fontenete, S.; Leite, M.; Cappoen, D.; Santos, R.; Ginneken, C. V.; Figueiredo, C.; Wengel, J.; Cos, P.; Azevedo, N. F. Fluorescence in vivo hybridization (FIVH) for detection of Helicobacter pylori infection in a C57BL/6 mouse model. *PLoS One* **2016**, *11*, e0148353.

Freund, I.; Deutsch, M. Second-harmonic microscopy of biological tissue. *Opt. Lett.* **1986**, *11*, 94-96.

Friedman, M. H.: *Principles and models of biological transport*; Springer Science & Business Media, 2008.

Frisch, M. J.; Trucks, G. W.; Schlegel, H. B.; Scuseria, G. E.; Robb, M. A.; Cheeseman, J. R.; Scalmani, G.; Barone, V.; Petersson, G. A.; Nakatsuji, H.; Li, X.; Caricato, M.;

Marenich, A. V.; Bloino, J.; Janesko, B. G.; Gomperts, R.; Mennucci, B.; Hratchian, H. P.; Ortiz, J. V.; Izmaylov, A. F.; Sonnenberg, J. L.; Williams; Ding, F.; Lipparini, F.; Egidi, F.; Goings, J.; Peng, B.; Petrone, A.; Henderson, T.; Ranasinghe, D.; Zakrzewski, V. G.; Gao, J.; Rega, N.; Zheng, G.; Liang, W.; Hada, M.; Ehara, M.; Toyota, K.; Fukuda, R.; Hasegawa, J.; Ishida, M.; Nakajima, T.; Honda, Y.; Kitao, O.; Nakai, H.; Vreven, T.; Throssell, K.; Montgomery Jr., J. A.; Peralta, J. E.; Ogliaro, F.; Bearpark, M. J.; Heyd, J. J.; Brothers, E. N.; Kudin, K. N.; Staroverov, V. N.; Keith, T. A.; Kobayashi, R.; Normand, J.; Raghavachari, K.; Rendell, A. P.; Burant, J. C.; Iyengar, S. S.; Tomasi, J.; Cossi, M.; Millam, J. M.; Klene, M.; Adamo, C.; Cammi, R.; Ochterski, J. W.; Martin, R. L.; Morokuma, K.; Farkas, O.; Foresman, J. B.; Fox, D. J.: Gaussian 16 Rev. B.01. Wallingford, CT, 2016.

Gaucher, G.; Dufresne, M.-H.; Sant, V. P.; Kang, N.; Maysinger, D.; Leroux, J.-C. Block copolymer micelles: preparation, characterization and application in drug delivery. *J. Controlled Release* **2005**, *109*, 169-188.

Ge, J.; Neofytou, E.; Cahill III, T. J.; Beygui, R. E.; Zare, R. N. Drug release from electric-field-responsive nanoparticles. *ACS nano* **2012**, *6*, 227-233.

Geiger, F. M. Second harmonic generation, sum frequency generation, and χ (3): dissecting environmental interfaces with a nonlinear optical Swiss Army knife. *Annu. Rev. Phys. Chem.* **2009**, *60*, 61-83.

Gh, M. S.; Wilhelm, M. J.; Dai, H.-L. Azithromycin-Induced Changes to Bacterial Membrane Properties Monitored in vitro by Second-Harmonic Light Scattering. *ACS Med. Chem. Lett.* **2018**, *9*, 569-574.

Gonella, G.; Dai, H.-L. Determination of adsorption geometry on spherical particles from nonlinear Mie theory analysis of surface second harmonic generation. *Phys. Rev. B* **2011**, *84*, 121402.

Gonella, G.; Dai, H.-L. Second harmonic light scattering from the surface of colloidal objects: theory and applications. *Langmuir* **2013**, *30*, 2588-2599.

Gonella, G.; Lütgebaucks, C.; De Beer, A. G.; Roke, S. Second harmonic and sum-frequency generation from aqueous interfaces is modulated by interference. *J. Phys. Chem. C* **2016**, *120*, 9165-9173.

Gong, J.; Chen, M.; Zheng, Y.; Wang, S.; Wang, Y. Polymeric micelles drug delivery system in oncology. *J. Controlled Release* **2012**, *159*, 312-323.

Goodman, A. M.; Hogan, N. J.; Gottheim, S.; Li, C.; Clare, S. E.; Halas, N. J. Understanding resonant light-triggered DNA release from plasmonic nanoparticles. *ACS nano* **2016**, *11*, 171-179.

Goodman, A. M.; Hogan, N. J.; Gottheim, S.; Li, C.; Clare, S. E.; Halas, N. J. Understanding resonant light-triggered DNA release from plasmonic nanoparticles. *ACS nano* **2016**, *11*, 171-179.

Goyal, P.; Goyal, K.; Kumar, S. V.; Singh, A.; Katare, O. P.; Mishra, D. N. Liposomal drug delivery systems–clinical applications. *Acta Pharm* **2005**, *55*, 1-25.

Gupta, P.; Vermani, K.; Garg, S. Hydrogels: from controlled release to pH-responsive drug delivery. *Drug Discovery Today* **2002**, *7*, 569-579.

Haber, L. H.; Kwok, S. J.; Semeraro, M.; Eisenthal, K. B. Probing the colloidal gold nanoparticle/aqueous interface with second harmonic generation. *Chem. Phys. Lett.* **2011**, *507*, 11-14.

Hamal, P.; Nguyenhuu, H.; Subasinghege Don, V.; Kumal, R. R.; Kumar, R.; McCarley, R. L.; Haber, L. H. Molecular Adsorption and Transport at Liposome Surfaces Studied by Molecular Dynamics Simulations and Second Harmonic Generation Spectroscopy. *J. Phys. Chem. B* **2019**, *123*, 7722-7730.

Hannesschlaeger, C.; Horner, A.; Pohl, P. Intrinsic Membrane Permeability to Small Molecules. *Chem. Rev.* **2019**, *119*, 5922-5953.

Hartland, G. V.; Besteiro, L. V.; Johns, P.; Govorov, A. O. What's so hot about electrons in metal nanoparticles? *ACS Energy Lett.* **2017**, *2*, 1641-1653.

Hayes, P. L.; Malin, J. N.; Jordan, D. S.; Geiger, F. M. Get charged up: Nonlinear optical voltammetry for quantifying the thermodynamics and electrostatics of metal cations at aqueous/oxide interfaces. *Chem. Phys. Lett.* **2010**, *499*, 183-192.

He, C.; Kim, S. W.; Lee, D. S. In situ gelling stimuli-sensitive block copolymer hydrogels for drug delivery. *J. Controlled Release* **2008**, *127*, 189-207.

Heald, R.; Cohen-Fix, O. Morphology and function of membrane-bound organelles. *Current opinion in cell biology* **2014**, *26*, 79-86.

Henglein, A. Small-particle research: physicochemical properties of extremely small colloidal metal and semiconductor particles. *Chem. Rev.* **1989**, *89*, 1861-1873.

Higuchi, W. I. Diffusional models useful in biopharmaceutics: drug release rate processes. *J. Pharm. Sci.* **1967**, *56*, 315-324.

Hirsch, L. R.; Stafford, R. J.; Bankson, J. A.; Sershen, S. R.; Rivera, B.; Price, R.; Hazle, J. D.; Halas, N. J.; West, J. L. Nanoshell-mediated near-infrared thermal therapy of tumors under magnetic resonance guidance. *PNAS* **2003**, *100*, 13549-13554.

Hirsch, L. R.; Stafford, R. J.; Bankson, J. A.; Sershen, S. R.; Rivera, B.; Price, R.; Hazle, J. D.; Halas, N. J.; West, J. L. Nanoshell-mediated near-infrared thermal therapy of tumors under magnetic resonance guidance. *PNAS* **2003**, *100*, 13549-13554.

Holthuis, J. C.; Menon, A. K. Lipid landscapes and pipelines in membrane homeostasis. *Nature* **2014**, *510*, 48.

Jen, S.-H.; Dai, H.-L.; Gonella, G. The effect of particle size in second harmonic generation from the surface of spherical colloidal particles. II: The nonlinear Rayleigh− Gans− Debye model. *J. Phys. Chem. C* **2010**, *114*, 4302-4308.

Karam, T. E.; Haber, L. H. Molecular adsorption and resonance coupling at the colloidal gold nanoparticle interface. *J. Phys. Chem. C* **2014**, *118*, 642-649.

Karam, T. E.; Khoury, R. A.; Haber, L. H. Excited-state dynamics of size-dependent colloidal TiO2-Au nanocomposites. *The Journal of chemical physics* **2016**, *144*, 124704.

Karam, T. E.; Siraj, N.; Zhang, Z.; Ezzir, A. F.; Warner, I. M.; Haber, L. H. Ultrafast and nonlinear spectroscopy of brilliant green-based nanoGUMBOS with enhanced near-infrared emission. *J. Chem. Phys.* **2017**, *147*, 144701.

Karam, T. E.; Siraj, N.; Zhang, Z.; Ezzir, A. F.; Warner, I. M.; Haber, L. H. Ultrafast and nonlinear spectroscopy of brilliant green-based nanoGUMBOS with enhanced near-infrared emission. *J. Chem. Phys.* **2017**, *147*, 144701.

Karam, T. E.; Smith, H. T.; Haber, L. H. Enhanced photothermal effects and excited-state dynamics of plasmonic size-controlled gold–silver–gold core–shell–shell nanoparticles. *The Journal of Physical Chemistry C* **2015**, *119*, 18573-18580.

Kästner, J. Umbrella sampling. *WIREs Comput Mol Sci* **2011**, *1*, 932-942.

Khoury, R. A.; Ranasinghe, J. C.; Dikkumbura, A. S.; Hamal, P.; Kumal, R. R.; Karam, T. E.; Smith, H. T.; Haber, L. H. Monitoring the Seed-Mediated Growth of Gold Nanoparticles using In-Situ Second Harmonic Generation and Extinction Spectroscopy. *J. Phys. Chem. C* **2018**, *122*, 244400-224406.

Kim, J.; Kim, M.-W. Temperature effect on the transport dynamics of a small molecule through a liposome bilayer. *Eur. Phys. J. E* **2007**, *23*, 313-317.

Kim, S. W.; Bae, Y. H.; Okano, T. Hydrogels: swelling, drug loading, and release. *Pharm. Res.* **1992**, *9*, 283-290.

Klopman, G.; Li, J.-Y.; Wang, S.; Dimayuga, M. Computer automated log P calculations based on an extended group contribution approach. *J. Chem. Inf. Model.* **1994**, *34*, 752-781.

Kolthoff, I.; Bovey, F.; Medalia, A.; Meehan, E. Emulsion Polymerization. *New York: Interscience* **1955**, 177.

Kučerka, N.; Nieh, M.-P.; Katsaras, J. Fluid phase lipid areas and bilayer thicknesses of commonly used phosphatidylcholines as a function of temperature. *Biochim. Biophys. Acta* **2011**, *1808*, 2761-2771.

Kumal, R. R.; Abu-Laban, M.; Hamal, P.; Kruger, B.; Smith, H. T.; Hayes, D. J.; Haber, L. H. Near-Infrared Photothermal Release of siRNA from the Surface of Colloidal Gold–Silver–Gold Core–Shell–Shell Nanoparticles Studied with Second-Harmonic Generation. *J. Phys. Chem. C* **2018**, *122*, 19699-19704.

Kumal, R. R.; Abu-Laban, M.; Landry, C. R.; Kruger, B.; Zhang, Z.; Hayes, D. J.; Haber, L. H. Plasmon-enhanced photocleaving dynamics in colloidal microRNA-functionalized silver nanoparticles monitored with second harmonic generation. *Langmuir* **2016**, *32*, 10394-10401.

Kumal, R. R.; Karam, T. E.; Haber, L. H. Determination of the surface charge density of colloidal gold nanoparticles using second harmonic generation. *J. Phys. Chem. C* **2015**, *119*, 16200-16207.

Kumal, R. R.; Landry, C. R.; Abu-Laban, M.; Hayes, D. J.; Haber, L. H. Monitoring the photocleaving dynamics of colloidal microrna-functionalized gold nanoparticles using second harmonic generation. *Langmuir* **2015**, *31*, 9983-9990.

Kumal, R. R.; Nguyenhuu, H.; Winter, J. E.; McCarley, R. L.; Haber, L. H. Impacts of Salt, Buffer, and Lipid Nature on Molecular Adsorption and Transport in Liposomes As Observed by Second Harmonic Generation. *J. Phys. Chem. C* **2017**, *121*, 15851-15860.

Kumar, S.; Rosenberg, J. M.; Bouzida, D.; Swendsen, R. H.; Kollman, P. A. The weighted histogram analysis method for free-energy calculations on biomolecules. I. The method. *J. Comput. Chem.* **1992**, *13*, 1011-1021.

Langevin, D.: *Light scattering by liquid surfaces and complementary techniques*; M. Dekker, 1992.

Lewis, R. N.; McElhaney, R. N. Calorimetric and spectroscopic studies of the thermotropic phase behavior of lipid bilayer model membranes composed of a homologous series of linear saturated phosphatidylserines. *Biophys. J.* **2000**, *79*, 2043-2055.

Li, H.; Xia, H.; Wang, D.; Tao, X. Simple synthesis of monodisperse, quasi-spherical, citrate-stabilized silver nanocrystals in water. *Langmuir* **2013**, *29*, 5074-5079.

Li, Y.; Choudhry, U.; Ranasinghe, J.; Ackerman, A.; Liao, B. Probing Surface Photovoltage Effect Using Photo-Assisted Secondary Electron Emission. *The Journal of Physical Chemistry A* **2020**.

Lindahl, E.; Sansom, M. S. Membrane proteins: molecular dynamics simulations. *Current opinion in structural biology* **2008**, *18*, 425-431.

Link, S.; Burda, C.; Wang, Z. L.; El-Sayed, M. A. Electron dynamics in gold and gold–silver alloy nanoparticles: The influence of a nonequilibrium electron distribution and the size dependence of the electron–phonon relaxation. *J. Chem. Phys.* **1999**, *111*, 1255-1264.

Liu, J.; Shang, X.; Pompano, R.; Eisenthal, K. B. Antibiotic assisted molecular ion transport across a membrane in real time. *Faraday Discuss.* **2005**, *129*, 291-299.

Liu, J.; Subir, M.; Nguyen, K.; Eisenthal, K. B. Second harmonic studies of ions crossing liposome membranes in real time. *J. Phys. Chem. B* **2008**, *112*, 15263-15266.

Liu, W.; Wang, Z.; Fu, L.; Leblanc, R. M.; Yan, E. C. Lipid compositions modulate fluidity and stability of bilayers: characterization by surface pressure and sum frequency generation spectroscopy. *Langmuir* **2013**, *29*, 15022-15031.

Liu, X.; Testa, B.; Fahr, A. Lipophilicity and its relationship with passive drug permeation. *Pharm. Res.* **2011**, *28*, 962-977.

Liu, Y.; Yan, E. C.; Eisenthal, K. B. Effects of bilayer surface charge density on molecular adsorption and transport across liposome bilayers. *Biophys. J.* **2001**, *80*, 1004-1012.

Liu, Y.; Yan, E. C.; Zhao, X.; Eisenthal, K. B. Surface potential of charged liposomes determined by second harmonic generation. *Langmuir* **2001**, *17*, 2063-2066.

Loo, C.; Lowery, A.; Halas, N.; West, J.; Drezek, R. Immunotargeted nanoshells for integrated cancer imaging and therapy. *Nano Lett.* **2005**, *5*, 709-711.

Macias-Romero, C.; Nahalka, I.; Okur, H. I.; Roke, S. Optical imaging of surface chemistry and dynamics in confinement. *Science* **2017**, *357*, 784-788.

Marsh, D. Electron spin resonance in membrane research: protein–lipid interactions. *Methods* **2008**, *46*, 83-96.

Marsh, D. Lipid-protein interactions and heterogeneous lipid distribution in membranes. *Molecular Membrane Biology* **1995**, *12*, 59-64.

McCarley, R. L. Redox-responsive delivery systems. *Annu. Rev. Anal. Chem.* **2012**, *5*, 391-411.

McCarley, R. L.; Forsythe, J. C.; Loew, M.; Mendoza, M. F.; Hollabaugh, N. M.; Winter, J. E. Release rates of liposomal contents are controlled by kosmotropes and chaotropes. *Langmuir* **2013**, *29*, 13991-13995.

Miller, C. C. The Stokes-Einstein law for diffusion in solution. *Proceedings of the Royal Society of London. Series A, Containing Papers of a Mathematical and Physical Character* **1924**, *106*, 724-749.

Mouritsen, O.; Boothroyd, A.; Harris, R.; Jan, N.; Lookman, T.; MacDonald, L.; Pink, D.; Zuckermann, M. Computer simulation of the main gel–fluid phase transition of lipid bilayers. *J. Chem. Phys.* **1983**, *79*, 2027-2041.

Mura, S.; Nicolas, J.; Couvreur, P. Stimuli-responsive nanocarriers for drug delivery. *Nature materials* **2013**, *12*, 991-1003.

Nguyen, T. T.; Conboy, J. C. High-throughput screening of drug–lipid membrane interactions via counter-propagating second harmonic generation imaging. *Anal. Chem.* **2011**, *83*, 5979-5988.

Ohno, P. E.; Chang, H.; Spencer, A. P.; Liu, Y.; Boamah, M. D.; Wang, H.-f.; Geiger, F. M. Beyond the gouy–chapman model with heterodyne-detected second harmonic generation. *J. Phys. Chem. Lett.* **2019**, *10*, 2328-2334.

Ohno, P.; Saslow, S.; Wang, H.-f.; Geiger, F.; Eisenthal, K.: Phase-referenced nonlinear spectroscopy of the α-quartz/water interface Nat. Commun, 2016.

Ong, W.; Yang, Y.; Cruciano, A. C.; McCarley, R. L. Redox-triggered contents release from liposomes. *J. Am. Chem. Soc.* **2008**, *130*, 14739-14744.

Pang, K. S. Modeling of intestinal drug absorption: roles of transporters and metabolic enzymes (for the Gillette Review Series). *Drug Metab. Dispos.* **2003**, *31*, 1507-1519.

Patching, S. G. Surface plasmon resonance spectroscopy for characterisation of membrane protein–ligand interactions and its potential for drug discovery. *Biochimica et Biophysica Acta (BBA)-Biomembranes* **2014**, *1838*, 43-55.

Perrault, S. D.; Chan, W. C. Synthesis and surface modification of highly monodispersed, spherical gold nanoparticles of 50− 200 nm. *J. Am. Chem. Soc.* **2009**, *131*, 17042-17043.
Pieranski, P. Colloidal crystals. *Contemporary Physics* **1983**, *24*, 25-73.

Pieranski, P.; Strzelecki, L.; Pansu, B. Thin colloidal crystals. *Phys. Rev. Lett.* **1983**, *50*, 900.

Pike, L. J. Lipid rafts: heterogeneity on the high seas. *Biochem. J* **2004**, *378*, 281-292.
Plimpton, S. Fast parallel algorithms for short-range molecular dynamics. *J. Comput. Phys.* **1995**, *117*, 1-19.

Raji, V.; Kumar, J.; Rejiya, C.; Vibin, M.; Shenoi, V. N.; Abraham, A. Selective photothermal efficiency of citrate capped gold nanoparticles for destruction of cancer cells. *Experimental cell research* **2011**, *317*, 2052-2058.

Ranasinghe, J. C.; Dikkumbura, A. S.; Hamal, P.; Chen, M.; Khoury, R. A.; Smith, H. T.; Lopata, K.; Haber, L. H. Monitoring the growth dynamics of colloidal gold-silver core-shell nanoparticles using in situ second harmonic generation and extinction spectroscopy. *J. Chem. Phys.* **2019**, *151*, 224701.

Rao, Y.; Guo, X.-m.; Tao, Y.-S.; Wang, H.-f. Observation of the direct S 2→ S 0 two-photon fluorescence between 370 and 480 nm and the hyperpolarizability of crystal violet (CV) from spectrally resolved hyper-Rayleigh scattering measurement. *J. Phys. Chem. A* **2004**, *108*, 7977-7982.

Rao, Y.; Kwok, S. J.; Lombardi, J.; Turro, N. J.; Eisenthal, K. B. Label-free probe of HIV-1 TAT peptide binding to mimetic membranes. *PNAS* **2014**, *111*, 12684-12688.

Rastinehad, A. R.; Anastos, H.; Wajswol, E.; Winoker, J. S.; Sfakianos, J. P.; Doppalapudi, S. K.; Carrick, M. R.; Knauer, C. J.; Taouli, B.; Lewis, S. C. Gold nanoshell-localized photothermal ablation of prostate tumors in a clinical pilot device study. *PNAS* **2019**, *116*, 18590-18596.

Roke, S.; Gonella, G. Nonlinear light scattering and spectroscopy of particles and droplets in liquids. *Annu. Rev. Phys. Chem.* **2012**, *63*, 353-378.

Roke, S.; Gonella, G. Nonlinear Light Scattering and Spectroscopy of Particles and Droplets in Liquids. *Annual review of physical chemistry* **2012**, *63*, 353-378.

Rossin, R.; van Duijnhoven, S. M.; Ten Hoeve, W.; Janssen, H. M.; Kleijn, L. H.; Hoeben, F. J.; Versteegen, R. M.; Robillard, M. S. Triggered drug release from an antibody–drug conjugate using fast “click-to-release” chemistry in mice. *Bioconjugate Chem.* **2016**, *27*, 1697-1706.

Salma, S. A.; Patil, M. P.; Kim, D. W.; Le, C. M. Q.; Ahn, B.-H.; Kim, G.-D.; Lim, K. T. Near-infrared light-responsive, diselenide containing core-cross-linked micelles prepared by the Diels–Alder click reaction for photocontrollable drug release application. *Polymer Chemistry* **2018**, *9*, 4813-4823.

Schanker, L. Mechanisms of drug absorption and distribution. *Annu. Rev. Pharmacol.* **1961**, *1*, 29-45.

Schmid, G. Large clusters and colloids. Metals in the embryonic state. *Chem. Rev.* **1992**, *92*, 1709-1727.

Schmid, G.; Chi, L. F. Metal clusters and colloids. *Adv. Mater.* **1998**, *10*, 515-526.

Schön, G.; Simon, U. A fascinating new field in colloid science: small ligand-stabilized metal clusters and possible application in microelectronics. *Colloid. Polym. Sci.* **1995**, *273*, 101-117.

Semrau, S.; Schmidt, T. Membrane heterogeneity–from lipid domains to curvature effects. *Soft Matter* **2009**, *5*, 3174-3186.

Sezgin, E.; Levental, I.; Mayor, S.; Eggeling, C. The mystery of membrane organization: composition, regulation and roles of lipid rafts. *Nature reviews Molecular cell biology* **2017**, *18*, 361.

Sezgin, E.; Schwille, P. Fluorescence techniques to study lipid dynamics. *Cold Spring Harbor perspectives in biology* **2011**, *3*, a009803.

Shang, X.; Liu, Y.; Yan, E.; Eisenthal, K. B. Effects of counterions on molecular transport across liposome bilayer: probed by second harmonic generation. *J. Phys. Chem. B* **2001**, *105*, 12816-12822.

Sharifian Gh, M.; Wilhelm, M. J.; Dai, H.-L. Label-free optical method for quantifying molecular transport across cellular membranes in vitro. *J. Phys. Chem. Lett.* **2016**, *7*, 3406-3411.

Sharifian Gh, M.; Wilhelm, M. J.; Moore, M.; Dai, H.-L. Spatially Resolved Membrane Transport in a Single Cell Imaged by Second Harmonic Light Scattering. *Biochemistry* **2019**, *58*, 1841-1844.

Sharma, A.; Sharma, U. S. Liposomes in drug delivery: progress and limitations. *Int. J. Pharm.* **1997**, *154*, 123-140.

Shih, Y.-L.; Huang, L.-T.; Tu, Y.-M.; Lee, B.-F.; Bau, Y.-C.; Hong, C. Y.; Lee, H.-l.; Shih, Y.-P.; Hsu, M.-F.; Lu, Z.-X. Active Transport of Membrane Components by Self-Organization of the Min Proteins. *Biophys. J.* **2019**, *116*, 1469-1482.

Shrestha, H.; Bala, R.; Arora, S. Lipid-based drug delivery systems. *Journal of pharmaceutics* **2014**, *2014*.

Silvers, W. C.; Prasai, B.; Burk, D. H.; Brown, M. L.; McCarley, R. L. Profluorogenic reductase substrate for rapid, selective, and sensitive visualization and detection of human cancer cells that overexpress NQO1. *J. Am. Chem. Soc.* **2013**, *135*, 309-314.

Smith, D.; Artursson, P.; Avdeef, A.; Di, L.; Ecker, G. F.; Faller, B.; Houston, J. B.; Kansy, M.; Kerns, E. H.; Kramer, S. D. Passive lipoidal diffusion and carrier-mediated cell uptake are both important mechanisms of membrane permeation in drug disposition. *Mol. pharmaceutics* **2014**, *11*, 1727-1738.

Smith, D.; Artursson, P.; Avdeef, A.; Di, L.; Ecker, G. F.; Faller, B.; Houston, J. B.; Kansy, M.; Kerns, E. H.; Kramer, S. D. Passive lipoidal diffusion and carrier-mediated cell uptake are both important mechanisms of membrane permeation in drug disposition. *Mol. pharmaceutics* **2014**, *11*, 1727-1738.

Souaille, M.; Roux, B. t. Extension to the weighted histogram analysis method: combining umbrella sampling with free energy calculations. *Comput. Phys. Commun.* **2001**, *135*, 40-57.

Srivastava, A.; Eisenthal, K. B. Kinetics of molecular transport across a liposome bilayer. *Chem. Phys. Lett.* **1998**, *292*, 345-351.

Steigerwald, M. L.; Brus, L. E. Semiconductor crystallites: a class of large molecules. *Acc. Chem. Res.* **1990**, *23*, 183-188.

Stroberg, W.; Schnell, S. On the origin of non-membrane-bound organelles, and their physiological function. *Journal of theoretical biology* **2017**, *434*, 42-49.

Szekely, P.; Dvir, T.; Asor, R.; Resh, R.; Steiner, A.; Szekely, O.; Ginsburg, A.; Mosenkis, J.; Guralnick, V.; Dan, Y. Effect of temperature on the structure of charged membranes. *J. Phys. Chem. B* **2011**, *115*, 14501-14506.

Thibaudau, F. Ultrafast photothermal release of DNA from gold nanoparticles. *The journal of physical chemistry letters* **2012**, *3*, 902-907.

Tran, R. J.; Sly, K. L.; Conboy, J. C. Applications of surface second harmonic generation in biological sensing. *Annu. Rev. Anal. Chem.* **2017**, *10*, 387-414.

Troiano, J. M.; McGeachy, A. C.; Olenick, L. L.; Fang, D.; Liang, D.; Hong, J.; Kuech, T. R.; Caudill, E. R.; Pedersen, J. A.; Cui, Q.; Geiger, F. M. Quantifying the electrostatics of polycation–lipid bilayer interactions. *J. Am. Chem. Soc.* **2017**, *139*, 5808-5816.

Van Meer, G.; Voelker, D. R.; Feigenson, G. W. Membrane lipids: where they are and how they behave. *Nat Rev Mol Cell Biol.* **2008**, *9*, 112.

Varshney, G.; Kintali, S.; Das, K. Effect of Curcumin Addition on the Adsorption and Transport of a Cationic Dye across DPPG-POPG Liposomes Probed by Second Harmonic Spectroscopy. *Langmuir* **2017**, *33*, 8302-8310.

Walter, A.; Gutknecht, J. Permeability of small nonelectrolytes through lipid bilayer membranes. *J. Membr. Biol.* **1986**, *90*, 207-217.

Wang, H.; Yan, E. C.; Borguet, E.; Eisenthal, K. B. Second harmonic generation from the surface of centrosymmetric particles in bulk solution. *Chem. Phys. Lett.* **1996**, *259*, 15-20.

Wang, H.; Yan, E. C.; Liu, Y.; Eisenthal, K. B. Energetics and population of molecules at microscopic liquid and solid surfaces. *J. Phys. Chem. B* **1998**, *102*, 4446-4450.

Wang, J.; Wolf, R. M.; Caldwell, J. W.; Kollman, P. A.; Case, D. A. Development and testing of a general amber force field. *J. Comput. Chem.* **2004**, *25*, 1157-1174.
Weller, H. Colloidal semiconductor q-particles: chemistry in the transition region between solid state and molecules. *Angewandte Chemie International Edition in English* **1993**, *32*, 41-53.

Wheeler, R. J.; Hyman, A. A. Controlling compartmentalization by non-membrane-bound organelles. *Philosophical Transactions of the Royal Society B: Biological Sciences* **2018**, *373*, 20170193.

Wilhelm, M. J.; Dai, H. L. Molecule-Membrane Interactions in Biological Cells Studied with Second Harmonic Light Scattering. *Chemistry–An Asian Journal* **2019**.

Wilhelm, M. J.; Sharifian Gh, M.; Dai, H.-L. Chemically Induced Changes to Membrane Permeability in Living Cells Probed with Nonlinear Light Scattering. *Biochemistry* **2015**, *54*, 4427-4430.

Wilhelm, M. J.; Sharifian Gh, M.; Dai, H.-L. Influence of molecular structure on passive membrane transport: A case study by second harmonic light scattering. *J. Chem. Phys.* **2019**, *150*, 104705.

Wilhelm, M. J.; Sheffield, J. B.; Gonella, G.; Wu, Y.; Spahr, C.; Zeng, J.; Xu, B.; Dai, H.-L. Real-time molecular uptake and membrane-specific transport in living cells by optical microscopy and nonlinear light scattering. *Chem. Phys. Lett.* **2014**, *605*, 158-163.

Yamashita, S.; Fukushima, H.; Niidome, Y.; Mori, T.; Katayama, Y.; Niidome, T. Controlled-release system mediated by a retro Diels–Alder reaction induced by the photothermal effect of gold nanorods. *Langmuir* **2011**, *27*, 14621-14626.

Yan, E. C.; Eisenthal, K. B. Effect of cholesterol on molecular transport of organic cations across liposome bilayers probed by second harmonic generation. *Biophys. J.* **2000**, *79*, 898-903.

Yan, E. C.; Liu, Y.; Eisenthal, K. B. New method for determination of surface potential of microscopic particles by second harmonic generation. *J. Phys. Chem. B* **1998**, *102*, 6331-6336.

Zeng, J.; Eckenrode, H. M.; Dai, H.-L.; Wilhelm, M. J. Adsorption and transport of charged vs. neutral hydrophobic molecules at the membrane of murine erythroleukemia (MEL) cells. *Colloids Surf., B* **2015**, *127*, 122-129.

Zeng, J.; Eckenrode, H. M.; Dounce, S. M.; Dai, H.-L. Time-resolved molecular transport across living cell membranes. *Biophys. J.* **2013**, *104*, 139-145.

Zhao, K.; Taylor, J. E.; Haber, L. H.; Zhang, J.; Plummer, E. W.; Saghayezhian, M. Probing the interfacial symmetry using rotational second-harmonic generation in oxide heterostructures. *The Journal of Physical Chemistry C* **2019**, *123*, 23000-23006.

Zhu, Y.; Liu, H.; Li, F.; Ruan, Q.; Wang, H.; Fujiwara, M.; Wang, L.; Lu, G. Dipolar molecules as impellers achieving electric-field-stimulated release. *J. Am. Chem. Soc.* **2010**, *132*, 1450-1451.

Vita

Prakash Hamal studied Chemistry at Southeastern Louisiana University where he received his B.S. in Chemistry with a concentration in Biochemistry in 2016. During his Bachelor's degree, he worked with Professor Thomas Sommerfeld and investigated the resonance energies and lifetimes of temporary anions using standard quantum chemistry methods. He joined Professor Louis Haber's research group in the Department of Chemistry at Louisiana State University in the fall semester of 2016, studying ultrafast and nonlinear spectroscopy of nanomaterials. Upon completion of his Ph.D., he will be working at Intel Corporation as a Thin Films Module Engineer.